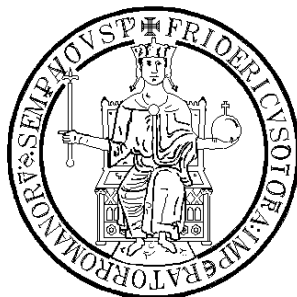


Università degli Studi di Napoli “Federico II”

Facoltà di Scienze Matematiche Fisiche e Naturali



***DOTTORATO DI RICERCA IN SCIENZE CHIMICHE
XXIV CICLO***

**MICROSTRUCTURAL CHARACTERIZATION
OF PHOSPHOLIPID MEMBRANES AND
STUDY OF THEIR INTERACTION WITH
PEPTIDES AND PROTEINS**

***Dottorando
Giuseppe Vitiello***

Tutore

Dr. Gerardino D'Errico

Relatore

Prof.ssa Delia Picone

Coordinatore

Prof. Lucio Previtera

Index

Introduction	5
 Chapter 1 – Biomembranes	
1.1 – Introduction.....	9
1.2 – Lipid composition	9
1.3 – Microstructural properties.....	12
1.4 – The role of cholesterol	13
1.5 – Lipid rafts.....	14
1.6 – Membranes formed by lipopolysaccharides	16
1.7 – Biomimicking systems.....	18
1.7.1 – Liposomes.....	18
1.7.1 – Supported Lipid Bilayers	21
<i>References</i>	24
 Chapter 2 – Role of lipids in membrane processes	
2.1 – Lipid-protein interactions	26
2.2 – Viral fusion	27
2.2.1 – Feline and Human Immunodeficiency Viruses	30
2.2.2 – Herpes simplex virus	32
2.3 – Biomembranes involvement in the β -amyloid aggregation process.....	34
<i>References</i>	40
 Chapter 3 – Materials and Methods	
3.1 – Materials	44
3.1.1– Lipid components	44

3.1.2 – Peptides	48
3.1.3 – Solvents.....	51
3.2 – Methods	51
3.2.1 – Liposomes preparation.....	51
3.2.2 – Supported Lipid Bilayers preparation.....	52
3.2.3 – Electron Spin Resonance spectroscopy measurements	53
3.2.4 – Neutron Reflectivity measurements.....	54
3.2.5 – Circular Dichroism experiments.....	55
3.2.6 – Spectrofluorimetric experiments.....	55
3.2.7 – Dynamic Light Scattering measurements	57
3.2.8 – Small Angle Neutron Scattering measurements	58
<i>References</i>	60

Chapter 4 – Results and Discussion *Part I*: Microstructural characterization of phospholipid membranes

4.1 – Introduction.....	63
4.2 – Lysophosphatidylcholine micellar aggregates: the structural basis for their use as biomembrane mimics	63
4.3 – Effect of cholesterol on the structure of POPC and DOPC membranes structure.....	76
4.4 – Characterization of PUFA-containing lipid membranes	83
4.5 – Characterization of liposomes formed by lipopolysaccharides from <i>Burkholderia cenocepacia</i> , <i>Burkholderia multivorans</i> and <i>Agrobacterium tumefaciens</i> : from the molecular structure to the aggregate architecture.....	86
<i>References</i>	100

Chapter 4 – Results and Discussion *Part II*: Lipid membrane-peptide

interactions

4.1– Interaction of short modified peptides deriving from gp36 of FIV with phospholipid membranes.....	104
4.2 – Interaction of the C8 peptide with POPC membranes.....	114
4.3 – Role of lipid composition on the C8-membranes interaction.....	130
4.4 – Interaction of the MPER domain of HIV gp41 with lipid bilayers.	141
4.5 – Interaction of peptides deriving from different domains of HSV-1 gH and gB glycoproteins with lipid membranes.	151
4.6 – Interaction of gH626-644 and gB632-650 peptides deriving from gH and gB glycoproteins with biomembranes.....	161
4.7 – Characterization of the membrane interaction of the two fusion loops of glycoprotein B from HSV-type I.	173
4.8 – Interaction of gH625 peptide from HSV-1 with lipid membranes.....	177
4.9 – Clickable functionalization of liposomes with the gH625 peptide from HSV-1 for intracellular delivery.....	185
4.10 – Membrane charge dependent states of the β -amyloid fragment A β (16-35) with differently charged micelle aggregates.	188
4.11 – Role of β -sheet breaker peptides in preventing A β self-aggregation.	194
4.12 – Interaction of a β -sheet breaker peptide with lipid membranes.....	194
4.13 – The iA β 5p β -breaker peptide regulates the interaction of the A β (25–35) fragment with lipid bilayers through a cholesterol-mediated mechanism.....	205
<i>References</i>	213
Conclusions	217
Appendix	219

INTRODUCTION

In the present thesis, a wide structural and functional study on biomembranes is presented. The research has been focused on the micro- and mesostructure of phospholipid bilayers and on their interactions with different peptides which are involved in important biological process. Particularly, the role of lipid composition and self-organization in regulating the membrane biophysical properties has been investigated.

Biomembranes externally define the cells and are constituted by a phospholipid bilayer in which many proteins, playing a variety of functional roles, are embedded. Indeed, beyond the role of interface between the intra and extracellular domains, biological membranes also play essential functions as selective filters and as area of cellular communication, thanks to the presence of the specific proteins which allow the exchange of information between the cytoplasm and the extracellular environment. The functionality of membrane-associated proteins is influenced by the surrounding lipids, either directly through molecular interactions or indirectly by the modulation of bilayer structural order and rigidity. For this reason, biomembrane lipid composition play a key role in many biological processes.

One of the most important processes involving lipid composition is the membrane fusion. This process is a decisive step of the cells natural cycle of life (e.g. endo- and exocytosis processes) but it is also crucial in the viral infection by “enveloped” viruses. These viruses are constituted by an additional lipid membrane, named envelope, that wraps the proteic capsid in which the viral DNA or RNA is contained. In the envelope specific glycoproteins with complex structural conformation are inserted, favoring the membrane fusion process. The most common examples of enveloped viruses are the Hepatitis C, Herpes Simplex, H1N1, and Human Immunodeficiency viruses and their analogues.

Through the fusion between the target cell and viral membranes, these viruses may introduce their genetic material into the host cell and then the replication can start. At the moment, a molecular comprehension of the physical mechanisms of membrane fusion is incomplete. Particularly, while many details concerning the role of glycoproteins are defined, information about the phospholipid counterpart is lacking.

Another important biological process in which biomembranes play a key role is the self-aggregation of the β -amyloid ($A\beta$) peptide with the consequent formation of fibrils and amyloid plaques, the principal hallmarks of the Alzheimer's Disease. Despite the large number of studies on this subject, the mechanism of $A\beta$ fibrillization has not been fully understood. Many studies have suggested that lipid membranes have a decisive role in favouring the β -amyloid aggregation. However, this point is still highly controversial.

In this scenario, the experimental study presented in this thesis is aimed to contribute to the analysis of the fine interplay between lipids and proteins/peptides in regulating processes involving biomembranes. The experimental work has been divided in two parts. In the former one, the attention has been focused on the formulation and the contemporary physico-chemical characterization of biomimicking lipid systems, as liposomes and supported lipid bilayers. Different classes of lipids were considered, including zwitterionic and anionic, mono- and bichained, mono-, bi- and polyunsaturated phospholipids. Cholesterol and sphingolipids were also used in order to discriminate the effect of lipid composition in modulating the microstructural properties of lipid bilayers and their mesoscopic organization. In the latter part of the research, the interaction of these lipid systems with peptides deriving from different viral glycoproteins as well as from the $A\beta$ peptide was analyzed.

The whole investigation was realized by a combined experimental approach in which many physico-chemical techniques were used in order to obtain a wide description of the systems structure and behavior. In particular, Electron Spin Resonance (ESR)

spectroscopy and Neutron Reflectivity (NR) have provided information about the lipid ordering and dynamics in the bilayer, while spectrofluorimetry and circular dichroism (CD) measurements have allowed the direct monitoring of the peptides behavior in the presence of membrane environment. Finally, Dynamic Light Scattering (DLS) and Small Angle Neutron Scattering (SANS) experiments have permitted a mesoscopic analysis of the different lipid supramolecular aggregates.

CHAPTER 1

Biomembranes

1.1 Introduction

The cellular membrane is the structure that defines the exterior of the cell, separating the intracellular from the extracellular compartment. In addition to the structural role, the plasma membrane has the essential function of selective filter, due to its position of interface favoring the passage of some substances rather than others. Liposoluble molecules move freely to the cytoplasm, while those not soluble are unable to cross this barrier without the contribute of specific transport proteins (carrier) or proteic channels. In second hand, the cellular membrane is the surface that makes possible the cellular communication, through the presence of specific proteins that allow the exchange of information between the cytoplasm and the extracellular environment.

1.2 Lipid composition

The structural organization of biological membranes consists principally of a lipid bilayer which is characterized by a thickness ~ 5 nm in which a variety of specific and dynamic proteins are inserted (Figure 1.2.1).

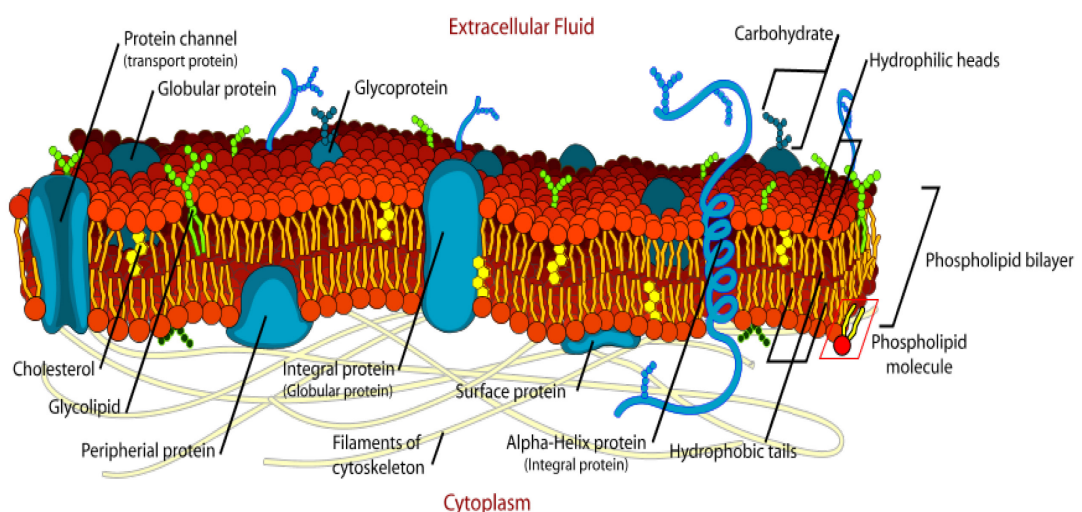


Figure 1.2.1 – The biomembrane structure [1].

Concerning the lipid content, it's possible to identify three principal classes of lipids which are present in the membrane of eukaryotic cells. These are: glycerophospholipids, sphingolipids, and cholesterol or closely-related sterols (Figure 1.2.2). The glycerophospholipids present a glycerol backbone, two ester-linked fatty acyl chains, and a phosphorylated alcohol, typically phosphorylcholine (PC), phosphoethanolamine (PE) or phosphorylserine (PS). The fatty acyl chains usually present an even number of carbon atoms, typically between 16 and 20 in total, with one hydrocarbon chain being saturated and the other unsaturated. There is also a small fraction of lysophospholipid (less than 5 mol% of the total phospholipids) constituted by a single chain, among which the most important class is represented by lysophosphatidylcholines (lysoPC).

The sphingolipids derive from the aliphatic amino alcohol sphingosine and contain a single amide-linked fatty acyl chain, which is usually saturated and may contain up to 24 carbon atoms, and either a phosphorylated alcohol, or one or more sugar molecules linked to the hydroxyl terminus of the sphingosine backbone. The sphingolipids comprise a complex range of lipids, the sphingomyelin (SM) being the most important example. It has structural similarities to phosphocholines but it has very different physical and biological properties.

Finally, cholesterol (CHOL) consists of a fused cyclic four-ring structure containing a single polar hydroxyl group and an isooctyl side chain, the cyclic ring system being fairly planar and rigid.

The membranes of eukaryotic cells present unusual higher levels of sphingolipids and cholesterol, and lower levels of glycerophospholipids than do other cell membrane systems. Although the relative proportions of these three lipid classes vary according to species and cell type in vertebrates, glycerophospholipids are typically present at levels of 40–60 mol.%, sphingolipids at levels of 10–20 mol.% and cholesterol at levels of 30–40 mol.% of the total plasma membrane lipids [2].

Another important property of the biological membranes is their transverse lipid compositional asymmetry. In fact, the lipid composition of the outer and inner leaflets of the bilayer is different: the zwitterionic glycerophospholipid phosphatidylcholine and the zwitterionic sphingophospholipid sphingomyelin are enriched in the outer monolayer, while the zwitterionic glycerophospholipid phosphatidylethanolamine and the anionic glycerophospholipid phosphatidylserine are enriched in or restricted to the inner leaflet, respectively [3].

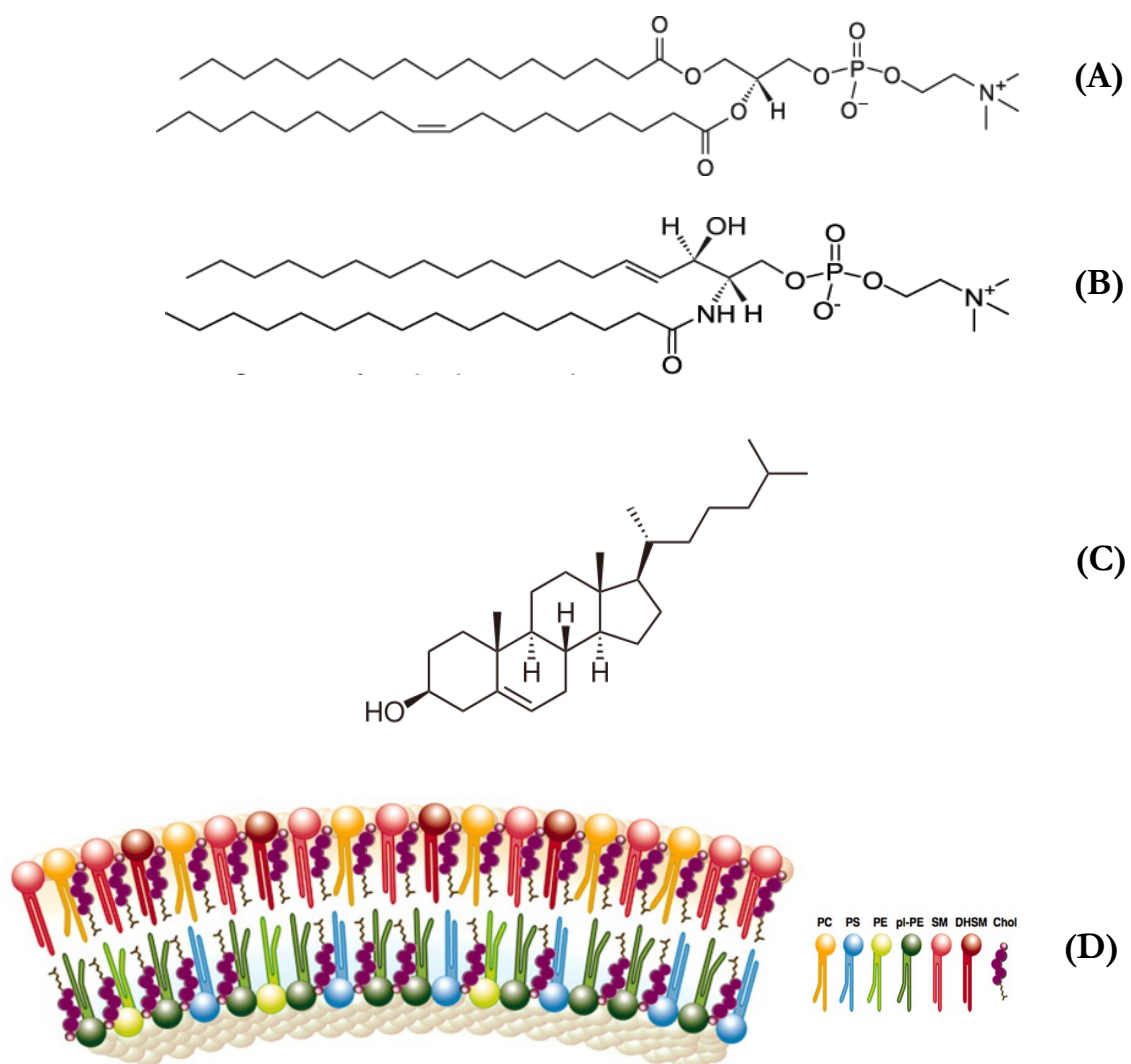


Figure 1.2.2 –The chemical structures of representatives of the three major classes of lipids found in biomembranes: phosphatidylcholine (A), sphingomyelin (B) and cholesterol (C). An example of lipid membranes with a compositional asymmetry is shown in snapshot (D).

The transverse distribution of cholesterol is less well understood, but because of its high rate of flip-flop between the inner and outer leaflets and roughly equal amounts of glycerol- and sphingolipids present in each leaflet, cholesterol is usually assumed to be roughly equally distributed across the lipid bilayer. However, CHOL shows a relatively higher affinity for SM and PC as compared to PS and PE [3]. For this reason, it is possible that cholesterol could be enriched to some degree in the outer lipid leaflet.

1.3 Microstructural properties

Biomembranes are not static but dynamic structures, characterized by a degree of fluidity. In physiological conditions, both the lipids and proteins molecules are able to move within their own monolayer. The main factors which influence the biomembrane fluidity are: i. temperature; ii. length of fatty acids; iii. degree of unsaturation of fatty acid tails of phospholipids; iv. characteristics of the polar head; v. concentration of cholesterol in the membrane.

Lipid membranes are characterized by a thermoreversible phase transition, during which the bilayer moves from a gel (L_{β}) to a fluid or liquid-crystalline (L_{α}) phase (Figure 1.3.1). This transition is an endothermic process and occurs in a range around the value of the main transition temperature (T_m). In particular, if the bilayer is made of pure lipids, the T_m is a well-defined values of temperature, otherwise for mixtures it's a wide range.

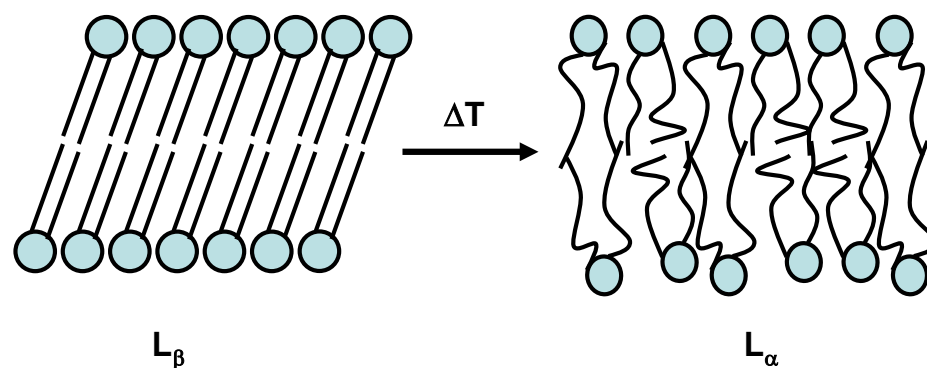


Figure 1.3.1 - The transition from the gel (L_{β}) to the liquid-crystalline phase (L_{α}).

The T_m depends on the type of phospholipid, that is the nature of the polar head, the length of acyl chains, increasing the number of carbon atoms, and the number of unsaturation, decreasing with the increase in the number of double bonds.

In the L_β phase, the phospholipid chains are in the fully extended all-trans conformation, the cross-sectional area of the phospholipid molecules is minimal, the thickness of the phospholipid bilayer is maximal, and both intra- and intermolecular motion are severely restricted. In contrast, in the L_α phase, the phospholipid chains contain some gauche rotational conformers, the cross-sectional area of the lipid molecules increase considerably, the phospholipid bilayer thins substantially, and relatively high rates of both intra- and intermolecular motion are present.

In the absence of cholesterol and under physiologically relevant conditions, the lipid bilayer exists at least predominantly if not exclusively in the L_α phase, which is required for normal cell growth and membrane function to occur. The mixture of glycerol- and sphingolipids of animal plasma membranes would be expected to exist as a mixture of L_α and L_β phases in the absence of cholesterol, due to the lower L_β/L_α phase transition temperatures (approx. 0 °C) of the unsaturated glycerophospholipids and the higher phase transition temperatures of the more saturated sphingolipids (approx. 37 °C) [4].

1.4 The role of cholesterol

One of the major effects of the incorporation of progressively increasing amounts of cholesterol into lipid bilayers is to reduce the enthalpy of the L_β/L_α phase transition, which is completely eliminated at 50 mol.% cholesterol content [5]. It also causes other structural variations: a decrease (increase) of the cross-sectional area of the phospholipid molecule in the L_α (L_β) phase, an increase (decrease) of the thickness of the phospholipid bilayer in the

L_α (L_β) phase, and an increase (decrease) of the orientational order and decrease (increase) of the rates of motion of the hydrocarbon chains in the L_α (L_β) phase.

The progressive addition of cholesterol also increases the mechanical rigidity and cohesiveness, reducing the permeability of phospholipids bilayers in the L_α phase, while also reducing the rotational and lateral diffusion rates of the phospholipid molecules. The addition of increasing amounts of cholesterol progressively induces the formation of a phase which has properties generally intermediate between those of gel (L_β) phase and fluid (L_α) phospholipid bilayers. This phase is termed “liquid-ordered” (or perhaps better “liquid-crystallineordered”) phase, denoted as L_o , to describe this intermediate state, while the L_α phase is termed the ‘liquid-disordered’ (better the “liquid-crystalline disordered”) phase and it is denoted as L_d (Figure 1.4.1) [5].

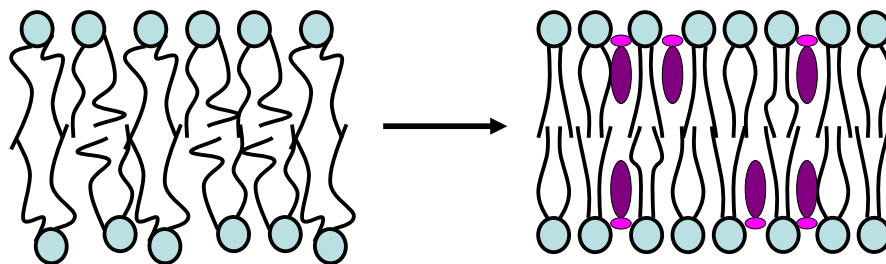


Figure 1.4.1 - The cholesterol induces the transition from the liquid-disordered (L_d) phase (*on the left*) to the liquid-ordered (L_o) phase (*on the right*).

1.5 Lipid rafts

For a long time, the idea was diffused that the lipids were randomly organized in the biological membranes, with the integral proteins floating in a two-dimensional lipid ‘sea’ and freely diffusing laterally in the lipid matrix unless their movements were restricted by associations with other cellular components. Since the early 1970s, many experimental evidences suggested that lipids could laterally segregate in membranes under certain conditions, forming distinct lipid domains with specific structural characteristics [6].

At nearly the same time, some studies proposed a ‘plate model’ of membrane structure in which the separation of ordered regions from the disordered regions (fluid) was a natural consequence of specific intermolecular interaction and lattice deformation. About this hypothesis, there were many conflicting positions and many scientists did not pay much attention to this new possibility until the 1997, when Simons and Ikonen postulated the “rafts hypothesis”, suggesting the existence of “lipid rafts”, which are microdomains enriched in sphingolipids and cholesterol that would be associated with specific proteins involved in cellular functions such as intracellular lipid traffic and cell signalling [7]. These rafts were originally conceived as relatively long-lived domains of appreciable size, which are depleted in phospholipids and many transmembrane proteins but which are enriched in cholesterol, sphingolipids and lipid-anchored proteins (see Figure 1.5.1). These discrete lipid raft domains were postulated to exist in a relatively ordered lamellar liquid-crystalline (L_o) phase while the continuous non-raft regions of the membrane exist in a relatively disordered lamellar liquid-crystalline (L_d) phase. Moreover, the different physical properties of the L_o and L_d phases were postulated to play a key role in the lateral segregation of the various classes of membrane proteins [8]. In this scenario, cholesterol was indicated to play an important role, facilitating a fluid–fluid lateral phase separation of glycerophospholipid- and sphingolipidenriched phases into separate domains, while simultaneously inhibiting the formation of sphingolipid-enriched L_β phases.

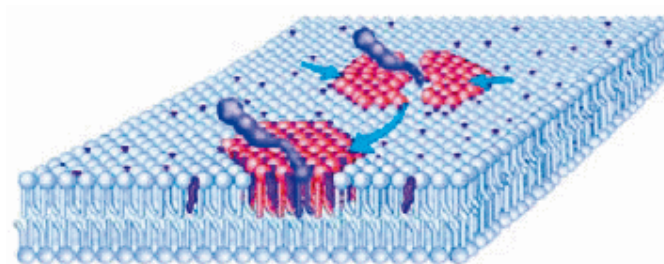


Figure 1.5.1 - A membrane with “lipid raft” domains.

In current research, lipid rafts are also considered as important protagonists in the sorting and targeting of lipids and proteins to various membrane systems, in signal transduction across the plasma membrane, and in many other cellular functions.

1.6 Membranes formed by lipopolysaccharides

Lipopolysaccharides (LPS) are heat-stable complex amphiphilic macromolecules consisting of a glycolipid moiety and a saccharide portion covalently linked which present important components of Gram-negative bacteria membranes. These bacteria possess a multilayer architecture of their cell membrane (Figure 1.6.1) [9].

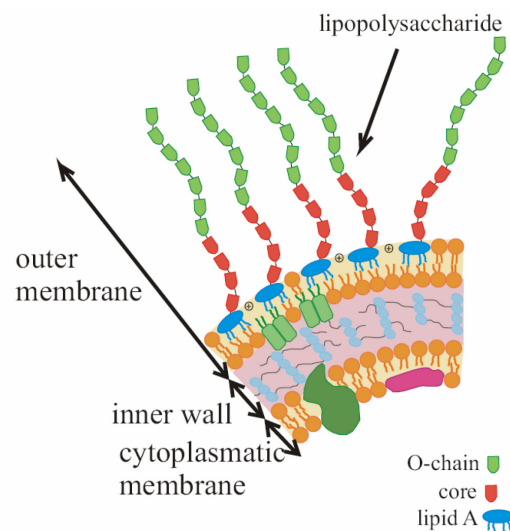


Figure 1.6.1 - Schematic representation of a Gram-negative cell wall.

The internal layer is quite thin (~3 nm) and is constituted by peptidoglycan, a polymer consisting of saccharide backbones cross-linked by peptide side chains, forming a mesh-like local microstructure. In contrast, the most external shell of these bacteria is formed by a thicker wall (~7 nm) whose composition is different among the two sides. The internal side is mainly characterized by the presence of glycerol-based phospholipids, whereas the external side is composed of LPS. LPS are also called endotoxins because, once released from the membrane, they play a key role in the pathogenesis of Gram-

negative infections due to their immunostimulatory properties. They are indispensable for the bacterial growth and viability and are responsible for the correct assembly of the membrane and its structural integrity, being able to protect the bacterial cell from physical and chemical attacks. LPS are composed of three parts:

- a glycolipid portion known as lipid A. This part is composed of a disaccharide with multiple fatty acid tails, embedded in the lipid bilayer while the rest of the LPS projects toward the external environment;

- a core oligosaccharide portion, covalently attached to the lipid A. In the core region the 3-deoxy-D-manno-octulosonic acid residue (Kdo) is always present as well as, in most cases, heptose residues;

- an external O-specific long polysaccharide chain, also known as O-chain, that extends from the core oligosaccharide. Although from a chemical point of view, the O-chain is essentially similar to the core oligosaccharide, they are biologically distinct. Indeed, the O-chain is a proper polysaccharide with a repeating oligosaccharide unit.

Usually, the presence or the absence of the O-chain determines whether the LPS are considered smooth or rough type, respectively, depending on the appearance of the bacterial colonies on agar plates. Full length O-chains make the LPS smooth type (S-LPS) whereas their absence makes the LPS rough type (R-LPS, also known as LOS, lipooligosaccharide) [10]. The LPS membranes are stabilized by electrostatic interaction of the negatively charged groups present in the lipid A and in the core region (phosphate groups, uronic acids) with divalent cations (Mg^{2+} , Ca^{2+}), which contribute to cross link the LPS molecules. Consequently, while a normal glycerophospholipid bilayer is a flexible and fluid system, the LPS layer is semi-rigid and displays a highly ordered structure. These membranes show low permeability toward hydrophobic solutes, explaining the lower susceptibility of Gram-negative microorganisms, with respect to Gram-positive, to hydrophobic host released antimicrobial peptides and to negatively charged antibiotic

molecules [11]. For these reason, structural and functional studies on lipid membranes formed by LPS can contribute to deepen the issue of the stability, low-permeability and resistance of Gram-negative outer membrane.

1.7 Biomimicking systems

From the previous description, it is evident that biological membranes are characterized by high complexity. This aspect has motivated the development of a wide variety of simpler model systems whose size, geometry, and composition can be tailored with great precision in order to realize lipid systems with an high biomimic character, useful to study many process in which biomembranes are directly involved. Different biomimic systems have been realized and they principally include bilayers in the form of liposomes (also called vesicles), with a large size range and planar supported lipid bilayers usually interacting directly with a solid substrate.

1.7.1 Liposomes

Liposomes are hollow microspheres formed by one or more phospholipid bilayers (Figure 1.7.1.1). Thanks to their structure and composition, they are considered good models of the cell membrane and are used in the study of interactions with proteins involved in various pathological mechanisms.

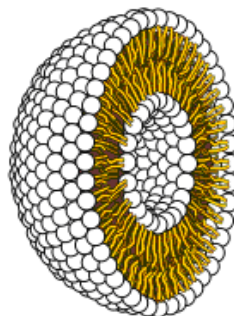


Figure 1.7.1.1 - A liposome formed by a single lipid bilayer.

Liposomes are generally classified according to their structural characteristics. In particular, the size and lamellarity, which indicates the number of lipid bilayers that constitute the liposome, are considered. In fact, liposomes can be composed by one or several concentric bilayers forming unilamellar or multilamellar structures, respectively, with sizes ranging between 20nm and hundreds of nanometers, in which each bilayer can have a thickness ranging between a few units and tens of nanometers (Figure 1.7.1.2).

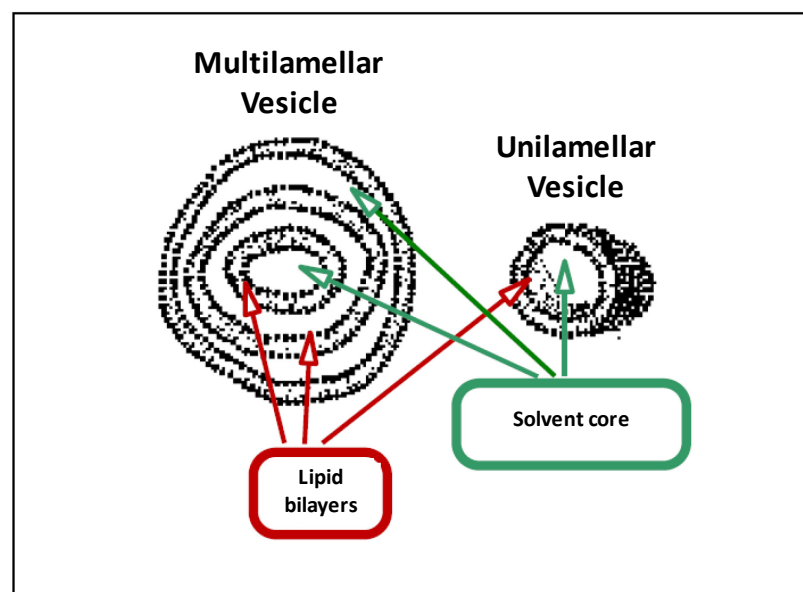


Figure 1.7.1.2 - Unilamellar and multilamellar structures.

According to on the physical structure, the number of lamellae and the size, liposomes are generally classified in four classes:

- MLVs = large multilamellar vesicles;
- SUVs = small unilamellar vesicles;
- LUVs = large unilamellar vesicles;
- GUVs = giant unilamellar vesicles.

MLVs are composed by concentric bilayers, trapping interposed layers of water, and possess relatively large diameters ($> 400\text{nm}$). SUVs are prepared from MLVs, which are transformed into unilamellar vesicles by specific techniques such as sonication or by extrusion at low or medium pressure through pores of finite size. The values of the diameters ranges between 20-100 nm, although this depends on the type of phospholipid. The radius of curvature of these vesicles are so small that the ratio of the number of molecules in the phospholipid monolayer inside and outside is about 1:2.

LUVs are similar to SUVs, but they have larger diameters, which generally vary between 100 and 500 nm (Figure 1.7.1.3).

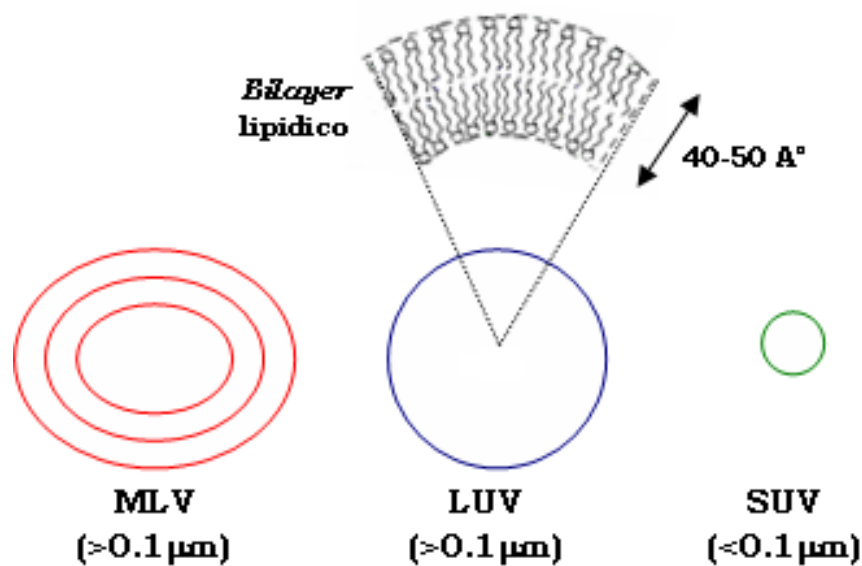


Figure 1.7.1.3 – Vesicle sizes

GUVs are large enough (several tens of micrometres) but are relatively fragile, time consuming to make and can only be produced in limited yield compared to SUVs.

The phospholipids nature and the method of preparation and isolation determine the characteristics of specific liposomes.

1.7.2 Supported Lipid Bilayers

Supported lipid bilayers (SLBs), functionalized with membrane constituents, are interesting cell-mimicking templates for studies of membrane-mediated processes.

SLBs can be formed with a wide range of lipid compositions and can be supported on several different materials, including unmodified or chemically modified metals and metal oxides. In order to support a high quality membrane (i.e. little or no defects and high lipid mobility) the surface should be hydrophilic, smooth, and clean. The best substrates are fused silica, borosilicate glass, mica, and oxidized silicon. Attempts have been made to deposit supported bilayers on single crystals of TiO_2 and SrTiO_2 as well as on thin films of SiO_2 on LiNbO_3 crystals. Thin films can be used as solid supports as observed with TiO_2 , indium-tin-oxide, gold, silver, and platinum. However, silica-based materials are by far the most commonly used substrates.

Lipid bilayers supported by solid substrates are more robust and stable than other bio-mimic systems and they can be studied using surface specific analytical techniques not available for other kind of lipid membranes. In solid supported systems membrane fluidity is maintained by a 10–20 Å layer of water trapped between the substrate and the bilayer (Figure 1.7.2.1).

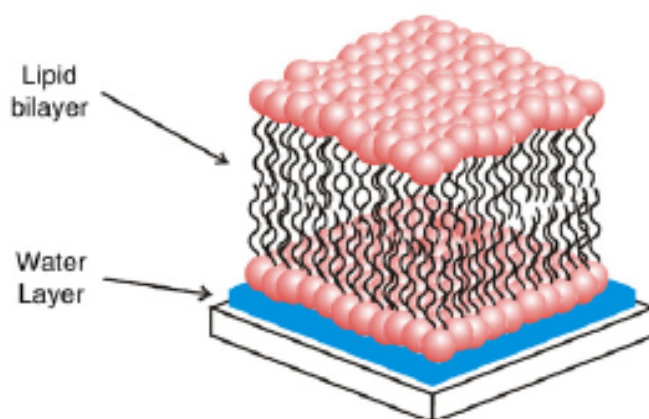


Figure 1.7.2.1- A single supported lipid bilayer [12].

SLBs can be obtained with a variety of techniques but there are three general methods for their formation on planar supports [12]: i. Langmuir-Blodgett methods, either alone or combined with Langmuir-Schaefer horizontal deposition; ii. vesicle fusion on a naked solid substrate; iii. vesicle fusion on a pre-covered solid substrate.

The first method involves the transfer of a lower leaflet of lipids from the air–water interface by the Langmuir–Blodgett technique (Figure 1.7.2.2a). This is followed by the transfer of an upper leaflet by the Langmuir–Schaefer procedure, which involves horizontally dipping the substrate to create the second layer.

A second method of supported bilayer formation is the adsorption and fusion of vesicles from an aqueous suspension to the substrate surface. Vesicle fusion to a substrate is one of the most convenient ways of preparing supported bilayers, as it does not require sophisticated equipment and reliably produces high quality supported bilayers (Figure 1.7.2.2b).

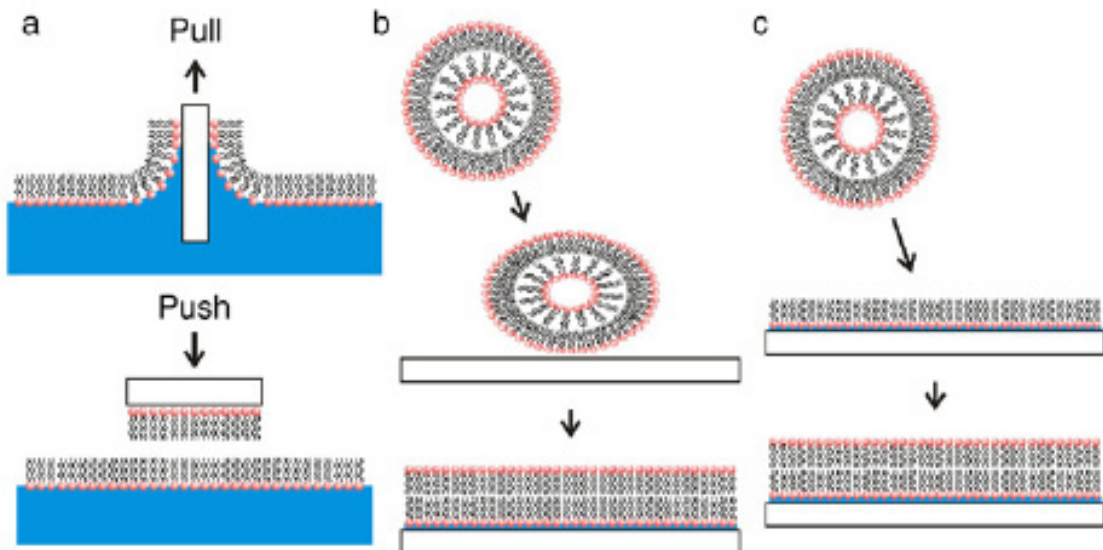


Figure 1.7.2.2 - Common techniques for the formation of supported lipid bilayers: (a) the Langmuir–Blodgett technique is carried out by pulling a hydrophilic substrate through a lipid monolayer and sequentially pushing it horizontally through another lipid monolayer; (b) vesicles adsorb and spontaneously fuse to the surface to form a SLB; (c) a combination of the Langmuir–Blodgett and vesicle fusion processes [12].

Also, a combination of the two methods can be employed by first transferring a monolayer via the Langmuir–Blodgett technique followed by vesicle fusion to form the upper layer (Figure 1.7.2.2c).

Each of the three deposition methods has its particular advantages and disadvantages. The main advantage in using solid supports is clearly the easy preparation and the increase in stability of the phospholipid bilayers. Almost equally important is the ability to probe interactions that occur at the membrane surface with powerful analytical techniques that are surface specific. While solid supported phospholipid bilayers are somewhat limited in terms of their substrate compatibility, their major disadvantage is that the supported membrane is not truly decoupled from the underlying substrate. Indeed, the system may not prevent transmembrane proteins from interacting unfavorably with the underlying substrate. Such interactions with the surface can cause proteins in the membrane to become immobile and hinder their function.

In SLB systems only the upper lipid leaflet of the bilayer is exposed to the bulk. For this reason, these systems are very useful to study the adsorption or penetration processes of molecules dissolved in the water phase, ensuring a precise control of the phospholipid molecular density and bilayer thickness.

References

- [1] <http://www.cellbiology.med.unsw.edu.au>
- [2] van Meer G. Lipid traffic in animal cells, *Annu. Rev. Cell. Biol.* 5 (1989) 247–275.
- [3] Op den Kamp J.A.F. Lipid asymmetry in membranes. *Annu. Rev. Biochem.* 48 (1979) 47–71.
- [4] McElhaney R.N. The use of differential scanning calorimetry and differential thermal analysis in studies of model and biological membranes. *Chem. Phys. Lipids* 30 (1982) 229–259.
- [5] McMullen T.P.W., Lewis R.N.A.H., McElhaney R.N. Cholesterol–phospholipid interactions, the liquid-ordered phase and lipid rafts in model and biological membranes, *Curr. Opin. Coll. Interf. Sci.* 8 (2004) 459–468.
- [6] Phillips M.C., Ladbrooke B.D., Chapman D. Molecular interactions in mixed lecithin systems, *Biochim. Biophys. Acta* 196 (1970) 35–44.
- [7] Simons K., Ikonen E. Functional rafts in cell membranes, *Nature* 387 (1997) 569–572.
- [8] Goñi F.M., Alonso A., Bagatolli L.A., Brown R.E., Marsh D., Prieto M., Thewalt J.L. Phase diagrams of lipid mixtures relevant to the study of membrane rafts, *Biochim. Biophys. Acta* 1781 (2008) 665–684.
- [9] Ruiz N., Kahne D., Thomas J.S. Advances in understanding bacterial outer-membrane biogenesis, *Nat. Rev. Microbiol.* 4 (2006) 57–66.
- [10] Holst O., Molinaro A. in *Microbial Glycobiology*, ed. A. P. Moran, Elsevier, London, 2009.
- [11] Brandenburg K., Seydel U. A comment on the preparation of liposomes from and on the beta .tautm. alpha acyl chain melting behavior of rough mutant lipopolysaccharide, *Biochim. Biophys. Acta* 1069 (1991) 1–4.
- [12] Castellana E.T., Cremer P.S. Solid supported lipid bilayers: From biophysical studies to sensor design, *Surf. Sci. Rep.* 61 (2006) 429–444.

CHAPTER 2

Role of lipids in membrane processes

2.1 Lipid-protein interactions

For a number of decades, the lipid bilayer was considered by most scientists as an “inert scaffold” with the only function of a physical barrier between the external and internal environments, whereas the membrane proteins were considered to be responsible for more specific membrane functions such as selective molecular transport, signal reception and transduction, and membrane-membrane interactions.

Many recent studies have changed this concept, revealing that lipids participate actively in a variety of membrane processes, either directly or indirectly influencing the function of membrane proteins [1]. In particular, lipids can affect protein structure and dynamics either *via* physicochemical characteristics of the membrane, such as elasticity, curvature, surface charge, hydration and the formation of domains, or by specific interactions involving the chemical structure, conformation and dynamics of the lipid head groups and acyl chains [2]. Consequently, much attention has been paid to the lipid composition of biomembranes and to their microstructural features.

Lipid–protein interactions play a key role in a wide variety of cellular processes, including signal transduction, intracellular transport, enzyme catalysis, energy conversion in the cell, antimicrobial defense, and control of membrane fusion [2]. Critical for all these functions are unique structural features of the lipid and protein molecules representing an ensemble of rapidly interconverting conformational substates highly sensitive to various environmental factors.

In this context, two important biological processes, which are object of this research project, are particularly relevant: the membrane fusion promoted by viral glycoproteins and the aggregation process of the β -amyloid peptide involved in the Alzheimer’s Disease. About this last process, many experimental evidences have suggested that the lipid membranes can play a fundamental role in catalyzing the β -amyloid self-aggregation, although the fibrils formation become in the extracellular environment.

2.2 Viral fusion

Biomembranes play a fundamental role in the virus cycle of life. Generally speaking, viruses infect cells by crossing the plasma membrane. Once viral replication is completed, new viruses are released to extracellular medium by crossing the membrane in the opposite direction. For viruses that replicate their genomes in the nucleus of the infected cell, nuclear membranes have also to be passed through. All these events occur through a variety of possible molecular mechanisms, depending on the virus and on the target cell. In the case of enveloped viruses (e.g., influenza virus, human immunodeficiency virus, herpes virus, hepatitis C virus), which present a lipid membrane, named envelope, covering their protein capsid (Figure 2.1), viral entry and egress requires a sequence of fusion and fission events between the viral envelope and the target cell membranes.

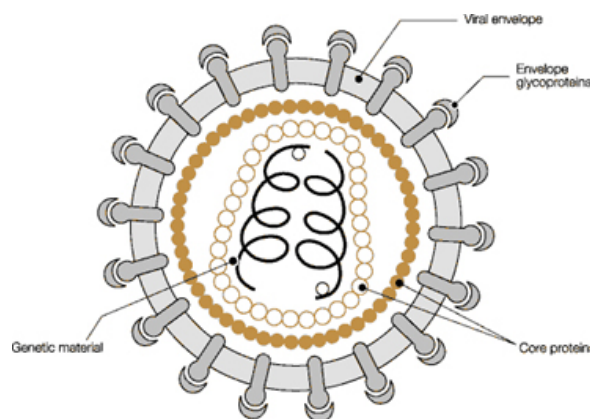


Figure 2.2 – A schematic representation of the structure of an envelope virus.

Fusion of two bilayer membranes is a thermodynamically favourable process, but there is a very high kinetic barrier which is associated to the mixing between the lipids molecules present in the two bilayers that are in contact, and their subsequent rearrangement in the new bilayer. Accumulated evidence suggests that one or more viral glycoprotein, which undergo conformational changes, lower the various kinetic barriers and, hence, catalyze the membrane fusion process, favouring lipid micro- and mesoscopic

re-arrangement [3]. Most commonly, fusion glycoproteins act as homo- or hetero-multimers. The physical events needed to promote membrane fusion induced by enveloped viruses are the exposure of hydrophobic peptides, loops or patches from one (or more) of the viral proteins and their insertion into the cellular membrane to disrupt the normal organization of the lipids in their vicinity.

The mechanism of the membrane fusion process promoted by viral fusion protein can be schematized into a sequence of events (Figure 2.2.2) [4].

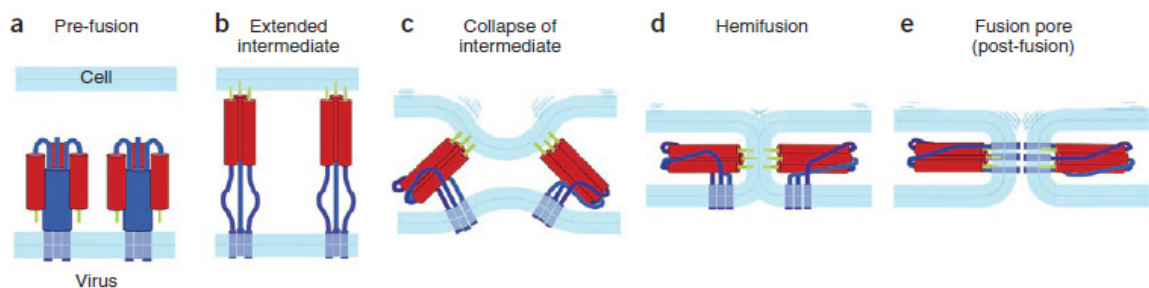


Figure 2.2.2 - A schematic representation of the sequence of events in membrane fusion promoted by a viral fusion glycoprotein: **(a)** the protein is in the pre-fusion conformation, with its fusion peptide (green) sequestered; **(b)** extended intermediate. The protein opens up, extending the fusion peptide or loop to interact with the target bilayer; **(c)** collapse of the extended intermediate; **(d)** hemifusion, with the proximal leaflets merge into a hemifusion stalk. **(e)** Fusion pore formation [4].

In the first step, the glycoprotein undergoes a conformational change that extends each subunit toward the target membrane (Figure 2.2.2a to Figure 2.2.2b) and forms a bridge between the two bilayers (Figure 2.2.2b) thanks to two membrane-interacting elements: a C-terminal transmembrane anchor that holds the protein in the viral membrane and a distinct hydrophobic patch, called ‘fusion peptide’, that ultimately interacts with the target membrane. In the second step, the bridge collapses (Figure 2.2.2c) so that the fusion peptide and the C-terminal transmembrane anchor come together. This collapse distorts the two bilayers, probably into a nipple-like configuration, with a relatively restricted area of close approach. Whether insertion of the fusion peptide potentiates this distortion in the target membrane, by perturbing the bilayer and lowering the distortion energy, remains

uncertain. In the third step, the distortion of the individual membranes lowers the energy barrier between separated and hemifused bilayers so that a hemifusion stalk forms (Figure 2.2.2d). In the fourth step, the hemifusion stalk opens to form a transient fusion pore. A final conformational step in the protein refolding renders the open state irreversible, and the pore expands (Figure 2.2.2e). In most cases, steps 3 and 4 probably require concerted action of more than one fusion-protein multimer [4].

Fusion glycoproteins present differences in term of structure, conformation and mechanism of action. On these bases, three different classes of glycoproteins have been defined. In particular, class I viral fusion proteins have been identified in several different viruses, for example, influenza, HIV and Ebola. Class I glycoproteins are synthesized in form of precursors, which are assembled into trimers and inserted into viral envelope. Class II proteins have been identified in alphaviruses and flaviviruses. In contrast to class I glycoproteins, which adopt α -helical structure, the ectodomains of class II glycoproteins adopt β -sheet folds. Finally, the glycoprotein B of Herpes simplex virus (HSV) and glycoprotein G of vesicular stomatitis virus (VSB) are examples of class III viral proteins, presenting significant differences in their structure with respect proteins of class I and II.

Even though many studies have been realized on this important membrane process, the exact mechanism of the protein/membrane interaction is still unknown. Recent studies suggest that several membranotropic regions of the fusion proteins participate to the membrane distortion necessary for fusion as a result of their high propensity to partition into the membrane interface [5]. Similarly to other membrane processes, there is increasing experimental evidence that lipids play a key role in membrane fusion and fission as chemically-defined molecules, affecting the protein activity. They may directly induce conformational changes into the protein, or create a local environment around the proteins favorable to the execution of their fusion properties.

Obviously, there is a large variety of enveloped viruses. They are generally classified in different families, according to their specific peculiarities which are related to the envelope structure and to the presence of one or more glycoproteins responsible for the fusion process.

In this work, the Human and Feline Immunodeficiency viruses and the Herpes simplex virus were considered.

2.2.1 Feline and Human Immunodeficiency Viruses

Both the feline immunodeficiency virus (FIV) and the human analogue (HIV) effect cell entry via a mechanism that involves a surface glycoprotein [6]. These glycoproteins, named gp41 and gp36, respectively, exhibit a common structural architecture consisting of different domains, as described in Figure 2.2.1.1: i) a outer subunit formed by the fusion peptide (FP) and a repetitive peptide sequence with α -helix conformation (NHR, N-terminal heptad repeat); ii) an inner subunit, formed by an amino acid sequence similar to the previous (CHR, C-terminal heptad repeat); iii) a pre-transmembrane (pre-TM) region, also called MPER (membrane-proximal external region) and iv.) a transmembrane domain (MSR).

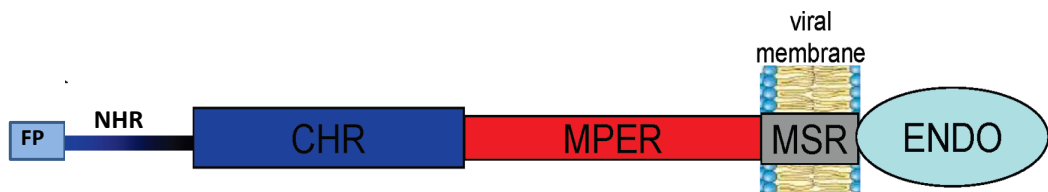


Figure 2.2.1.1 – Schematic representation of the Immunodeficiency viruses glycoprotein.

In particular, this region presents an unusual clustering of tryptophan residues [7,8] and is located very close to the viral membrane, but definitely protruding from it. Once the fusion peptide has entered the target-cell membrane and subsequent conformational changes in the glycoprotein have brought the two membranes into close proximity, the

MPER domain could destabilize the bilayers, thus promoting membrane fusion. Consequently, the presence of the MPER domain has been shown to be crucial in the infection pathway. The MPER domain of HIV gp41 shows a hydrophobic character in which the presence of aromatic residues confers a potential high tendency to partition into the membrane [9]. This makes this sequence a suitable candidate to be a membrane-perturbing agent [10], playing a crucial role in the fusion process. For this reason, great attention is given to the characterization of the interaction of this protein domain with lipid membranes.

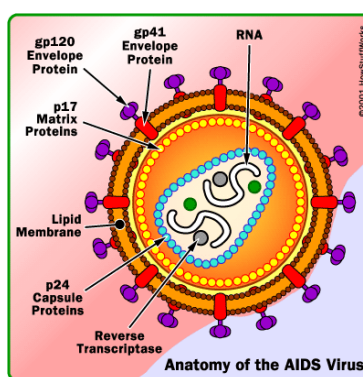


Figure 2.2.1.2 – The structure on the enveloped HIV Virus [11].

In addition, many studies have demonstrated that peptides deriving from MPER of gp41 and gp36 are able to prevent HIV- and FIV-cell membrane fusion [12,13]. The antiviral activity is likely to derive from adsorption of the peptide on the external surface of the target-cell membrane, where it competes with the TM glycoprotein of the virus. As an example, a 20-mer peptide named P59, corresponding to the ⁷⁶⁷L-G⁷⁸⁶ sequence of (TM) gp36, was found to exert potent inhibitory activity on FIV replication [14] and it tends to associate with lipid bilayers by binding at the membrane surface or polar–apolar interface.

Numerous studies have indicated that lipids, in both viral and cellular membranes, play an important role in the HIV-1 replication cycle. In fact, it is well documented that the HIV-1 lipid envelope is enriched in cholesterol (CHOL) and sphingomyelin (SM) relative to the host cell plasma membrane [15]. These components form the micro domains, named

“lipid rafts”, which occurs as a consequence of the different biophysical properties of lipids found in the plasmamembrane, and their differential self-association properties, resembling those of the liquid-ordered (L_o) phases observed to coexist with liquid-disordered (L_d) phases in model membranes. In particular, the gp41 MPER domain presents the amino acid segment Leu-Trp-Thr-Ile-Lys, also known as CRAC (cholesterol recognition/interaction amino acid consensus), that bind preferentially to lipid membranes with an high content of cholesterol. It tends to destabilize the bilayer structure, preserving this feature and its activity during the fusion process [16]. In addition to cholesterol, sphingomyelin may promote surface aggregation of the gp41 Leu-Trp-Thr-Ile-Lys motif into an ordered domain, potentially enhancing gp41-mediated fusion of viral and cellular membranes.

In the following chapters, the octapeptide named C8, corresponding to the ⁷⁷⁰Trp-Ile⁷⁷⁷ sequence of the MPER domain of FIV gp36 and the 19-mer peptide corresponding to the ⁶⁶⁵Lys-Lys⁶⁸³ sequence of the MPER domain of HIV gp41 were considered, focusing the attention on the effect which they show on destabilizing the structure of lipid membranes.

2.2.2 Herpes simplex virus

Herpes simplex virus 1 and 2 (HSV-1 and HSV-2) are two members of the herpes virus family, Herpesviridae, that infect humans. Both HSV-1, which produces most cold sores, and HSV-2, which produces most genital herpes, are ubiquitous and contagious. They can be spread when an infected person is producing and shedding the virus.

HSV enters cells by fusion of the viral and host-cell membranes; however, the mechanisms underlying the merging of these membranes are still unclear. Understanding the molecular basis of the fusion process is of critical importance for the design and development of therapeutic agents that could aid in the treatment of HSV-related illnesses. The core fusion machinery, conserved throughout the herpesvirus family, involves

glycoprotein B (gB) and the non-covalently associated complex of glycoproteins H and L (gH/gL). Although it is now clear that both gB and gH play a fusogenic role in herpesviruses, their precise mechanism of function is still unknown [17]. Based on the crystal structure, gB was proposed to be a fusion protein belonging to the new class III together with vesicular stomatitis virus (VSV) G protein and baculovirus gp64 [17]. However, gB does not function as a fusion protein in the absence of gH/gL [18].

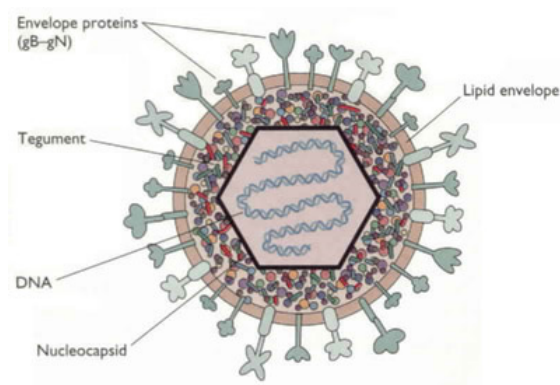


Figure 2.2.1.1 – The structure of the HSV-1 Virus [19].

In fact, in a transfection model, only gH/gL is able to induce hemifusion while gB helps in accomplishing complete fusion [20]. Recently, it has been reported that both gB and gH possess several hydrophobic domains necessary for efficient induction of fusion, and synthetic peptides corresponding to these regions are able to associate to membranes and induce fusion of artificial liposomes [21].

As hinted above, there is converging evidence that protein domains other than the fusion peptide play an important and cooperative role in inducing fusion between a viral envelope and a cell membrane. This is particularly true for the complex fusion mechanism adopted by HSV where at least two proteins, gB and gH, act in concert to gain access into the cells. Thus, it is likely that different protein domains cooperate in driving membrane fusion, but their membranotropic characteristics may differ, according to the role played by each single region.

For this reason, the behaviour of peptides deriving from different domain on the two most fusogenic glycoproteins, gB and gH, were considered. In particular, the attention has focused on gH626–644, gH776–802, gB168–186, gB254–270 and gB632–650 fragments, corresponding to the ⁶²⁶Gly-Phe⁶⁴⁴, ⁷⁷⁶Ser-Ala⁸⁰², ¹⁶⁸Val-Phe¹⁸⁶, ²⁵⁴Tyr-Asn²⁷⁰ and ⁶³²Pro-Phe⁶⁵⁰ sequences of gH and gB glycoproteins, respectively, and to their interaction with different lipid membranes, in order to discriminate transmembrane pore formation from other membrane perturbations.

2.3 Biomembranes involvement in the β -amyloid aggregation process

Alzheimer's disease (AD) is a progressive neurodegenerative disorder that was first described by the German psychiatrist and neuropathologist Alois Alzheimer in 1906. AD destroys brain cells, causing progressive memory loss and problems with mind and behavior severe enough to affect work, lifelong activities and social life. AD is the most common form of dementia in adults, affecting nearly 35 million individuals worldwide in 2010 [22]. The morphological hallmarks found in the brains of AD patients (Figure 2.3.1) are intracellular neurofibrillary tangles, composed of paired helical filaments of hyperphosphorylated Tau protein, and extracellular senile plaques, composed of insoluble β -amyloid peptide ($A\beta$) fibrillar aggregates [23].

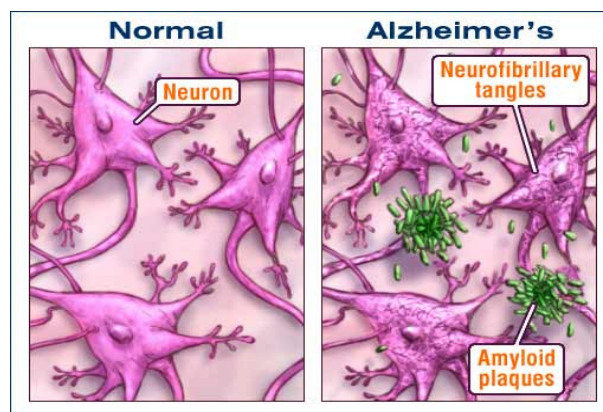


Figure 2.3.1 – Differences between normal (*left*) and with AD (*right*) neuronal cells [24].

β -amyloid peptides are 39-43 amino acid long and derive from the proteolytic cleavage of amyloid precursor protein (APP), a type I integral membrane glycoprotein (695–770 residues). The predominant forms are $A\beta(1-40)$ and $A\beta(1-42)$ [25]. In Figure 2.3.2 is schematically described the formation process of the $A\beta$ peptide.

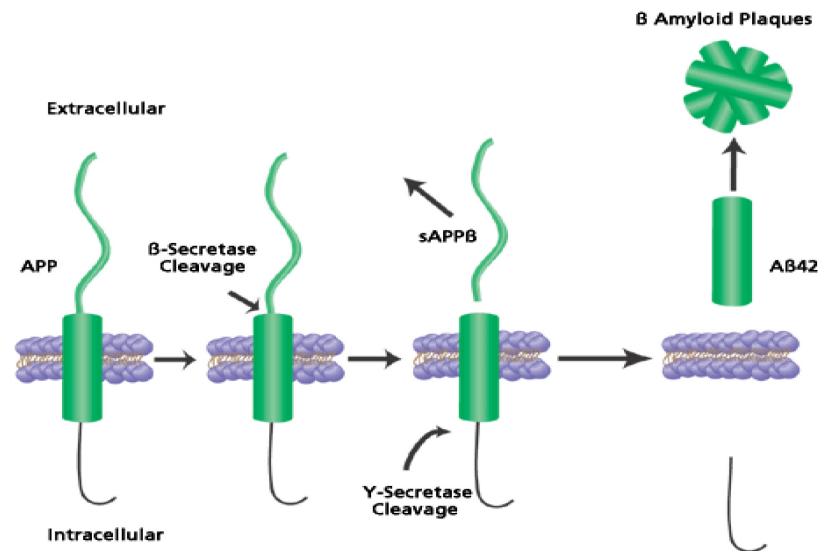


Figure 2.3.2 – Representation of β -amyloid formation process [26].

Once $A\beta$ is produced, it can be released as a soluble, unfolded unimer into the aqueous environment and be removed (healthy individuals) or it could accumulate, and eventually self-aggregate in ordered fibrils, undergoing a conformational transition to β -sheet structure (AD individuals). Indeed, the mechanisms for $A\beta$ aggregation and its induced neurotoxicity are not fully understood. In the past years, amyloid fibrils were generally regarded as the cause of the symptoms of Alzheimer disorder. More recently, increasing evidence indicates that soluble protofibrillar oligomeric forms of $A\beta$ are the primary neurotoxic species as they are correlated with the severity of the disease better than the presence of plaques [27].

External conditions play a key role in driving or accelerating $A\beta$ self-aggregation. As an example, formation of fibrils is much faster at weakly acidic pH (~ 5.5), where $A\beta$ is

electrically uncharged. Fibrillogenesis has been also proposed to be catalyzed by the presence of lipid membranes [28], although this point is still controversial. In fact, A β inherits an amphipatic character from its precursor protein, with the hydrophilic N-terminal domain (residues 1-28) corresponding to a segment of the APP ectodomain, and the hydrophobic C-terminal domain (residues 29-39/43) corresponding to a segment of the APP transmembrane domain. This amphipatic character makes A β an ideal candidate for membrane interaction. However, various peptide-membrane interaction mechanisms can be hypothesized. First of all, a fraction of A β peptide might be retained in the membrane upon its formation. Furthermore, once released to the extracellular medium, A β peptide can come back to interact with the cellular membrane, and either reinsert or adsorb on its surfaces. Not necessarily all of these membrane interaction modes favor peptide-self-aggregation. Particularly, this has been proposed to be catalyzed by peptide adsorption on membrane surface, acting as two-dimensional folding template [29], see Figure 2.3.3.

The chemical nature of membrane lipids is fundamental in modulating the A β -membrane interactions mode, thus influencing the formation of protofibrillar and fibrillar structures. Most studies have reported that A β presents no or very weak interactions with zwitterionic phosphocholines (PC) at neutral pH and that these phospholipids have no effect on the time-dependence of β -sheet formation. In contrast, anionic phospholipids, mostly phosphatidylglycerol (PG) or phosphatidylserine (PS), favor A β aggregation and the subsequent fibrillization [28,29].

Another aspect that has attracted the researchers' interest is the role of cholesterol (CHOL) in the A β aggregation. Accumulating clinical evidences suggest that an elevated CHOL level is a risk factor of AD. In particular, high cholesterol levels in mid-life were found to be correlated strongly with the A β deposition and the risk of developing AD, while conversely, patients taking the cholesterol-lowering statin drugs were found to have

a lower incidence of the disease [30], suggesting a key role of CHOL in regulating the A β production and consequently amyloid plaques formation.

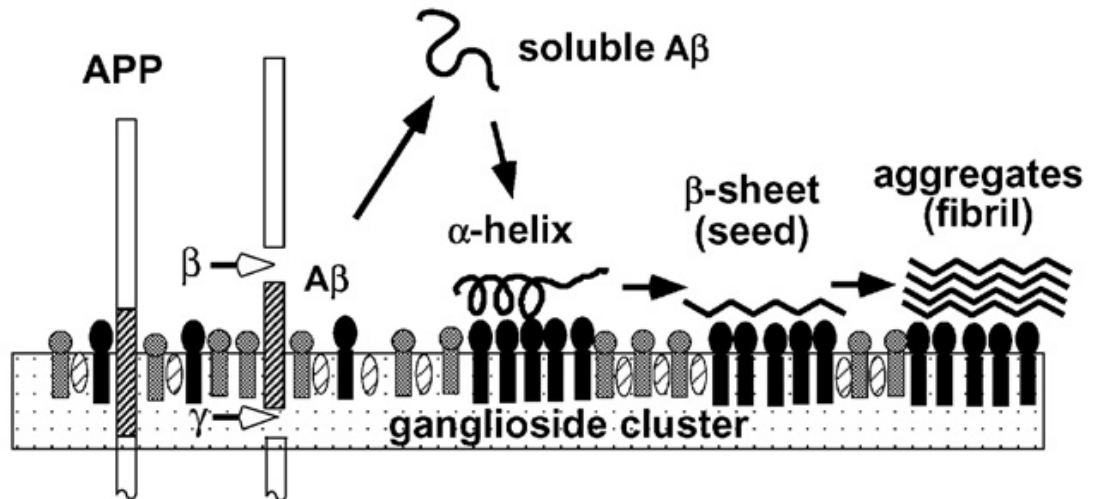


Figure 2.3.3 – A hypothetical model of the aggregation of A β induced by lipid membranes [29].

In addition, heterogeneity of lipid bilayers has also to be considered. In the presence of CHOL, sphingomyelin (SM) and glycosphingolipids, lipid rafts can form, which are small microdomains more ordered and tightly structured than the surrounding fluid mosaic. A β has been proposed to preferentially bind to lipid raft and the high local peptide concentration would promote its self-aggregation [29].

This small summary concerning what is known, or simply hypothesized, on the role of lipid membranes in A β self-aggregation has pointed out the lack of an exhaustive, comprehensive model of this process. Indeed, although many studies have been conducted on this subject, it is still highly controversial and not fully understood.

The comprehension of the A β fibrillation mechanism is also fundamental to define a therapeutic strategy. In fact, a widely employed approach in the research of anti-Alzheimer agents involves the identification of substances that are able to prevent amyloid aggregation, or to disaggregate the amyloid fibrils through a direct structural interaction

with soluble or aggregated peptides. A promising approach employed to make inhibitors of amyloid plaques formation was the design of specific peptides, deriving from A β itself, which bind to it and prevent its aggregation. In particular, Tyernberg and coworkers demonstrated that the A β hydrophobic domain KLVFF is fundamental for the peptide self-aggregation [31]. They showed that a peptide containing this segment was able to bind to A β , thus slackening its assembly into amyloid fibrils. However, the therapeutic usefulness of this peptide is restricted because of its no negligible ability to incorporate into amyloid fibrils. Successively, Soto et al. claimed that short synthetic peptides, called β -sheet breakers, are capable of binding A β but are unable to become part of a β -sheet structure [32]. These peptides destabilize the amyloidogenic A β conformer and hence preclude amyloid plaques formation. To design β -sheet breakers that specifically bind to the A β region implicated in β -sheet formation, these authors focused on the central hydrophobic region within the N-terminal domain of the A β protein (amino acids 17–21: LVFFA). Several β -sheet breaker peptides, from 11 to 5 amino acids long with homology to this region, were generated and tested *in vitro* [33]. Proline residues were added in the β -breakers' sequence to disrupt β -sheet formation, as incorporation of this amino acid within a β -pleated structure is highly unfavorable. Finally, charged residues were put at the C-terminal part of these peptides to increase solubility. One of these β -sheet breaker peptides is the iA β 5. This pentapeptide (LPFFD) and its end-protected version, acetylated at the N-terminus and amidated at the C-terminus, Acetyl-LPFFDamide: iA β 5p (Figure 2.3.4), were shown to bind to A β with high affinity and to inhibit A β misfolding and aggregation [34].

Furthermore, it also induced the disassembly of preformed fibrils *in vitro*. The ability of iA β 5 to inhibit peptide self-aggregation and disassembly amyloid fibrils was also demonstrated *in vivo*. These results support the notion that synthetic β -sheet breakers may be useful in stabilizing the normal protein conformation by converting the β -sheet rich conformer back into the normal form [35].

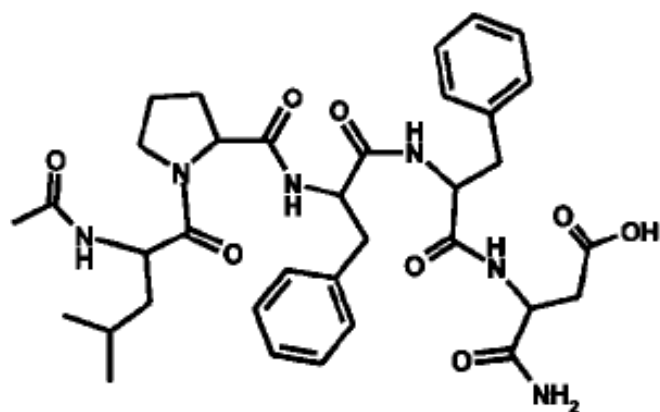


Figure 2.3.4 – Chemical structure of the β -sheet breaker peptide, iA β 5p.

In this experimental thesis, the attention was focused on A β (25-35) and A β (16-35) fragments in the presence of biomimic systems to analyze their role in the favoring or disfavoring the process. These fragments have been chosen because, in fibril structural models, they represent the repetitive unit of β -amyloid peptide aggregates and are able to self-aggregate following the same mechanism of the full-length peptides. Furthermore, owing to the membrane implication in the processes leading to A β misfolding and aggregation, the iA β 5p behaviour in the presence of membrane models was investigated in order to analyze the activity of the β -sheet breaker against A β fibrillization in membrane systems.

References

- [1] Phillips R., Ursell T., Wiggins P., Sens P. Emerging roles for lipids in shaping membrane-protein function, *Nature* 459 (2009) 379–385.
- [2] Van Meer G., Voelker D.R., Feigenson G.W. Membrane lipids: where they are and how they behave, *Nat. Rev. Mol. Cell. Biol.* 9 (2009) 112–124.
- [3] Chernomordik L.V., Kozlov M.M. Mechanics of membrane fusion, *Nat. Struct. Mol. Biol.* 15 (2008) 675–683.
- [4] Harrison S.C. Viral membrane fusion, *Nat. Struct. Mol. Biol.* 15 (2008) 690–698.
- [5] Peisajovich S.G., Shai Y. Viral fusion proteins: multiple regions contribute to membrane fusion, *Biochim. Biophys. Acta* 1614 (2003) 122–129.
- [6] Serres P.F. Molecular mimicry between the trimeric ectodomain of the transmembrane protein of immunosuppressive lentiviruses (HIV-SIV-FIV) and interleukin 2. *C.R. Acad. Sci. III* 323 (2000) 1019–1029.
- [7] Giannecchini S., Bonci F., Pistello M., Matteucci D., Sichi O., Rovero P., Bendinelli M. The membrane-proximal tryptophan-rich region in the transmembrane glycoprotein ectodomain of feline immunodeficiency virus is important for cell entry, *Virology* 320 (2004) 156–166.
- [8] Suarez T., Nir S., Goni F.M., Saez-Cirion A., Nieva J.L. The pretransmembrane region of the human immunodeficiency virus type-1 glycoprotein: a novel fusogenic sequence, *FEBS Lett.* 477 (2000) 145–149.
- [9] Lorizate M., Cruz A., Huarte N., Kunert R., Perez-Gil J., Nieva J.L. Recognition and blocking of HIV-1 gp41 pre-transmembrane sequence by monoclonal 4E10 antibody in a raft-like membrane environment. *J. Biol. Chem.* 281 (2006) 39598-39606.
- [10] Apellániz B., García-Sáez A., Nir S., Nieva J.L. Destabilization exerted by peptides derived from the membrane-proximal external region of HIV-1 gp41 in lipid vesicles supporting fluid phase coexistence. *Biochim. Biophys. Acta* 1808 (2011) 1797-1805.
- [11] <http://www.health.howstuffworks.com>
- [12] Kilby J.M., Lalezari J.P., Eron J.J., Carlson M., Cohen C., Arduino R.C., Goodgame J.C., Gallant J.E., Volberding P., Murphy R.L., Valentine F., Saag M.S., Nelson E.L., Sista P.R., Dusek A. The safety, plasma pharmacokinetics, and antiviral activity of subcutaneous enfuvirtide (T-20), a

- peptide inhibitor of gp41-mediated virus fusion, in HIV-infected adults, *AIDS Res. Hum. Retroviruses* 18 (2002) 685–693.
- [13] Giannecchini S., Di Fenza A., D’Ursi A.M., Matteucci D., Rovero P., Bendinelli M. Antiviral activity and conformational features of an octapeptide derived from the membrane-proximal ectodomain of the feline immunodeficiency virus transmembrane glycoprotein, *J. Virol.* 77 (2003) 3724–3733.
- [14] Esposito C., D’Errico G., Armenante M.R., Giannecchini S., Bendinelli M., Rovero P., D’Ursi A.M. Physicochemical characterization of a peptide deriving from the glycoprotein gp36 of the feline immunodeficiency virus and its lipoylated analogue in micellar systems, *Biochim. Biophys. Acta* 1758 (2006) 1653–1661.
- [15] Waheed A.A., Freed E.O. Lipids and membrane microdomains in HIV-1 replication, *Virus Res.* 143 (2009) 162-176
- [16] Vishwanathan S.A., Thomas A., Brasseur R., Epand R.F., Hunter E., Epand R.M. Large changes in the CRAC segment of gp41 of HIV do not destroy fusion activity if the segment interacts with cholesterol, *Biochemistry* 47 (2008) 11869-11876.
- [17] White J.M., Delos S.E., Brecher M., Schornberg K. Structures and mechanisms of viral membrane fusion proteins: multiple variations on a common theme, *Crit. Rev. Biochem. Mol. Biol.* 43 (2008) 189–219.
- [18] Farnsworth A., Wisner T.W., Webb M., Roller R., Cohen G., Eisenberg R., Johnson D.C. Herpes simplex virus glycoproteins gB and gH function in fusion between the virion envelope and the outer nuclear membrane, *Proc. Natl. Acad. Sci.* 104 (2007) 10187–10192.
- [19] <http://www.bio.davidson.edu>
- [20] Subramanian R.P., Geraghty R.J. Herpes simplex virus type 1 mediates fusion through a hemifusion intermediate by sequential activity of glycoproteins D, H, L, and B, *Proc. Natl. Acad. Sci.* 104 (2007) 2903–2908.
- [21] **a)** Galdiero S., Falanga A., Vitiello M., Raiola L., Fattorusso R., Browne H., Pedone C., Isernia C., Galdiero M. Analysis of a membrane interacting region of herpes simplex virus type1 glycoprotein H, *J. Biol. Chem.* 283 (2008) 29993–30009. **b)** Galdiero S., Vitiello M., D’Isanto M., Falanga A., Cantisani M., Browne H., Pedone C., Galdiero M. The identification and characterisation of fusogenic domains in herpesvirus glycoprotein B molecules, *ChemBioChem* 9 (2008) 758–767.

- [22] Prince M., Jackson J. World Alzheimer Report 2009. Alzheimer's Disease International: London.
- [23] Selkoe D.J. Alzheimer's disease: genotypes, phenotypes, and treatments, *Science* 275 (1997) 630–631.
- [24] <http://lancastria.net/blog.html>
- [25] Selkoe D.J. Translating cell biology into therapeutic advances in Alzheimer's disease, *Nature* 399 (1999) A23–A31.
- [26] <http://alfin2100.blogspot.com/2008/01/new-alzheimers-treatment-approach.html>
- [27] Mclean C.A., Cherny R., Fraser F.W., Fuller S.J., Smith M.J., Beyreuther K., Bush A.I., Masters C.L. Soluble pool of A β amyloid as a determinant of severity of neurodegeneration in Alzheimer's disease, *Ann. Neurol.* 46 (1999) 860–866.
- [28] Gorbenko G.P., Kinnunen P.K. The role of lipid-protein interactions in amyloidtype protein fibril formation, *Chem. Phys. Lipids* 141 (2006) 72–82.
- [29] Matsuzaki K. Physicochemical interactions of amyloid β -peptide with lipid bilayers. *Biochim. Biophys. Acta* 1768 (2007) 1935–1942.
- [30] Taylor D.R., Hooper N.M. Role of lipid rafts in the processing of the pathogenic prion and Alzheimer's amyloid- β proteins, *Semin. Cell. Develop. Biol.* 18 (2007) 638–648.
- [31] Tyernberg L.O., Naslund J., Lindqvist F., Johansson J., Karlstrom A.R., Thyberg J., Terenius L., Nordstedt C. Arrest of β -amyloid fibril formation by a pentapeptide ligand, *J. Biol. Chem.* 271 (1996) 8545–8548.
- [32] Soto C., Sigurdsson E.M., Morelli L., Kumar R.A., Castano E.M., Frangione B. β -Sheet breaker peptides inhibit fibrillogenesis in a rat brain model of amyloidosis: implications for Alzheimer's therapy., *Nat. Med.* 4 (1998) 822–826.
- [33] Soto C. Plaque busters: strategies to inhibit amyloid formation in Alzheimer's disease, *Mol. Med. Today* 5 (1999) 343–350.
- [34] Estrada L.D., Soto C. Disrupting β -amyloid aggregation for Alzheimer disease treatment, *Curr. Top. Med. Chem.* 7 (2007) 115–126.
- [35] Permanne B., Adessi C., Saborio G.P., Fraga S., Frossard M.J., Van Dorpe J., Dewachter I., Banks W.A., Van Leuven F., Soto C. Reduction of amyloid load and cerebral damage in a transgenic mouse model of Alzheimer's disease by treatment with a β -sheet breaker peptide, *FASEB J.* 16 (2002) 860–862.

CHAPTER 3

Materials and Methods

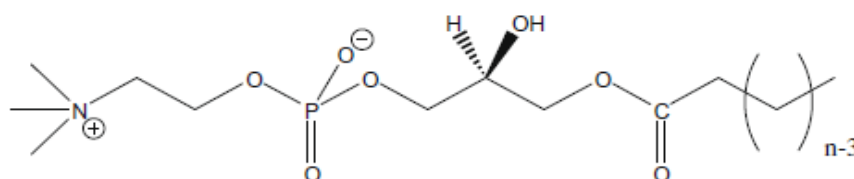
3.1 Materials

3.1.1 Lipid components

Lipids with different headgroup charges, chain lengths and unsaturated lengths were used.

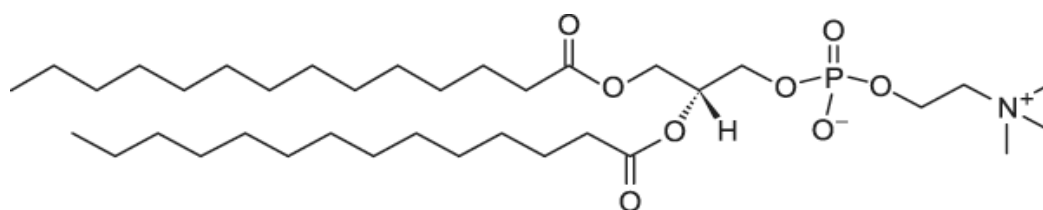
Monochained phospholipids:

- 1-Hexanoyl-2-Hydroxy-*sn*-Glycero-3-Phosphocholine (C₆lysoPC), 1-Octanoyl-2-Hydroxy-*sn*-Glycero-3-Phosphocholine (C₈lysoPC), 1-Decanoyl-2-Hydroxy-*sn*-Glycero-3-Phosphocholine (C₁₀lysoPC), and 1-Lauroyl-2-Hydroxy-*sn*-Glycero-3-Phosphocholine (C₁₂lysoPC), with a purity > 99%, were obtained from Avanti Polar Lipids (Birmingham, AL, USA).

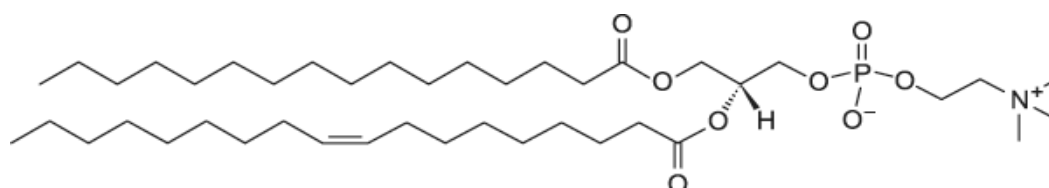


Zwitterionic phospholipids:

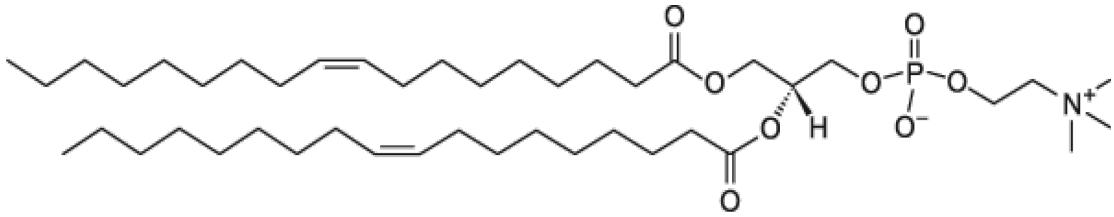
- 1,2-dimyristoyl-*sn*-glycero-3-phosphocholine (DMPC) was obtained from Avanti Polar with a purity >99%.



- 1-palmitoyl-2-oleoyl-*sn*-glycero-3-phosphocholine (POPC) was obtained from Avanti Polar with a purity >99%.

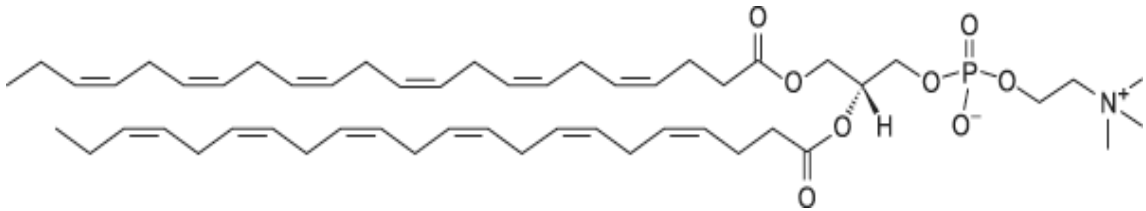


- 1,2-oleoyl-*sn*-glycero-3-phosphocholine (DOPC) was obtained from Avanti Polar with a purity >99%.



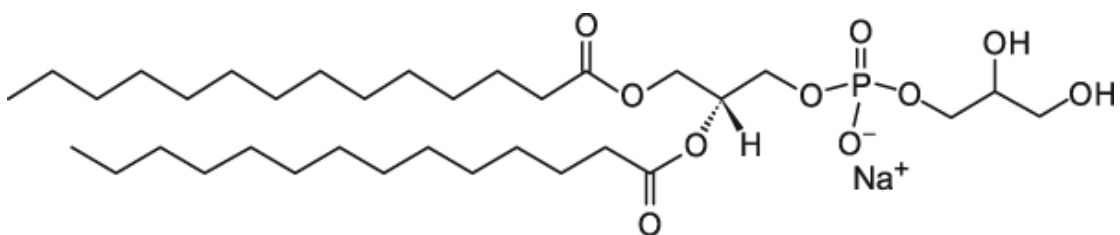
Poliunsaturared phospholipid:

- 1,2-didocosahexaenoyl-*sn*-glycero-3-phosphocholine, also indicated as PUFA, was obtained from Avanti Polar with a purity >99%.

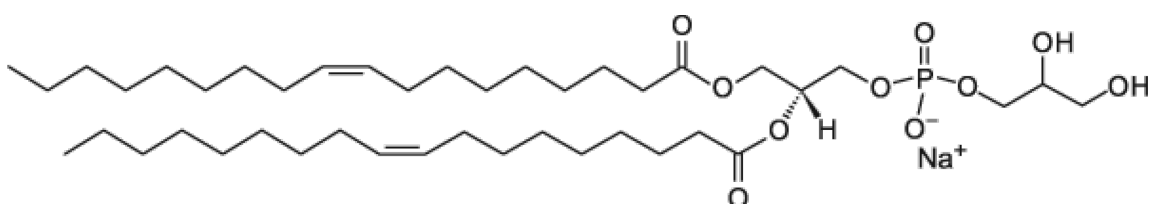


Anionic phospholipids:

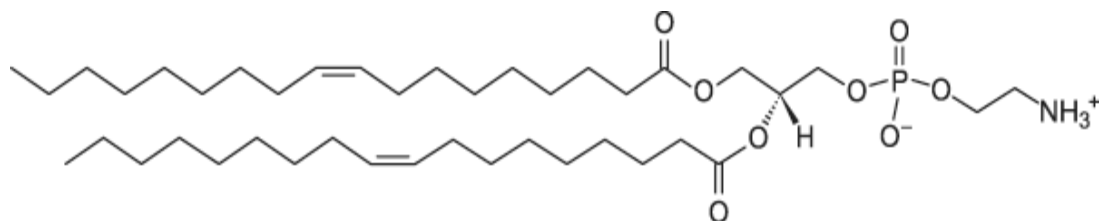
- 1,2-dimyristoyl-*sn*-glycero-3-phospho-1'-*rac*-glycerol (DMPG) was obtained from Avanti Polar with a purity >99%.



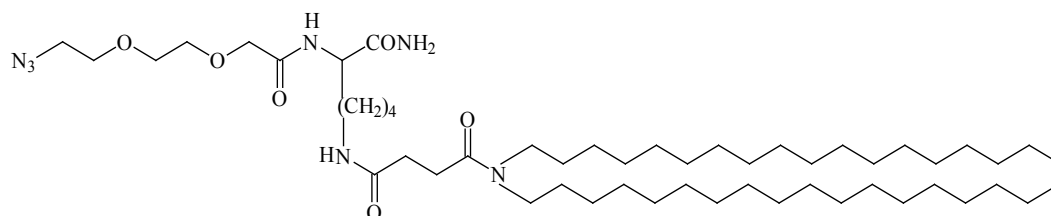
- 1,2-dioleoyl-*sn*-glycero-3-phospho-1'-*rac*-glycerol (DOPG) was obtained from Avanti Polar with a purity >99%.



- 1,2-dioleoyl-*sn*-glycero-3-phosphoethanolamine(DOPE) was obtained from Avanti Polar with a purity >99%.

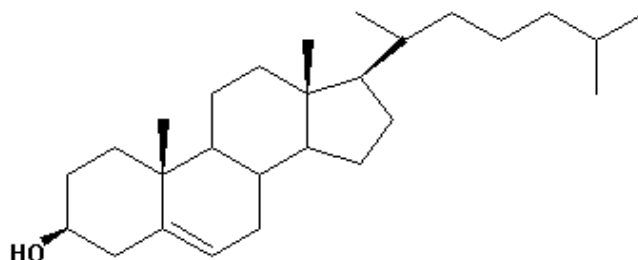


- Azide-AdOO-Lys(C(O)CH₂CH₂C(O)N-(C₁₈H₃₇)₂)-amide, (C₁₈)₂L-N₃, monomer was synthesized in solid phase under standard conditions using Fmoc/tBu strategy [1].



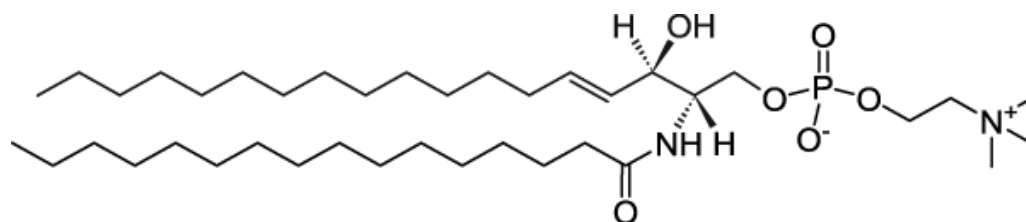
Sterols:

- Cholesterol (CHOL) was obtained from Sigma with a purity >99%.



Sphingolipids:

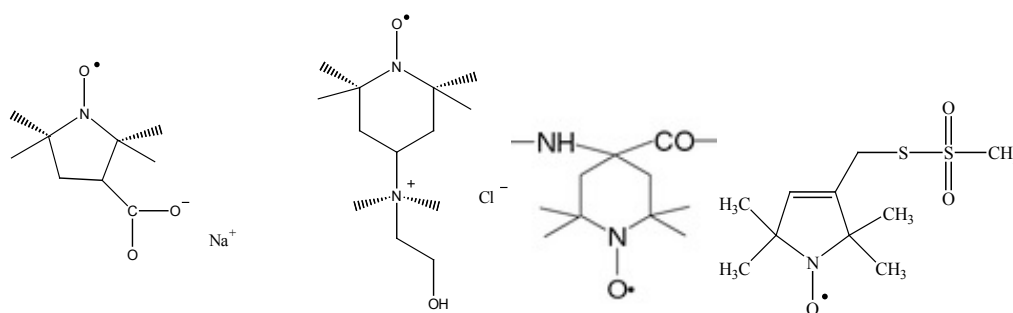
- Sphingomyelin (SM) was obtained from Sigma with a purity >99%.



Spin-probes:

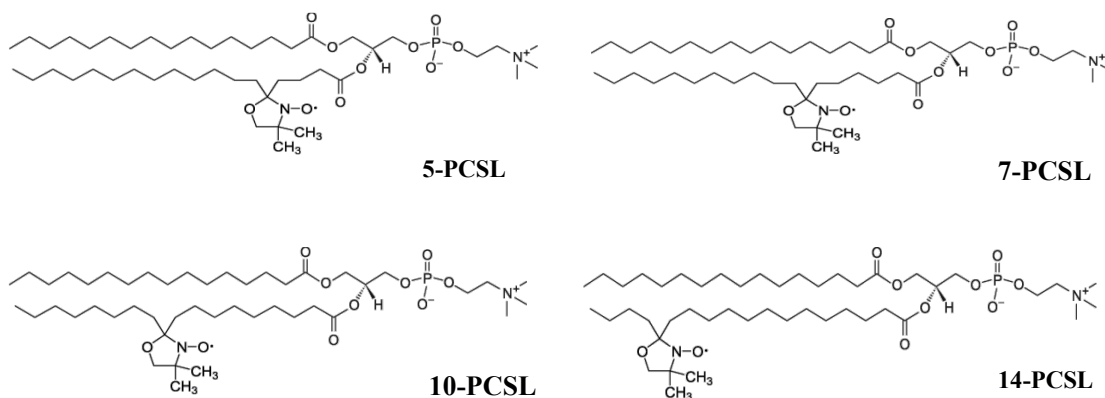
- The spin-probes 4-(N,N-dimethyl-N-(2-hydroxyethyl)ammonium-2,2,6,6-tetramethylpiperidine-1-oxyl chloride (TEMPO-choline) and 3-carboxy-2,2,5,5-tetramethyl-1-pyrrolidinyloxy (3-carboxy-PROXYL) were obtained from Molecular Probes (purity > 99%) and Sigma–Aldrich (purity > 98%), respectively.

(2,2,6,6-tetramethylpiperidine-N-oxide-4-(9 fluorenylmethyloxy carbonyl-amino)-4 carboxylic acid (TOAC) and methyl 3-(2,2,5,5-tetramethyl-1-oxypyrrolinyl) methanethiol sulfonate (MTSL), used to label the peptides, were synthesized according to the procedures reported in literature [2,3].



Spin-labeled phospholipids:

- Spin-labeled phosphatidylcholines (*n*-PCSL) with the nitroxide group at different positions, *n*, in the *sn*-2 acyl chain, as well as spin-labeled phosphatidic acid, phosphatidylethanolamine, phosphatidylglycerol and phosphatidylserine with the nitroxide group at the fifth position of the *sn*-2 chain (5-PASL, 5-PESL, 5-PGSL, 5-PSSL, respectively) were synthesized as described in Marsh and Watts [2,3].



3.1.2 Peptides

Peptides deriving from glycoproteins of Feline and Human Immunodeficiency Viruses (FIV and HIV, respectively) and Herpes simplex virus-type I (HSV-1), were synthesized and investigated in their interaction with lipid membranes by different techniques. Also, β -amyloid fragments and a short β -sheet breaker peptide, an inhibitor of the β -amyloid aggregation, were considered. These last peptides and those deriving from FIV and HIV glycoproteins were synthesised from the research group of Prof.ssa Anna Maria D’Ursi, Department of Pharmaceutical Sciences, University of Salerno. The peptides deriving from HSV glycoproteins were synthesised from the research group of Dr.ssa Stefania Galdiero, Department of Biological Sciences, University of Naples “Federico II”.

Peptides derived from MPER domain of Immunodeficiency Viruses glycoproteins.

- Four peptides, deriving from MPER domain of glycoprotein gp36 of Feline Immunodeficiency Virus, were designed and synthesized on a solid phase, using standard Fmoc/tBu chemistry, with a purity >97%. Their amino-acid sequences are shown in Table 4.2.1.

Peptides	Sequences
1 (C8)	Ac-Trp-Glu-Asp-Trp-Val-Gly-Trp-Ile-NH ₂
2	Ac-Lys-Trp- β Ala-Trp- β Ala-Trp-Ile-NH ₂
3	Ac-Bip-Glu-Asp-Bip-Val-Gly-Bip-Ile-NH ₂
4	Ac-Nal2-Glu-Asp-Nal2-Val-Gly-Nal2-Ile-NH ₂

Table 4.2.1 - Sequence of the peptides derived from FIV gp36.

- Deuterated C8 peptide, C8-*d*_{5all}, was synthesized including Trp-*d*₅ in all the Trp positions, applying the Fmoc/tBu solid phase peptide synthesis (SPPS) procedure.

- A peptide (HOOC-Lys-Trp-Ala-Ser-Leu-Trp-Asn-Trp-Phe-Asn-Ile-Thr-Asn-Trp-Leu-Trp-Tyr-Ile-Lys-NH₂) corresponding to the ⁶⁶⁵Lys-Lys⁶⁸³ sequence of MPER domain of HIV glycoprotein gp41 was designed and synthesized on a solid phase, using standard Fmoc/tBu chemistry, with a purity >97%.

Peptides derived from Herpes simplex virus – type I (HSV-1) glycoproteins.

- Peptides deriving from HSV-1gH and gB glycoproteins (Table 4.2.2) were synthesised by a solid-phase method using the Fmoc strategy and subsequently purified, see Table 4.2.2.

Peptides	Sequences
gH626-644	NH ₂ -GLASTLTRWAHYNALIRAF-CONH ₂
gH776-802	NH ₂ -STALLLFPNGTVIHLLAFDTQPVA AIA-CONH ₂
gB168-186	NH ₂ -VTVSQVWFGHRYSQFMGIF-CONH ₂
gB254-270	NH ₂ -YNPSRVEAFHRYGTTVN-CONH ₂
gB632-650	NH ₂ -PCTVGHRRYFTFGGGYVYF-CONH ₂

Table 4.2.2 – Amino acid sequences of peptides deriving from HSV glycoproteins.

- The fusion peptide of HIV gp41 glycoprotein and melittin peptide (Table 4.2.3) were also synthesised by a solid-phase method using the Fmoc strategy and subsequently purified and used as control peptides, in order to compare their behaviour with that of membranotropic peptides deriving from gB and gH.

Control Peptides	Sequences
gp41-FP	NH ₂ -AVGIGALFLGFLGAAGSTMGARS-CONH ₂
Melittin	NH ₂ -GIGAVLKVLTTGLPALISWIKRKRQQ-CONH ₂

Table 4.2.3 – Amino acid sequences of control peptides.

- gH625 peptide and its analogues labeled in four different position of amino acid backbone with the ((2,2,6,6-tetramethylpiperidine-N-oxide-4-(9-fluorenylmethoxy

carbonyl-amino)-4-carboxylic acid) spin-probe, TOAC, were synthesized introducing the spin label directly in solid phase (Table 4.2.4) in substitution of Ala residues.

Peptides	Sequences
gH625	NH ₂ -HGLASTLTRWAHYNALIRAF-CONH ₂
gH625-Pra	NH ₂ -HGLASTLTRWAHYNALIRAF-Pra-CONH ₂
A643K(TOAC)-gH625-Pra	NH ₂ -HGLASTLTRWAHYNALIRK(TOAC)F-Pra-CONH ₂
A639K(TOAC)-gH625-Pra	NH ₂ -HGLASTLTRWAHYNK(TOAC)LIRAF-Pra-CONH ₂
A635K(TOAC)-gH625-Pra	NH ₂ -HGLASTLTRWK(TOAC)HYNALIRAF-Pra-CONH ₂
A628K(TOAC)-gH625-Pra	NH ₂ -HGLK(TOAC)STLTRWAHYNALIRAF-Pra-CONH ₂

Table 4.2.4 – Spin-labeled analogues of gH625 peptide.

Aβ peptides and thier analogues spin-labeled with MTSL

- Aβ(25-35), Aβ(16-35) and its three spin-labeled analogues bearing the 2,2,5,5-tetramethyl-1-oxypyrroline-3-carboxylic acid (MTSL) spin label at the N-terminus, in the middle of the sequence and at the C-terminus (Figure 4.2.2), were synthesized containing the spin-probe were synthesized applying the Fmoc/tBu solid phase peptide synthesis procedure.

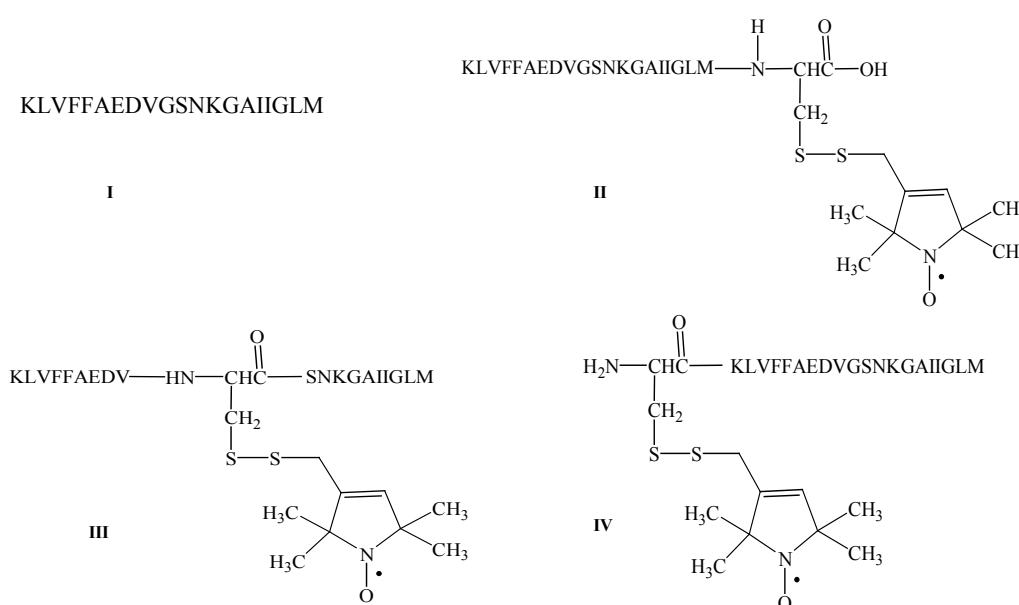


Figure 4.2.1 - Aminoacid sequence of Aβ (16-35) (I), Aβ (16-35) bearing MTSL spin label at the C-terminus (II), in the middle of the sequence (III) and at the N-terminus (IV).

Peptide β -sheet breaker

- The iA β 5p peptide and its two spin-labeled analogues bearing the MTSL spin label at the N-terminus and at the C-terminus (Table 4.2.5) were synthesized according to published methods using standard solid-phase synthesis techniques, with a purity of 98%.

Peptides	Sequences
iA β 5p	Ac-LPFFD-NH ₂
iA β 5p-MTSL ^{Cterm}	Ac-LPFFDC-NH ₂
iA β 5p-MTSL ^{Nterm}	Ac-CLPFFD-NH ₂

Table 4.2.5 – Amino acid sequences of iA β 5p and its spin-labeled analogues.

3.1.3 Solvents

- Organic solvents: Dichloromethane, Chloroform, Ethanol, Methanol and Hexafluoroisopropanol (HFIP), used for the preparation of lipid and peptide samples were obtained from Sigma with a purity >99%.
- 10 mM phosphate buffer, 137 mM NaCl, 2.7 mM KCl, pH 7.4 (PBS); 10 mM HEPES, 5 mM EDTA, 150 mM NaCl, pH 7.4 buffer (HBS); 5 mM HEPES, 100 mM NaCl, pH 7.4, were used to prepare liposome solutions. All salts were obtained from Sigma with a purity >99%.

All these chemical substances were used without additional purifications.

3.2 Methods

3.2.1 Liposomes preparation

For all the experiments, liposomes with different sizes were prepared. Small and Large Unilamellar Vesicles (SUVs and LUVs, respectively) and MultiLamellar Vesicles (MLVs) were used to investigate the interactions with the peptides objects of this research.

Liposomes were prepared by pouring appropriate amounts of lipid dissolved in dichloromethane/methanol (2/1 v/v) in small test tubes. For ESR experiments, 1% wt/wt of spin-labeled phosphatidylcholines in ethanol was also added. A thin film of the lipid was produced by evaporating the solvent with dry nitrogen gas. Final traces of solvent were removed by subjecting the sample to vacuum desiccation for at least 3 h. The samples were then hydrated with 20-50 μL of buffer and vortexed, obtaining a suspension of MLVs. For ESR experiments this suspension was transferred to a 25 μL glass capillary and flame sealed. LUVs were obtained from MLVs by nine-fold extrusion through a polycarbonate membrane of 100-nm pore size. SUVs, of 25-35 nm in diameter, were formed by vortexing and sonicating for 3 \times 10 min the MLVs suspension. Liposomal samples containing the peptides were prepared in a similar manner, except that the lipid film was hydrated directly with a peptide solution in buffer. In contrast, samples containing the spin-labeled peptides were prepared by mixing appropriate amounts of the peptide dissolved in HFIP with the lipid organic solutions.

3.2.2 Supported Lipid Bilayers preparation

For Neutron Reflectivity experiments, Supported Single Lipid Bilayers (SSLBs) were prepared by adsorption of small vesicles on solid supports [4]. The SUVs suspension (0.5 mg mL⁻¹) was prepared following the previously described procedure and injected into the NR cell (Figure 4.2.3), allowed to diffuse and adsorb to the silicon surfaces over a period of 30 min. Afterward the sample cell was rinsed once with deuterated water to remove excess lipid. Finally, the peptide solution was added after bilayer formation. The used solid supports were 8 \times 5 \times 1 cm³ silicon single crystals cut to provide a surface along the (111) plane. These were polished by Siltronix (Archamps, F) and cleaned for 15 min in a mixture of 1:4:5 H₂O₂/H₂SO₄/H₂O at 80-85 °C, followed by ozonolysis [4]. This treatment leaves a natural oxide layer of 7-20 Å thickness and 3-5 Å roughness.

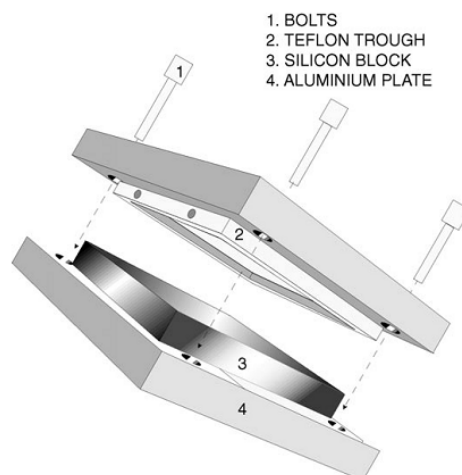


Figure 4.2.3 – An example of atypical cell used for NR experiments [5].

3.2.3 Electron Spin Resonance spectroscopy measurements

ESR spectra of lipid and lipid/peptide samples were recorded with a 9 GHz Bruker Elexys E-500 spectrometer (Bruker, Rheinstetten, Germany). Capillaries containing the samples were placed in a standard 4 mm quartz sample tube containing light silicone oil for thermal stability. The temperature of the sample was regulated at 37 °C and maintained constant during the measurement by blowing thermostated nitrogen gas through a quartz Dewar. The instrumental settings were as follows: sweep width, 120 G; resolution, 1024 points; modulation frequency, 100 kHz; modulation amplitude, 1.0 G; time constant, 20.5 ms, incident power, 5.0 mW. Several scans, typically 16, were accumulated to improve the signal-to-noise ratio. Quantitative analysis of ESR spectra was realized determining the fundamental parameters which describe them. Particularly, for isotropic spectra, the “isotropic hyperfine coupling constant”, A_N or a'_N , and the correlation time, τ_C , were determined, while the values of the outer hyperfine splitting, $2A_{\max}$, were determined for the anisotropic spectra by measuring, through a home-made MATLAB-based routine, the difference between the low-field maximum and the high-field minimum [6]. The main source of error on the $2A_{\max}$ value is the uncertainty in composition of samples prepared by mixing few microliters of mother solutions. For this reason, reproducibility of $2A_{\max}$

determination was estimated by evaluating its value for selected independently prepared samples with the same nominal composition. Generally, it was found to be ± 0.4 G.

A more detailed description of the ESR technique principles is reported in the Appendix section.

3.2.4 Neutron Reflectivity measurements

NR measurements were performed on the FIGARO and D17 reflectometers [7,8] at the high flux reactor of the Institut Laue-Langevin (ILL, Grenoble, France) in time-of-flight mode using a spread of wavelengths between 2 and 20 Å with two incoming angles of 0.8 and 3.2°.

Lipid samples were measured using H₂O, SMW (silicon-matched water), 4MW and D₂O as solvent contrasts. SMW ($\rho = 2.07 \times 10^{-6} \text{ \AA}^{-2}$) is a mixture of 38 vol % D₂O ($\rho = 6.35 \times 10^{-6} \text{ \AA}^{-2}$) and 62 vol % H₂O ($\rho = -0.56 \times 10^{-6} \text{ \AA}^{-2}$) with the same refraction index for neutrons as a bulk silicon, while 4MW ($\rho = 4 \times 10^{-6} \text{ \AA}^{-2}$) consists of 66 vol % D₂O and 34 vol % H₂O. The measurement of samples in different solvent contrasts greatly enhances the sensitivity of the technique [9]. Neutron Reflectivity profiles were analyzed by box model fitting using the AFIT and MOTOFIT programs [10,11]. They allow the simultaneous analysis of reflectivity profiles from the same sample in different water contrasts, characterizing each layer by its thickness, ρ , solvent volume fraction, and interfacial roughness. These parameters are varied until the optimum fit to the data is found. Although more than one model can be found for a given experimental curve, the number of possible models is greatly reduced by a prior knowledge of the system, which allows defining upper and lower limits of the parameters to be optimized, by the elimination of the physically meaningless parameters, and most importantly by the use of different isotopic contrasts [9]. A more detailed description of the NR technique principles is reported in the Appendix section.

3.2.5 Circular Dichroism experiments

Circular Dichroism (CD) experiments were performed at 37 °C on a 810-Jasco spectropolarimeter, using a quartz cuvette with a path length of 1 mm. CD spectra of peptides were measured in PBS and in the presence of unilamellar vesicles. The spectra are an average of three consecutive scans from 250 to 200 nm, recorded with a bandwidth of 2.0 nm, a time constant of 16 s, and a scan rate of 5 nm/min. Mean residues ellipticities, $[\theta]$, were calculated as $(MRW \times \theta) / (10 \times d \times c)$. $MRW = M / (n - 1)$, where M is the molecular mass of the peptide and n is the number of amino acids ($n - 1$ is the number peptide bonds). θ is the observed ellipticity in degrees, d is the pathlength in cm and c is the concentration in g mL^{-1} . During all the measurements, the trace of the high tension voltage was checked to be less than 700 V, which should ensure reliability of the data obtained [12]. Base lines of either solvent or vesicular suspensions without peptide were subtracted from each respective sample to yield the peptide contribution.

The propensity of the peptide to assume a helical conformation was estimated from measurements of helical mean residue ellipticity at 222nm [13]. We used $[\theta]_{222}$ values of 0 and -40,000 ($1 - 2.5/n$) degrees $\text{cm}^2 \text{dmol}^{-1}$ per amino acid residue for 0% and 100% helicity. The correction for aromatic CD contributions to $[\theta]_{222}$ due to two internal Trp residues has been applied ($[\theta]_{222}^{\text{aromatic}} = -2.300$ per residue). Finally, the fraction of helix was calculated as $[\theta]_{222} / ([\theta]_{222}^{\text{helix}} + [\theta]_{222}^{\text{aromatic}})$.

3.2.6 Spectrofluorimetric experiments

Peptides-phospholipid interactions were also studied by monitoring the changes in the Trp fluorescence emission spectra of the peptide upon addition of increasing amounts of POPC unilamellar vesicles. Fluorescence measurements were performed at 37 °C using a Jasco FP750 spectrofluorimeter, equipped with a thermostatically controlled cuvette

holder. The excitation wavelength was 280 nm and emission spectra were recorded between 310 and 450 nm, with slit widths of 2 nm.

The titration was performed by adding measured amounts of a solution containing the peptide and suspended lipid vesicles to a weighed amount of a solution of the peptide at the same concentration, initially put into the spectrofluorimetric cuvette. In this way, the lipid concentration was progressively increased (from 0 to $\sim 1 \times 10^{-3}$ M), while the peptide concentration remained constant during the whole titration. After each addition there was a 20-min wait to ensure equilibrium had been reached.

The change in the peptide fluorescence has been reported by Christiaens et al. [14] to follow the relation:

$$F = \frac{(F_0[P_F] + F_1[PL])}{([P_F] + [PL])} \quad (3.2.6.1)$$

where F is the fluorescence intensity at a given added lipid concentration. F_0 and $[P_F]$ are the fluorescence intensity and concentration of the unbound peptide, respectively, while F_1 and $[PL]$ are the fluorescence intensity and concentration of the peptide-lipid complex. $[PL]$ can be obtained *via* the definition of the dissociation (association) constant:

$$K_d = \frac{1}{K_a} = \frac{([P_F][L_F])}{[PL]} \quad (3.2.6.2)$$

with K_d dissociation constant, K_a association constant, and $[L_F]$ free lipid concentration.

Eqn (3.2.6.2) can be rearranged to the following quadratic equation:

$$[PL]^2 - [PL]\left([P_{tot}] + \frac{[L_{tot}]}{n} + K_d'\right) + \frac{[L_{tot}]}{n}[P_{tot}] = 0 \quad (3.2.6.3)$$

The parameter n , representing the formal number of phospholipid molecules that are involved in a binding site for one peptide, is introduced in order to account for the formal

stoichiometry of binding ($K'_d = K_d/n$). The solution of this quadratic equation is thus given by:

$$[\text{PL}] = \frac{\left\{ S \pm (S^2 - 4\left(\frac{[\text{L}_{\text{tot}}]}{n}\right)[\text{P}_{\text{tot}}]^{1/2}) \right\}}{2} \quad (3.2.6.4)$$

with

$$S = [\text{P}_{\text{tot}}] + \frac{[\text{L}_{\text{tot}}]}{n} + K'_d$$

Substitution of Eqn (3.2.6.4) into Eqn (3.2.6.1) yields an equation of F as a function of $[\text{P}_{\text{tot}}]$ and $[\text{L}_{\text{tot}}]$. By plotting the measured fluorescence intensity as a function of $[\text{L}_{\text{tot}}]$, K'_d and n can be determined through a non-linear best fitting procedure of the experimental fluorescence intensities at a fixed wavelength. K_d is obtained by multiplying of K'_d by n .

3.2.7 Dynamic Light Scattering measurements

Dynamic Light Scattering (DLS) investigations were performed with a setup composed by a Photocor compact goniometer, a SMD 6000 Laser Quantum 50 mW light source operating at 5325 Å and a PMT and correlator obtained from Correlator.com. All the measurements were performed at (25.00 ± 0.05) °C with the temperature controlled through the use of a thermostat bath. In dynamic light scattering, the intensity autocorrelation function $g^{(2)}(t)$ is measured and related to the electric field autocorrelation $g^{(1)}(t)$ by the Siegert relation [15]:

$$g^{(2)}(t) = 1 + \beta |g^{(1)}(t)|^2 \quad (3.2.7.1)$$

where $\beta(\leq 1)$ is the coherence factor, which accounts for the deviation from ideal correlation and depends on the experimental geometry. The parameter $g^{(1)}(t)$ can be written as the Laplace transform of the distribution of the relaxation rate Γ used to calculate the translational diffusion coefficient D :

$$g^{(1)}(t) = \int_{-\infty}^{+\infty} \tau A(\tau) \exp\left(-\frac{t}{\tau}\right) d \ln \tau \quad (3.2.7.2)$$

where $\tau = 1/\Gamma$. Laplace transforms were performed using a variation of CONTIN algorithm incorporated in Precision Deconvolve software. From the relaxation rates, the z -average of the diffusion coefficient D may be obtained as [16]:

$$D = \lim_{q \rightarrow 0} \frac{\Gamma}{q^2} \quad (3.2.7.3)$$

where $q = 4\pi n_0 / \lambda \sin(\theta/2)$ is the modulus of the scattering vector, n_0 is the refractive index of the solution, λ is the incident wavelength and θ represents the scattering angle. Thus D is obtained from the limit slope of Γ as a function of q^2 , where Γ is measured at different scattering angles.

3.2.8 Small Angle Neutron Scattering measurements

SANS measurements were performed at 25 °C with the KWS2 instrument located at the Heinz Meier Leibnitz Source, Garching Forschungszentrum (Germany). Neutrons with a wavelength spread $\Delta\lambda/\lambda \leq 0.2$ were used. A two-dimensional array detector at three different wavelength (W)/collimation (C) /sample-to-detector(D) distance combinations ($W_{7\text{\AA}}C_{8\text{m}}D_{2\text{m}}$, $W_{7\text{\AA}}C_{8\text{m}}D_{8\text{m}}$ and $W_{19\text{\AA}}C_{8\text{m}}D_{8\text{m}}$), measured neutrons scattered from the samples. These configurations allowed collecting data in a range of the scattering

vector modulus between 0.0019 \AA^{-1} and 0.179 \AA^{-1} . The investigated samples were contained in a closed quartz cell, in order to prevent the solvent evaporation, and kept under measurements for a period such to have ~ 2 million counts of neutrons. The obtained raw data were then corrected for background and empty cell scattering. Detector efficiency corrections, radial average and transformation to absolute scattering cross sections $d\Sigma/d\Omega$ were made with a secondary plexiglass standard [17,18].

References

- [1] Tarallo R., Accardo A., Falanga A., Guarnieri D., Vitiello G., Netti P., D'Errico G., Morelli G., Galdiero S. Clickable functionalization of liposomes with gH625 peptide from Herpes simplex virus type I for intracellular delivery, *Chemistry* 17 (2011) 12659-12668.
- [2] Marsh D. Electron spin resonance in membrane research: protein-lipid interactions, *Methods* 46 (2008) 83-96.
- [3] Marsh D., Watts A. Spin-labelling and lipid-protein interactions in membranes, In: Jost PC, Griffith OH (eds) Lipid-protein interactions, vol 2. *Wiley Interscience*, New York, (1982) 53-126.
- [4] Wacklin H.P., Thomas R K. Spontaneous formation of asymmetric lipid bilayers by adsorption of vesicles, *Langmuir* 23 (2007) 7644-7651.
- [5] Fragneto-Cusani G. Neutron reflectivity at the solid/liquid interface: examples of applications in biophysics, *J. Phys. Condens. Matter* 13 (2001) 4973-4989.
- [6] Schorn K., Marsh D. Extracting order parameters from powder EPR lineshapes for spin-labelled lipids in membranes, *Spectrochim. Acta A* 53 (1997) 2235-2240.
- [7] Cubitt R., Fragneto G. D17: The new reflectometer at the ILL, *Appl. Phys. A (Suppl.)* 74 (2004) S329-S331.
- [8] Campbell R.A., Wacklin H.P., Sutton I., Cubitt R., Fragneto G. FIGARO: The new horizontal neutron reflectometer at the ILL, *Eur. Phys. J. Plus* 126 (2011)107-
- [9] Fragneto G., Thomas R.K., Rennie A.R., Penfold J. Neutron Reflection from hexadecyl trimethyl ammonium bromide adsorbed on smooth and rough silicon surfaces, *Langmuir* 12 (1996) 6036-6043.
- [10] Thirtle P.N. *Afit simulation program*, v. 3.1, Oxford University, 1997.
- [11] Nelson A.J. Co-refinement of multiple-contrast neutron/X-ray reflectivity data using MOTOFIT, *Appl. Crystallogr.* 39 (2006) 273-276.
- [12] Kelly S. M., Jess T. J., Price N. C. How to study proteins by circular dichroism, *Biochim. Biophys. Acta* 1751 (2005) 119-139.
- [13] Chakrabarty A., Kortemme T., Baldwin R.L. Helix propensities of the amino acids measured in alanine-based peptides without helix-stabilizing side chain interactions. *Protein Sci.* 3 (1994)843-852.

- [14] Christiaens B., Symoens S., Vanderheyden S., Engelborghs Y., Joliot A., Prochiantz A., Vandekerckhove J., Rosseneu M., Vanloo B. Tryptophan fluorescence study of the interaction of penetratin peptides with model membranes, *Eur. J. Biochem.* 269 (2002) 2918-2926.
- [15] Berne B. J., Pecora R. *Dynamic Light Scattering: with Applications to Chemistry, Biology, and Physics*(1975).
- [16] Brehm G.A., Bloomfield V.A. Analysis of polydispersity in polymer solutions by inelastic laser light scattering, *Macromolecules* 8 (1975) 663-665.
- [17] Wignall G.D., Bates F.S. Absolute calibration of small-angle neutron scattering data, *J. Appl. Crystallogr.* 20 (1987)28–40.
- [18] Russell T.P., Lin J.S., Spooner S., Wignall G.D. Intercalibration of small-angle X-ray and neutron scattering data, *J. Appl. Crystallogr.* 21 (1988) 629–638.

CHAPTER 4

Results and Discussion

Part I

Microstructural characterization of phospholipid membranes

4.1 Introduction

In this chapter, a wide physico-chemical characterization of different phospholipid self-aggregates is presented. In particular, the focus is on their microstructural properties as determined by the molecular geometry and charge distribution of the various components. In addition, the relationship between the aggregate microstructure and its mesoscopic properties is analysed. Indeed, although the considered systems present many differences in terms of components and composition, the driving forces ruling the aggregation process and the properties of the resulting aggregates have a common origin: hydrophobic attraction among the apolar moieties, and electrostatic repulsion among the charged moieties. Steric constraints also play a fundamental role. This study was realized by an approach combining different experimental techniques, which have furnished a more clear description of the system behavior. This combined experimental approach was used for all systems described in the following sections, which are:

- Lysophosphatidylcholine aggregates;
- POPC and DOPC phospholipid membranes containing CHOL;
- POPC membranes containing polyunsaturated (PUFA) phospholipids;
- Liposomes formed by lipopolysaccharides (LPS).

4.2 Lysophosphatidylcholine micellar aggregates: the structural basis for their use as biomembrane mimics

Lysophospholipids are amphiphilic single-chain molecules and constitute an important subclass of phospholipids that exhibit unique physical and biological properties not found in their parent bi-chained phospholipids [1]. Lysophospholipids make up less than 5 mol % of the total phospholipids in a normal cell and higher lysophospholipid concentrations are associated with certain disease states, cell fusion and cell lysis, since they can disrupt the structure of biological membranes. Lysophosphatidylcholines (lysoPC)

is the most important class of lysophospholipids, which are products of phospholipase A2 catabolism of diacylphosphatidylcholine [2]. Due to their relatively large hydrophilic group in relation to the hydrocarbon chain, lysophospholipids are more soluble in aqueous medium with respect to their bi-chained analogues, and they can aggregate into micelles, which are largely used as mimics of biological membranes, above a critical micelle concentration (CMC) [3].

For this reason, a physicochemical characterization of the self-aggregation properties of lysoPC's with different acyl chain lengths (C_n lysoPC, $n=6, 8, 10, 12$, see Figure 4.2.1 for the molecular structure) was performed by a combined experimental strategy, including Pulsed Gradient Spin Echo (PGSE)-NMR and spin-probing Electron Spin Resonance (ESR) [4].

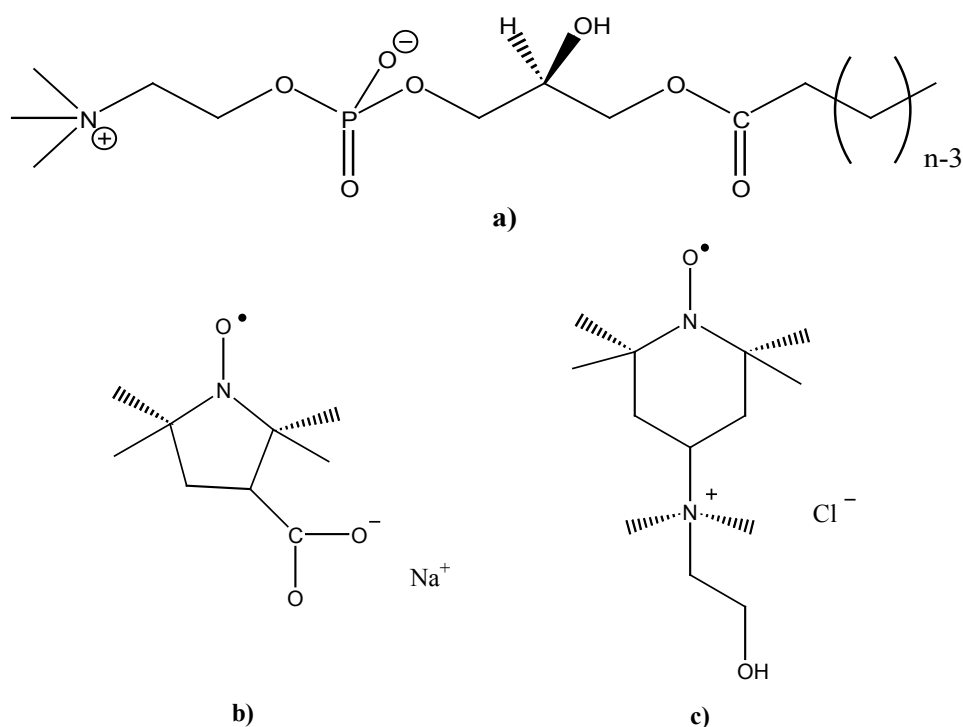


Figure 4.2.1 - Molecular structures of a) C_n lysoPC, b) deprotonated 3-carboxy-PROXYL (CP), c) TEMPO-choline (TC).

PGSTE-NMR has provided accurate intradiffusion coefficients for the random thermal motion of surfactants in systems of uniform chemical composition, allowing to put in evidence the formation of micelles, and to estimate their dimension. Moreover, the water

mobility could be followed, furnishing information on the solute hydration [5]. ESR spectroscopy, via the introduction in the system of paramagnetic molecular probes, has allowed a characterization of intermolecular interactions in micellar systems, taking advantage by the direct relation existent between the spectra of spin probes and the micro-environment in which they were embedded [6].

The experimental intradiffusion coefficients of C_n lysoPC in aqueous mixtures are shown, as a function of the phospholipid molality, in Figures 4.2.2A-4.2.2C. In all cases, D_p shows a sigmoidal trend which presents a change of slope at the CMC. The measured CMC values are collected in Table 4.2.1 and they are in good agreement with literature values reported in the same table [7].

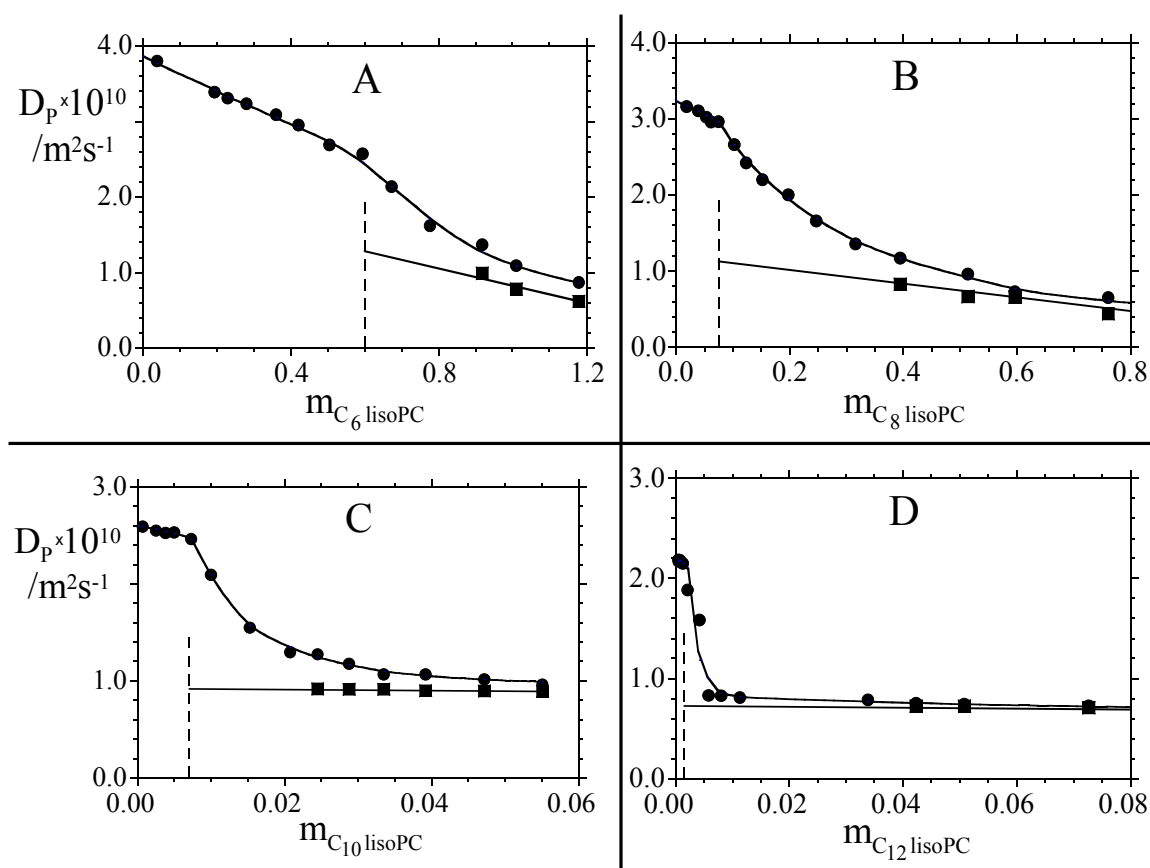


Figure 4.2.2 - (●) Phospholipid intradiffusion coefficients, D_p , and (■) TMS intradiffusion coefficients, D_p^M , in C_n lysoPC aqueous solutions at 25 °C. A, C_6 lysoPC; B, C_8 lysoPC; C, C_{10} lysoPC; D, C_{12} lysoPC.

	CMC (mol kg ⁻¹)	CMC ^a (mol kg ⁻¹)	D _P [◦] × 10 ¹⁰ (m ² s ⁻¹)	α (mol ⁻¹ kg)	D _P ^{M,CMC} × 10 ¹¹ (m ² s ⁻¹)	β (mol ⁻¹ kg)	r × 10 ⁹ (m)	l × 10 ⁹ (m)
C ₆ lysoPC	0.6	-	3.82±0.03	-0.57±0.02	13.9±1.6	-0.97±0.14	1.4	0.65
C ₈ lysoPC	0.07	0.057	3.24±0.03	-1.23±0.18	11.2±0.6	-0.84±0.04	1.8	0.91
C ₁₀ lysoPC	0.007	0.0057	2.60±0.02	-6.9±1.7	9.33±0.03	-0.94±0.12	2.2	1.16
C ₁₂ lysoPC	0.001	0.0006	2.20±0.02	-18±7	7.56±0.06	-0.98±0.06	2.6	1.41

^aData from Ref. 7

Table 4.2.1 - Critical Micelle Concentration and limiting intradiffusion coefficients for the C_nlysoPC aqueous mixtures, as evaluated by PSGE-NMR spectroscopy.

The trend of log₁₀(CMC) vs the number of carbon atoms in the phospholipid acyl chain, *n*, is well described by the following linear relation:

$$\log_{10}(\text{CMC}) = A + Bn \quad (4.2.1)$$

with $A = 2.56 \pm 0.07$ and $B = -0.465 \pm 0.008$. In the case of nonionic surfactants, the plot of log₁₀(CMC) vs *n* usually presents a linear trend with slope 0.5 [8], while the slope is 0.3 for ionic surfactants [9]. Zwitterionic surfactants present a slope value intermediate between these limits, depending on the surfactant headgroup structure [10]. Thus, from this viewpoint, the C_nlysoPC behavior seems to be similar to that of nonionic surfactants.

In the premicellar composition range, the D_P data may be fitted as a function of phospholipid molality:

$$D_P = D_P^\circ(1 + \alpha m) \quad (4.2.2)$$

The fitting parameters, D_P[◦] and α, are reported in Table 4.2.1. The D_P[◦] values linearly scale with the hydrophobic chain length (D_P[◦]/10⁻¹⁰ m²s⁻¹ = (5.3 ± 0.02) - (0.27 ± 0.02) × *n*) with a slope which is similar to that found for nonionic ethoxylated surfactants [11]. The α values increase with *n*, indicating that hydrophobic interactions establish among the phospholipid monomers.

Given the rapid exchange between free and micellized phospholipid molecules, in the micellar composition range the experimental phospholipid intradiffusion coefficient is a mean value between that of free monomers, D_P^F , and that of the micellized molecules, D_P^M [12]. Thus:

$$D = p_F D_P^F + (1 - p_F) D_P^M = \frac{m_F}{m} D_P^F + \frac{(1 - m_F)}{m} D_P^M \quad (4.2.3)$$

where p_F is the fraction of amphiphile in the monomeric state and m_F is the free monomer molality. D_P^M was experimentally estimated by the addition of tetramethylsilane (TMS) to the system. In fact, for a compound which is entirely confined into the micelles and has a negligible solubility in the intermicellar solution, the observed intradiffusion coefficient will be the same as the intradiffusion coefficient of the micelles [13]. To be sure that the TMS insertion does not change the shape and dimension of micelles, two measurements were performed for each solution, before and after the TMS addition, checking that the phospholipid intradiffusion coefficients were the same. Inspection of Figures 4.1.2A-4.2.2D shows that $D_P^M \rightarrow D_P$ as the phospholipid molality increases and the monomeric contribution becomes negligible.

Since the CMC can be considered as the infinite dilution for micelles, the concentration dependence of D_P^M can be appropriately expanded as a function of $(m - \text{CMC})$,

$$D_P^M = D_P^{M,\text{CMC}} [1 + \beta(m - \text{CMC})] \quad (4.2.4)$$

The fitting parameters of Eq. (4.2.4) are also collected in Table 4.2.1. The micelle intradiffusion coefficient extrapolated at the CMC, $D_P^{M,\text{CMC}}$, can be related to the

hydrodynamic size of the aggregates by using the Stokes–Einstein equation to calculate the apparent radius, r :

$$r = \frac{K_B T}{6\pi\eta D_p^{M,CMC}} \quad (4.2.5)$$

where η is the viscosity of the aqueous medium. The r values obtained through Eq. (4.2.2) are collected in Table 4.2.1. It is possible to compare these values with those of the extended hydrophobic chain of the phospholipid, computed according to the Tanford relation [14]. In doing that, the carbonyl group has been considered as part of the hydrophilic headgroup. Inspection of Table 4.2.1 shows that, for all considered phospholipids, l is much lower than r , indicating that the C_n lysoPC micelle structure present a thick hydrophilic layer ($r - l \approx 1 \cdot 10^{-9}$ m).

The water intradiffusion coefficient, D_w , in water- C_n lysoPC mixtures is shown in Figs. 4.2.3A-4.2.3D. In all cases, it decreases with an increase of the phospholipid concentration, showing a slope change at the CMC. This slope change becomes more marked with increasing the length of the acyl chain. In the premicellar region, the decreasing D_w trend can be attributed to the fact that some water molecules enter the monomer hydration shell, thus becoming slower with respect to the free ones. Quantitatively, it can be written that:

$$D_w = p_w^F D_w^F + p_w^{H,m} D_w^{H,m} = \frac{n_w^F}{n_w} D_w^F + \frac{n_w^{H,m}}{n_w} D_w^{H,m} \quad (4.2.6)$$

In the molality scale, $n_w=55.5$, while the moles of water molecules hydrating phospholipid monomers equal to the phospholipid molality multiplied by the number of water molecules hydrating each phospholipid molecule ($n_w^{H,m} = m \times h^m$). In the hypothesis

that D_W^F is the self diffusion coefficient of neat water, and hydrating water molecules diffuse together with the hydrated phospholipid ($D_W^{H,m} = D_P$), fitting of Eq. (4.2.6) to the premicellar D_W data allows estimating h^m .

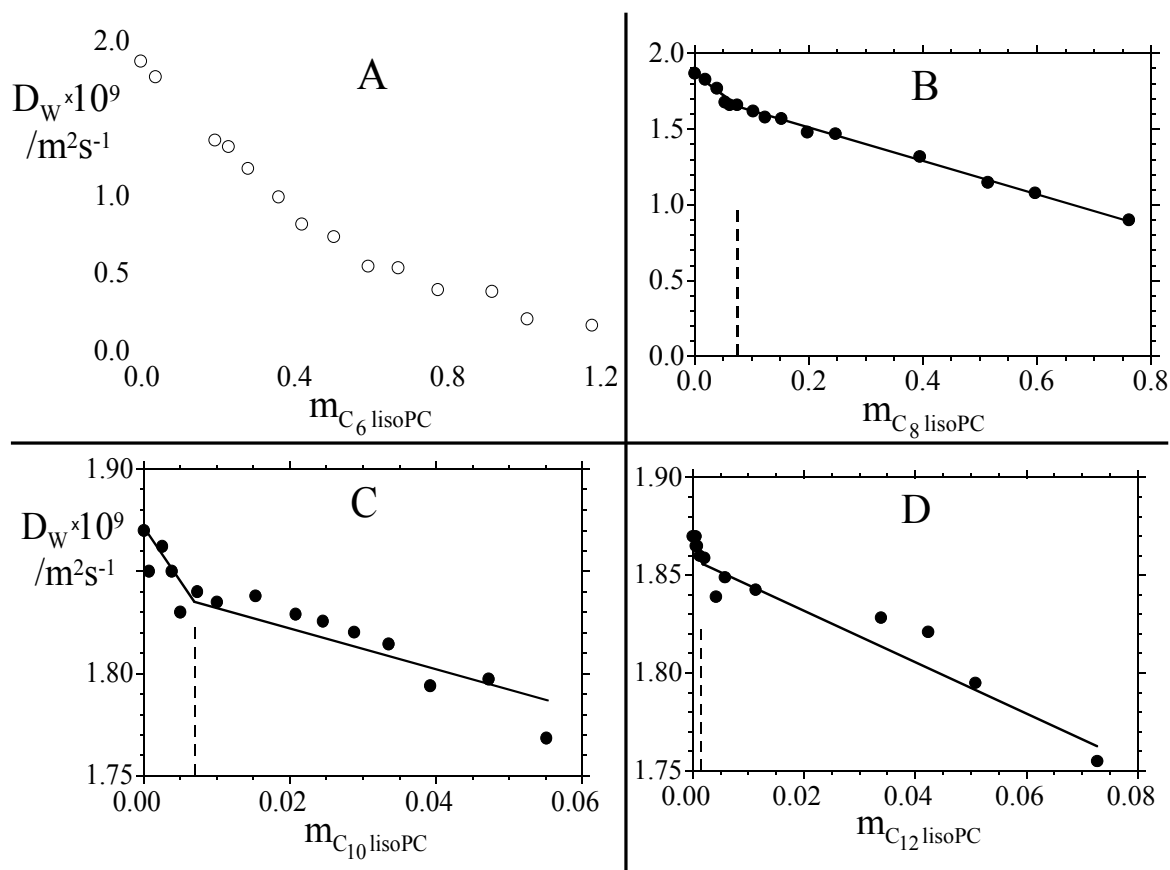


Figure 4.2.3 - Solvent intradiffusion coefficients, D_W , in C_n lysoPC aqueous solutions at 25 °C. A, C_6 lysoPC; B, C_8 lysoPC; C, C_{10} lysoPC; D, C_{12} lysoPC.

The values are collected in Table 4.2.2. It has to be emphasized that intradiffusion coefficients allow to estimate the total number of water molecules whose motion is slowed down by the interaction with a solute.

	h^m	h^M	N
C_6 lysoPC	73 ± 2	37 ± 4	9 ± 2
C_8 lysoPC	98 ± 6	32 ± 1	16 ± 4
C_{10} lysoPC	160 ± 30	29 ± 4	28 ± 4
C_{12} lysoPC	209 ± 40	27 ± 2	49 ± 7

Table 4.2.2 - Phospholipid hydration and aggregation numbers for the C_n lysoPC aqueous mixtures, as evaluated by PSGE-NMR spectroscopy.

Particularly, in the case of amphiphilic molecules, such as monomeric C_n lysoPC, this approach includes, besides the water molecules hydrating the polar headgroup, those forming the cage around the hydrophobic moieties of the solute.

Above the CMC, the smaller reduction of D_W with increasing phospholipid concentration indicates that the number of water molecules hydrating the micellized phospholipid is lower than that of molecules hydrating monomers. Indeed, upon the C_n lysoPC selfaggregation, the water molecules involved in the hydrophobic interaction with the acyl chain are released. Quantitatively, in the micellar composition range the water intradiffusion coefficient, D_W , is an average value between the contributions of free water molecules and molecules hydrating the phospholipid monomers and micelles:

$$D_W = p_W^F D_W^F + p_W^{H,m} D_W^{H,m} + p_W^{H,M} D_W^{H,M} = \frac{n_W^F}{n_W} D_W^F + \frac{n_W^{H,m}}{n_W} D_W^{H,m} + \frac{n_W^{H,M}}{n_W} D_W^{H,M} \quad (4.2.7)$$

The diffusivity of water molecules hydrating micellized phospholipid can be assumed to be equal to that of the micellar aggregates ($D_W^{H,M} = D_p^M$). $n_W^{H,M}$ are the moles of water hydrating micellized C_n lysoPC, and can be computed as the hydration number of aggregated phospholipid multiplied by its molality ($n_W^{H,M} = (m - \text{CMC}) \times h^M$)

Fitting of Eq. (4.2.7) to the experimental D_W data, in the micellar concentration range, allows to obtain the h^M values summarized in Table 4.2.2. The average h^M values for C_n lysoPC is 31 ± 4 . This indicates that the thick layer formed by phospholipid headgroups in the micelles is strongly hydrated. Indeed, perusal of the table reveals that h^M slightly decrease with increasing the phospholipid acyl length. This is probably related to the reduction of the micelle curvature, which brings the headgroups close to each other. The r and h^M values can be used to compute the aggregation number of the micelles,

N. In fact, assuming a spherical shape, N can be computed by the ratio between the experimental and calculated hydrodynamic volumes, according to the relation:

$$N = \frac{\frac{4}{3} \pi r^3}{V_p^{\text{mic}} + h^M V_w} \quad (4.2.8)$$

where V_p^{mic} is the molar volume of the micellized phospholipid [15] and V_w is the molar solvent volume. The N values obtained through Eq. (4.2.8), collected in Table 4.2.2, are of the same order of magnitude of those obtained for ionic surfactants [5], generally lower than those expected for nonionic ones [16].

Furthermore, how the zwitterionic C_n lysoPC headgroup interacts with both cationic (TC) and anionic (CP⁻) radicals was investigated. For both the spin labels, in all the systems considered in the present work, the ESR spectrum shows the lineshape typical of fast motion, without superimposition of different signals and/or sudden increase of the line width. The trend of the nitrogen coupling constant of CP⁻ and TC, A_N , and correlation time, τ_C , as a function of the phospholipid molality, m , are shown in Figs. 4.2.4A-4.2.4D and Figs. 4.2.5A-4.2.5D, respectively. A_N depends on the polarity of the medium in which the nitroxide is embedded; its value increases with both the solvent polarity and H-bonding ability. At the same time, τ_C clearly shows changes in the probe rotational mobility, as determined by the microenvironment viscosity and/or by specific interactions [6].

In all cases, A_N decreases and τ_C increases with increasing m , indicating that the spin labels experience a progressively less polar environment and that their rotational motion is slackened. However, perusal of the figures reveals that the extent of these variations depend on the considered spin label and C_n lysoPC. Note that, in order to make the comparison easier, the figures relative to the same phospholipid (e.g. Fig. 4.2.4A and Fig. 4.2.5A for C_6 lysoPC) present the same scale on each axis, even if on different absolute

values. Indeed, the ESR parameters also depend on the peculiar molecular structure of each spin probe, thus preventing a direct comparison between their absolute values.

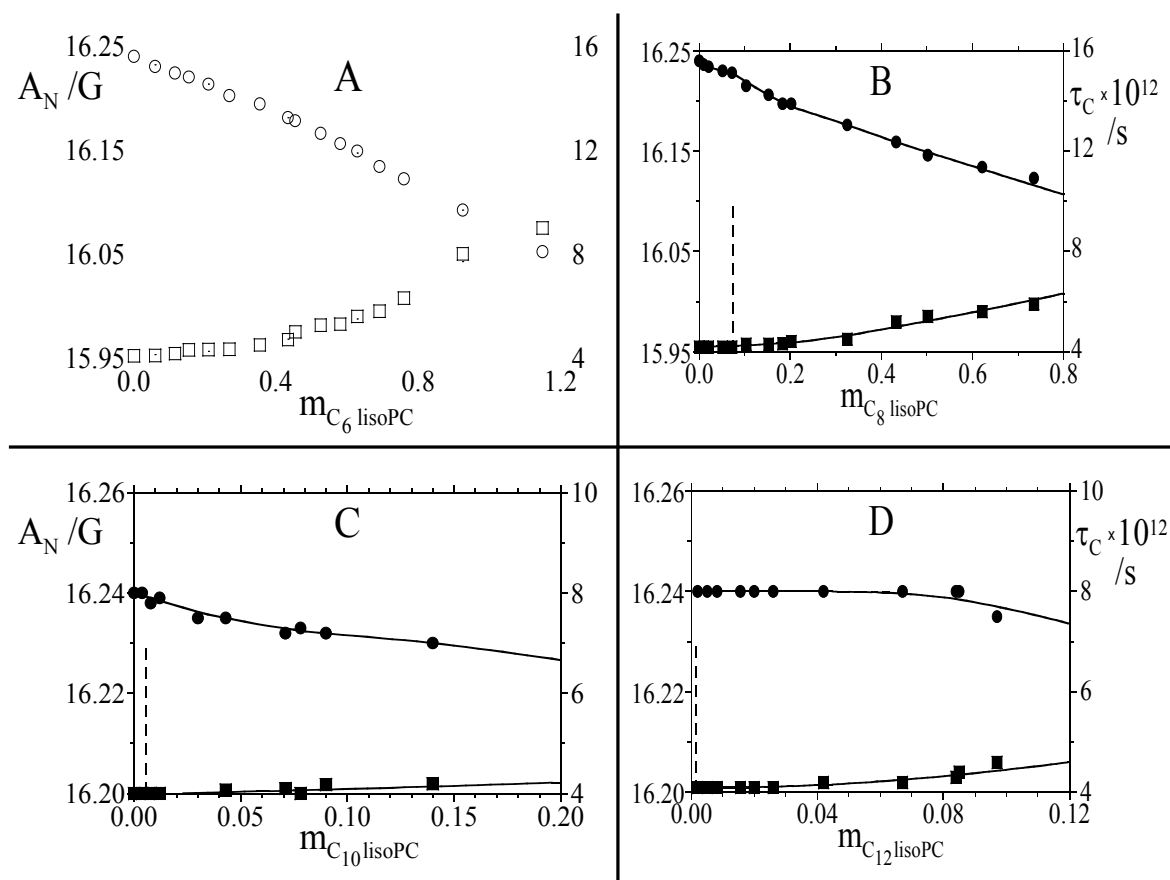


Figure 4.2.4 - (●) Nitrogen hyperfine coupling constant, A_N , and (■) correlation time, τ_C , of CP⁻ in C_n lysoPC aqueous solutions at 25 °C. A, C_6 lysoPC; B, C_8 lysoPC; C, C_{10} lysoPC; D, C_{12} lysoPC.

C_6 lysoPC establishes comparable interactions with both TC and CP⁻, as evidenced by the similar magnitude of the A_N and τ_C variations. In the case of C_8 lysoPC, while the A_N variation is still comparable, τ_C increases much more markedly for TC than for CP⁻, indicating that the cationic probe experiences a more viscous microenvironment than the anionic one. For C_{10} lysoPC and C_{12} lysoPC, the CP⁻ ESR parameters show very slight changes, while for the TC ones the variation is much more evident. Particularly, the τ_C increase becomes progressively higher with increasing the phospholipid acyl chain. These evidences can be interpreted in terms of the structure of the micellar aggregates formed by

the various C_n lysoPC. With increasing the phospholipid acyl chain, more compact micellar aggregates form. Particularly, the hydrophilic headgroups become closer one each other.

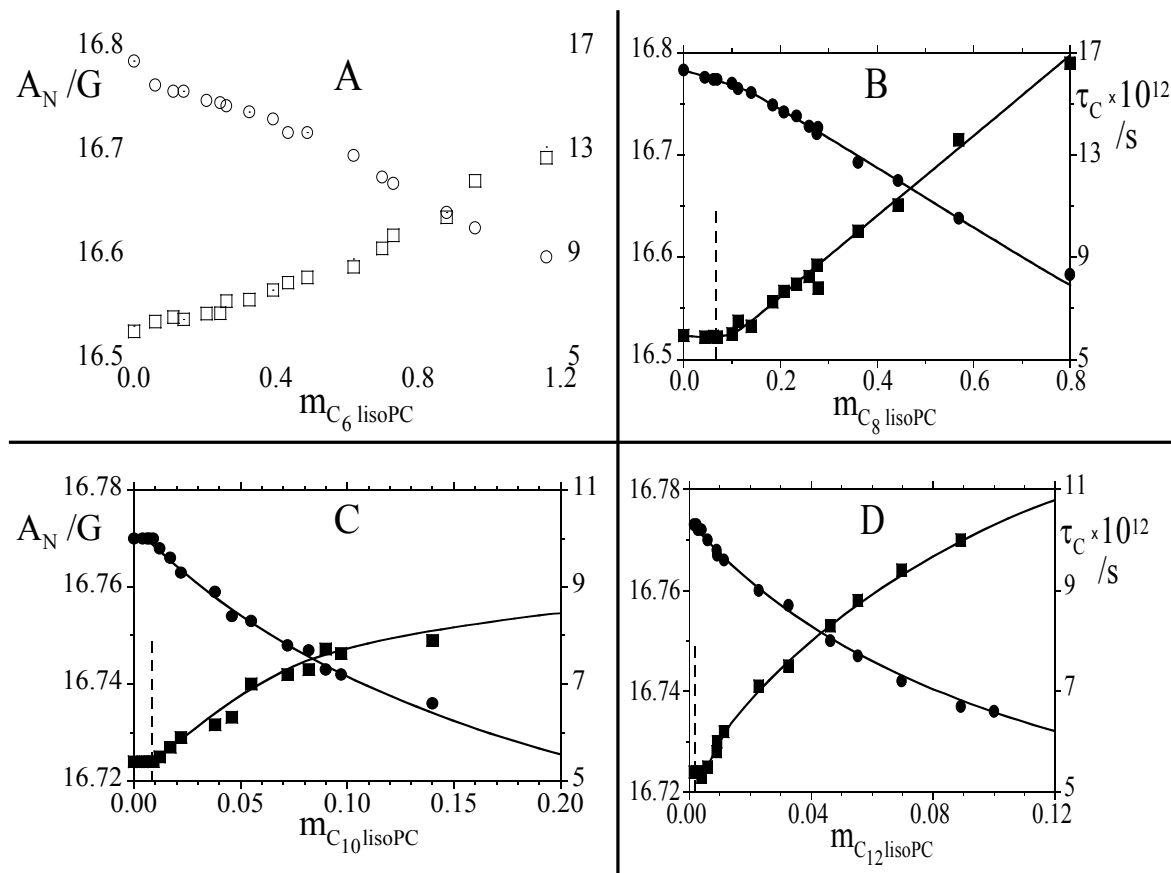


Figure 4.2.5 - (●) Nitrogen hyperfine coupling constant, A_N , and (■) correlation time, τ_C , of TC in C_n lysoPC aqueous solutions at 25 °C. A, C_6 lysoPC; B, C_8 lysoPC; C, C_{10} lysoPC; D, C_{12} lysoPC.

This could also be the reason of the slight decrease of h^M observed in Table 4.2.2.

In the case of CP^- ions, which interact with the terminal choline group, these changes result in a “squeezing” of the spin probes from the micelle interior. In other words, CP^- ions are preferably adsorbed on the micellar surface, with the nitroxide protruding in the aqueous medium, as put in evidence by the limited A_N and τ_C variations. In contrast TC ions, which interact with the inner phosphate group, are embedded in the hydrophilic external layer of the micelles, which becomes more compact and viscous with increasing the phospholipid acyl chain, thus explaining the τ_C increase.

Another consideration has to be done by comparing the trends of the ESR parameters of the cationic probe TC: in the case of C_6 lysoPC and C_8 lysoPC, only a slight

slope change is detectable in correspondence of the CMC. In the case of C₁₀lysoPC and C₁₂lysoPC, they show an almost abrupt slope change. This evidence confirms that micellization is not a first order transition, and becomes progressively sharper with increasing the phospholipid acyl chain [5,16].

Indeed, for C₁₀lysoPC and C₁₂lysoPC, above the CMC, the TC ESR parameters show a typical saturation trend. Because of the low CMC values, spin labels interaction with the monomers can be neglected, so that in the micellar concentration range, the evaluated A_N are mean values between the nitrogen coupling constant of TC localized in the aqueous bulk, A_N^W, and that of TC interacting with the micelles, A_N^M:

$$A_N^M = \frac{n_{TC}^W}{n_{TC}} A_N^W + \frac{n_{TC}^M}{n_{TC}} A_N^M \quad (4.2.9)$$

where n_{TC}^W and n_{TC}^M represent the moles of TC in the aqueous and in the micellar medium, respectively; n_{TC} = n_{TC}^W + n_{TC}^M is the total number of TC moles in the system. Rizzi et al. defined the micelle-water distribution coefficient of a spin label as [17]:

$$K_d = \frac{n_{TC}^M / n^M}{n_{TC}^W / n^W} \quad (4.2.10)$$

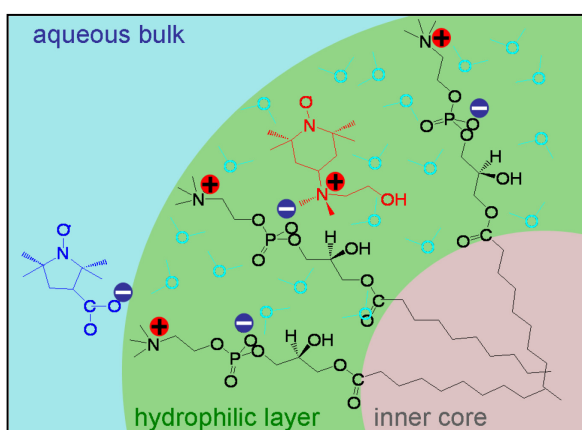
where n^W is number of water moles in the medium and n^M is the number of moles of micellized phospholipid (in our case, n^W = 55.5 and n^M = m - CMC). By fitting Eqns. (4.2.9) and (4.2.10) to the experimental data we obtained the K_d and A_N^M values that are collected in Table 4.2.3. The A_N^M value is the same for both C₁₀lysoPC and C₁₂lysoPC, while the K_d value only slightly increases.

Concerning τ_C , in the lack of a quantitative theory, its value in micellar environment can be estimated as the intercept of the plot of τ_C as a function of $1/m$. The τ_C^M value is significantly higher for C_{12} lysoPC than for C_{10} lysoPC, see Table 4.2.3.

	A_N^M (G)	K_d	$\tau_C^M \times 10^{12}$ (s)
C_{10}lysoPC	16.63 ± 0.02	150 ± 11	10.9 ± 0.2
C_{12}lysoPC	16.65 ± 0.02	250 ± 30	15.4 ± 0.3

Table 4.2.3 - Isotropic hyperfine constant and correlation time of TC in C_n lysoPC micellar environment.

In conclusion, the experimental results show that LysoPCs behave as zwitterionic surfactants, forming micellar aggregates with relatively low aggregation number. These micelles present a thick external region constituted by highly hydrated



glycerophosphocholine groups. In addition, these results furnish some indications in using these systems as mimics of biological membranes in order to study membrane interaction with peptides. Lysophosphatidylcholine micelles can

establish a variety of interaction with guest molecules, including electrostatic interactions with both anions and cations, H-bonding and hydrophobic interaction. Particularly, the micellar external hydrophilic can deform in order to accommodate in its interior guest molecules or portion of them.

4.3 Effect of cholesterol on the POPC and DOPC membranes structure

Phosphocholines are the fundamental components of biomembranes and can show different characteristics in terms of chains length and of unsaturated bonds along the acyl chains. These properties can be influence the bilayer structure. Also, cholesterol (CHOL) is a major components of mammalian cell, consequently it is fundamental to consider its presence in formulating biomimicking systems.

An ESR characterization of the 1-palmitoyl-2-oleoyl-*sn*-glycero-3-phosphocholine (POPC) and 1,2-oleoyl-*sn*-glycero-3-phosphocholine (DOPC) membranes, containing variable amounts of CHOL, was realized by incorporating phosphatidylcholine spin-labeled in different positions of the *sn*-2 chain (*n*-PCSL, with $n = 5, 7, 10, 14$) in the lipid bilayers. ESR spectra of 5-PCSL, which presents the nitroxide group close to its hydrophilic headgroup, show clearly defined axially anisotropic lineshapes, see Figure 4.3.1. Increasing the cholesterol content, the anisotropic character becomes more evidente, as a consequence of the decrease of the nitroxide mobility. A similar behavior was observed in the case of POPC and DOPC membranes. The same effect was observed for the ESR spectra (not shown) of 7 and 10-PCSL, which also present anisotropic lineshapes, although with a lower anisotropy than that observed for the 5-PCSL spectra. Lipid bilayers including phosphatidylcholine spin labeled on the 14 C-atom of the *sn*-2 chain (14-PCSL), in which the nitroxide group is positioned close to the terminal methyl region of the chain, were also investigated. The corresponding spectra are shown in Figure 4.3.2. In this case, significant differences were observed between 14-PCSL spectra in POPC and DOPC-based bilayers. In particular, a narrow quasi isotropic three-line spectrum is obtained for POPC and POPC:CHOL 90:10 samples, as shown in Figure 4.3.2A-B. The higher isotropy of the 14-PCSL spectrum with respect to that obtained for 5-PCSL indicates a flexibility increase in segmental chain mobility in going from the polar headgroups to the inner hydrophobic core, which is a characteristic hallmark of the liquid-crystalline state of fluid phospholipid

bilayers. Increasing the cholesterol content, a second component appears in the ESR spectra, as shown in Figure 4.3.2C-D. This second component is resolved in the outer wings of the spectra and corresponds to spin-labeled lipid chains whose motion is restricted.

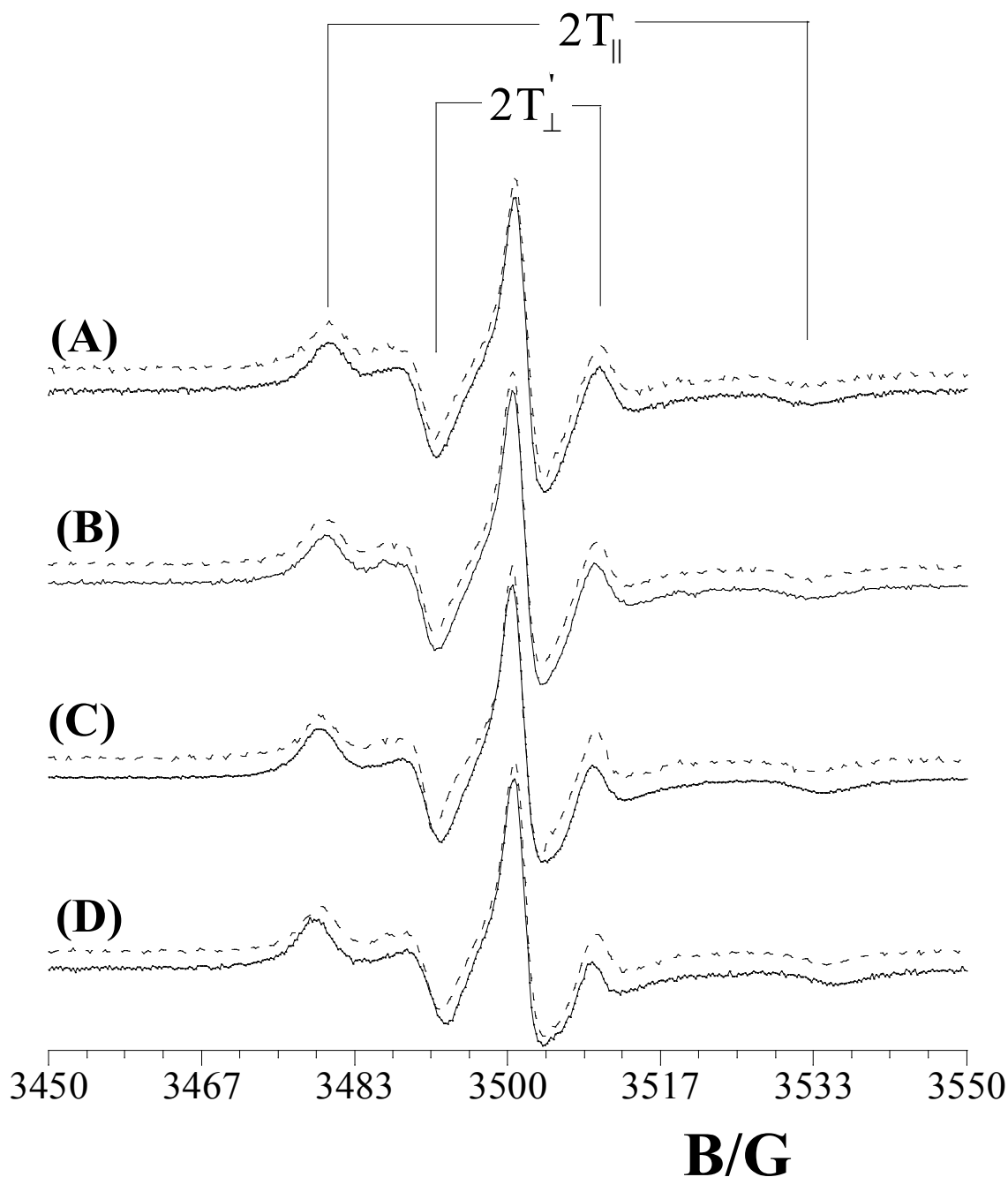


Figure 4.3.1 – ESR spectra of 5-PCSL in lipid bilayers of **(A)** pure POPC (continuous line) and pure DOPC (dotted line), **(B)** POPC:CHOL90:10 wt/wt (continuous line) and DOPC:CHOL 90:10 wt/wt (dotted line), **(C)** POPC:CHOL 80:20 wt/wt (continuous line) and DOPC:CHOL 80:20 wt/wt (dotted line), **(D)** POPC:CHOL 70:30 wt/wt (continuous line) and DOPC:CHOL 70:30 wt/wt (dotted line).

In the case of DOPC-based membranes, the increase of 14-PCSL anisotropy is less evident than in the case of POPC-based membranes. In particular, the second component observed in the 14-PCSL spectra of POPC bilayers with an high cholesterol content, (see Figure 4.3.3) indicating that the terminal segments of DOPC acyl chains have a major possibility of motion with respect to those of POPC.

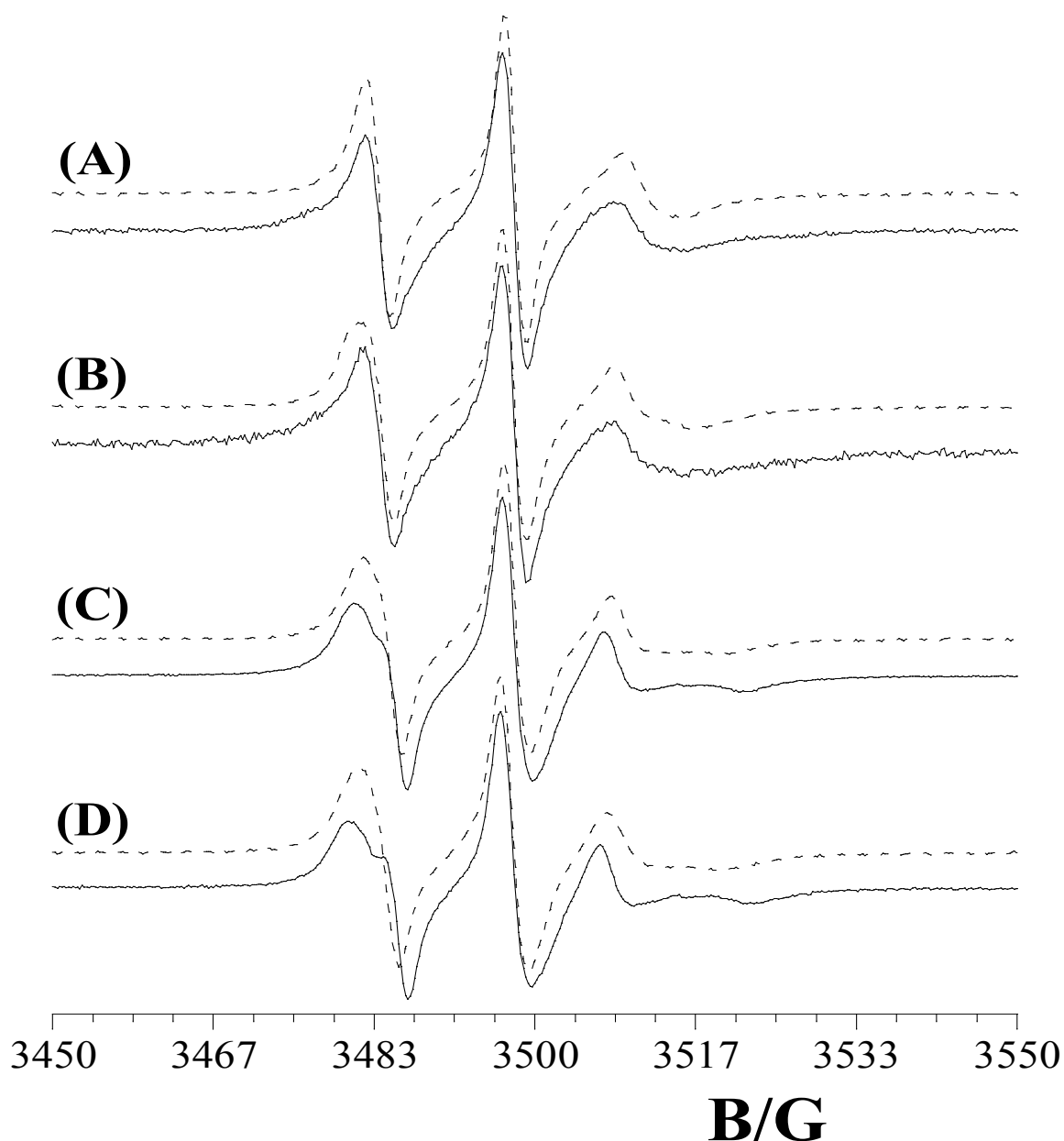


Figure 4.3.2 – ESR spectra of 14-PCSL in lipid bilayers of (A) pure POPC (continuous line) and pure DOPC (dotted line), (B) POPC:CHOL 90:10 wt/wt (continuous line) and DOPC:CHOL 90:10 wt/wt (dotted line), (C) POPC:CHOL 80:20 wt/wt (continuous line) and DOPC:CHOL 80:20 wt/wt (dotted line), (D) POPC:CHOL 70:30 wt/wt (continuous line) and DOPC:CHOL 70:30 wt/wt (dotted line).

In an attempt to quantitatively analyze the spectra, we determined the order parameter, S . This parameter is related to the angular amplitudes of motion of the label, which in turn reflects the motion of the acyl chain segment to which the label is bound. In particular, S was calculated according to the relation [18]:

$$S = \frac{(T_{\parallel} - T_{\perp}) a_{\text{N}}}{(T_{\text{zz}} - T_{\text{xx}}) a'_{\text{N}}} \quad (4.3.1)$$

where T_{\parallel} and T_{\perp} are two phenomenological hyperfine splitting parameters which can be determined experimentally for each spin-labeled phospholipid as shown in Figure 4.4.8 (note that $2T'_{\perp} = 2T_{\perp} - 1.6$, see ref. 19). T_{xx} and T_{zz} are the principal elements of the real hyperfine splitting tensor in the spin Hamiltonian of the spin-label, which can be measured from the corresponding single-crystal ESR spectrum and are reported in the literature ($T_{\text{xx}} = 6.1$ G and $T_{\text{zz}} = 32.4$ G, ref. 20). a_{N} and a'_{N} are the isotropic hyperfine coupling constants for the spin-label in crystal state and in the membrane, respectively, given by:

$$a_{\text{N}} = \frac{1}{3}(T_{\text{zz}} + 2T_{\text{xx}}) \quad (4.3.2)$$

$$a'_{\text{N}} = \frac{1}{3}(T_{\parallel} + 2T_{\perp}) \quad (4.3.3)$$

The isotropic hyperfine coupling constant is an index of the micropolarity experienced by the nitroxide; in particular, it increases with the environmental polarity. The $a_{\text{N}}/a'_{\text{N}}$ ratio in eqn (4.3.1) corrects the order parameter for polarity differences between the crystal state and the membrane.

The S values obtained from the spectra of n -PCSL in POPC and DOPC lipid bilayers are in Figures 4.3.3 and 4.3.4. Inspection of the figures shows that, for all spin-labels, the order parameter S increase with CHOL content, both in POPC and DOPC bilayers.

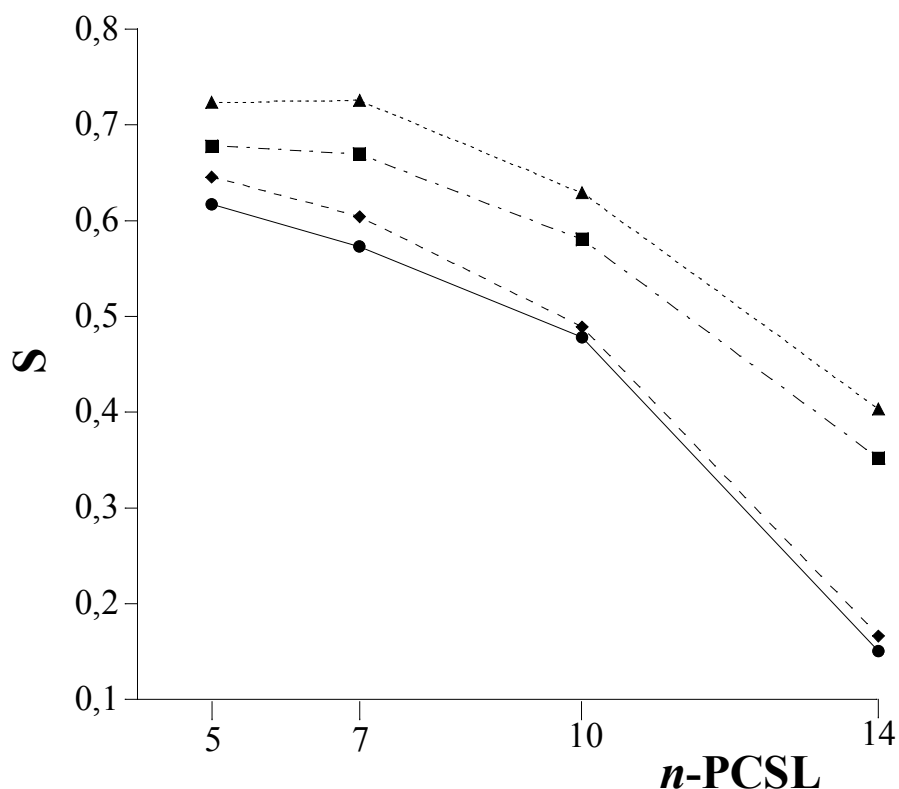


Figure 4.3.3- Order parameter, S , of n -PCSL in membranes of pure POPC (●), POPC:CHOL 90:10 mol/mol (◆), POPC:CHOL 80:20 wt/wt (■) and POPC:CHOL 70:30 wt/wt (▲) as function of n .

These results indicate that CHOL affects the lipid packing of phospholipids chains, finely tuning the microstructural properties of lipid membranes and confirming that it causes a transition from the liquid-disorder phase (L_d) to the liquid-ordered phase (L_o). In addition, it is possible to note that while the S increase for of DOPC membranes is gradual with the CHOL concentration, for POPC bilayers S strongly increases going from 10% to 20% CHOL content, suggesting a significant effect induced by the CHOL in influencing the bilayer structure and the phospholipids packing.

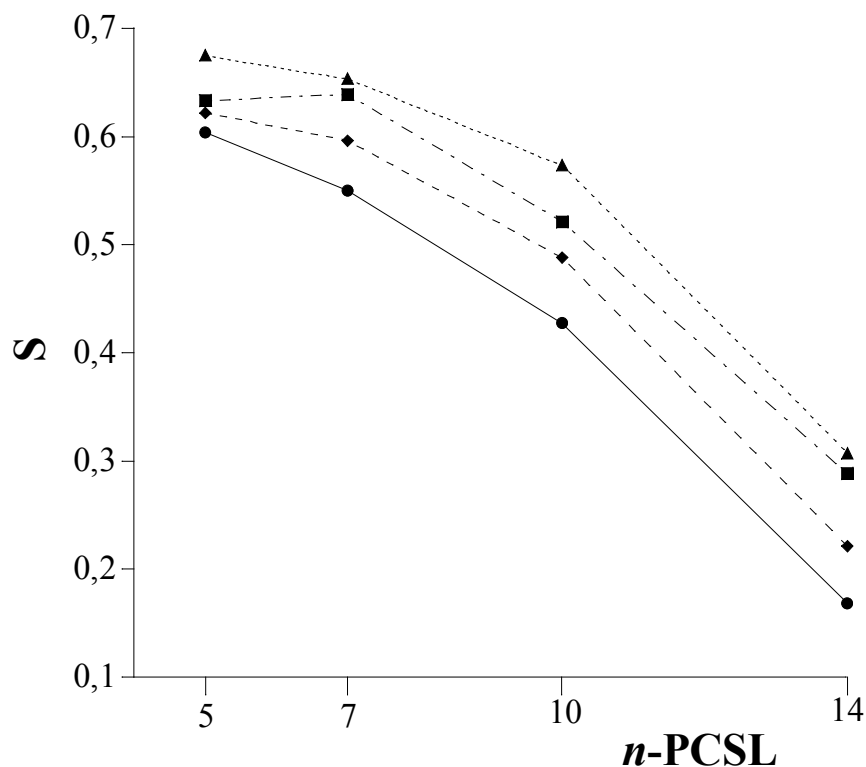


Figure 4.3.4 - Order parameter, S , of n -PCSL in membranes of pure DOPC (●), DOPC:CHOL 90:10 mol/mol (◆), DOPC:CHOL 80:20 wt/wt (■) and DOPC:CHOL 70:30 wt/wt (▲) as function of n .

In addition, comparing the behaviour of POPC and DOPC-based membranes, it is possible to note that in the absence and in the presence of CHOL at 10% the S values for the the two phospholipids systems are paragonable at all spin-label positions. In contrast, for 20% an 30% CHOL content, the S values for POPC bilayers are higher than those calculated for DOPC bilayers. This evidence indicates that the CHOL causes an increase in lipid order that is higher for the membranes composed by phospholipids with one double bonds than for those with two unsaturations in the acyl chains.

In Table 4.3.1 the isotropic hyperfine coupling constant values, a'_N , for all lipid samples as function of n -PCSL are reported. For both POPC and DOPC lipid membranes, a'_N values decrease with the nitroxide position, n , in the acyl chains for all systems with different CHOL content, indicating a reduction of the local polarity going from the surface region to the inner core. For POPC membranes, no significant changes in a'_N values for 5,

7 and 10-PCSL spectra were observed with increasing the CHOL content, while an increase of a'_N was observed for the 14-PCSL spectra going from 0 to 30% CHOL (~ 0.6 G). This result indicates that the presence of CHOL in the lipid bilayers causes a weakening of hydrophobic interactions and an increase in the polarity of the more inner region. This difference is more evident going from 10% to 20% of CHOL, confirming the trend of order parameter, S . For DOPC membranes, no particular changes were observed in the a'_N values of different spin-labels with the CHOL increase, indicating that the local polarity is not particularly influenced by the CHOL addition.

Systems	a'_N /G			
	5-PCSL	7-PCSL	10-PCSL	14-PCSL
<i>POPC</i>	15.3 ± 0.01	15.1 ± 0.02	14.8 ± 0.01	13.5 ± 0.01
<i>POPC:CHOL 90:10 wt/wt</i>	15.1 ± 0.02	15.1 ± 0.01	14.8 ± 0.02	13.5 ± 0.01
<i>POPC:CHOL 80:20 wt/wt</i>	15.2 ± 0.01	15.2 ± 0.01	14.9 ± 0.01	13.9 ± 0.01
<i>POPC:CHOL 70:30 wt/wt</i>	15.3 ± 0.01	15.3 ± 0.01	15.0 ± 0.01	14.1 ± 0.02
<i>DOPC</i>	15.3 ± 0.01	14.9 ± 0.01	14.7 ± 0.01	14.3 ± 0.01
<i>DOPC:CHOL 90:10 wt/wt</i>	15.3 ± 0.02	15.3 ± 0.01	15.0 ± 0.01	14.0 ± 0.02
<i>DOPC:CHOL 80:20 wt/wt</i>	15.4 ± 0.01	15.2 ± 0.02	14.8 ± 0.02	14.1 ± 0.01
<i>DOPC:CHOL 70:30 wt/wt</i>	15.4 ± 0.01	15.3 ± 0.01	14.9 ± 0.01	14.1 ± 0.01

Table 4.3.1 – Values of the isotropic hyperfine coupling constant, a'_N , of n -PCSL in lipid bilayers of POPC and DOPC membranes with different CHOL concentrations.

Summarizing, these results point put a similar stiffening effect on POPC and DOPC bilayers. However, this effect is weaker in the latter case, probably because of the higher flexibility of unsaturated chains which can favor the CHOL accomodation in the lipid bialyer.

4.4 Characterization of PUFA-containing lipid membranes

Polyunsaturated fatty acids (PUFA) are fatty acids that contain more than one double bond in their backbone. This class includes many important compounds, such as essential fatty acids and those that give drying oils their characteristic property. Some of these compounds are *N*-3 fatty acids, popularly referred to as ω -3 fatty acids or omega-3 fatty acids, which are essential unsaturated fatty acids with a double bond (C=C) starting after the third carbon atom from the end of the carbon chain. An example of omega-3 fatty acids is represented by docosahexaenoic acid (DHA) that is a primary structural component of the human brain and retina. In chemical structure, DHA is a carboxylic acid with a 22-carbon chain and six *cis* double bonds; the first double bond is located at the third carbon from the omega end.

An ESR characterization of the DHA effect on lipid membranes structure was realized by incorporating phosphatidylcholine which presents the nitroxide group close to its hydrophilic headgroup (5-PCSL) in POPC and POPC:CHOL 75:25 wt/wt bilayers. Different DHA concentrations were considered and the corresponding 5-PCSL spectra are shown in Figure 4.4.1. In all cases, the spectra present a clearly defined axially anisotropic lineshapes, typical of spin-labels which presents the nitroxide group close to its hydrophilic headgroup. The quantitative analysis of the spectra was realized determining the $2A_{\max}$ parameter, related to the fluidity of the bilayer and to the lipid packing.

Observing the Figure 4.4.2 concerning the POPC membranes, it is possible to note that addition of low DHA amounts (~ 0.1 weight ratio) causes a $2A_{\max}$ decrease, indicating an increase of chains mobility which suggest a major fluidity to the bilayer structure. Increasing the DHA concentrations, no particular effects were observed in the $2A_{\max}$ values, confirming that the a major presence of polyunsaturated phospholipids does not induce more changes in the lipid bilayers structure. These results are similar in both cases of POPC and POPC:CHOL membranes, although with a difference.

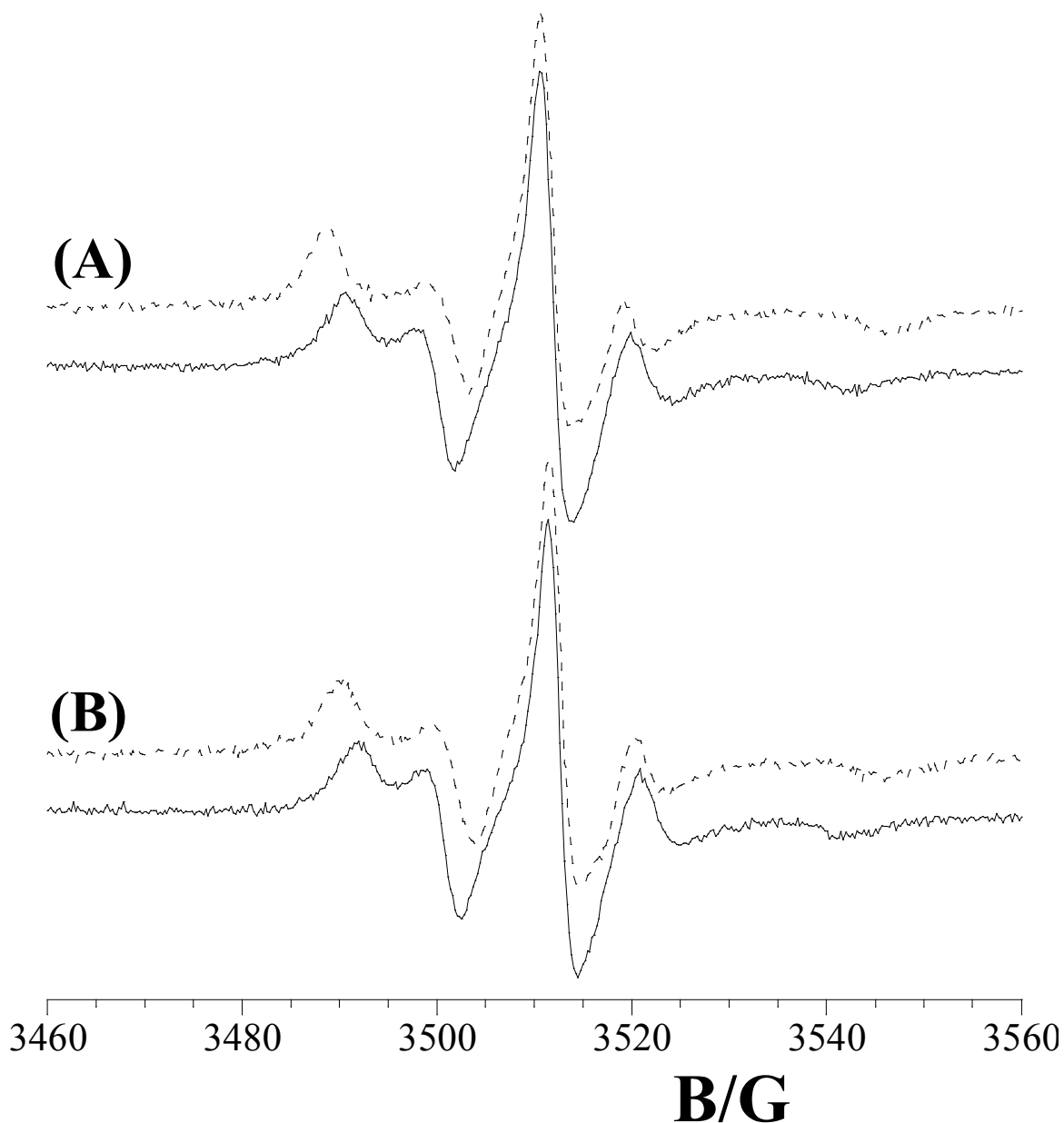


Figure 4.4.1 – ESR spectra of 5-PCSL in lipid membranes of (A) pure POPC in the absence (continuous line) and in the presence (dotted line) of DHA at 0.25 weight ratio, (B) POPC:CHOL in the absence (continuous line) and in the presence (dotted line) of DHA at 0.25 weight ratio.

In fact, analyzing the $2A_{\max}$ values of the two lipid systems, it is possible to note that the $\Delta 2A_{\max}$, calculated between 0 and 0.1 weight DHA/total lipid ratio, is more high in the case of POPC:CHOL membranes (~ 2 G) than in the case of pure POPC bilayers (~ 1 G), indicating that the polyunsaturated phospholipids induce a stronger effect on the lipid structure when in the presence of CHOL.

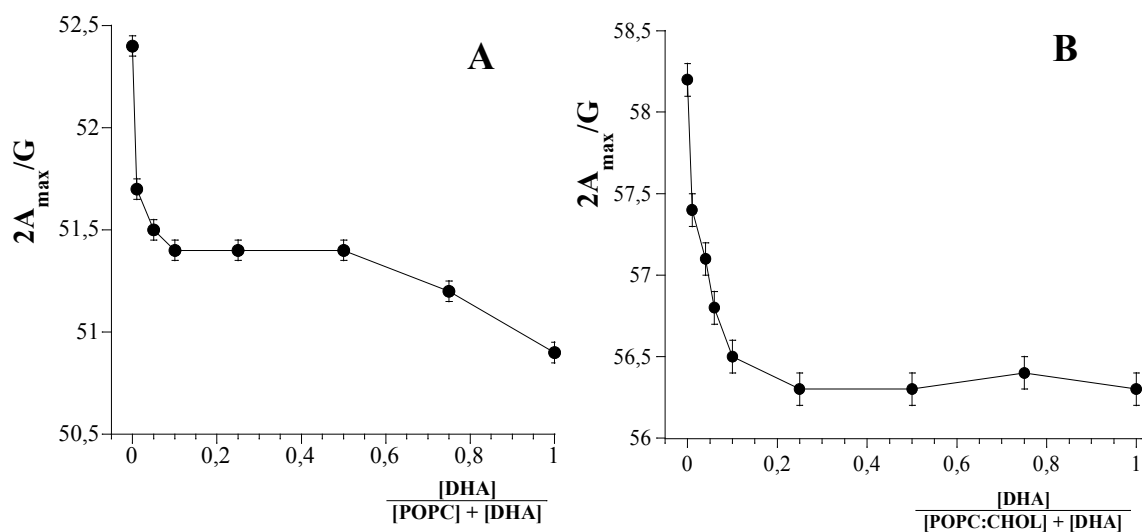


Figure 4.4.2 – Trend of the outer hyperfine splitting, $2A_{max}$, of 5-PCSL in lipid membranes of POPC (A) and POPC:CHOL (B) containing DHA at different concentrations.

Summarizing, the ESR results indicate that low amounts of polyunsaturated phospholipids are sufficient to induce a major fluidity in the lipid membranes, although with different intensities. Indeed, as demonstrated by $2A_{max}$ changes, this fluidization effect is higher in the case of CHOL-containing membranes than for pure POPC bilayers. This evidence suggests the tendency of DHA phospholipids in inducing a more significant flexibility of the acyl chains in the lipid bilayers with CHOL, modifying their microstructural properties.

4.5 Characterization of liposomes formed by lipopolysaccharides from *Burkholderia cenocepacia*, *Burkholderia multivorans* and *Agrobacterium tumefaciens*: from the molecular structure to the aggregate architecture.

The microstructure of liposomes formed by the lipopolysaccharides (LPS) derived from *Burkholderia cenocepacia* ET-12 type strain LMG 16656, *Burkholderia multivorans* strain C1576 and *Agrobacterium tumefaciens* strain TT111 (see Figure 4.5.1 for the molecular structures) has been investigated by a combined experimental strategy, including DLS, SANS and ESR techniques [21].

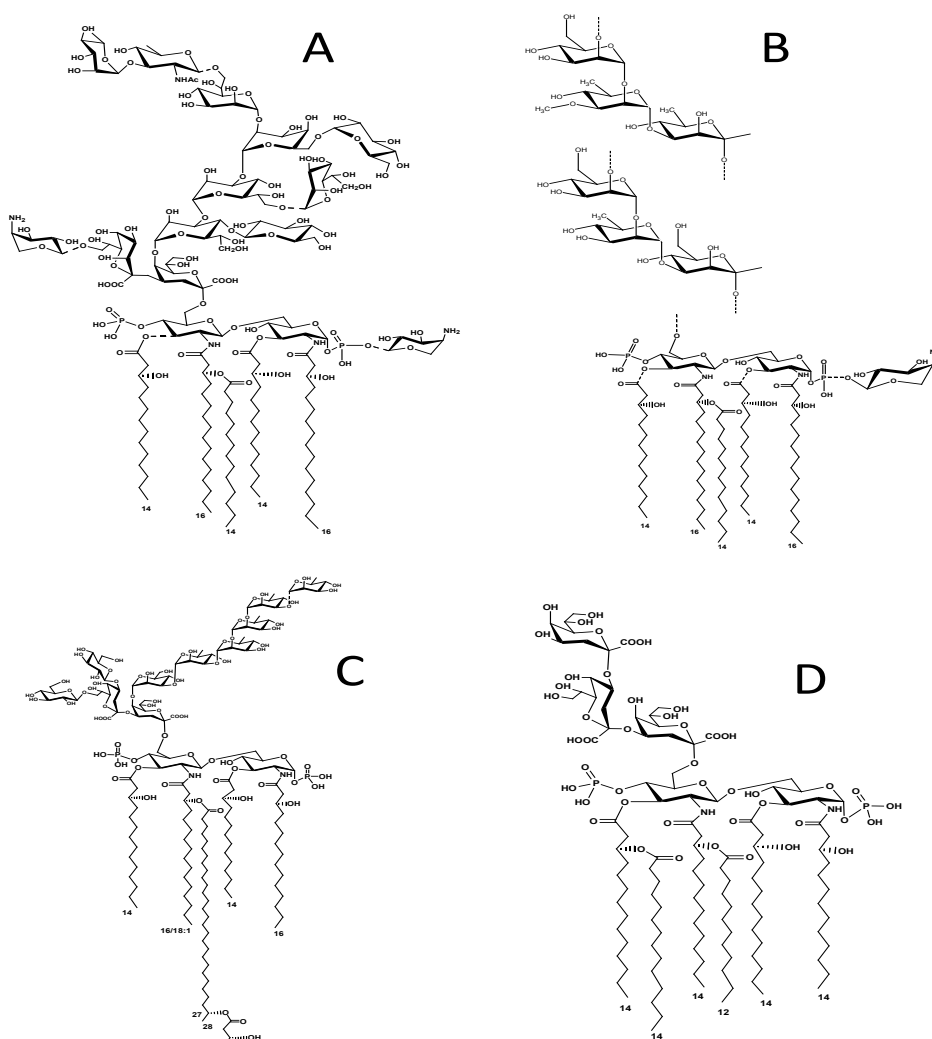


Figure 4.5.1- Molecular structure of LPS from *Burkholderia cenocepacia* (A, m.w.=3500 a.m.u.), *Burkholderia multivorans* (B, m.w.≈10000 a.m.u.), *Agrobacterium tumefaciens* (C, m.w.=3671 a.m.u) and *Salmonella minnesota* (D, m.w.=2400).

The aim of this study is to realize a structural and functional investigation on liposomes formed by LPS molecules in order to can greatly increase the knowledge on the stability, low permeability and high resistance of the outer membrane of Gram negative bacteria and also on their biological activity. This information may, in turn, lead to new strategies for the design and synthesis of new molecules capable of penetrating into the cell wall and causing the bacterium death. DLS experiments have furnished an estimation liposome dimension, SANS measurements have permitted to analyze the aggregate morphology and to estimate the thickness of the lipid bilayer, while ESR experiments have furnished informations on the dynamics of the lipid hydrophobic tail in the bilayer.

Size of aggregates formed by LPS in buffer at pH 7.4, and LPS-DOPE mixtures at pH 7.4 and 9 have been obtained through DLS measurements, carried out in the angular range 30°-120°. The relaxation time distribution, obtained by regularized inverse Laplace transformation of the correlation functions, are shown in Figures 4.5.2-4.5.4.

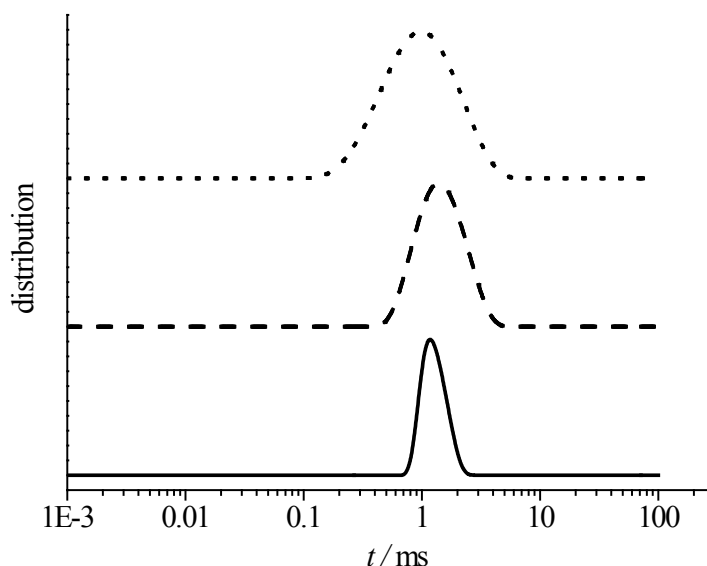


Figure 4.5.2 - Relaxation time distributions at 25°C and $\theta = 90^\circ$ for the following aqueous systems: LPS from *Burkholderia cenocepacia* at pH 7.4 (continuous line); LPS from *Burkholderia cenocepacia* – DOPE (3:1) at pH 7.4 (dashed line); LPS from *Burkholderia cenocepacia* – DOPE (3:1) at pH 9 (dotted line).

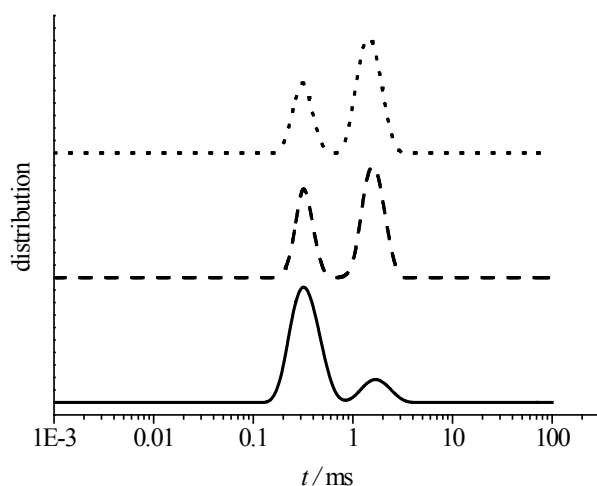


Figure 4.5.3 - Relaxation time distributions at 25°C and $\theta = 90^\circ$ for: LPS from *Burkholderia multivorans* at pH 7.4 (continuous line); LPS from *Burkholderia multivorans* – DOPE (3:1) at pH 7.4 (dashed line); LPS from *Burkholderia multivorans* – DOPE (3:1) at pH 9 (dotted line).

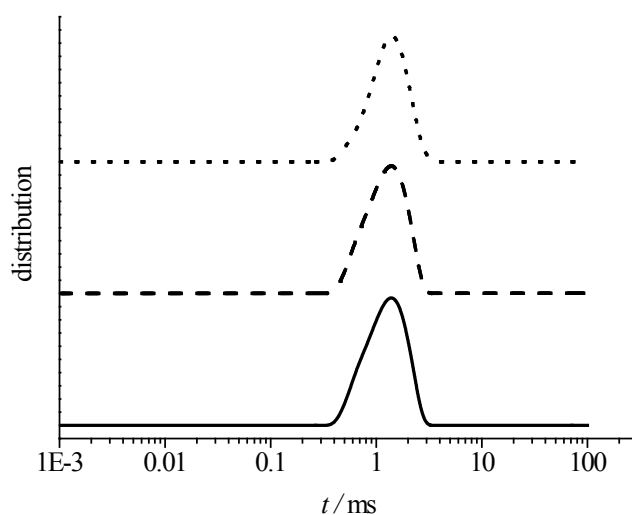


Figure 4.5.4 - Relaxation time distributions at 25°C and $\theta = 90^\circ$ for: LPS from *Agrobacterium tumefaciens* at pH 7.4 (continuous line); LPS from *Agrobacterium tumefaciens*– DOPE (3:1) at pH 7.4 (dashed line); LPS from *Agrobacterium tumefaciens*– DOPE (3:1) at pH 9 (dotted line).

For pure LPS (solid lines), they are monomodal for all the systems except for that constituted by S-LPS from *B. multivorans* that showed a bimodal distribution, indicating the presence of two well-distinct species in solution. The experimental translational diffusion coefficients, D , obtained from the relaxation rates as described in experimental

section, are reported in Table 4.5.1. In the same table the literature datum relative to *S. minnesota* is also reported [22].

In the approximation of very diluted solutions, D can be directly related to the hydrodynamic radius of the aggregates, R_H , through the Stokes-Einstein equation, which holds for infinitely diluted hard spheres diffusing in a continuous medium [23]

$$R_H = \frac{k_B T}{6\pi\eta D} \quad (4.5.1)$$

where k_B is the Boltzmann constant, T is the absolute temperature, and η is the viscosity of the medium (i.e. the solvent). R_H values of LPS aggregates are reported in Table 4.5.1.

System	$\frac{10^{12} D}{\text{m}^2 \text{ s}^{-1}}$	$\frac{R_H}{\text{nm}}$
<i>Salmonella minnesota</i> ^a	2.7 ± 0.9	80 ± 20
<i>Burkholderia cenocepacia</i> pH 7.4	1.66 ± 0.15	146 ± 13
<i>Burkholderia cenocepacia</i> – DOPE pH 7.4	1.39 ± 0.06	175 ± 7
<i>Burkholderia cenocepacia</i> – DOPE pH 9.1	2.14 ± 0.05	113 ± 3
<i>Burkholderia multivorans</i> pH 7.4	9.59 ± 0.15	25.3 ± 0.8
	1.78 ± 0.11	136 ± 8
<i>Burkholderia multivorans</i> – DOPE pH 7.4	8.75 ± 0.18	27.8 ± 0.6
	1.33 ± 0.06	183 ± 8
<i>Burkholderia multivorans</i> – DOPE pH 9.1	8.8 ± 0.2	27.6 ± 0.6
	1.32 ± 0.07	184 ± 10
<i>Agrobacterium tumefaciens</i> pH 7.4	1.64 ± 0.03	148 ± 3
<i>Agrobacterium tumefaciens</i> – DOPE pH 7.4	1.86 ± 0.02	130 ± 2
<i>Agrobacterium tumefaciens</i> – DOPE pH 9.1	1.64 ± 0.04	148 ± 4

^aData from ref. 22.

Table 4.5.1 - Translational diffusion coefficients, D , and hydrodynamic radii, R_H , obtained through DLS measurements at 25°C. In the table, LPS are indicated by the name of the bacterium from which they are obtained.

From inspection of the table, it is possible to infer the presence of large diffusing aggregates with radii ranged between ~ 100 nm and ~ 180 nm, compatible with the presence of liposomal aggregates. For the system composed by *B. multivorans* S-LPS, smaller aggregates with $R_H \approx 25$ nm are also present. The presence of DOPE in the liposome formulation does not change the kind of aggregates present in each system at both pH values investigated, see Figures 4.5.2-4.5.4. In the case of S-LPS derived from *B. multivorans*, DOPE alters the relative populations of the two kinds of aggregates, in that the relative volume fraction of larger aggregates increases.

Structural parameters of the aggregates have been obtained by SANS measurements [24], which have been performed for all the systems in the absence and in the presence of DOPE, at pH 7.4 and 9.1, see Figures 4.5.5-4.5.7. In particular, the scattering cross section pattern $d\Sigma/d\Omega$ for the aqueous dispersion of R-LPS derived from *B. cenocepacia* and *A. tumefaciens* are reported in figure 4.5.5 and 4.5.7, respectively (open circles).

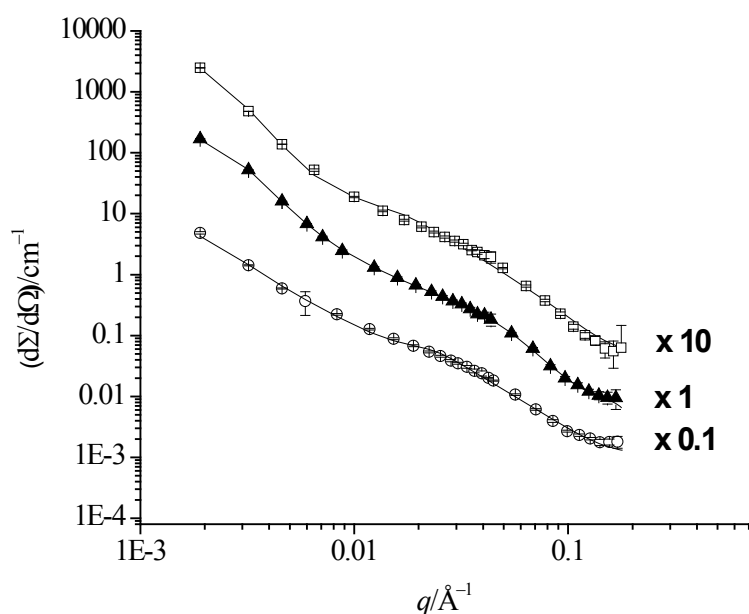


Figure 4.5.5 - Scattering cross sections at 25°C for: LPS from *Burkholderia cenocepacia* at pH 7.4 (open circles); LPS from *Burkholderia cenocepacia* – DOPE (3:1) at pH 7.4 (full triangles); LPS from *Burkholderia cenocepacia* – DOPE (3:1) at pH 9 (open squares). For a better comparison, data have been multiplied by a scale factor, as indicated. Fitting curves to the experimental data through the models reported in the text are also shown.

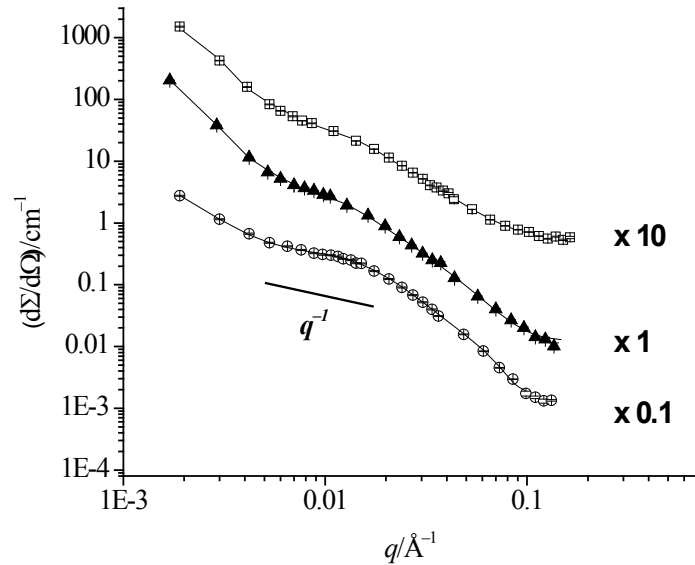


Figure 4.5.6 - Scattering cross sections at 25°C for the following aqueous systems: LPS from *Burkholderia multivorans* at pH 7.4 (open circles); LPS from *Burkholderia multivorans* – DOPE (3:1) at pH 7.4 (full triangles); LPS from *Burkholderia multivorans* – DOPE (3:1) at pH 9 (open squares). For a better comparison, data have been multiplied by a scale factor, as indicated. Fitting curves to the experimental data through the models reported in the text have are also shown.

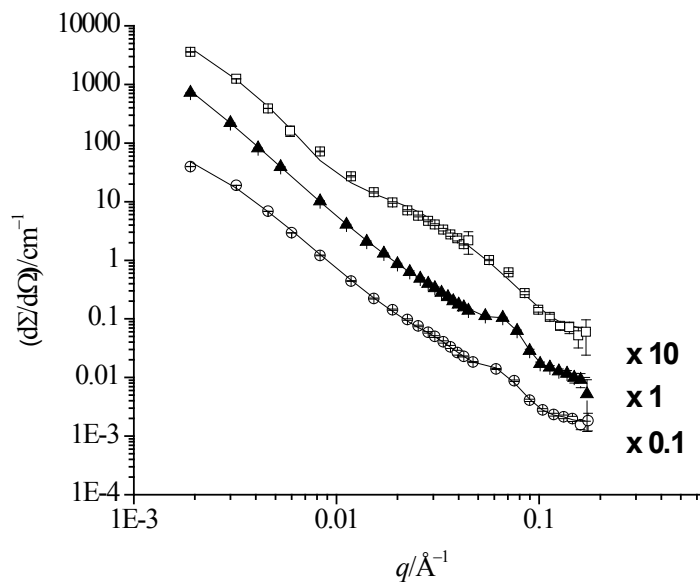


Figure 4.5.7 - Scattering cross sections at 25°C for the following aqueous systems: LPS from *Agrobacterium tumefaciens* at pH 7.4 (open circles); LPS from *Agrobacterium tumefaciens* – DOPE (3:1) at pH 7.4 (full triangles); LPS from *Agrobacterium tumefaciens* – DOPE (3:1) at pH 9 (open squares). For a better comparison, data have been multiplied by a scale factor, as indicated. Fitting curves to the experimental data through the models reported in the text have are also shown.

Qualitative analysis of the cross sections allows revealing the presence of a power law $d\Sigma/d\Omega \propto q^{-\alpha}$ in the small q region ($q \leq 0.005 \text{ \AA}^{-1}$), with the exponent $\alpha > 2$. Furthermore, in the intermediate q region ($q \cong 0.05 \text{ \AA}^{-1}$) a shoulder is present. All these features, consistently with the molecular architecture of the molecules, are typical characteristics of the presence of multilamellar vesicles/liposomes.

Indeed, the value of the exponent α depends on the average lamellarity of the vesicles whereas the shoulder should arise from the interference occurring among the concentric vesicular layers. In spite of the presence in literature of more complex models for multilamellar vesicles [25], in order to reduce the number of fitting parameters, we have used the simplest model available for structural characterization of such aggregates. Accordingly, the scattering function has been modeled considering the liposomes as a collection of one-dimensional paracrystalline stack. The theoretical expressions of $d\Sigma/d\Omega$ is:

$$\frac{d\Sigma}{d\Omega}(q) = \frac{1}{q^2} \langle |f(q)|^2 \rangle \left(1 + \frac{\langle |f(q)| \rangle^2}{\langle |f(q)|^2 \rangle} (S(q) - 1) \right) + \left(\frac{d\Sigma}{d\Omega} \right)_{\text{incoh}} \quad (4.5.3)$$

where $f(q)$ is the form factor of a bilayer, whereas $S(q)$ is the structure factor that takes into account the interferences occurring among the bilayers belonging to a single stack. Finally, $(d\Sigma/d\Omega)_{\text{incoh}}$ represents the incoherent contribution to the cross section measured, mainly due to the presence of hydrogenated molecules. Both form and structure factors depend in a complex way on the geometrical parameters of the stack, namely the number of layers in the stack, N , the mean layer thickness, d , and the distance between the centers of two consecutive layers d_l . Thus, optimized values of these parameters have been obtained from data fitting. Actually, the number of layers N is only approximately

determined; it determines the upturn in scattering at low q values where the total thickness of the stack is seen. Furthermore, because of the low scattering contrast existing between the highly hydrated LPS hydrophilic moieties and D₂O bulk, the obtained d values represent the thickness of the hydrophobic layer constituted by the acyl chains rather than the whole thickness of LPS bilayer. Both d and d_l have been allowed to be polydisperse: the former with a Schulz-Zimm distribution function related to the Zimm polydispersity index Z , the latter with a Gaussian distribution with a standard deviation σ_{d_l} . In particular, the ratio σ_{d_l}/d_l , named Hosemann factor, have been estimated. The values of all the parameters are collected in Table 4.5.1. It is worth pointing out that, because of the limited instrument resolution, the polydispersity parameters, Z and σ_{d_l}/d_l tend to be overestimated, since both the resolution and the polydispersity smear out the oscillations contained in the form factor of equation Inter-particle structure factor may be approximated to the unity because of the low amount of LPS (0.5 mmol dm^{-3} , corresponding to a volume fraction of $\cong 0.07\%$ of solute volume fraction).

Different experimental evidences have been obtained for the S-LPS derived from *B.multivorans*. In this case the scattering profile obtained for the aqueous dispersion (open circles in Figure 4.5.6) is typical of two different size scattering objects: in the region at high q ($q > 0.006 \text{ \AA}^{-1}$) the cross-section shows a power law decrease, $(d\Sigma/d\Omega) \propto q^{-1}$, characteristic of elongated cylindrical micelles, whose theoretical expression, in the region where the power law holds, can be written as [26]

$$\frac{d\Sigma}{d\Omega}(q) = \frac{\phi_{cyl}(1-\phi_{cyl})\pi^2 R^2 (\rho_c - \rho_0)^2}{q} \exp\left(-\frac{q^2 R^2}{4}\right) + \left(\frac{d\Sigma}{d\Omega}\right)_{\text{incoh}} \quad (4.5.4)$$

where R is the radius of the base, ϕ_{cyl} the cylinder volume fraction, and $\rho_c - \rho_0$ the scattering length density difference between the cylinders and the solvent. In the low q region ($q < 0.006 \text{ \AA}^{-1}$) the trend is similar to what found for the *B. cenocepacia* and *A. tumefaciens*, denoting the presence of multilamellar liposomes. In this case, scattering cross sections have been analyzed assuming each kind of aggregate to scatter independently from the other and expressing $(d\Sigma/d\Omega)$ as the sum of the equations (4.5.3) and (4.5.4), taking into account for the relative number density of the objects, strictly connected to the volume fractions ϕ_{cyl} and ϕ_{lip} . This procedure allows the estimation of the micelle radius R that results to be (4.2 ± 0.2) nm, while the liposome structural parameters are reported in Table 4.5.2. Although the lack of the Guinier regime for the micelles does not allow obtaining a value of the length of cylindrical micelles, l , nonetheless an estimation for such value can be obtained from the knowledge of the DLS hydrodynamic radius R_H that for a cylinder is given by [27]:

$$R_H = \sqrt[3]{\frac{3}{4} R^2 l (1.0304 + 0.0193x + 0.06229x^2 + 0.00476x^3 + 0.00166x^4 + 2.66 \cdot 10^{-6} x^7)} \quad (4.5.5)$$

where R is the cylinder radius and $x = \ln[l/(2R)]$. From eqn (4.5.5) the length of the micelles formed by *B. multivorans* S-LPS has been estimated to be (68 ± 2) nm.

In Table 4.5.2 we also report the structural parameters obtained for *S. minnesota* R-LPS [22]. In this case, only unilamellar liposomes were detected.

In the presence of DOPE in aggregate formulation, at both investigated pH values, the scattering profile is quite similar for all three LPS considered in the present work. In all cases, $d\Sigma/d\Omega$ shows a power law decrease with $\alpha > 2$ at low q and a shoulder at higher q ($q \cong 0.02 \text{ \AA}^{-1}$ for both *B. cenocepacia* R-LPS and *B. multivorans* S-LPS and $q \cong 0.07 \text{ \AA}^{-1}$

for *A. tumefaciens* R-LPS). Consequently the experimental data were fitted modeling the systems as constituted by multilamellar vesicles. The fitting parameters are reported in Table 4.5.2. Interestingly, in the presence of DOPE, also in the case of S-LPS derived from *B. multivorans* no evidence of smaller aggregate was detected.

System	N	$\frac{d}{\text{nm}}$	Z	$\frac{d_l}{\text{nm}}$	$\frac{\sigma_{d_l}}{d_l}$	ϕ_{cyl}	ϕ_{tip}
<i>Salmonella minnesota</i> ^a	1	4.3±0.2					
<i>Burkholderia cenocepacia</i> pH 7.4	4±1	2.6±0.2	10.5±0.1	17.0±0.3	0.59±0.01		
<i>Burkholderia cenocepacia</i> – DOPE pH 7.4	3±1	2.4±0.6	10.3±0.1	26.4±0.4	0.55±0.01		
<i>Burkholderia cenocepacia</i> – DOPE pH 9.1	4±1	2.8±0.2	10.3±0.1	23.4±0.4	0.81±0.02		
<i>Burkholderia multivorans</i> pH 7.4 ^b	2±1	4.9±0.2	10.4±0.1	30.0±0.5	0.60±0.01	0.0018± 0.0002	0.0049± 0.0005
<i>Burkholderia multivorans</i> – DOPE pH 7.4	4±1	5.0±0.1	10.3±0.1	32.0±0.5	0.60±0.01	0.0019 0.0002	0.0048 0.0005
<i>Burkholderia multivorans</i> – DOPE pH 9.1	5±1	4.2±0.1	10.5±0.1	27.8±0.5	0.62±0.01	0.0020± 0.0002	0.0047± 0.0005
<i>Agrobacterium tumefaciens</i> pH 7.4	3±1	4.7±0.4	10.3±0.1	13.7±0.5	0.60±0.01		
<i>Agrobacterium tumefaciens</i> – DOPE pH 7.4	5±1	4.8±0.4	10.3±0.1	11.5±0.4	0.60±0.01		
<i>Agrobacterium tumefaciens</i> – DOPE pH 9.1	4±1	4.5±0.2	10.3±0.1	16.9±0.3	0.60±0.01		

^a Data from ref. 22

^b In this sample cylindrical micelles were also present, with radius $R = (4.2 \pm 0.2)$ nm and length (68 ± 2) nm.

Table 4.5.2 - Structural parameters at 25°C for the liposomes formed by LPS, obtained through the fitting of the model described in the text to SANS data. The table reports the number of lamellae, N , the average lamellar thickness, d , the Zimm index of the thickness distribution function, Z , the mean distance between two consecutive lamellae, d_l , and the Hosemann factor, σ_{d_l} / d_l . In the table, LPS are indicated by the name of the bacterium from which they are obtained.

The ESR spectroscopy, by using spin-labeled lipids, has furnished substantial information on the acyl chains structuring in the lipid bilayers formed by LPS. The samples investigated were phosphatidylcholine spin-labeled on the 5 or 14 C-atom of the sn-2 chain (5-PCSL and 14-PCSL, respectively) incorporated in LPS liposomes, shown in Figure 4.5.8 and 4.5.9. Incorporation, and molecular dispersion, of the spin-label into the LPS bilayer is highlighted by the absence of any evidence of spin-exchange in the registered spectra, as it would be expected in the case of spin-label self-aggregation.

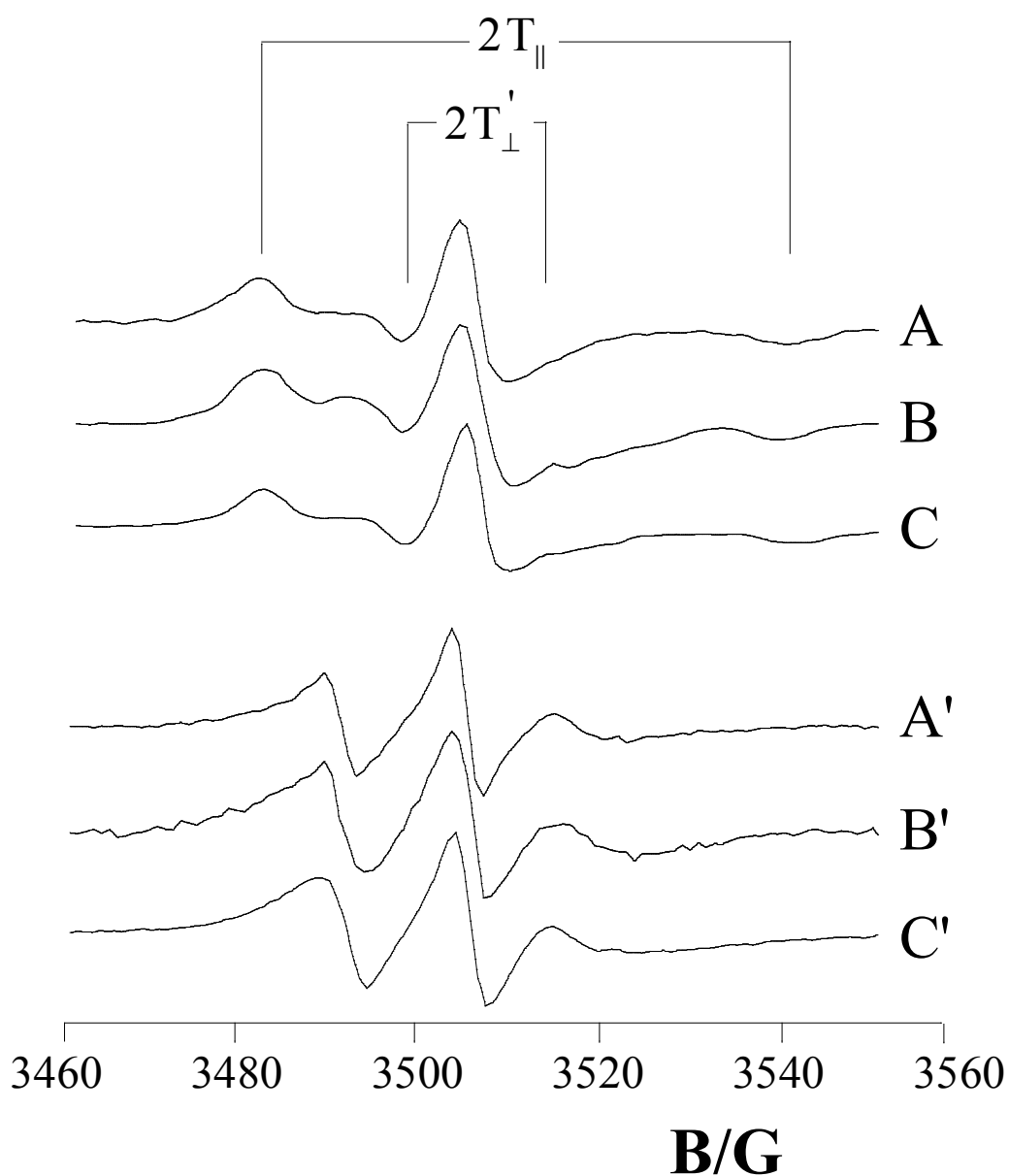


Figure 4.5.8 - ESR spectra of 5-PCSL and 14-PCSL in liposomes formed by LPS from *Burkholderia cenocepacia* (A and A' for 5- and 14-PCSL, respectively), *Burkholderia multivorans* (B, B'), *Agrobacterium tumefaciens* (C, C') at pH 7.4 and 25 °C.

5-PCSL bears the radical label close to the molecule headgroup, and consequently allows to monitor the behavior of the region of the membrane inner core closer to the polar external layers. In contrast, 14-PCSL bears the radical label close to the terminal methyl group of the acyl chain, thus allowing to monitor the behavior of the more internal region of the membrane hydrophobic core. In all the systems analyzed in the present work, the 5-PCSL spectrum presents a clearly defined axial anisotropy, see Figure 4.5.8, thus indicating that, in all cases, the mobility of the label in the region of the bilayer just below the hydrophilic external surface is strongly reduced. In contrast, all the 14-PCSL spectra show an almost isotropic three-line signal, indicative of a rather free motion of the radical label. In an attempt to quantitatively analyze the spectra, we determined the order parameter, S , which is related to the angular amplitudes of motion of the label, reflecting the motion of the acyl chain segment to which the label is bound and the isotropic hyperfine coupling constant, a'_N , which is an index of the micropolarity experienced by the nitroxide; in particular, it increases with the environmental polarity. The S and a'_N values obtained from the spectra registered at 25 °C are collected in Table 4.5.3.

In the case of *S. minnesota* R-LPS the value determined from the 5-PCSL spectrum reported in literature was reported [22]. By comparing the results obtained for 5-PCSL and 14-PCSL it is possible to observe that both parameters decrease with increasing the depth at which the label is inserted in the bilayer, indicating that both the acyl chains ordering and the environmental polarity decrease. Concerning variations due to the peculiar LPS, it is to be observed that the values obtained for 5-PCSL show that liposomes formed by R-LPS from *S. minnesota* present values of order parameter substantially lower than those observed in the case of *B. cenocepacia* and *A. tumefaciens* R-LPS. For S-LPS from *B. multivorans* an intermediate value is obtained. It is interesting to observe that ordering of acyl chains in the LPS bilayer is higher than that observed for typical phospholipids ($S \approx 0.6$

for 5-PCSL). The lower S values obtained for 14-PCSL reflect the higher fluidity of the more internal region of the bilayer hydrophobic core. Among the various LPS, the same trend found for 5-PCSL is observed. For both spin-labels, Table 4.5.3 shows that the a'_N values do not depend on the considered LPS.

System	S	$\frac{a'_N}{G}$
5-PCSL		
<i>Salmonella minnesota</i> ^a	0.69 ± 0.01	15.4 ± 0.1
<i>Burkholderia cenocepacia</i> pH 7.4	0.77 ± 0.02	15.6 ± 0.2
<i>Burkholderia multivorans</i> pH 7.4	0.73 ± 0.01	15.5 ± 0.2
<i>Agrobacterium tumefaciens</i> pH 7.4	0.76 ± 0.02	15.6 ± 0.2
14-PCSL		
<i>Burkholderia cenocepacia</i> pH 7.4	0.24 ± 0.01	13.6 ± 0.2
<i>Burkholderia multivorans</i> pH 7.4	0.20 ± 0.01	13.5 ± 0.2
<i>Agrobacterium tumefaciens</i> pH 7.4	0.27 ± 0.01	13.6 ± 0.2
^a Data computed from the spectrum reported in ref. 22		

Table 4.5.3 - Microstructural parameters at 25°C for the liposomes formed by the systems described, through the quantitative analysis of ESR data described in the text. The table reports the order parameter, S , and the isotropic hyperfine coupling constant, a'_N . In the table, LPS are indicated by the name of the bacterium from which they are obtained.

In the case of 5-PCSL, we also studied the S and a'_N variation with temperature, see Figure 4.5.9. In all cases, a continuous decrease was registered, thus indicating that the dynamics of the lipid chain significantly increases with the temperature. In the case of R-LPS from *S. minnesota*, perusal of the figure reveals a very broad sigmoidal trend, with the inflection centered between 30 and 35 °C; this evidence is related to a transition from gel- to fluid-phase of the LPS acyl chain arrangement in the bilayer. For all the other LPS considered, only a slight slope change is observed in the same temperature range. Even in this case, no significant a'_N variation was observed (mean value 15.6±0.3 G).

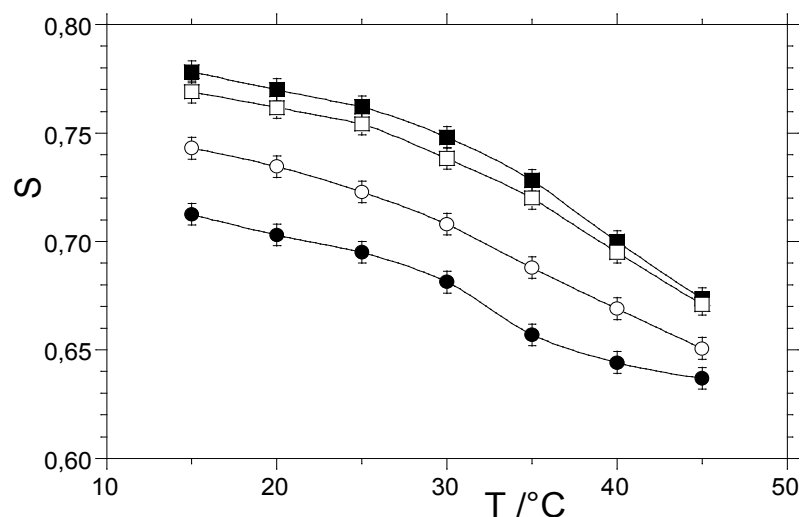


Figure 4.5.9 - Order parameter, S , of 5-PCSL in liposomes formed by LPS from *Burkholderia cenocepacia* (full squares), *Burkholderia multivorans* (open circles), *Agrobacterium tumefaciens* (open squares) *Salmonella minnesota* (full circles), at pH 7.4 as a function of the temperature.

In conclusion, this study have highlighted that the LPS molecular structure determines, through a complex interplay of hydrophobic, steric and electrostatic interactions, the morphology of the aggregates formed in aqueous medium. All the considered LPS form liposomes that in most cases present a multilamellar arrangement. The thickness of the hydrophobic domain of each bilayer and the local ordering of the acyl chains are determined notonly by the molecular structure of the LPS glycolipid portion (lipid A), but also, indirectly, by the bulkiness of the saccharidic portion. In the case of a long polysaccharidic chain, such as that ofthe LPS derived from *Burkholderia multivorans*, liposomes coexist with elongated micellaraggregates, whose population decreases if a typical phospholipid, such as dioleoylphosphatidylethanolamine (DOPE) is introduced in the liposome formulation. The effect of temperature has also been considered: for all the considered LPS an extremely smooth transition of the acyl chain self-organization from a gel to a liquid crystalline phase is detected around 30–35 °C. In the biological context, our results suggest that the rich biodiversity of LPS molecular structure could be fundamental to finely tune the structure and functional properties of the outer membrane of Gram negative bacteria.

References

- [1] Stafford R.E., Dennis E.A. Lysophospholipids as Biosurfactants, *Colloids Surf.* 30 (1988) 47-64.
- [2] Roberts M.F., Dennis E.A., in: D.E. Vance (Ed.), Phosphatidylcholine Metabolism, CRC Press, Boca Raton, FL, 1989, 21.
- [3] Eriksson P.O., Lindblom G., Arvidson G. NMR studies of micellar aggregates in 1-acyl-sn-glycerophosphocholine systems. The formation of a cubic liquid crystalline phase, *J. Phys. Chem.* 91 (1987) 846–853.
- [4] Vitiello G., Ciccarelli D., Ortona O., D’Errico G. Microstructural characterization of lysophosphatidylcholine micellar aggregates: the structural basis for their use as biomembrane mimics, *J. Coll. Interf. Sci.* 336 (2009) 827–833.
- [5] D’Errico G., Ortona O., Paduano L., Vitagliano V. Transport properties of aqueous solutions of alkyltrimethylammonium bromide surfactants at 25 °C. *J. Coll. Interf. Sci.* 239 (2001) 264-271.
- [6] Tedeschi A.M., D’Errico G., Busi E., Basosi R., Barone V. Micellar aggregation of sulfonate surfactants studied by electron paramagnetic resonance of a cationic nitroxide: an experimental and computational approach, *Phys. Chem. Chem. Phys.* 4 (2002) 2180-2188.
- [7] Kumar V.V., Baumann W.J. Lanthanide-induced phosphorus-31 NMR downfield chemical shifts of lysophosphatidylcholines are sensitive to lysophospholipid critical micelle concentration, *Biophys. J.* 59 (1991) 103-107.
- [8] Wennerstrom H., Lindman B. Micelles. Physical chemistry of surfactant association, *Phys. Rep.* 52 (1979) 1-86.
- [9] Paduano L., Sartorio R., Vitagliano V., Costantino L. Equilibrium and transport properties of aqueous pentaethyleneglycol-1-hexyl ether and sodium hexanesulfonate at 25 °C, *J. Coll. Interf. Sci.* 189 (1997) 189-198.
- [10] Lomax E.G., Amphoteric Surfactants, Marcel Dekker, New York, 1996.
- [11] Ortona O., D’Errico G., Ciccarelli D., Vitagliano V. Effect of chain length in ethoxylated and sulfonate surfactants upon the limiting diffusion coefficients in water at 25.0° C, *Phys. Chem. Chem. Phys.* 2 (2000) 1961-1965.
- [12] Hertz H.G. The intermolecular proton-relaxation rate in diamagnetic electrolyte solutions, *Ber. Bunsenges Physik. Chem.* 71 (1967) 999-1008.

- [13] Jansson M., Warr G.G. Self-diffusion coefficients in attractive ionic micelle solutions, *J. Coll. Interf. Sci.* 140 (1990) 541-544.
- [14] Tanford C. The hydrophobic effect – formation of micelles and biological membranes, Wiley, New York, 1980.
- [15] Petrache H.I., Feller S.E., Nagle J.F. Determination of component volumes of lipid bilayers from simulations, *Biophys. J.* 72 (1997) 2237-2242.
- [16] Annunziata O., Costantino L., D'Errico G., Paduano L., Vitagliano V. Transport properties for aqueous sodium sulfonate surfactants - 2. Intradiffusion measurements: Influence of the obstruction effect on the monomer and micelle mobilities, *J. Coll. Interf. Sci.* 216 (1999) 16-24.
- [17] Rizzi R., Lauricella B., Tuccio B., Bouteiller C., Cerri V., Tordo P. Spin-trapping of free radicals by PBN-type β -phosphorylated nitrones in the presence of SDS micelles, *J. Chem. Soc., Perkin Trans. 2* (1997) 2507-2512.
- [18] Hubbell W., McConnell H.M. Molecular motion in spin-labelled phospholipids and membranes, *J. Am. Chem. Soc.* 93 (1971) 314–326.
- [19] Gordon L. M., Sauerheber R. D. Studies on spin-labeled egglecithin dispersions, *Biochim. Biophys. Acta, Biomembr.* 466 (1977) 34–43.
- [20] Gordon L.M., Curtain C.C. Electron spin resonance analysis of model and biological membranes, in: R.C. Aloia, C.C. Curtain, L.M. Gordon (Eds.), *Advances in Membrane Fluidity 1: Methods for Studying Membrane Fluidity*, Alan R. Liss, New York, 1988, 25–89.
- [21] D'Errico G., Silipo A., Mangiapia G., Vitiello G., Radulescu A., Molinaro A., Lanzetta R., Paduano L. Characterization of liposomes formed by lipopolysaccharides from *Burkholderia cenocepacia*, *Burkholderia multivorans* and *Agrobacterium tumefaciens*: from the molecular structure to the aggregate architecture, *Phys. Chem. Chem. Phys.* 12 (2010) 13574–13585.
- [22] D'Errico G., Silipo A., Mangiapia G., Molinaro A., Paduano L., Lanzetta R. Mesoscopic and microstructural characterization of liposomes formed by the lipooligosaccharide from *Salmonellaminnesota* strain 595 (Re mutant), *Phys. Chem. Chem. Phys.* 11 (2009) 2314–2322.
- [23] Tyrrell H. J. V., Harris K. R. *Diffusion in Liquids: A Theoretical and Experimental Study*, Butterworths, London, 1984.
- [24] Kotlarchyk M., Chen S. H. Analysis of small angle neutrons scattering spectra from polydisperse interacting colloids, *J. Chem. Phys.* 79 (1983) 2461–2469.

- [25] Frielinghaus H. Small-angle scattering model for multilamellar vesicles, *Physical Review E: Statistical, Nonlinear, and Soft Matter Physics* 76 (2007) 051603/1–051603/8.
- [26] Radulescu A., Mathers R. T., Coates G. W., Richter D., Fetters L. J. A SANS Study of the self-assembly in solution of syndiotactic polypropylene homopolymers, atactic polypropylene-block-poly(ethylene-co-propylene) diblock copolymers, and an alternating atactic-Isotactic multisegment polypropylene, *Macromolecules* 37 (2004) 6962–6971.
- [27] Hansen S. Translational friction coefficients for cylinders of arbitrary axial ratios estimated by Monte Carlo simulation, *J. Chem. Phys.* 121 (2004) 9111–9115.

CHAPTER 4

Results and Discussion

Part II

Lipid membrane-peptide interactions

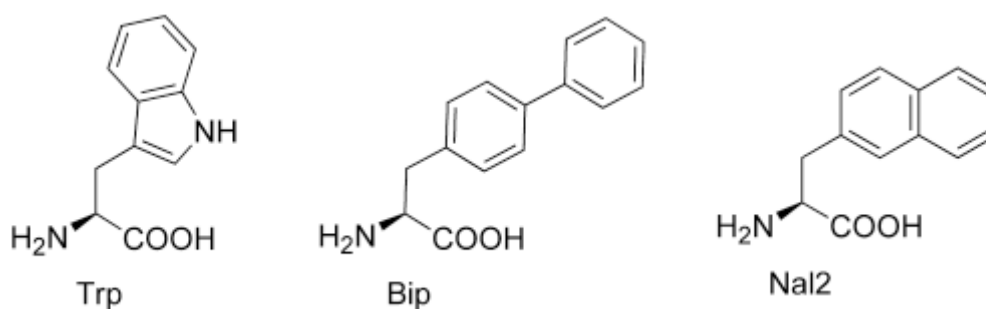
4.1 Interaction of short modified peptides deriving from gp36 of FIV with phospholipid membranes

The interaction of four peptides, designed on the basis of a specific amino-acids sequence of the gp36 MPER domain, and lipid membranes was investigated by using spin-label ESR and fluorescence spectroscopy. Particularly, substitution of the Trp residues or change of the spacing between them was considered (see Table 4.1.1). Our aim is twofold: on one hand we wish to test the connection between antiviral activity of the peptide and its interaction with the membrane; on the other hand we wish to investigate more deeply the role played by the MPER domain in fusion of the virus and target-cell membranes [1].

Peptide 1, also named C8, corresponds to the ⁷⁷⁰Trp-Ile⁷⁷⁷ sequence of FIV gp36, with three Trp residues separated by two dipeptide units. The other three peptides have been strategically chosen among a series of C8 mutants whose antiviral activity was tested as reported in a previous study [2]. The changes in their molecular structure allow the analysis of the peptide molecular features driving the peptide/membrane interaction. Particularly, we have focused our attention on the spacing between the Trp residues and on their replacements with other non-natural aromatic residue (see Scheme 4.1.1). In peptide 2, the two dipeptides have been replaced by a shorter spacer: 3-aminopropionic acid (or β -alanine; β Ala), which reduces the distance along the peptide backbone by two atoms for each dipeptide replaced by β Ala. In order to compensate for the increased hydrophobicity of peptide 2, an additional Lys residue has been added at the N-terminus. Lys is the amino acid occurring naturally at the corresponding position of the gp36 sequence. In peptide 3, the Trp residues have been replaced by a non-natural aromatic residue: 3-biphenyl-4-yl-L-alanine (Bip). In peptide 4, the Trp residues have been replaced with a naphthylalanine isomer: 3-naphthalen-2-yl-L-alanine (Nal2).

No.	Sequence	IC ₅₀ /μM
1(C8)	Ac- Trp -Glu-Asp- Trp -Val-Gly- Trp -Ile-NH ₂	0.22±0.12
2	Ac-Lys- Trp -βAla- Trp -βAla- Trp -Ile-NH ₂	>50
3	Ac- Bip -Glu-Asp- Bip -Val-Gly- Bip -Ile-NH ₂	>50
4	Ac- Nal2 -Glu-Asp- Nal2 -Val-Gly- Nal2 -Ile-NH ₂	0.09±0.08

Table 4.1.1 – Sequence of the peptides and results of FIV inhibition assays



Scheme 4.1.1 -Structures of non-natural aromatic amino-acid residues. Bip = 3-biphenyl-4-yl-L-alanine, Nal2 = 3-naphthalen-2-yl-L-alanine.

Association of the four peptides with lipid membranes has been detected from the perturbation of the chain mobility of spin-labeled lipids by using ESR spectroscopy. The samples investigated were spin-labeled phosphatidylcholine (5-PCSL) in dimyristoyl phosphatidylcholine (DMPC) membranes, in the presence and absence of peptides. As an example, ESR spectra from DMPC membranes in the presence and absence of peptide 1 (C8), recorded at temperatures above and below the chain-melting transition of DMPC (24 °C), are shown in Figure 4.1.1. Significant perturbations due to the peptide are detectable (compare solid and dashed lines). A quantitative analysis of this effect can be done by plotting the temperature dependences of the outer hyperfine splittings ($2A_{max}$) of 5-PCSL, as shown in Figure 4.1.2. In the absence of any peptide, a sharp decrease in $2A_{max}$ is evident at the chain-melting temperature, corresponding to the increase in the spin-label rotational mobility on transition from the gel to the fluid phase [3].

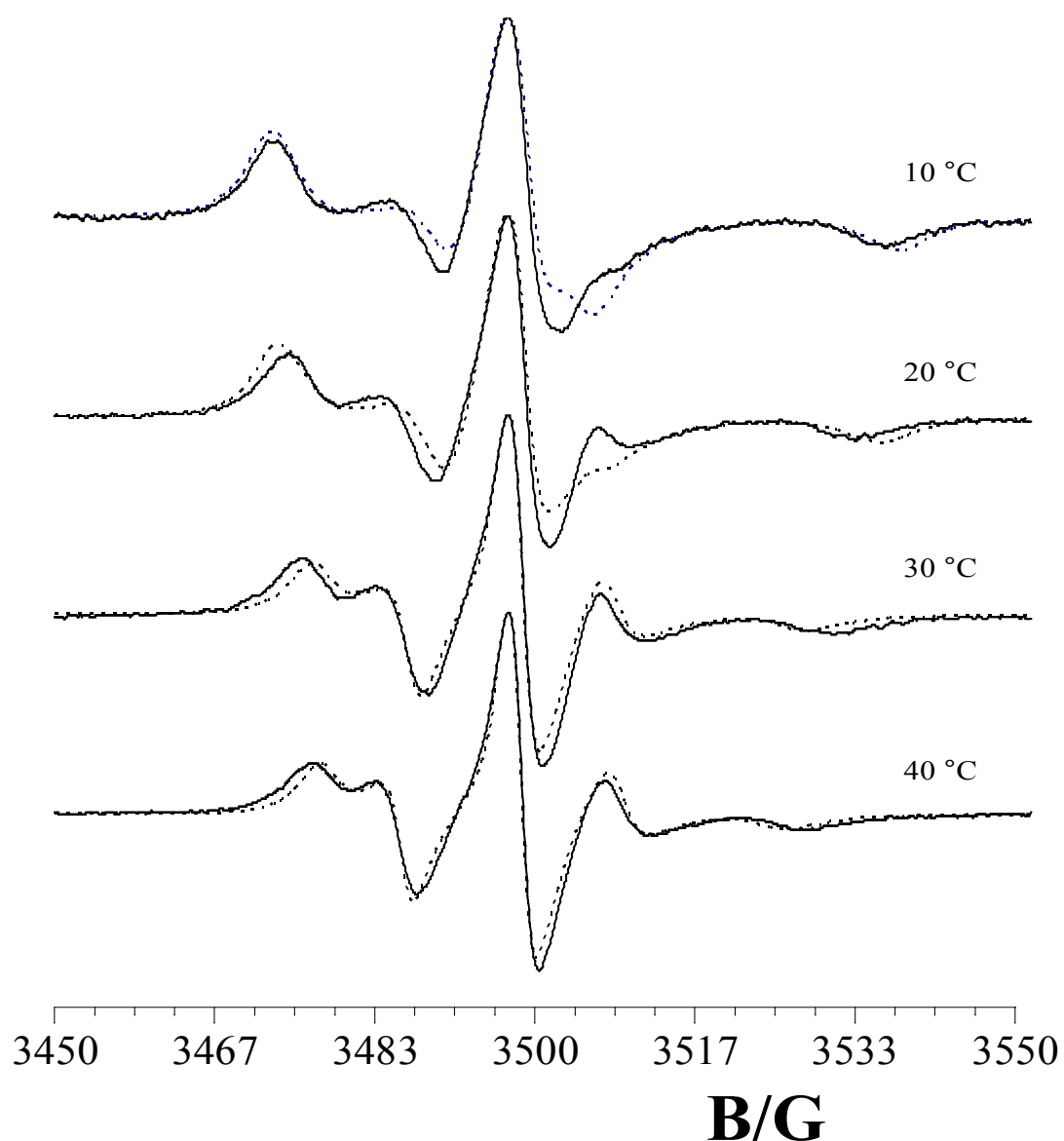


Figure 4.1.1- ESR spectra of 5-PCSL in dimyristoyl phosphatidylcholine bilayer membranes, in the presence (solid line) and in the absence (dashed line) of 0.7:1 wt/wt peptide 1 (C8). The total scan range is 100 G.

Addition of 0.7:1 wt/wt peptide to DMPC membranes causes changes in $2A_{max}$, the extent of which depends on the particular peptide. This peptide/lipid ratio has been chosen because, in the case of interacting peptides, it ensure the bilayer to be completely perturbed, see the following subsection. Peptide 1 (C8) causes the largest effects of the peptides studied. The chain-melting transition is broadened almost beyond detection by the interaction with C8: $2A_{max}$ decreases in the gel phase and increases strongly in the fluid phase. Peptide 2 shows negligible interaction, hardly changing the transition and values of

$2A_{max}$. Peptide 3 also produces only small perturbation of $2A_{max}$, i.e., little interaction with lipid membranes. In the presence of peptide 4, the cooperativity of the DMPC chain-melting transition is strongly reduced, even if its position remains approximately the same. Above the transition temperature, peptide 4 causes a very significant increase in $2A_{max}$, although less than that observed for peptide 1.

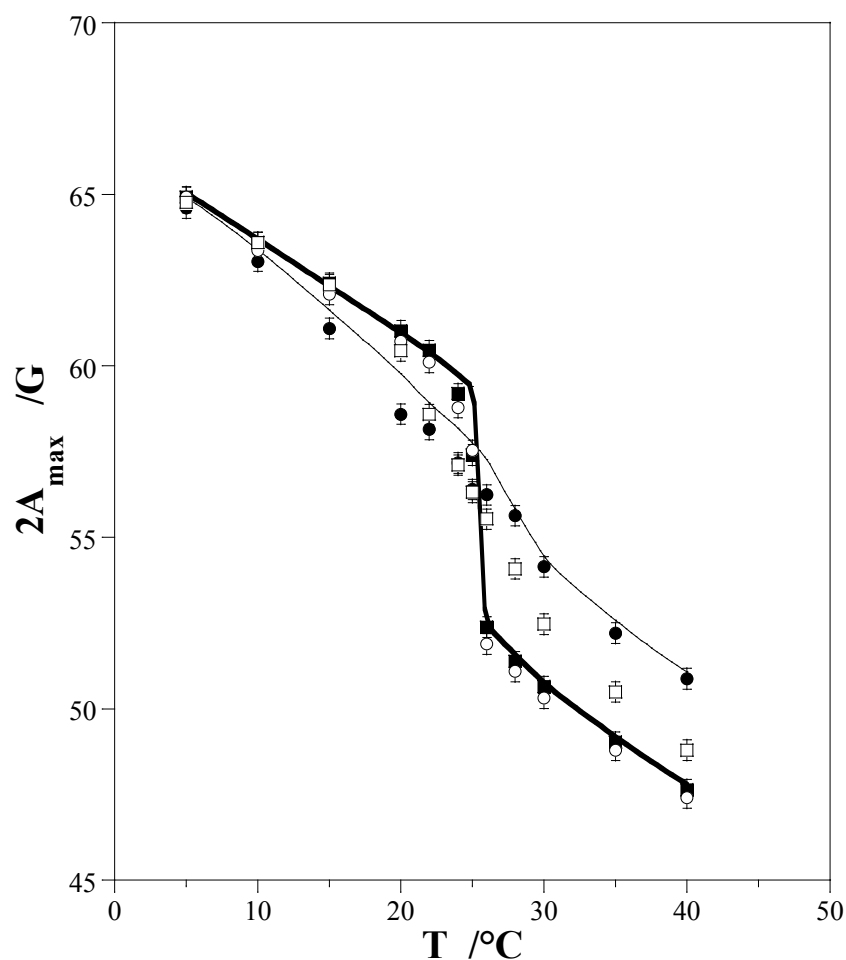


Figure 4.1.2 - Temperature dependence of the outer hyperfine splitting, $2A_{max}$, of 5-PCSL in DMPC membranes in the absence (bold line) and in the presence of 0.7:1 wt/wt peptide: peptide 1 (solid circles), peptide 2 (solid squares), peptide 3 (open circles), peptide 4 (open squares). For comparison, the temperature dependence in the case of peptide P59 is given by the thin line, from [4].

Because peptides 1 and 4 showed appreciable effects on lipid mobility, we investigated their interaction with DMPC bilayers further. Figure 4.1.3 shows the increase

in outer hyperfine splitting, $\Delta 2A_{max}$, of 5-PCSL in DMPC membranes with increasing peptide concentration.

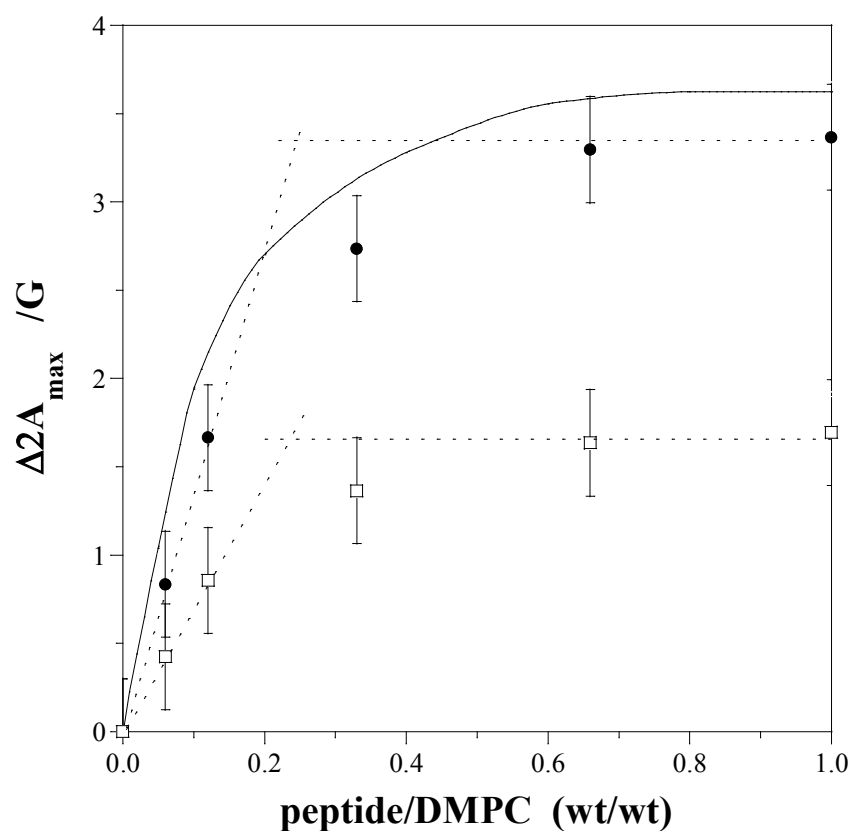


Figure 4.1.3 - Dependence of the increase, $\Delta 2A_{max}$, in outer hyperfine splitting of 5-PCSL at 30 °C on peptide/DMPC ratio for peptide 1 (solid circles) and peptide 4 (open squares). Data for 20-mer peptide P59 (continuous line) is also shown, from [4]. Dashed lines refer to the procedure to evaluate the stoichiometry of the peptide-lipid interaction.

With both peptides, a typical saturation trend is registered: the decrease in lipid chain mobility saturates with a value of $\Delta 2A_{max} \approx 3.3$ G for peptide 1 and $\Delta 2A_{max} \approx 1.7$ G for peptide 4. The stoichiometry of the interaction can be estimated by extrapolation of the increase in $\Delta 2A_{max}$, on initial tight binding, to the saturation value of $\Delta 2A_{max}$. In both cases, this yields a stoichiometry of one peptide molecule bound per 6 lipids. It should be noted that addition of peptide 1 to multi-lamellar dispersions of DMPC solubilises the bilayer structures, so that systems with a peptide to lipid ratio higher than 0.8 wt/wt appear transparent, a phenomenon already observed for the P59 peptide [4]. However, the ESR

spectra of the spin-labeled lipid are insensitive to this change, showing that the lipid chains continue to be substantially restricted in their motion. No evidence of liposome solubilisation was found for the other peptides investigated in this work.

Perturbation of the ESR spectra of lipids spin-labeled at different positions, n , in the $sn-2$ chain that is induced by binding peptide 1 or peptide 4 was also investigated. Figure 4.1.4 gives the ESR spectra of the n -PCSL phosphatidylcholine spin-label positional isomers in fluid DMPC bilayer membranes ($T=30\text{ }^{\circ}\text{C}$), in the presence and absence of peptide 1 at a peptide to lipid ratio of 0.7:1 wt/wt. In the absence of peptide, the outer hyperfine splitting decreases progressively with increasing n , as the spin-label position is stepped down the chain toward the center of the membrane. This flexibility gradient in segmental chain mobility is a characteristic hallmark of the liquid-crystalline state of fluid phospholipid bilayers [3].

In the presence of bound peptides 1 or 4, the outer hyperfine splitting is increased at all spin-label chain positions. Figure 4.1.5 shows the dependence of the outer hyperfine splitting, $2A_{max}$, on chain position, n , for the n -PCSL spin labels in fluid DMPC membranes, with and without a saturating amount of peptide. For both peptides, the characteristic flexibility gradient with chain position of the fluid lipid bilayer membranes is preserved. In the presence of bound peptides 1 or 4, the outer hyperfine splitting is increased at all spin-label chain positions. This indicates that the increase in lipid packing density, which is induced by surface association of the peptide propagates throughout the chain region. For either peptide, there is no appearance of a second, more motionally restricted component in the spectra of the spin labels positioned toward the terminal methyl ends of the chains. This is evidence that the peptides bind solely at the membrane surface and do not penetrate appreciably into the membrane interior, as does, for instance, the myelin basic protein or apocytochrome c [5]. A similar behaviour was observed in the case of the P59 peptide [4].

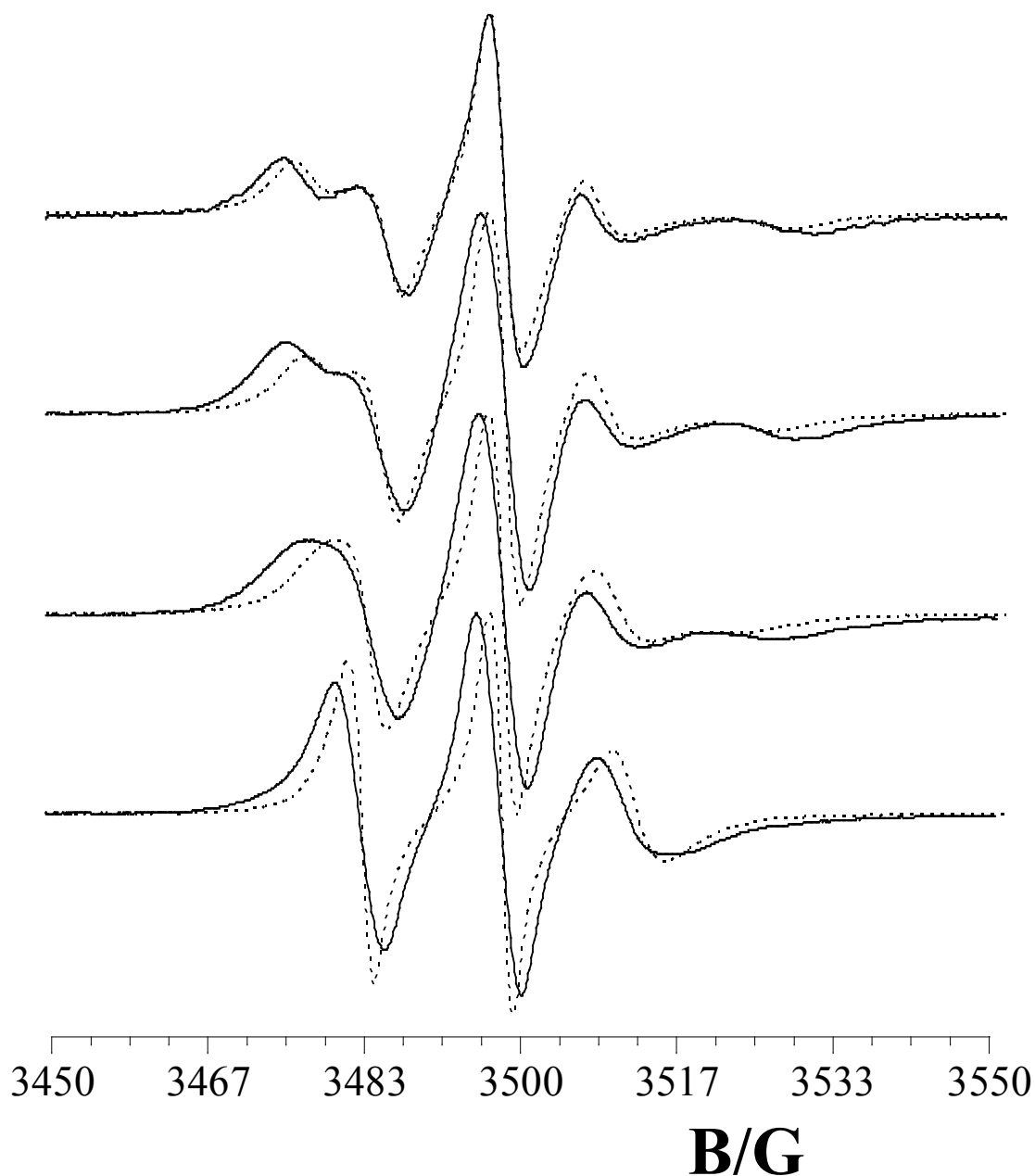


Figure 4.1.4 - ESR spectra of *n*-PCSL positional isomers of spin-labeled phosphatidylcholine in fluid-phase dimyristoyl phosphatidylcholine bilayer membranes, in the presence (solid line) and in the absence (dashed line) of 0.7:1 wt/wt peptide 1 (C8) at 30 °C.

To verify the effect of the peptide/lipid ratio on the perturbations of the lipid chain flexibility profile, a set of measurements was also performed at a lower C8/DMPC weight ratio (0.12:1 wt/wt). The results, not shown, are qualitatively similar to those discussed above, even if the $\Delta 2A_{max}$ variation is almost one half of that reported in Figure 4.1.5 at all spin-label chain position.

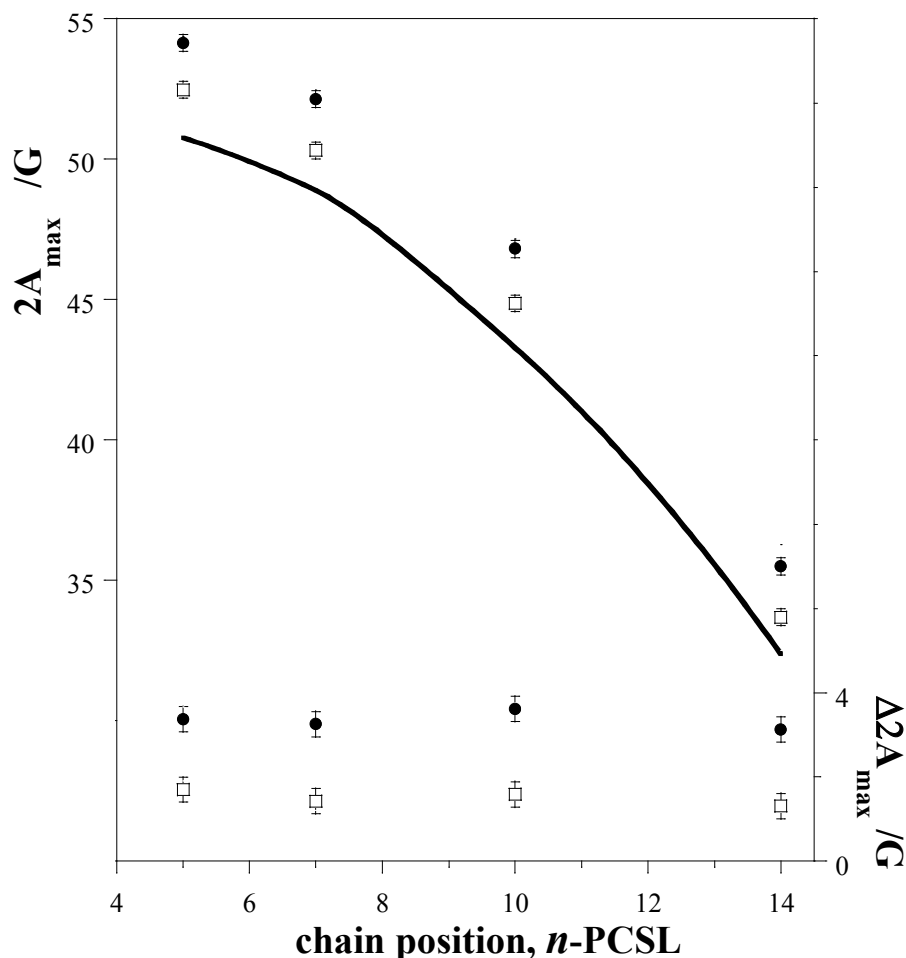


Figure 4.1.5 - Dependence on spin-label position, n , of the outer hyperfine splitting, $2A_{max}$ (left-hand ordinate), of n -PCSL in fluid-phase membranes of DMPC, in the absence (bold line) and in the presence of 0.7:1 wt/wt peptide 1 (solid circles) or peptide 4 (open squares). $T=30$ °C. Right-hand ordinate: increase in outer hyperfine splitting, $\Delta 2A_{max}$, on adding peptide 1 (solid circles) or peptide 4 (open squares). Corresponding data for peptide P59, from [4], are also shown (thin lines).

The fluorescence intensities of some fine vibronic structures in the tryptophan fluorescence spectrum show strong environmental dependence [6]. In particular, the emission maximum shifts from 354 to 329 nm when going from water to an apolar medium. The quantum yield can also undergo large changes, the direction and extent of which depend on the system under consideration [7]. Consequently, fluorescence experiments allow evaluation of the polarity experienced by the tryptophans of peptide 1 in DMPC liposomes.

C8 in water (Figure 4.1.6) gives a Trp emission spectrum typical of an aqueous environment ($\lambda_{\max} \approx 352$ nm), indicating that the Trp side chains are exposed to the aqueous medium. The presence of DMPC liposomes causes a weak shift of the emission maximum to shorter wavelength ($\lambda_{\max} = 347$ nm) and a reduction of the fluorescence quantum yield. These results indicate that, despite the evident interaction between C8 and DMPC liposomes, the Trp residues of this peptide are not significantly inserted into the apolar inner core of the bilayer.

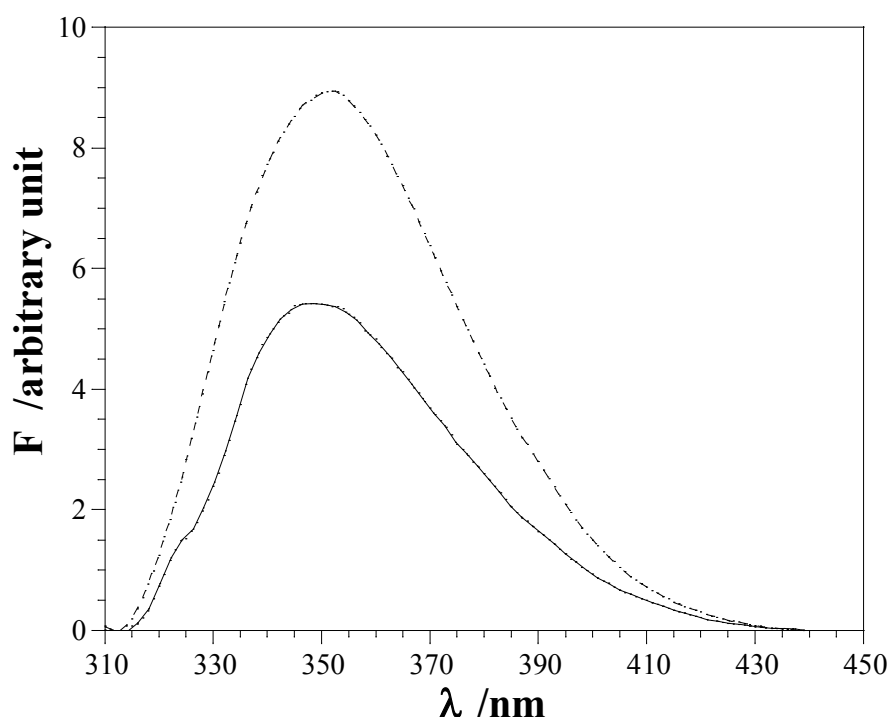


Figure 4.1.6 - Tryptophan emission spectra (range 310–450 nm) of peptide 1 in aqueous phosphate buffer (dashed line), and in DMPC unilamellar liposomes (solid line).

An investigation on the conformational preferences of peptides 1 and 2 in buffer and in the presence of DMPC liposomes was performed by means of CD spectroscopy. Both peptides in buffer present a spectrum with the typical shape of a random coil structure, including a negative band at 202 nm. The presence of DMPC liposomes does not significantly affect the CD spectrum of peptide 2. In contrast, the peptide 1 spectrum

assumes the double-well shape typical of a turn-helical structure, including negative bands at 205 and 217 nm (Figure 4.1.7).

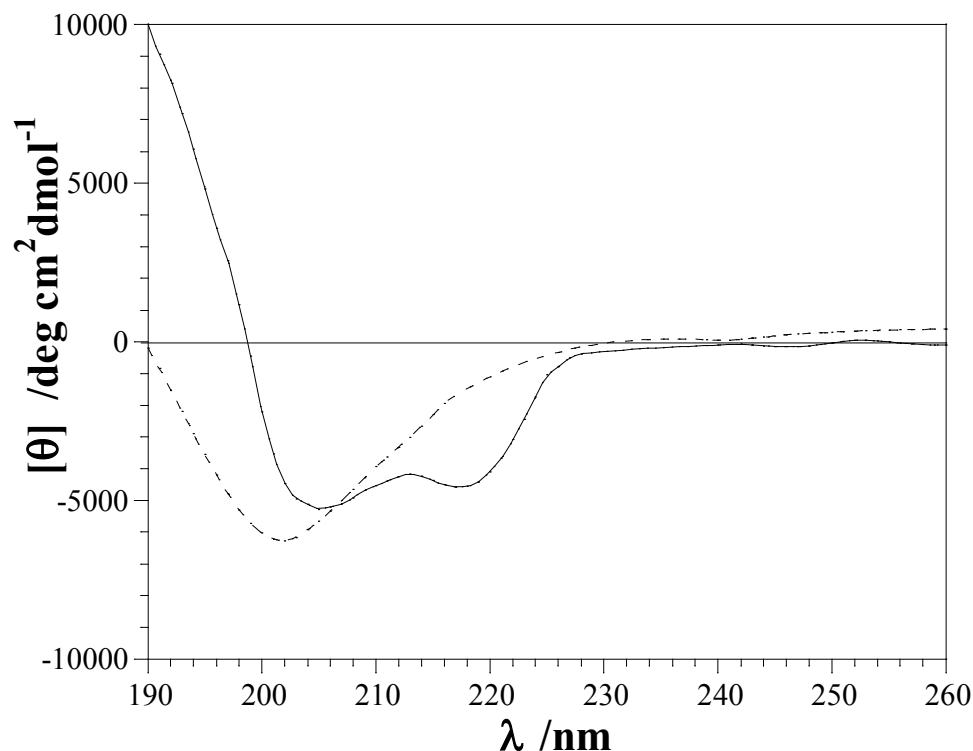


Figure 4.1.7- CD spectra (range 190–260 nm) of peptide 1 in aqueous phosphate buffer (dashed line), and in DMPC unilamellar liposomes (solid line).

This study indicates that C8 adsorbs strongly on the DMPC bilayer surface, causing a perturbation of the lipid chains motion. In addition, the experimental evidences suggest that the tryptophan residues play a major role in driving the interaction between C8 and lipid membranes. In particular, membrane binding requires not only the presence of the Trp residues in the sequence, but also their common orientation on the same side of the putative helix that is engendered by the WX_2WX_2W motif. Finally, the membrane interaction correlates closely with peptide antiviral activity, indicating that the membrane is essential in stabilizing the peptide conformation that will be able to inhibit viral infection.

4.2 Interaction of the C8 peptide with POPC membranes

Subsequently, a micro-structural study on C8-palmitoyl oleoyl phosphatidylcholine (POPC) bilayers interaction was realized by Neutron Reflectivity (NR), ESR, CD and spectrofluorimetry experiments which were combined with molecular dynamics (MD) simulations [8]. POPC was chosen because it includes both a saturated (C16) and an unsaturated (C18) fatty acid, like most of phospholipids present in mammalian cell membranes [9]. The purpose of this work is to present a clear description at a molecular level of the effect of the C8-POPC interactions on the lipid bilayer microstructure to provide a high-resolution picture of the early events of the fusion process.

First, the pure POPC bilayer was characterized by Neutron Reflectivity measurements using D₂O, SMW and H₂O as isotopic contrast solvents. The curves are shown in Figure 4.2.1 and the parameters used to fit the curves simultaneously from all the contrasts are given in Table 4.2.1.

(a)	interfacial layer	thickness (Å)	% solvent	roughness (Å)
	water	3±1	100	8±1
	inner headgroups	8±1	31±10	9±1
	chains region	28±1	-	11±1
	outer headgroup	8±1	33±10	8±1
(b)	interfacial layer	thickness (Å)	% solvent	roughness (Å)
	water	3±1	100	8±1
	inner headgroups	6±1	52±10	9±1
	chains region	31±1	-	11±1
	outer headgroup	5±1	66±10	9±1
	interacting peptide	5±1	54±10	8±1

Table 4.2.1 - Parameters derived from model fitting the reflectivity profiles for (a) the pure POPC and (b) after C8 addition.

A five box model was found to best fit the data. The first two correspond to the silicon block and to the thin solvent layer interposed between the silicon surface and the adsorbed bilayer. The three other boxes describe the lipid bilayer, which is subdivided in

the inner headgroups, the hydrophobic chains, and the outer headgroups layers. The theoretical scattering length density, ρ , was calculated through $\rho(z) = \sum_j n_j(z) b_j$ where $n_j(z)$ is the number of nuclei per unit volume and b_j is the scattering length of nucleus j [10]. ρ of the lipid headgroups was equal to $1.86 \times 10^{-6} \text{ \AA}^{-2}$, while the ρ of acyl chains is equal to $-0.29 \times 10^{-6} \text{ \AA}^{-2}$ [11]. These values were kept constant during the data analysis, since their optimization was found to give no fitting improvement. Thus the parameters obtained from the best fit procedure are the thickness and the roughness of each box plus the solvent content expressed as volume percent.

Inspection of Table 4.2.1 shows that the overall thickness of the bilayer is $44 \pm 1 \text{ \AA}$, while the roughness of all the boxes is the same as for the bare block.

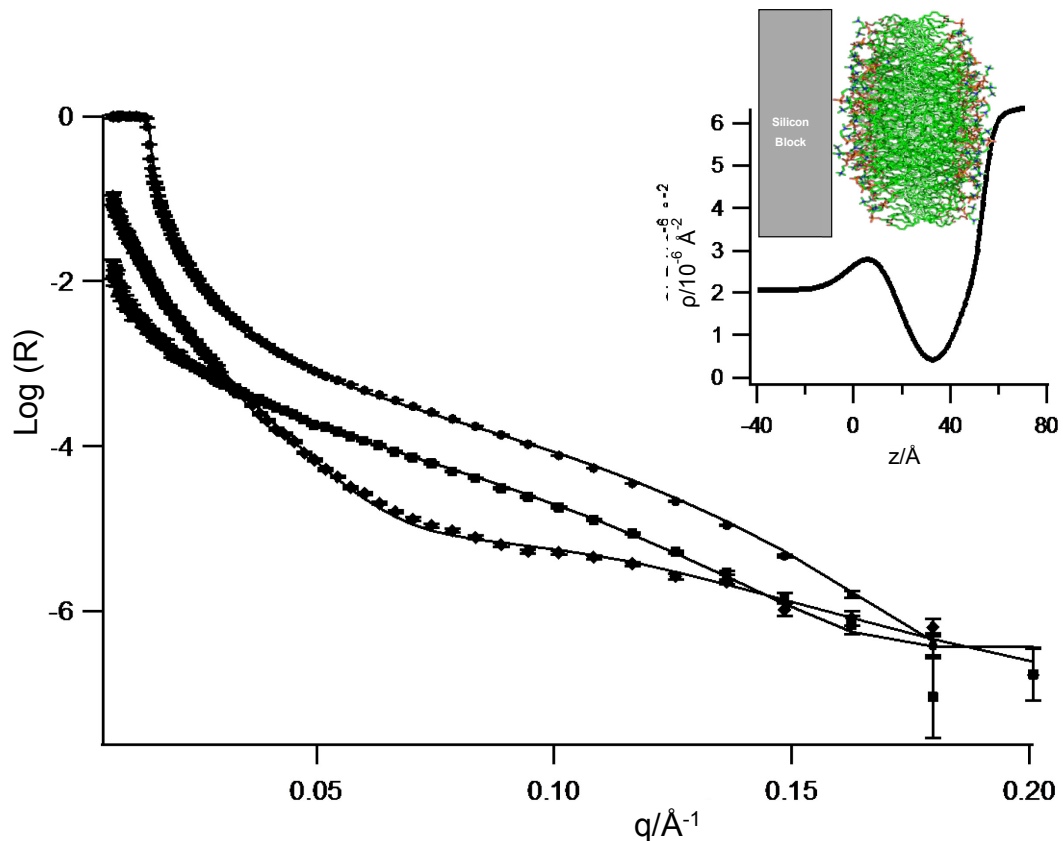


Figure 4.2.1 - Neutron Reflectivity profiles (points) and best fits (continuous lines) corresponding to pure POPC bilayer in (●) D_2O , (■) SMW and (◆) H_2O solvents. The inset shows the ρ profile for the POPC bilayer in D_2O .

The effect of the presence of C8 peptide in the bilayer was studied by measuring the neutron reflectivity curves of the fully hydrogenated POPC to which the peptide with deuterated Trp residues was added. Four contrasts, D₂O, 4MW, SMW and H₂O, were used and NR curves are shown in Figure 4.2.2.

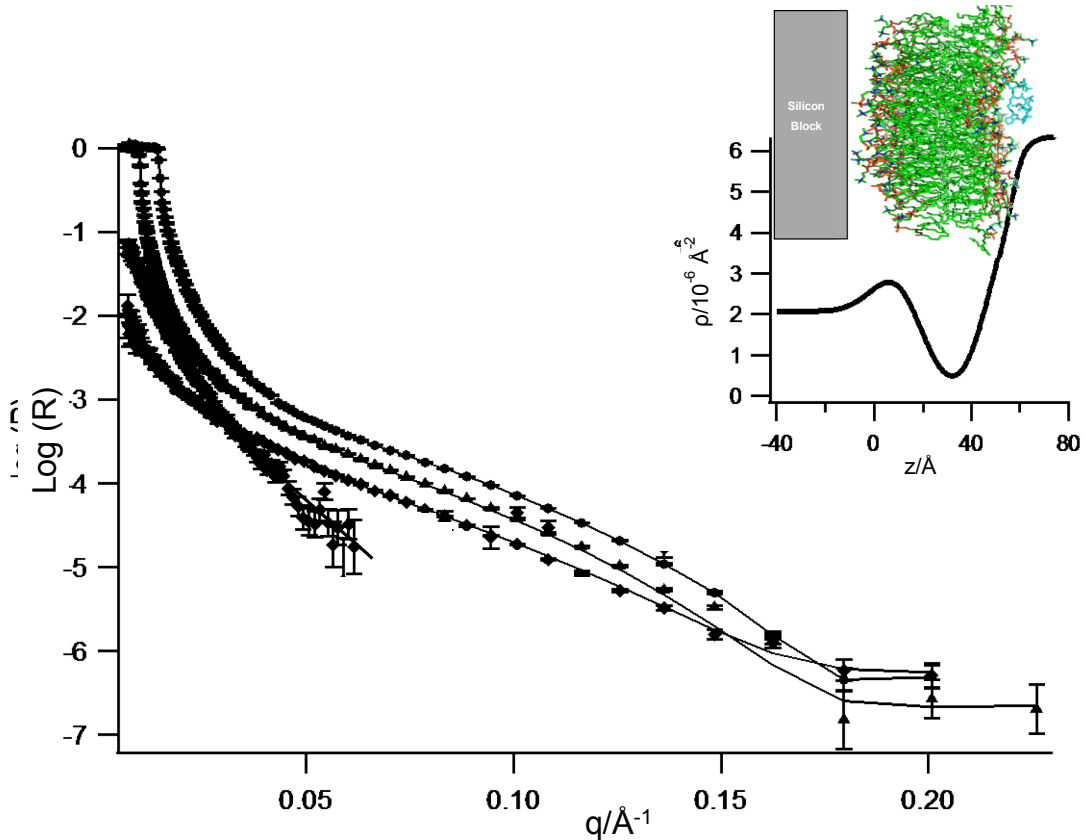


Figure 4.2.2 - Neutron Reflectivity profiles (points) and best fits (continuous lines) corresponding to POPC bilayer with C8 peptide in (●) D₂O, (▲) 4MW, (■) SMW and (◆) H₂O solvents. In the last set, data at high q fall quickly into the background due to the roughness of the layer and incoherent scattering of the solvent. The inset shows the ρ profile for the bilayer in D₂O after peptide addition.

Data from peptide-interacting bilayer were fitted by an additional layer with respect to the case of pure POPC model. This layer prominently consists of the peptides interacting with the outer bilayer surface; its ρ is equal to $3.66 \times 10^{-6} \text{\AA}^{-2}$. In Table 4.2.2, all values of molecular properties of both phospholipid and peptide are reported. Interestingly, in order to obtain a good curves fitting, the ρ of the chains region was changed from $-0.29 \times 10^{-6} \text{\AA}^{-2}$ to $-0.20 \times 10^{-6} \text{\AA}^{-2}$ and, for the external headgroups leaflet, from $1.86 \times 10^{-6} \text{\AA}^{-2}$ to 2.10

$\times 10^{-6} \text{ \AA}^{-2}$. This indicates that the presence of the peptide effectively perturbs the outer hydrophilic layer of the POPC membrane and that this perturbation propagates in the chain region.

	POPC	C8 peptide
$V_{\text{headgroup}} (\text{\AA}^3)$	322.1	
$\rho_{\text{headgroup}} (\times 10^{-6} \text{ \AA}^{-2})$	1.86	
$V_{\text{chains}} (\text{\AA}^3)$	933.7	
$\rho_{\text{chains}} (\times 10^{-6} \text{ \AA}^{-2})$	-0.29	
$V_{\text{mol}} (\text{\AA}^3)$		1410.3 ^a
$M (\text{g mol}^{-1})$		1129
$\rho (\times 10^{-6} \text{ \AA}^{-2})$		3.66
^a Peptide molecular volume is calculated from amino acid volume data reported from Zamyatin [12].		

Table 4.2.2- Molecular properties of POPC phospholipid and C8 peptide.

The values of all parameters optimized in curves fitting are reported in Table 5.2.1. Please note that a model without the water layer between the substrate and the bilayer gave a worse fit to the data. No changes in the roughness of the bilayer occurred upon the introduction of peptide. In contrast, the thickness and the solvent content of the various boxes are different with respect to the pure POPC bilayer. The thickness values of both layers corresponding to the polar headgroups slightly decrease while the thickness of the chains region increases. The total thickness of the bilayer decreases by $\sim 2 \text{ \AA}$. The more evident variations are observed for the solvent content values of both inner and outer headgroups layers that dramatically increase, even though to a different extent. While in the case of the outer hydrophilic headgroups layer the this increase is directly related to the peptide binding, the changes in the inner headgroups layer indicate that the peptide effectively perturbs the whole bilayer structure. The lower extent of perturbation of the inner leaflet with respect to the outer one originates an asymmetry in the bilayer structure.

The perturbation caused by C8 binding to POPC bilayers is investigated by analysing changes in the ESR spectra of spin-labeled lipids included in the membrane. Four phosphatidylcholines spin-labeled at different positions in the *sn*-2 chain, *n*-PCSL ($n = 5, 7, 10, 14$), were employed, with the aim to monitor the changes in structuring and dynamics of the hydrophobic inner region of the bilayer. Figure 4.2.3 shows the *n*-PCSL ESR spectra in the presence and absence of C8 at a peptide to lipid ratio of 0.5:1 wt/wt. In the presence of C8, slight but significant perturbations in the spectra of all spin-labeled lipids are found.

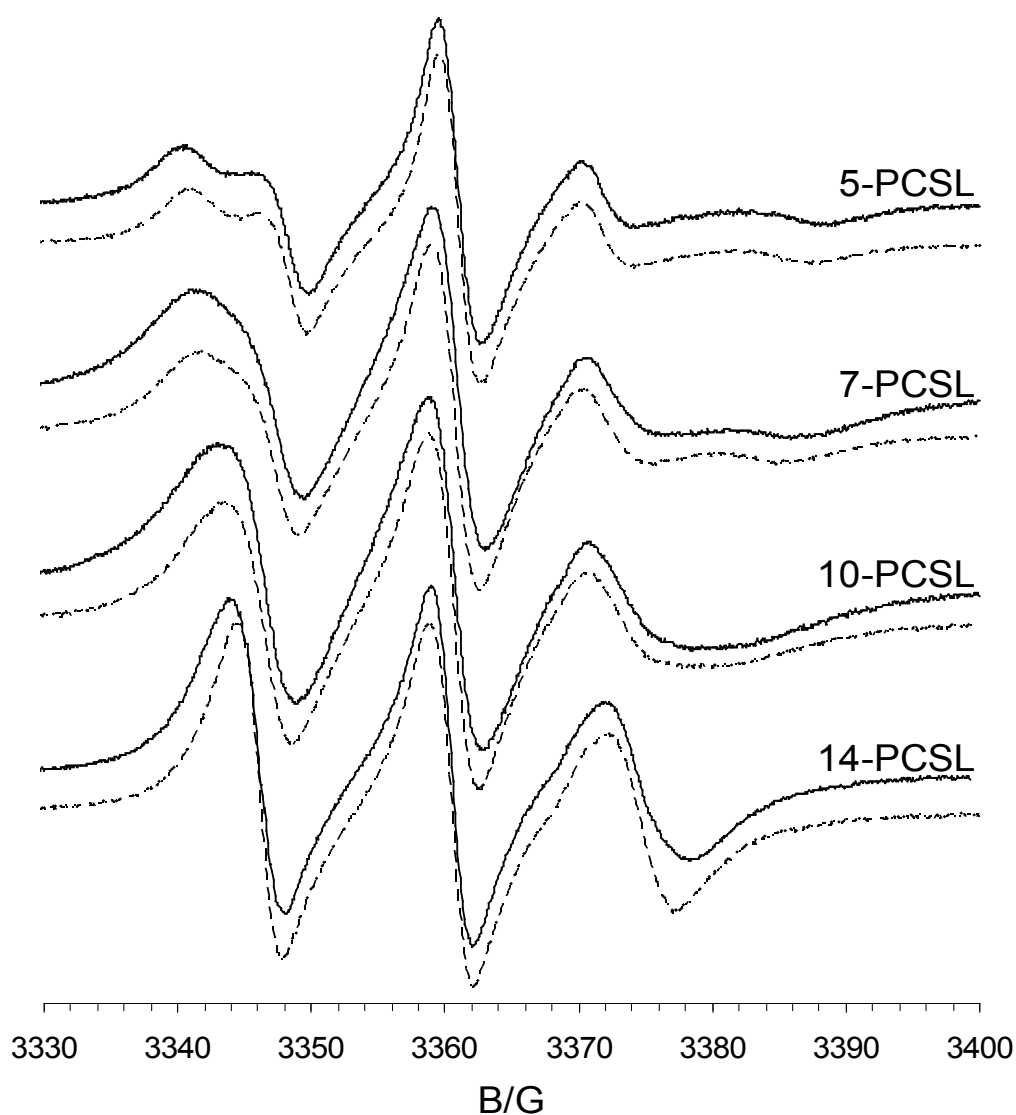


Figure 4.2.3 - ESR spectra of *n*-PCSL positional isomers of spin-labeled phosphatidylcholine in fluid-phase palmitoyl oleoyl phosphatidylcholine bilayer membranes, in the presence (solid line) and in the absence (dashed line) of 0.5:1 wt/wt peptide 1 (C8) at 37 °C.

In an attempt to quantitatively describe this behaviour, we evaluated the outer hyperfine splitting, $2A_{max}$, which is a reliable and easy-to-perform estimate of the segmental chain mobility. $2A_{max}$ is defined as separation, expressed in Gauss, between the low-field maximum and the high-field-minimum, and tends to increase with increasing the restriction in local chain mobility.

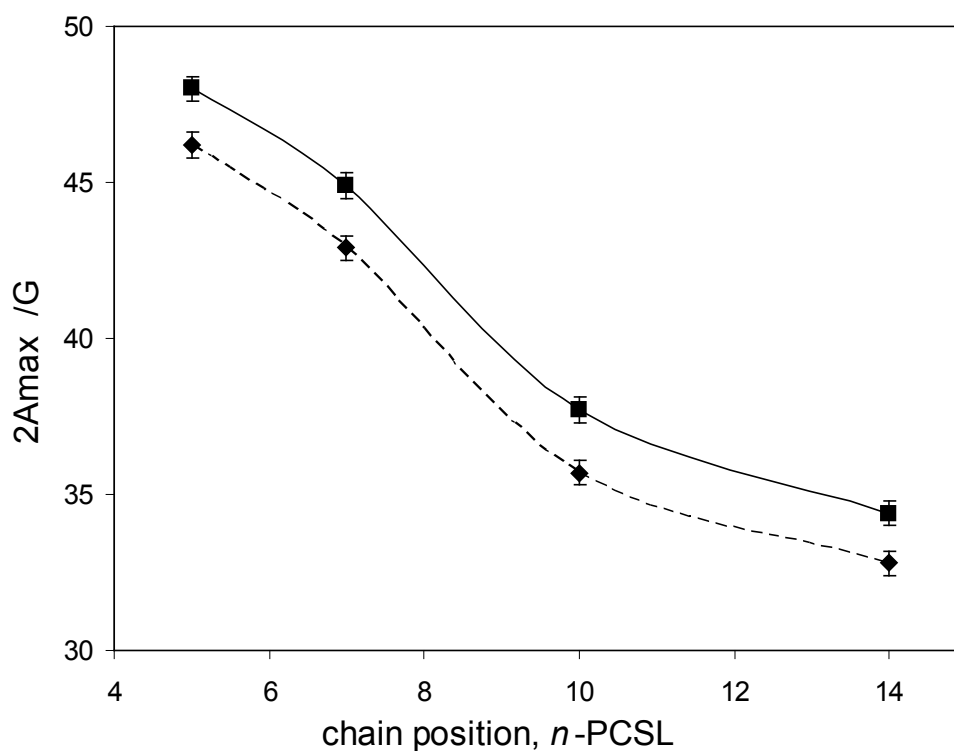


Figure 4.2.4 - Dependence on spin-label position, n , of the outer hyperfine splitting, $2A_{max}$, of n -PCSL in membranes of POPC, in the absence (dashed line, solid diamonds) and in the presence of 0.5:1 wt/wt C8 (continuous line, solid squares). $T=37$ °C.

Figure 4.2.4 shows the dependence of the outer hyperfine splitting, $2A_{max}$, on chain position, n , for the n -PCSL spin-labels in fluid POPC membranes, with and without a saturating amount of peptide. In both cases, $2A_{max}$ decreases with increasing n . In the presence of C8 the characteristic flexibility gradient with chain position of the fluid lipid bilayer membranes is preserved, but $2A_{max}$ is increased at all spin-label chain positions by roughly the same extent (≈ 2 G). Particularly, for what concerns the spin-label presenting the nitroxide in a deeper position, 14-PCSL, there is no appearance of a second component

in the spectra, corresponding to spin-labeled lipid chains whose motion is restricted. This is evidence that the peptide binds solely at the membrane surface and does not penetrate appreciably into the membrane interior, as does, for instance, the HIV fusion peptide gp41-FP [13]. Thus, in the case of C8, ESR results indicate that perturbations induced by surface association of the peptide, propagates throughout the lipid chains, resulting in a reduction of the segmental mobility of the methylen groups with $n \geq 5$. In order to ensure that variations in the spectra lineshape is determined by changes in segmental acyl chain mobility and not in magnetic parameters, simulations of 5-PCSL and 14-PCSL spectra, in the absence and in the presence of C8, were performed (see Figure 4.2.5 and 4.2.6) thanks to the collaboration of Dr. Elena Busi, Department of Chemistry, University of Siena. Results show that, while magnetic parameters remain unchanged, the perpendicular components of the diffusion anisotropic tensor vary, giving the reorientational times τ_c reported in Table 4.2.3. The τ_c trends are consistent with the $2A_{max}$ trends discussed above.

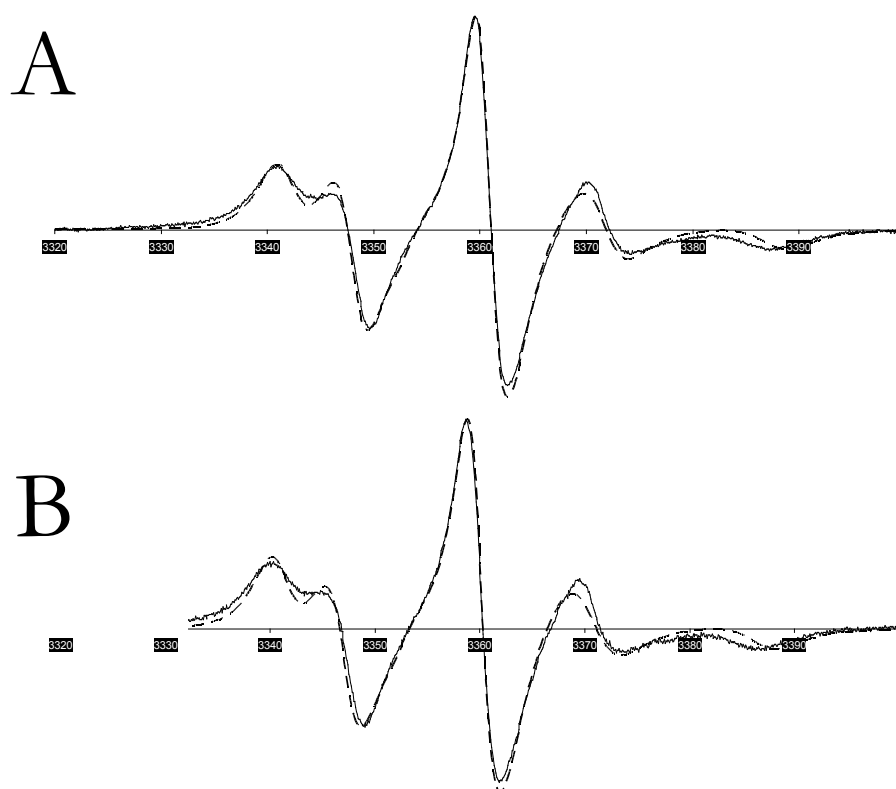


Figure 4.2.5- ESR spectra of 5-PCSL in POPC bilayers at 37 °C in the absence (A) and in the presence (B) of 0.5:1 wt/wt C8 peptide 1 (continuous lines) paired with their best simulation (dashed lines).

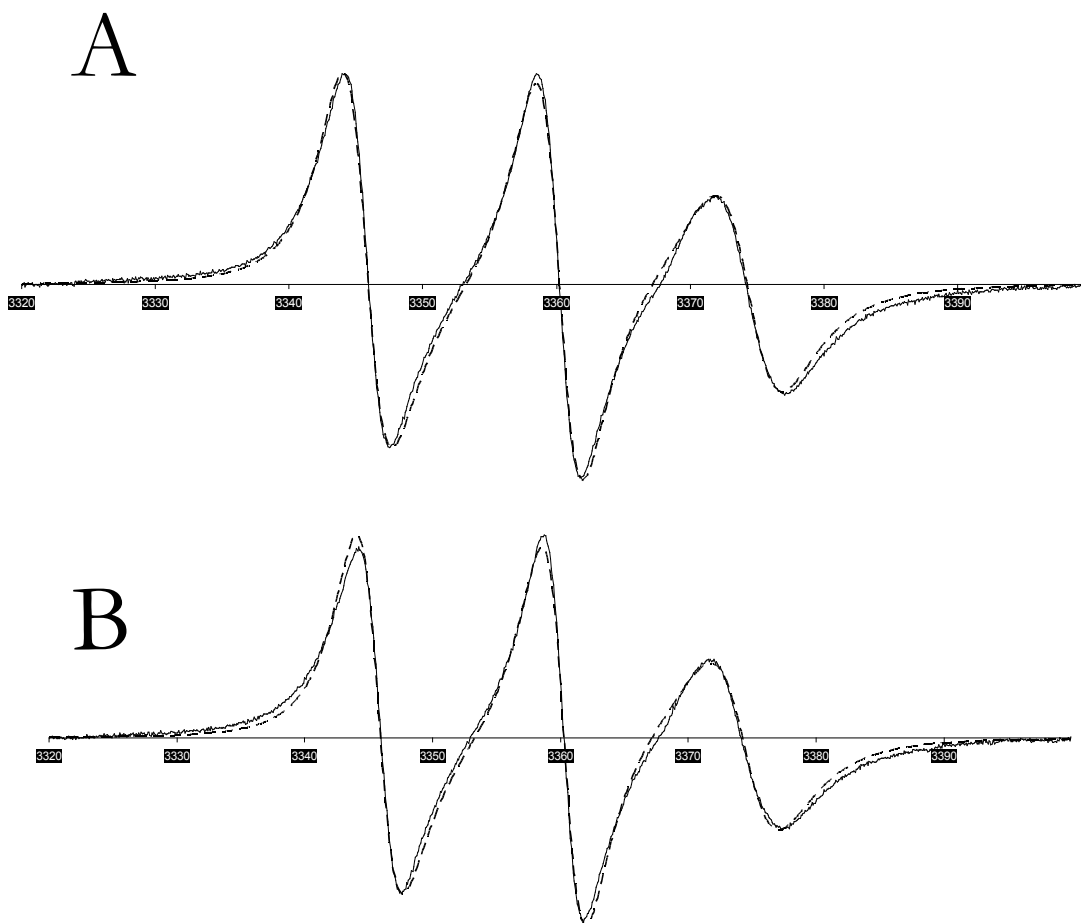


Figure 4.2.6 - ESR spectra of 5-PCSL in POPC bilayers at 37°C in the absence (A) and in the presence (B) of 0.5:1 wt/wt C8 peptide 1 (continuous lines) paired with their best simulation (dashed lines).

	POPC	POPC-C8	POPC	POPC-C8
	5-PCSL		14-PCSL	
$g_{xx} (\pm 0.0002)$	2.0100	2.0100	2.0186	2.0186
$g_{yy} (\pm 0.0002)$	2.0088	2.0086	2.0001	2.0001
$g_{zz} (\pm 0.0002)$	2.0054	2.0053	2.0058	2.0058
$A_{xx} / G (\pm 0.2)$	2.8	2.9	6.9	7
$A_{yy} / G (\pm 0.2)$	12.6	12.3	10.7	10.6
$A_{zz} / G (\pm 0.2)$	27	27.1	21.5	21.3
$\tau_{(C)xx} / ns (\pm 1)$	139	163	19	24
$\tau_{(C)yy} / ns (\pm 1)$	7	7	2	3
$\tau_{(C)zz} / ns (\pm 1)$	5	5	2	2

Table 4.2.3 - Magnetic and dynamic parameters derived from the simulation of the ESR spectra of 5-PCSL and 14-PCSL in POPC bilayers, in the absence and in the presence of the C8 peptide.

Peptide positioning relative to POPC bilayer was further investigated by intrinsic Trp fluorescence emission measurements. The Trp emission spectra of C8 peptide, measured either in buffer or in the presence of increasing amounts of lipid vesicles are shown in Figure 4.2.7. As previously observed, C8 in water gives a Trp emission spectrum typical of an aqueous environment ($\lambda_{\text{max}} = 354 \text{ nm}$), indicating that the Trp side chains are exposed to the aqueous medium. The presence of POPC liposomes causes a slight blue shift of the emission maximum to shorter wavelength ($\lambda_{\text{max}} = 347 \text{ nm}$) and a reduction of the fluorescence quantum yield. No shoulder at lower wavelength appears. The limited extent of the shift indicates that the Trps are greatly exposed to the solvent [6]. These results indicate that, despite the interaction between C8 and POPC liposomes, all the Trp residues of this peptide are not significantly inserted in the apolar inner core of the bilayer.

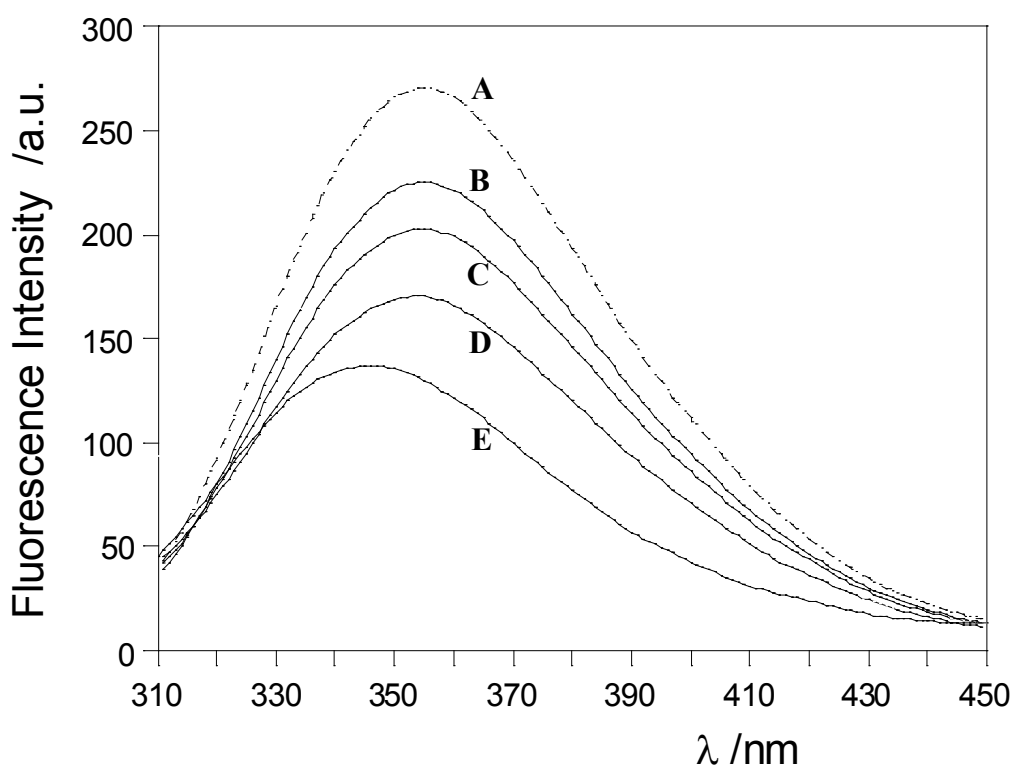


Figure 4.2.7 - Fluorescence emission spectra of C8 peptide in aqueous phosphate buffer (A, dashed line), and in POPC unilamellar liposomes (solid line) at different lipid concentration: B 0.16 mM, C 0.39 mM, D 0.6 mM and E 0.92mM. T=37 °C.

The C8 fluorescence intensities at 354 nm are plotted as a function of the lipid concentration in Figure 4.2.8. Fitting these data to the equation reported in the methods section, allows to evaluate the apparent peptide-lipid association constant, K_a , and the number of phospholipid molecules, n , required to bound a peptide. It was obtained $K_a = (8.3 \pm 0.6) \times 10^5 \text{ M}^{-1}$ and $n = 6 \pm 2$, respectively.

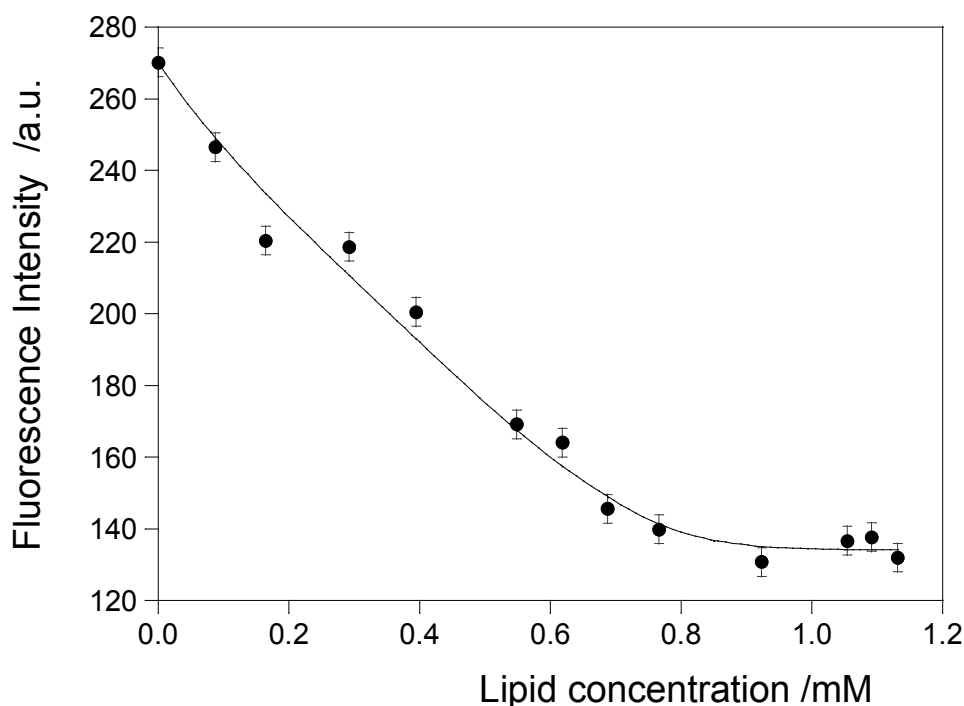


Figure 4.2.8 - Fluorescence titration curve of C8 with phospholipid liposomes at $T=37 \text{ }^\circ\text{C}$.

The conformational preferences of C8 in the presence of POPC liposomes was investigated by means of CD spectroscopy. The peptide in buffer presents a spectrum with the typical shape of a random coil structure, including a negative band at 202 nm. In the presence of POPC liposomes the spectrum assumes the double-well shape typical of a turn-helical structure, including negative bands at 205 and 216 nm (Figure 4.2.9). From $[\theta]_{222}$ the helix content has been estimated to be $\sim 20\%$. In the case of a short peptide like C8, this value has to be regarded as a time-averaged propensity to assume turn-helical structures.

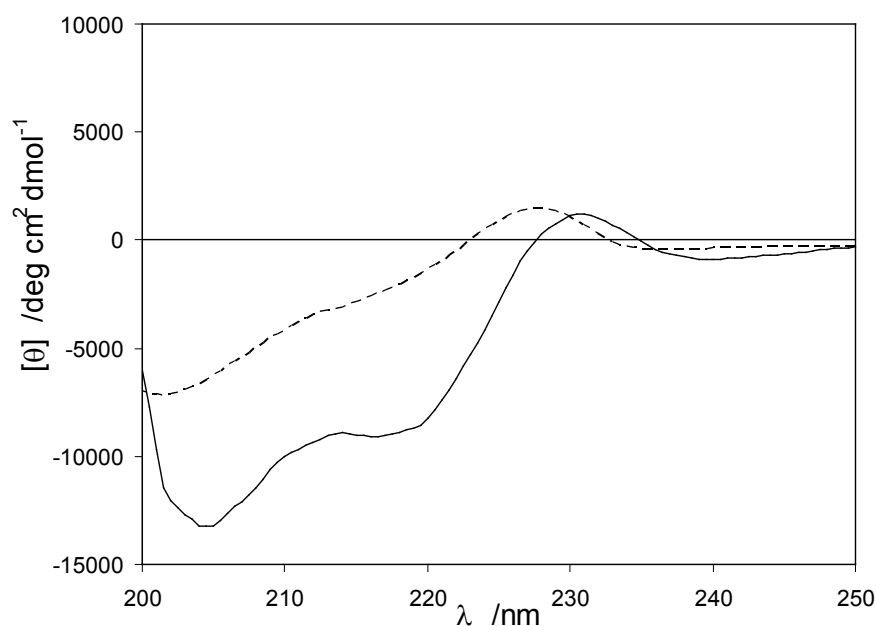


Figure 4.2.9 - C8 CD spectra in aqueous phosphate buffer (dashed line), and in POPC unilamellar liposomes (solid line). T=37 °C.

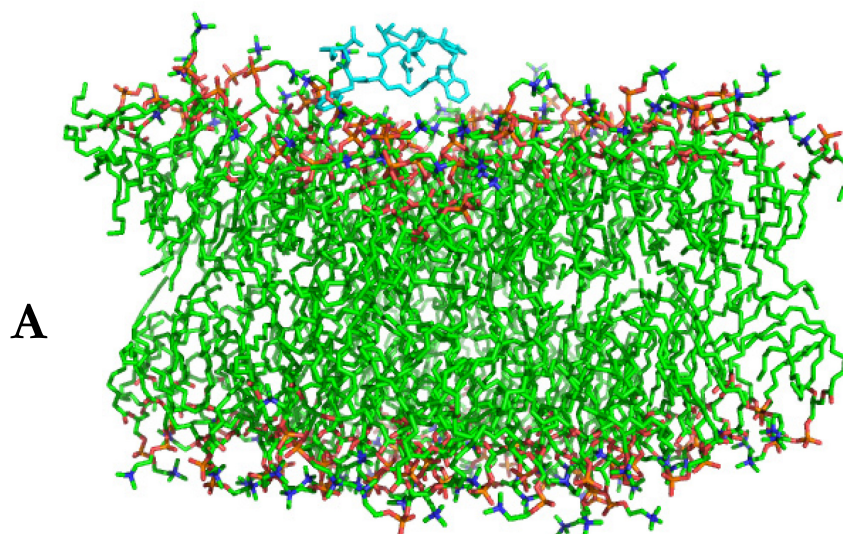
The experimental results on the destabilizing effect of C8 on the lipid bilayer structure was also confirmed by the computational investigation realized in collaboration with Dr. Antonello Merlino, Department of Chemistry, University of Naples “Federico II”.

First, MD simulations of C8 peptide in solution were analyzed. These simulations were used as a test of the protein force field to determine whether MD data are in agreement with those obtained experimentally and to exclude possible artifacts induced by the force field choice. A 70ns simulation of C8 in aqueous solution, starting from the NMR structure, showed that the peptide had very little propensity to form α -helical structure in water. Similarly, starting from a random model, no significant formation of α -helical structure was observed during an additional 70ns simulation. These results are consistent with CD data suggesting that C8 is unstructured in solution.

In the study of C8 interaction with POPC bilayer, three initial positions of the NMR structure were chosen to eliminate any bias due to the starting configuration. In all cases, the minimum distance between the peptide and the bilayer is 0.7 nm. C8 was attracted to the surface of the bilayer in all simulations, independent of the starting position. The

peptide comes into close contact with the bilayer headgroups within the first nanosecond and equilibrates at the surface for the remainder of the simulation (up to 70 ns). The secondary structure of the peptide drastically changes throughout the simulations. The peptide loses most of its starting secondary structure to become a random coil within the first nanosecond and subsequently it only transiently folds as a 3_{10} helix with turn structures. At the bilayer-water interface, the structure was maintained throughout with 2-4 residues of the peptide being helical and turn structures randomly sampled. In the path taken for binding, C8 peptide approaches the POPC bilayer surface without making significant contacts. Upon binding to membrane, strong interactions are observed between the peptide and the phospholipid headgroups.

A model displaying the location of C8 on the bilayer surface, together with representative interactions with lipid molecules is shown in Figure 4.2.10. The peptide orients such that the side chains of Trp770 and 776 form hydrogen bonds as well as hydrophobic interactions with the lipids, and the charged Glu and Asp residues (Glu771 and Asp772) remain hydrogen bonded with the oxygens of the lipid headgroups. Indoles present the plane either parallel to the lipid chains or at an oblique angle to the membrane normal (Figure 4.2.10B-C). No conserved hydrogen bonds between the peptide backbone and the headgroups of the lipid bilayer are found.



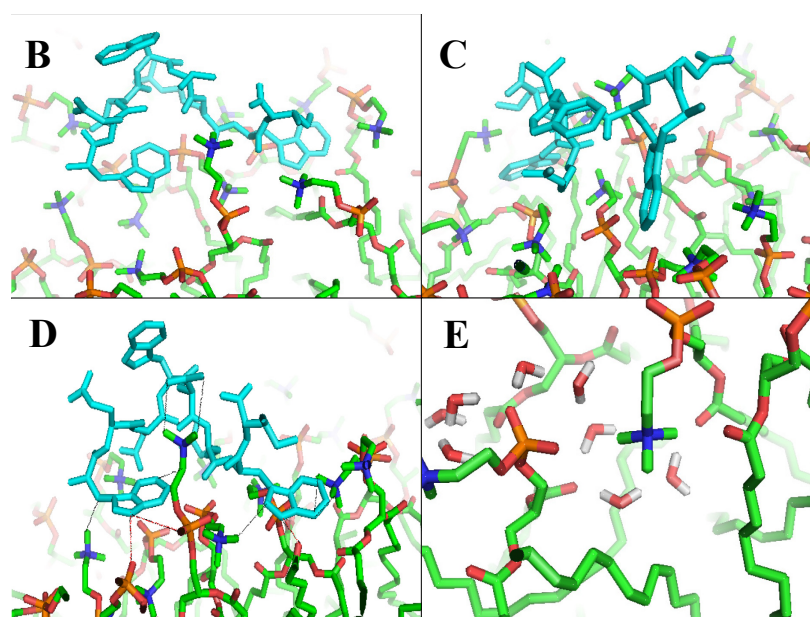


Figure 5.2.10 -Configuration of the system when C8 has moved to the surface of the bilayer (panel A). Snapshots selected from the trajectories (panel B-E). C8 is displayed in cyan, carbon atoms of POPC are coloured in green, oxygen atoms in red, nitrogen atoms in blue and phosphorous in orange, water molecules are omitted. In panel D, hydrogen bonds are indicated in red, hydrophobic interactions in black. In panel E, water molecules in the headgroup region of the leaflet in contact with the peptide are shown.

In total, during the simulations, C8 is in contact with atoms belonging to 24-30 different POPC molecules, although, typically, the peptide binds 8-10 POPC molecules simultaneously. Peptide binding induces a decreasing of 0.5-1 nm² of solvent accessible surface for POPC oxygen and nitrogen atoms, which is likely to be due to their involvement in the lipid-peptide H-bonding. At the same time MD results indicate an increase of 2-4 nm² of the solvent accessible surface for POPC carbon atoms. This last result has to be interpreted as an increase of exposure to the solvent of the carbon atoms present in the lipid headgroup (i.e., those of glycerol and choline group). A snapshot showing water molecules in the lipid headgroup region is reported in Figure 4.2.10E. Water molecules form a network of hydrogen bonds with the oxygen atoms of glycerol and choline groups and hydrate carbon atoms. No water molecules are found in the acyl chain region. POPC bilayer thickness, with and without the presence of C8, is reported in Table 4.2.4.

	POPC molecules -starting conformation	POPC molecules in contact with C8 before the binding	POPC molecules in contact with C8 upon the binding
P-P thickness (nm)	4.12*	4.00-4.03 (± 0.02)	3.60-3.71 (± 0.03)

*The value of bilayer thickness in absence of the peptide, measured as the average distance between the phosphorous atoms of the upper and lower leaflets of POPC, is in agreement with previous computational[14] and experimental[15] studies.

Table 4.2.4 - POPC bilayer properties obtained by MD simulations.

By comparison of these values, it can be concluded that the C8 binding provokes a thinning effect of 3-5 Å. The local reduction of the bilayer thickness induced by the peptide is confirmed by visual inspection of the trajectories and also suggested by Figure 4.2.10, where the formation of a hollow on the bilayer surface can be detected. MD simulations also show that peptide binding to the bilayer surface reflects in the microstructuring and dynamics of the lipid molecules. The calculated order parameters of the lipids in direct contact with the peptide compared with those of the other lipids constituting the bilayer are reported in Figure 4.2.11A.

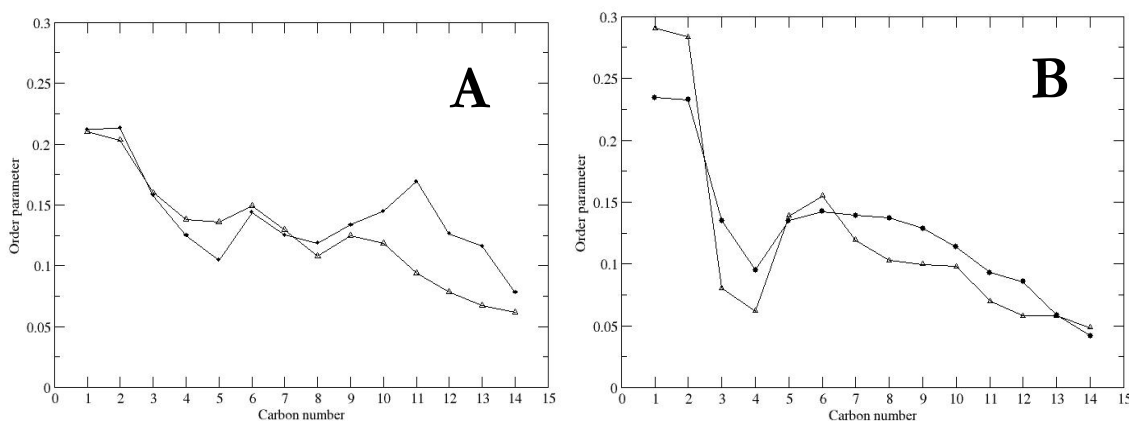


Figure 4.2.11 - Calculated order parameters for POPC palmitic chains in direct contact with C8 (circle) and for those not in contact with the peptide (triangle) (panel A). Calculated order parameters for POPC palmitic chains of the leaflet in direct contact with the peptide (circle) and for those of the opposite side of the bilayer (triangle) (panel B).

For POPC molecules in contact with C8, calculated values are slightly higher in magnitude (indicating more order in the system), particularly for the last atoms of the chain ($n \geq 8$). Similar results have been obtained comparing the root mean square deviations of POPC molecules in the presence and in the absence of the peptide. Interestingly, a slightly different effect of peptide binding on the two monolayers is also observed. Inspection of Figure 4.2.11B shows that, in the peptide-bound leaflet, acyl chain mobility is slightly higher close to the interface ($n = 2, 3$) and somewhat lower in more internal region ($n \geq 7$).

In order to have a direct comparison between NR and computational results, the experimental scattering length density profile, $\rho(z)$, of the two analyzed systems, using thickness values obtained by MD simulations, has been calculated (Figure 4.2.12). The results of this analysis confirms a close correlation between NR and MD data.

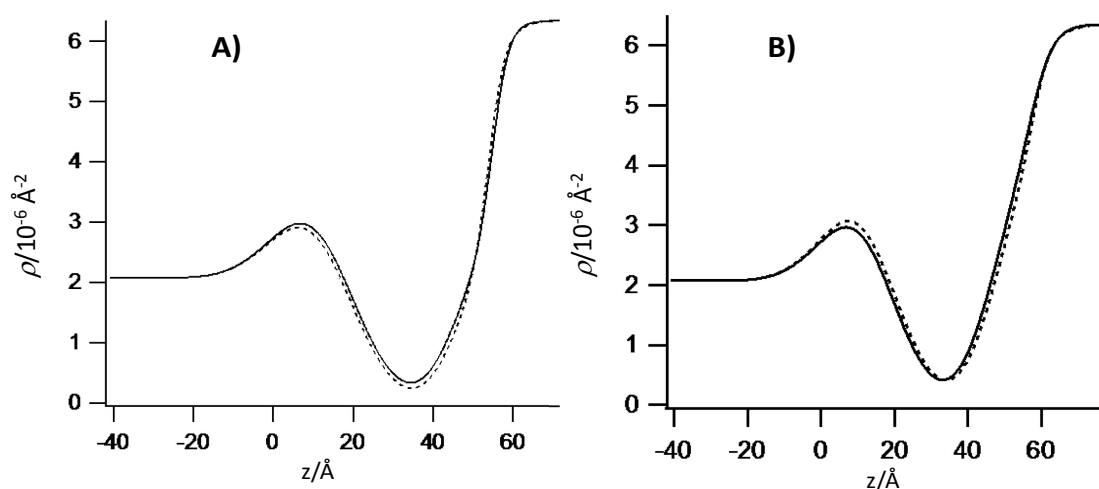


Figure 4.2.12 – Comparison between the scattering length density, $\rho(z)$, profile of pure POPC (A) and POPC with C8 (B) bilayers, obtained by experimental (continuous line) and computational (dotted line) data. The thickness of the chains region, headgroups and interacting peptide layers has been estimated from the MD simulations as follows atoms of the: the chains region thickness has been calculated as the average distance between the carbons in α to the carboxylic groups of the lipid acyl chains of the two opposing leaflet. The headgroups layers thickness has been calculated by subtracting the thickness of chains region to the average distance between the nitrogen atoms of the choline groups of the two opposing leaflets. The thickness of the interacting peptide layer has been calculated as the average distance between the peptide atoms closest and farthest to the lipid headgroups.

The experimental strategy set up for this study has proved to be extremely informative of the microstructure and dynamics of complex systems such as lipid membranes interacting with peptides/proteins. Particularly, MD simulations have been found to be a valuable tool to rationalize all the experimental results obtained by Neutron Reflectivity, CD, ESR and fluorescence spectroscopy. The findings of the present investigation could help in shedding light on the mechanism through which viral glycoproteins help to overcome the energetic barrier inherent with the fusion between the target cell plasma membrane and the viral envelope, and particularly on the role played by the MPER protein domain in the process. The experimental data suggest that lipid bilayer destabilization could be a consequence of the asymmetric perturbation of the bilayer that starts with an increased hydration of lipid headgroups coupled to an increase of lipid ordering in the leaflet exposed to the approaching viral glycoprotein. In particular, since water organization at membrane interface has been proposed to control the fusion dynamics [14], the increment of bilayer hydration could be a fundamental part of role played by the MPER fusion protein domain during the process.

4.3 Role of lipid composition on the C8-membranes interaction

Subsequently, a study on the effect of cholesterol (CHOL) and sphingomyelin (SM) presence on the C8-POPC bilayers interaction was realized. Supported Lipid Bilayers (SLBs) and Multi-Lamellar Vesicles (MLVs), composed by POPC and CHOL at different weight content (from 0 to 30%) and by POPC, SM and CHOL at 1:1:1 weight ratio, were analyzed by a combined experimental approach, performing NR and ESR measurements.

First, lipid bilayers composed by POPC:CHOL at different weight ratio (90:10, 80:20 and 70:30) and POPC:SM:CHOL at 1:1:1 weight ratio were characterized by NR and ESR measurements, in order to obtain micro-structural information depending from the different lipid composition.

NR characterization was performed using D₂O, SMW and H₂O as isotopic contrast solvents. The experimental curves are shown in Figure 4.3.1A-D and the parameters used to fit the curves simultaneously from all the contrasts are given in Table 4.3.1. For all lipid systems, a five box model was found to best fit the data. The first two correspond to the silicon block and to the thin solvent layer interposed between the silicon surface and the adsorbed bilayer. The three other boxes describe the lipid bilayer, which is subdivided in the inner headgroups, the hydrophobic chains, and the outer headgroups layers. For all considered bilayers, a model without the water layer between the substrate and the bilayer gave a worse fit to the data. For POPC headgroups, ρ_{\square} is equal to $1.86 \times 10^{-6} \text{ \AA}^{-2}$ while for the acyl chains is equal to $-0.29 \times 10^{-6} \text{ \AA}^{-2}$ [11]. For CHOL ρ_{\square} is equal to $0.22 \times 10^{-6} \text{ \AA}^{-2}$. In the case of SM, ρ_{\square} was estimated to be equal to $\sim 1.60 \times 10^{-6} \text{ \AA}^{-2}$ for the headgroups and to $\sim -0.29 \times 10^{-6} \text{ \AA}^{-2}$ for the acyl chains. Thus the parameters obtained from the best fit procedure are the thickness and the roughness of each box plus the solvent content expressed as volume percent (see Table 4.3.1).

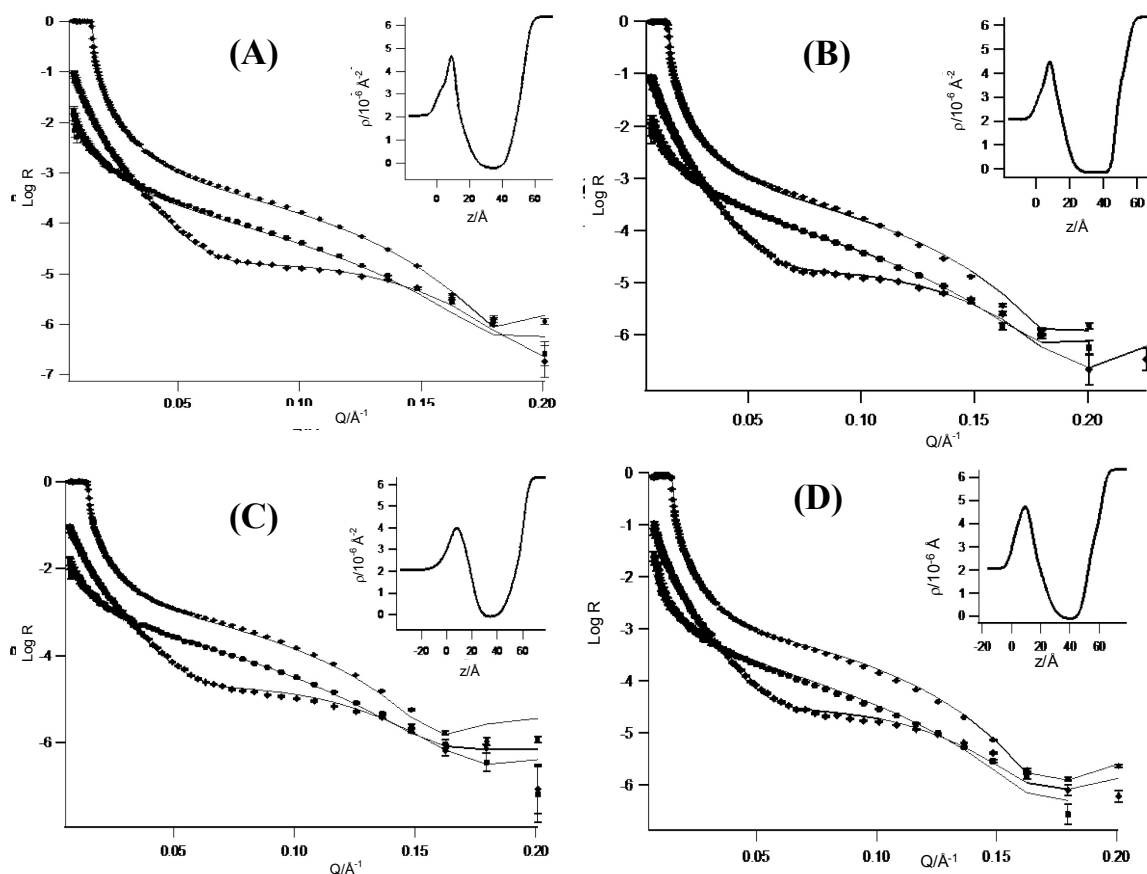


Figure 4.3.1 - Neutron Reflectivity profiles (points) and best fits (continuous lines) corresponding to bilayers of **(A)** POPC:CHOL 90:10 wt/wt, **(B)** POPC:CHOL 80:20 wt/wt, **(C)** POPC:CHOL 70:30 wt/wt and **(D)** POPC:SM:CHOL 1:1:1 wt/wt/wt bilayers in (●) D₂O, (■) SMW and (◆) H₂O solvents. The insets show the ρ profiles for the lipid bilayers in D₂O.

The presence of cholesterol influences the overall thickness of the lipid bilayer. In fact, it increases proportionally with the cholesterol content, varying from $44 \pm 1 \text{ \AA}$, obtained for the pure POPC bilayers [8], to $50 \pm 1 \text{ \AA}$ obtained in the case of 30% wt/wt content. In particular, the presence of cholesterol causes an increase of the thickness of the hydrophobic region, going from $28 \pm 2 \text{ \AA}$ (pure POPC) to $33 \pm 2 \text{ \AA}$. In addition, the ρ values corresponding to this region increase with the cholesterol content, from -0.29 to $-0.11 \times 10^{-6} \text{ \AA}^{-2}$. This evidence is a clear confirmation that cholesterol has a tendency to position in the hydrophobic core between the phospholipid chains. Then, a small increase of the solvent content in the headgroups region is observed, probably due to the different chains packing density related to the presence of cholesterol in the bilayer.

Finally, for all bilayer systems, the roughness values were similar to those obtained for the corresponding silicon bare. In the case of the lipid bilayer also containing SM, a total thickness of $49 \pm 1 \text{ \AA}$, a roughness equal to that obtained for the silicon surface and a solvent content in the headgroups region of 40% and $44\% \pm 10$ for the inner and outer polar layers, respectively, were obtained. ρ values equal to $-0.11 \times 10^{-6} \text{ \AA}^{-2}$ for the acyl chains region, confirming the presence of cholesterol in this domain, while the ρ value for the headgroup region was equal to $1.7 \times 10^{-6} \text{ \AA}^{-2}$, that is a medium value between the theoretic ones corresponding to phosphatidylcholine and myelin groups which form the headgroups polar layers.

ESR investigation was realized incorporating phosphatidylcholine spin-labeled on the different positions of the *sn*-2 chain (*n*-PCSL, with $n = 5, 7, 10, 14$) in the lipid bilayers. Analysis of *n*-PCSL' spectra for all lipid samples was realized determining the outer hyperfine splitting ($2A_{\text{max}}$). ESR spectra of 5-PCSL, which presents the nitroxide group close to its hydrophilic headgroup, are shown in Figure 4.3.2. They show clearly defined axially anisotropic lineshapes, with a value of the outer hyperfine splitting, $2A_{\text{max}}$, equal to $52.5 \pm 0.1 \text{ G}$ for the pure POPC. Increasing the cholesterol content, the $2A_{\text{max}}$ values increase with it up to a value of $56.7 \pm 0.1 \text{ G}$. The same effect was observed for the ESR spectra (not shown) of 7 and 10-PCSL, which also present anisotropic lineshapes, although lower than that observed for the 5PCSL spectra (see reported in Table 4.3.2). We also investigated lipid bilayers including phosphatidylcholine spin labeled on the 14 C-atom of the *sn*-2 chain (14-PCSL), in which the nitroxide group is positioned close to the terminal methyl region of the chain. The corresponding spectra are shown in Figure 4.3.3. In this case, a narrow, three-line, quasi isotropic spectrum is obtained for POPC and POPC:CHOL 90:10 samples, as shown in Figure 4.3.3A-B. The higher isotropy of the 14-PCSL spectrum with respect to that obtained for 5-PCSL indicates a flexibility increase in segmental chain mobility in going from the polar headgroups to the inner hydrophobic

core, which is a characteristic hallmark of the liquid-crystalline state of fluid phospholipid bilayers.

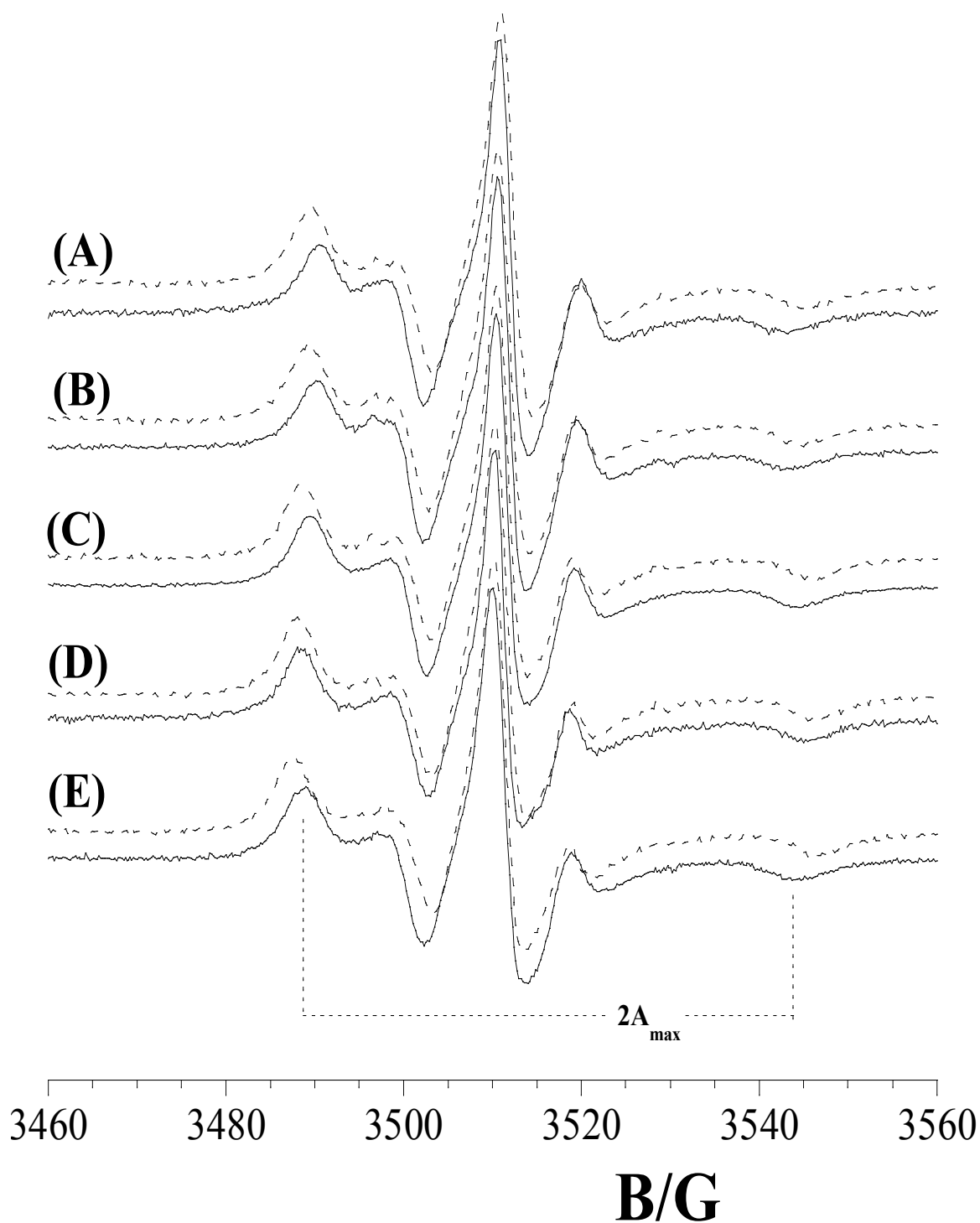


Figure 4.3.2 – ESR spectra of 5-PCSL in lipid bilayers of pure POPC (A), POPC:CHOL at weight ratios of 90:10 (B), 80:20 (C), 70:30 (D) and POPC:SM:CHOL (E) in absence (continuous lines) and presence (dashed lines) of C8 peptide.

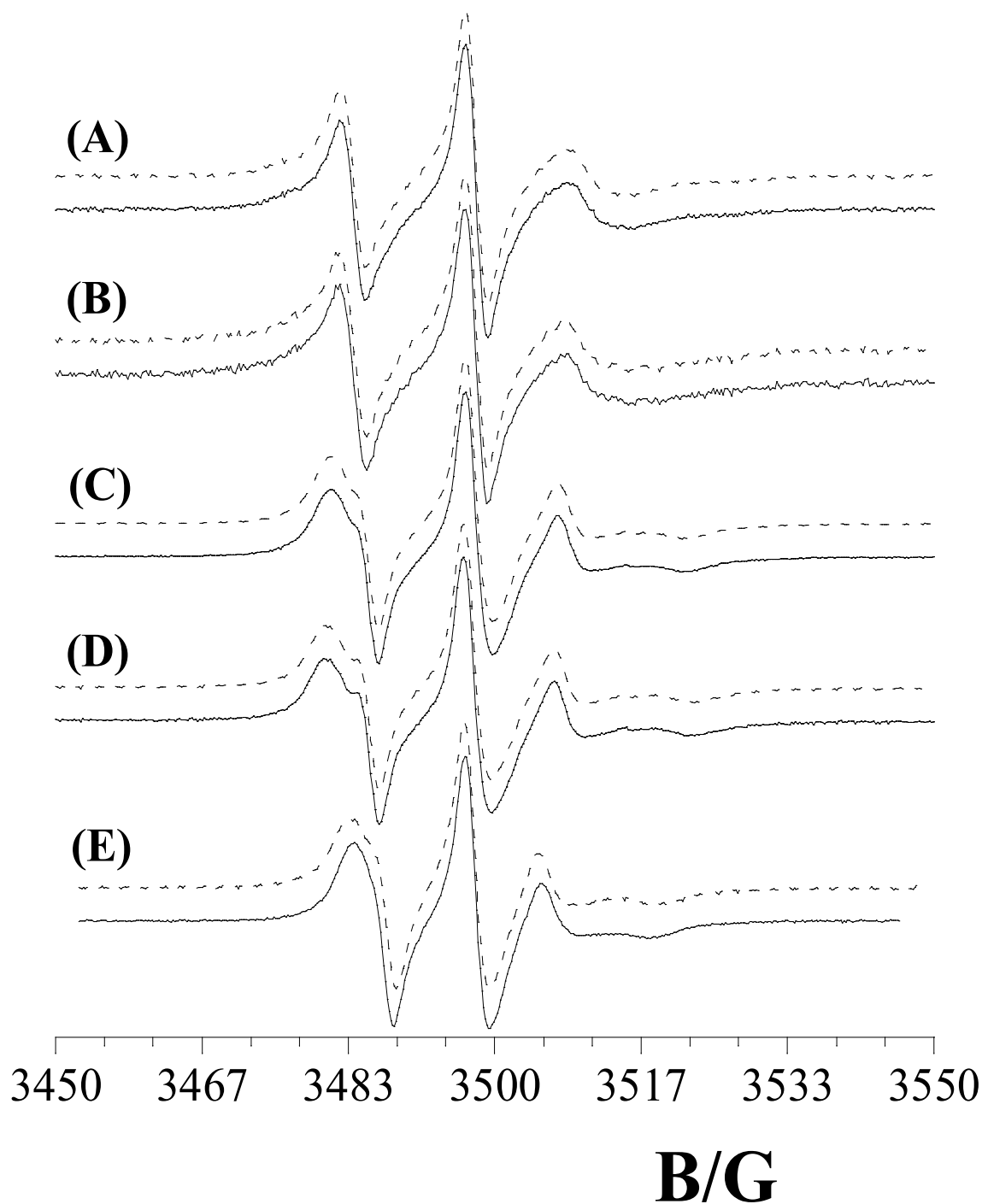


Figure 4.3.3 – ESR spectra of 14-PCSL in lipid bilayers of pure POPC **(A)**, POPC:CHOL at 90:10 **(B)**, 80:20 **(C)**, 70:30 **(D)** weight ratios and POPC:SM:CHOL **(E)** in absence (continuous lines) and presence (dashed lines) of C8 peptide.

Increasing the cholesterol content, a second component appears in the ESR spectra, as shown in Figure 4.3.3C-E. This second component is resolved in the outer wings of the spectra and corresponds to spin-labeled lipid chains whose motion is restricted. In addition,

the $2A_{\max}$ values are much higher than those calculated for 14-PCSL spectra in pure POPC and POPC:CHOL 90:10 bilayers.

<i>n</i> -PCSL	$2A_{\max}/G$				
	POPC	POPC:CHOL	POPC:CHOL	POPC:CHOL	POPC:SM:CHOL
		90:10	80:20	70:30	
5-PCSL	52.5 ± 0.1	53.5 ± 0.1	55.1 ± 0.1	56.7 ± 0.1	56.4 ± 0.1
7-PCSL	50.5 ± 0.1	52.1 ± 0.1	54.4 ± 0.1	56.2 ± 0.1	55.7 ± 0.1
10-PCSL	47.7 ± 0.2	48.5 ± 0.2	50.2 ± 0.2	52.8 ± 0.2	51.4 ± 0.2
14-PCSL	32.6 ± 0.3	32.9 ± 0.3	40.6 ± 0.2	41.7 ± 0.2	40.8 ± 0.2
<i>after the C8 addition</i>					
5-PCSL	54.9 ± 0.1	55.7 ± 0.1	57.5 ± 0.1	57.0 ± 0.1	59.6 ± 0.1
7-PCSL	52.8 ± 0.1	54.3 ± 0.1	55.5 ± 0.1	56.0 ± 0.1	59.3 ± 0.1
10-PCSL	50.0 ± 0.2	49.8 ± 0.2	50.7 ± 0.2	52.6 ± 0.2	53.7 ± 0.2
14-PCSL	34.0 ± 0.3	33.1 ± 0.2	41.1 ± 0.2	41.5 ± 0.2	42.5 ± 0.2

Table 4.3.2 - Outer hyperfine splitting, $2A_{\max}$, values of *n*-PCSL in POPC, POPC:CHOL and POPC:SM:CHOL bilayers in absence and presence of C8 peptide.

These results indicate that high concentrations of CHOL produce a strong effect on the lipid packing of phospholipids chains, reducing their mobility also in the terminal methyl region. This evidence confirms that CHOL causes, in the POPC bilayer, a transition from the liquid-disorder phase (L_d) to the liquid-ordered phase (L_o). In the case of bilayers formed by POPC:SM:CHOL, a similar situation was observed. The reduced mobility involves the 14PCSL spin-label and the spectrum also presents the second component, even though it is less evidence of that observed for POPC:CHOL 70:30 bilayer, as demonstrated by $2A_{\max}$ values reported in Table 4.3.2.

The effect of the presence of C8 peptide in the bilayer was studied by measuring NR curves of the fully hydrogenated lipids to which the peptide with deuterated Trp

residues was added. Four contrasts, D₂O, 4MW, SMW and H₂O, were used and the NR curves are shown in Figure 4.3.4A-D.

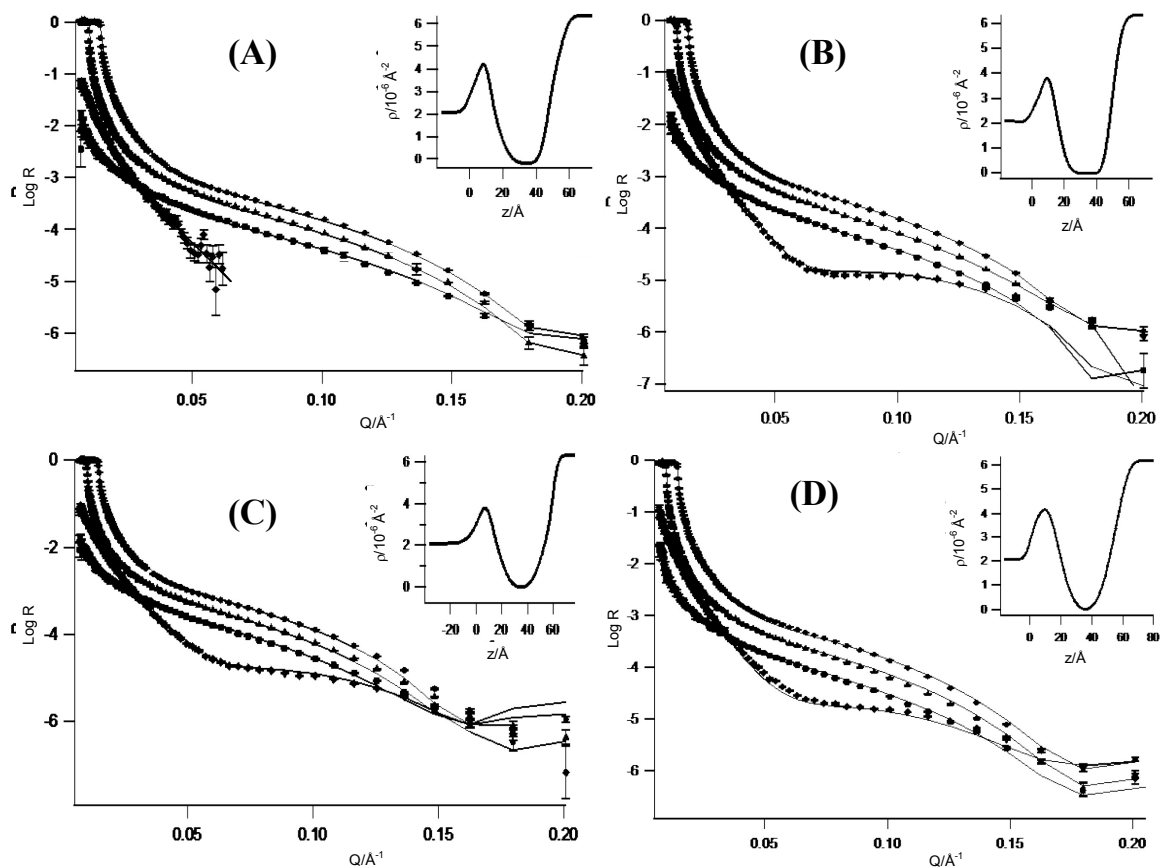


Figure 4.3.4- Neutron Reflectivity profiles (points) and best fits (continuous lines) corresponding to bilayers of (A) POPC:CHOL 90:10 wt/wt, (B) POPC:CHOL 80:20 wt/wt, (C) POPC:CHOL 70:30 wt/wt and (D) POPC:SM:CHOL 1:1:1 wt/wt/wt bilayers with C8-*d*₅₁ obtained in (●) D₂O, (▲) 4MW, (■) SMW and (◆) H₂O solvents. The insets show the ρ profiles for the bilayers in D₂O.

In the case of POPC:CHOL 90:10 and POPC:CHOL 80:20 bilayers, an additional layer with respect to the case of pure lipid models was necessary to obtain a good curves fitting. This layer prominently consists of the peptide interacting with the bilayer leaflet and it was characterized by a ρ value equal to $3.66 \times 10^{-6} \text{ \AA}^{-2}$, which corresponds to the theoretic value of the deuterated peptide [8]. For both lipid bilayers, the ρ of the external headgroups layer varies from $1.86 \times 10^{-6} \text{ \AA}^{-2}$ to $\sim 2 \times 10^{-6} \text{ \AA}^{-2}$, indicating that the presence of the peptide effectively perturbs the outer hydrophilic region of the two considered membranes. In contrast, no variations were observed in the ρ values corresponding to the

hydrophobic region and inner headgroup layer. The values of all parameters optimized in curves fitting are also reported in Table 4.3.1.

POPC:CHOL 90:10 mol/mol	interfacial layer	thickness (Å)	% solvent content	roughness (Å)
	water	3±1	100	3±1
	inner headgroups	6±1	30±10	3±1
	chains region	30±1	-	6±1
	outer headgroup	7±1	22±10	4±1
with C8	water	3±1	100	3±1
	inner headgroups	6±1	30±10	3±1
	chains region	30±1	-	6±1
	outer headgroup	5±1	36±10	4±1
	interacting peptide	5±1	60±10	5±1
POPC:CHOL 80:20 mol/mol	interfacial layer	thickness (Å)	% solvent content	roughness (Å)
	water	3±1	100	3±1
	inner headgroups	7±1	40±10	3±1
	chains region	31±1	-	5±1
	outer headgroup	7±1	35±10	3±1
with C8	water	3±1	100	3±1
	inner headgroups	7±1	30±10	3±1
	chains region	31±1	-	7±1
	outer headgroup	5±1	20±10	5±1
	interacting peptide	5±1	75±10	3±1
POPC:CHOL 70:30 mol/mol	interfacial layer	thickness (Å)	% solvent content	roughness (Å)
	water	3±1	100	8±1
	inner headgroups	9±1	35±10	5±1
	chains region	33±1	-	5±1
	outer headgroup	8±1	44±10	7±1
with C8	water	3±1	100	8±1
	inner headgroups	9±1	30±10	6±1
	chains region	33±1	-	5±1
	outer headgroup	8±1	35±10	7±1
POPC:SM:CHOL 1:1:1	interfacial layer	thickness (Å)	% solvent content	roughness (Å)
	water	5±1	100	5±1
	inner headgroups	8±1	40±10	3±1
	chains region	31±1	-	7±1
	outer headgroup	10±1	44±10	4±1
with C8	water	5±1	100	5±1
	inner headgroups	8±1	33±10	6±1
	chains region	30±1	-	7±1
	outer headgroup	7±1	42±10	5±1
	interacting peptide	5±1	80±10	4±1

Table 4.3.1 - Parameters derived from model fitting the reflectivity profiles for pure the lipid bilayers and after C8- d_{5all} addition.

Interestingly, the thickness and the solvent content of the model box of external headgroups layers are different with respect to the pure lipid bilayers. In particular, the thickness values of both layers corresponding to the polar headgroups slightly decrease from 7 ± 1 to 5 ± 1 Å, while the thickness of the additional peptide layer presents a thickness of 5 ± 1 Å. The more evident variations are observed for the solvent content values of outer headgroups layers that dramatically increase with respect to the cases of pure lipid bilayers. This increase is directly related to the peptide binding which effectively perturbs the external bilayer structure. In contrast, no changes occurred for the chains and inner headgroups layers, indicating that the interaction involves only the external bilayer leaflet in which the peptide adsorbs on the membrane surface.

In the case of POPC:CHOL 70:30, the best fit of NR profiles required only five model boxes and no particularly changes were observed in the values of all fitting parameters. This is a clear evidence that no interaction occurs between the considered lipid bilayer and C8 peptide. It is probably due to the particular bilayer micro-structural properties induced by the high content of cholesterol, which inhibits the membrane-peptide interaction.

Finally, NR profiles corresponding to the POPC:SM:CHOL bilayers were analyzed. Different changes were caused by the peptide addition. First, an additional layer with respect to the case of pure lipid models was necessary to obtain a good curves fitting. It consists of the peptide ($\rho_{\square} = 3.66 \times 10^{-6} \text{ \AA}^{-2}$). As observed for the bilayers with the lower content of cholesterol, the ρ of the external headgroups region increase to value $\sim 2 \times 10^{-6} \text{ \AA}^{-2}$, indicating an effect of C8 presence. Also in this case, no variations were observed in the ρ values corresponding to the hydrophobic region and inner headgroup layers. The thickness of external headgroups layer decreases from 10 ± 1 to 7 ± 1 Å, while its value for the layer corresponding to the peptide presence is equal to 5 ± 1 Å. This is an evidence of a surface interaction of the peptide. No significant changes occur in the solvent content and

roughness. Finally, no variations of fitting parameters corresponding to the inner bilayer leaflet, indicating that the membrane-peptide interaction involves only the external surface.

C8-membrane interaction was also investigated by ESR measurements. 5-PCSL spectra for the considered lipid systems were shown in Figure 4.3.2 (dashed lines). Figure 4.3.4 shows the dependence of the outer hyperfine splitting, $2A_{\max}$, on chain position, n , for the n -PCSL spin-labels in lipid membranes, with and without C8 peptide. For POPC:CHOL 90:10 bilayers, in the presence of C8, the characteristic flexibility gradient with chain position of the fluid lipid bilayer membranes is preserved, but $2A_{\max}$ is increased at 5 and 7 chain positions by the same extent (~ 2.2 G). For the 10-PCSL spectrum, a slight $2A_{\max}$ increase was observed while, for what concerns the spin-label presenting the nitroxide in a deeper position, 14-PCSL, no particular changes in the ESR spectrum were caused by the C8 addition (see Figure 4.3.3B). This is evidence that the peptide binds solely at the membrane surface and does not penetrate appreciably into the membrane interior. ESR results confirm that the only external bilayer leaflet was involved in the interaction with the peptide and that its surface association does not influence the phospholipids chains mobility, probably as a consequence of cholesterol presence which induces a higher order in the hydrophobic region.

Similar results were obtained in the case of POPC:CHOL 80:20 bilayers. In fact, also in this case, an increase of $2A_{\max}$ of 5-PCSL and 7-PCSL spectra was obtained while, for 10-PCSL and 14-PCSL, the same behaviour of the previous lipid system occurred. For POPC:CHOL 70:30 bilayer, no significant changes in all spin-labels spectra were caused by the C8 peptide addition, indicating no membrane-peptide interaction. This result suggests that the presence of an high content of cholesterol influences the bilayers microstructural properties so as to inhibit the interaction with the peptide. Finally, the POPC:SM:CHOL lipid bilayers are considered. In the presence of C8, significant perturbations in the spectra of all spin-labeled lipids are found. In particular, an high

increase of $2A_{\max}$ values was detected, as shown in Figure 4.3.4, indicating an interaction between the peptide and lipid bilayers.

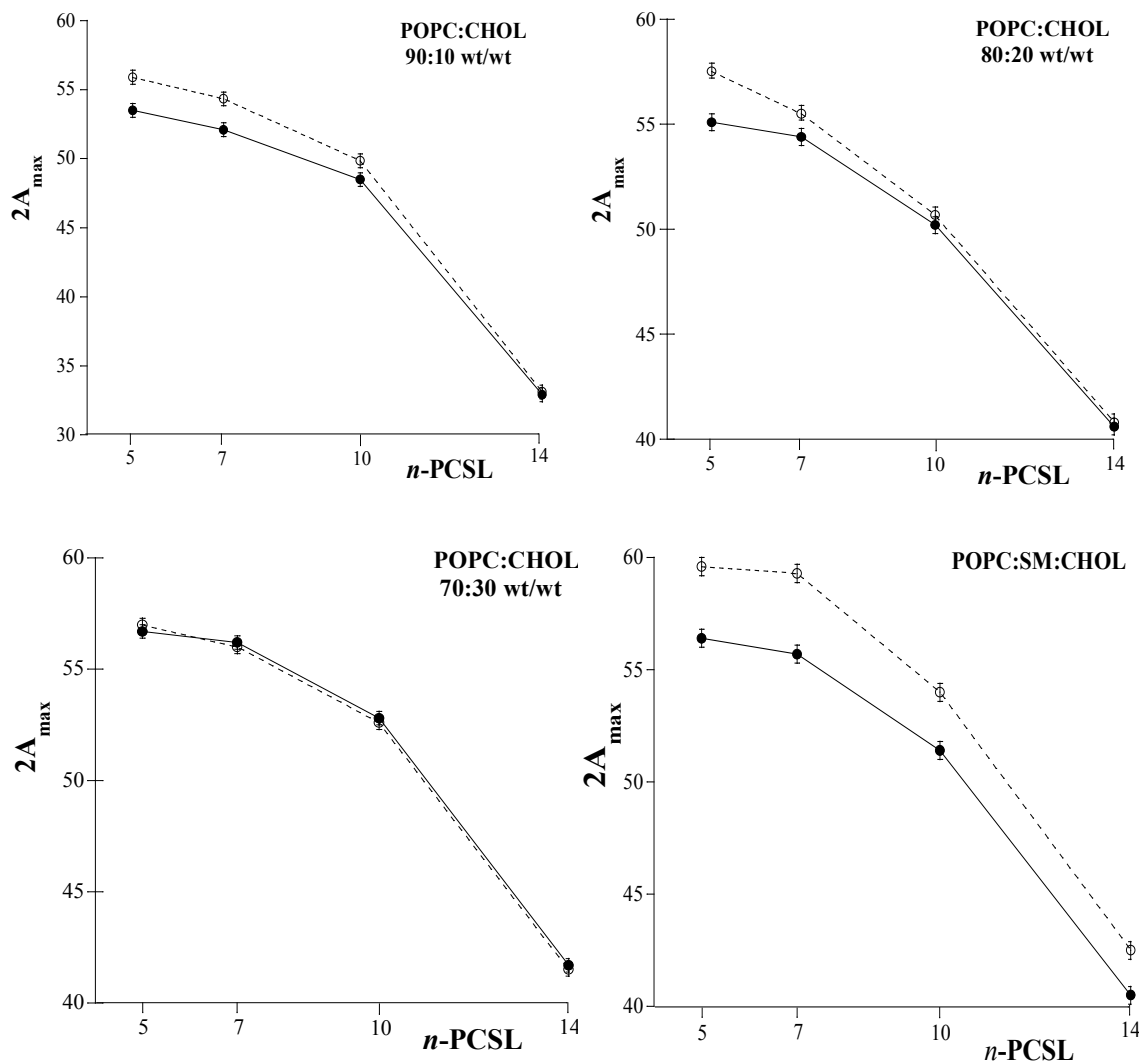


Figure 4.3.4 - Outer hyperfine splitting, $2A_{\max}$, of n -PCSL in bilayers of POPC:CHOL at 90:10 (\blacktriangle), 80:20 (\blacklozenge), 70:30 (\bullet) and POPC:SM:CHOL (\blacksquare) as a function of the nitroxide position, n , on the phospholipid acyl chains in absence (solid points) and presence (open points) of C8 peptide.

These results suggest that the presence of sphingomyelin determines specific microstructural properties of the membrane which favor the interaction with the peptide, confirming the idea of the a specific role of the lipids on influencing biological processes.

4.4 Interaction of the MPER domain of HIV gp41 with lipid bilayers

After the investigation on the behaviour of the peptide deriving from the MPER domain of FIV gp36, the attention was focused on the mechanism of action of the MPER domain of the HIV gp41 in the presence of biomembranes with different lipid composition.

Preliminarily, POPC membranes incorporating phosphatidylcholine spin-labeled on the *n* C-atom of the *sn*-2 chain (*n*-PCSL) were investigated. ESR spectra of *n*-PCSL are showed in Figure 4.4.1 (solid lines).

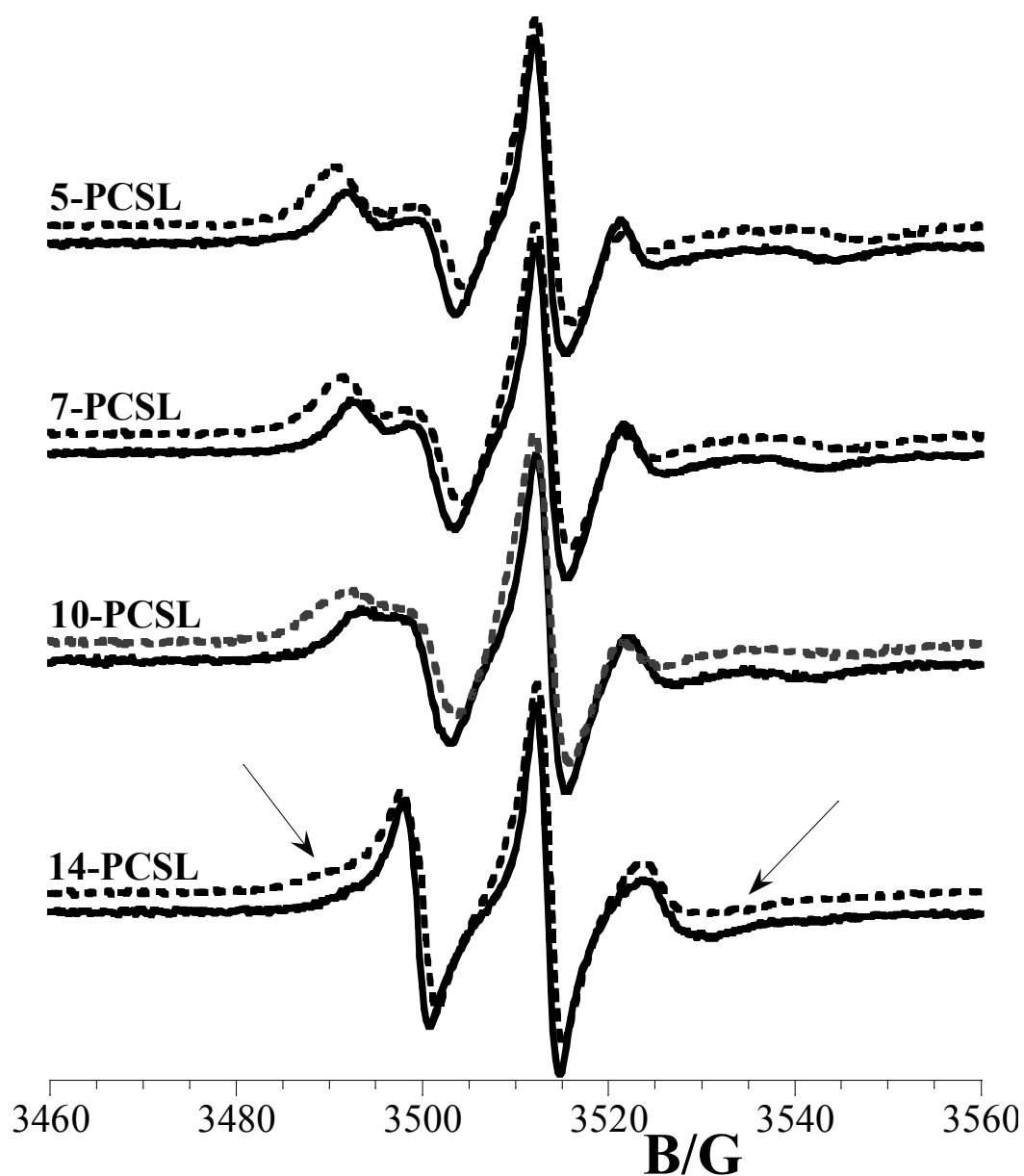


Figure 4.4.1 - ESR spectra of *n*-PCSL in POPC bilayers, in the absence (solid line) and in the presence (dashed line) of 1:1 wt/wt peptide.

In the case of 5-PCSL, which presents the nitroxide group close to the hydrophilic headgroup, the spectrum shows a clearly defined axially anisotropic lineshape. Spectra of 7-PCSL and 10-PCSL spin-labels also have an anisotropic lineshape, but this character is less evident as the nitroxide group is located close to the terminal methyl region of the chain. In fact, in this case of 14-PCSL a three-line, quasi-isotropic spectrum is obtained, see Figure 4.4.1 (lower spectrum, solid line). The higher isotropy of the 14-PCSL spectrum with respect to that obtained for 5-PCSL indicates a flexibility increase in segmental chain mobility in going from the polar headgroups to the inner hydrophobic core, which is a characteristic hallmark of the liquid-crystalline state of fluid phospholipids bilayers.

Association of the peptide to the phospholipid bilayers causes a significant variation in the ESR spectra of spin-labeled phospholipids. Particularly, the spin-labels presenting the nitroxide group in the positions $n = 5, 7, 10$ present a clearly $2A_{\max}$ increase, as shown in Figure 4.4.1 (dotted lines). Strikingly, for what concerns the 14-PCSL, the presence of the peptide causes the appearance of a second component in the ESR spectrum, see Figure 4.4.1 (lower spectrum, dotted line). This second component is resolved in the outer wings of the spectrum and corresponds to spin-labeled lipid chains whose motion is restricted. This is a feature already encountered for all the peptides and proteins which stably inserts in the lipid bilayer, such as integral membrane proteins [13]. The slow motional component is due to spin-labeled lipids participating to the “annular” structure surrounding the guest molecule, while the fluid component is due to relatively unperturbed spin-labels in bulk lipid. It is interesting to consider that in the case of peptides which adsorb on the membrane surface, we observe only an increase of $2A_{\max}$ value but no anisotropy in the spectrum of 14-PCSL [4].

All $2A_{\max}$ values corresponding to the ESR spectra of n -PCSL in pure POPC bilayers in the absence and in the presence of peptide are reported in Table 4.4.1. Figure 4.4.2 shows the dependence of the outer hyperfine splitting, $2A_{\max}$, on chain position for

the n -PCSL spin-labels in fluid POPC membranes, with and without the peptide. The values determined in the presence of the peptide are all greater than those determined in its absence, and they are approximately constant at about 56 ± 0.3 G. In the case of 14-PCSL spectrum, the second minimum is not well defined so the $2A_{\max}$ is not determined to avoid a very large experimental error.

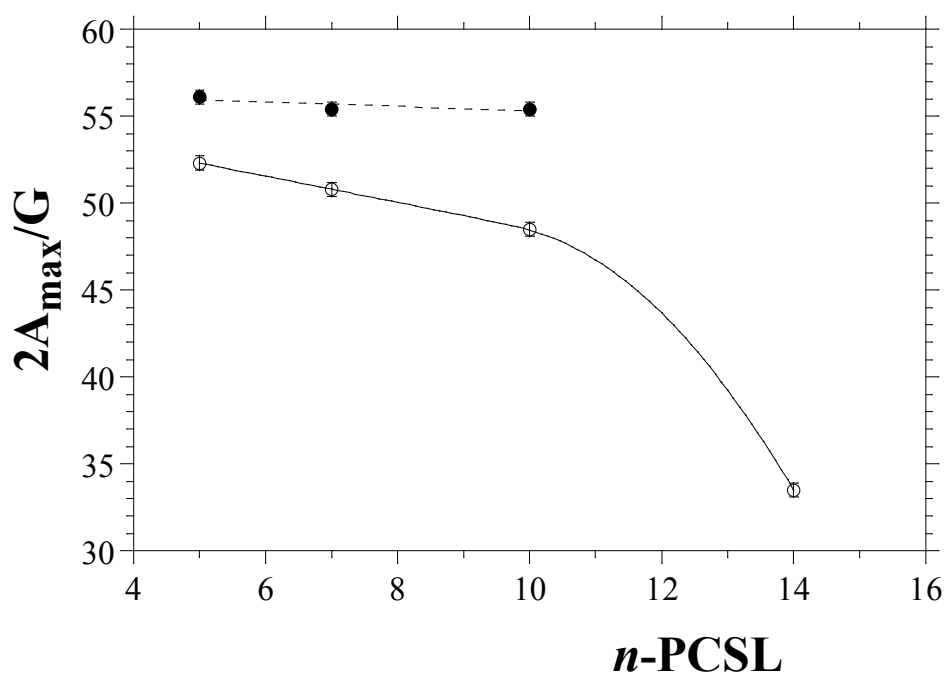


Figure 4.4.2 - Dependence on spin-label position, n , of the outer hyperfine splitting, $2A_{\max}$, of the n -PCSL phosphatidylcholine spin labels in POPC membranes in the absence (*open circles*) and presence (*solid circles*) of 1:1 (wt/wt) peptide.

n -PCSL	$2A_{\max}$ (G)			
	POPC	POPC + Peptide	POPC:SM:CHOL	POPC:SM:CHOL + Peptide
5-PCSL	52.4 ± 0.3 G	56.1 ± 0.3 G	55.6 ± 0.1 G	59.5 ± 0.1 G
7-PCSL	51.6 ± 0.3 G	55.4 ± 0.3 G	52.9 ± 0.1 G	59.9 ± 0.1 G
10-PCSL	48.7 ± 0.3 G	55.4 ± 0.3 G	48.8 ± 0.1 G	59.4 ± 0.1 G
14-PCSL	33.5 ± 0.3 G	—	40.1 ± 0.1 G	53.0 ± 0.1 G

Table 4.4.1 - $2A_{\max}$ values of n -PCSL in POPC and POPC:SM:CHOL bilayers in the absence and presence of the peptide, obtained from ESR measurements.

To better explore the effect of the peptide interaction on the bilayer structure, spectra of 5-PCSL at 0.5:1 and 0.2:1 wt/wt peptide/lipid ratios were also recorded. The values of $2A_{\max}$ are showed in Figure 4.4.3. A careful analysis of the figure suggests that the $2A_{\max}$ stabilizes to value of 56G at the 0.6:1 wt/wt peptide/lipid ratio. From this saturation value, it was estimated that one peptide molecule interacts with two POPC molecules. This value is much lower than that obtained by the same method for peptides derived from gp36 of FIV. This can be interpreted as being due to the different modes of interaction (insertion of the peptide against its surface adsorption), and/or to the peptide autoaggregation. This second hypothesis is supported by an extensive literature showing the formation of a trimers.

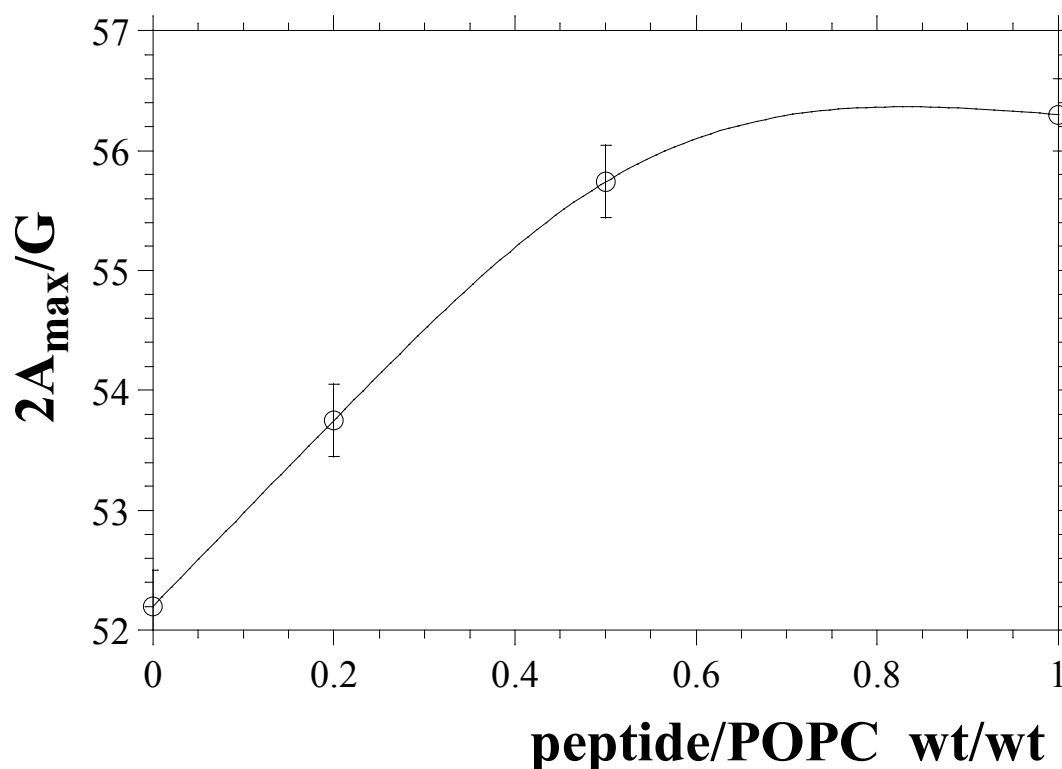


Figure 4.4.3 - Dependence on peptide/POPC ratio of the outer hyperfine splitting, $2A_{\max}$, of the 5-PCSL.

The second lipid system studied is a liposomal suspension consisting of POPC, SM and CHOL at 1:1:1 wt/wt/wt ratio. This lipid mixture is used as a model of domains of

hard cell membrane, commonly referred to as lipid rafts, which are characterized by a very high content of cholesterol and sphingomyelin. In this case, the spectra of all spin-labels present a clear anisotropy, as showed in Figure 4.4.4.

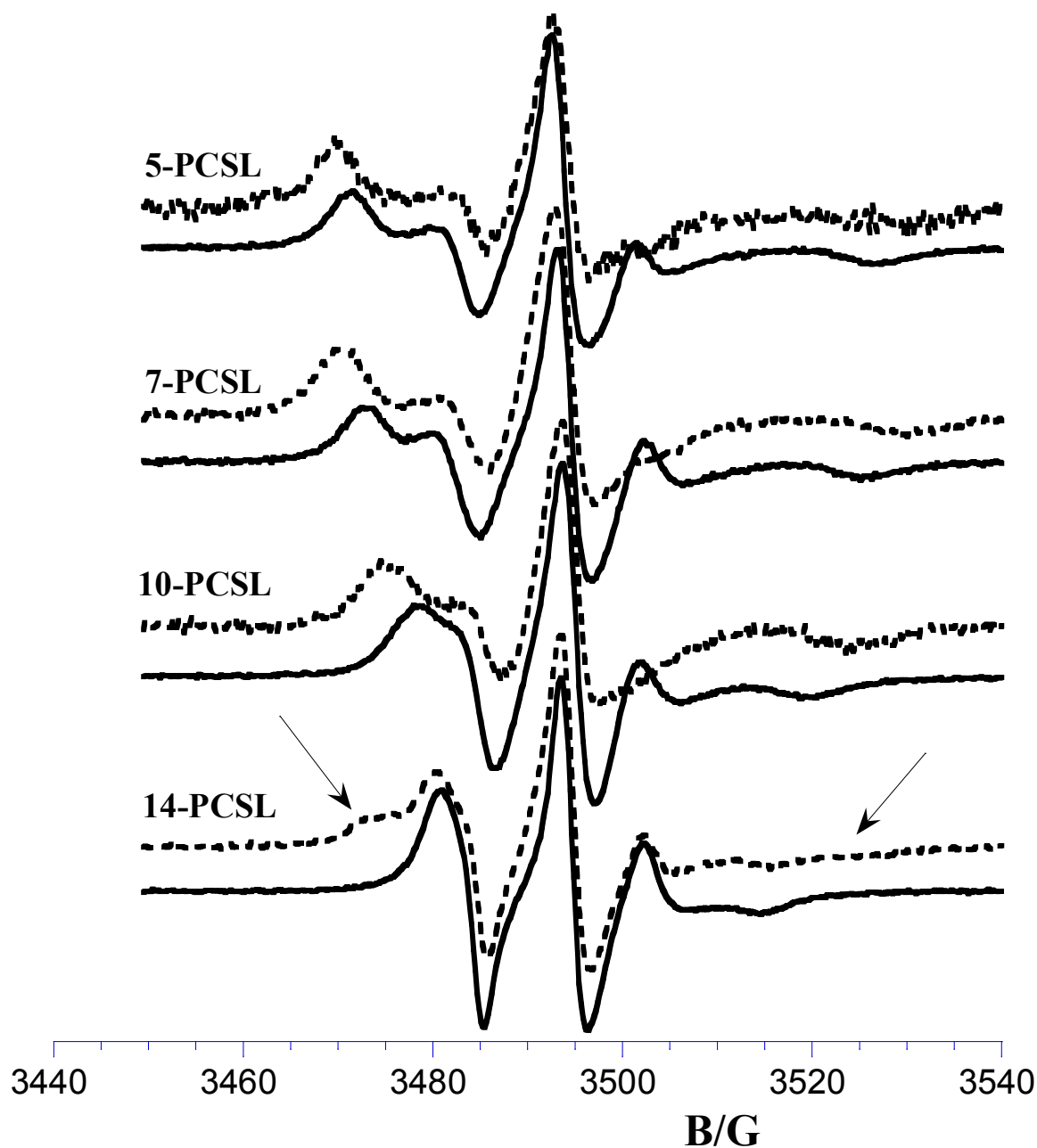


Figure 4.4.4 - ESR spectra of *n*-PCSL in POPC:SM:CHOL bilayers, in the absence (solid line) and in the presence (dashed line) of 1:1 wt/wt peptide.

The evidence that the spin-label 14-PCSL presents a restriction of its motion freedom is due to fluid liquid crystalline order of the lipid bilayer which is much more rigid than the pure POPC bilayer. The corresponding $2A_{\max}$ values are summarized in

Table 4.4.1 and indicating an increasing flexibility of membrane from the hydrophilic surface to the hydrophobic inner core.

In the presence of the peptide, a clear broadening of the all spin-labels spectra was observed, as shown in Figure 4.4.4. Particularly, in the 14-PCSL spectrum a slow motion component appears and, as to the pure POPC, it is highlighted by a shoulder in the low-field maximum and by an additional high-field minimum. In this case, it was possible to determine the $2A_{\max}$ value. For all spin-labels, the presence of peptide causes a large increase of $2A_{\max}$, but the values corresponding to the 5, 7 and 10-PCSL spectra are quite similar, as well shown in Figure 4.4.5. These findings indicate that the peptide hardly penetrate into the lipid bilayer.

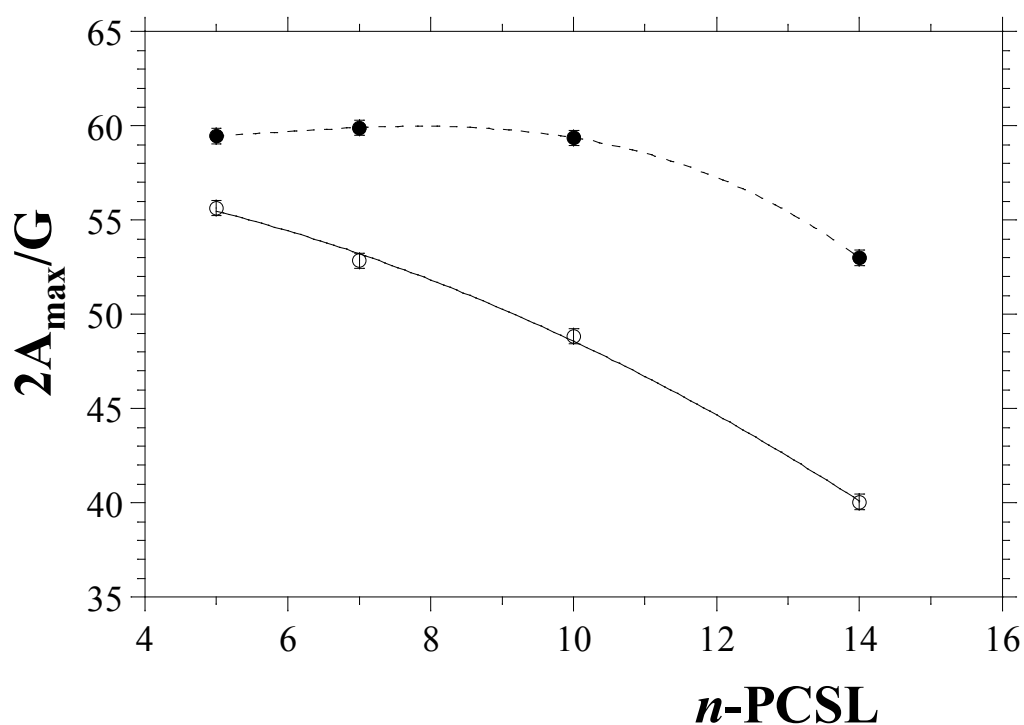


Figure 4.4.5 -Dependence on spin-label position, n , of the outer hyperfine splitting, $2A_{\max}$, of the n -PCSL phosphatidylcholine spin labels in POPC:SM:CHOL membranes in the absence (*open circles*) and presence (*solid circles*) of 1:1 (wt/wt) peptide.

ESR spectra at several peptide/lipid ratios were also recorded. Particularly, 0.1:1, 0.2:1, 0.5:1 and 0.7:1 wt/wt ratios are considered. The increase of the outer hyperfine splitting observed in the 5-PCSL spectra is not gradual, as shown in Figure 4.4.6. An initial

increase in the $2A_{\max}$ is clear up to about 0.2:1 wt/wt peptide/lipid ratio, when it gets to a plateau. $2\Delta A_{\max}$ with respect to the pure lipid bilayer is just over 3 G, which is comparable to the increase found in the case of pure POPC.

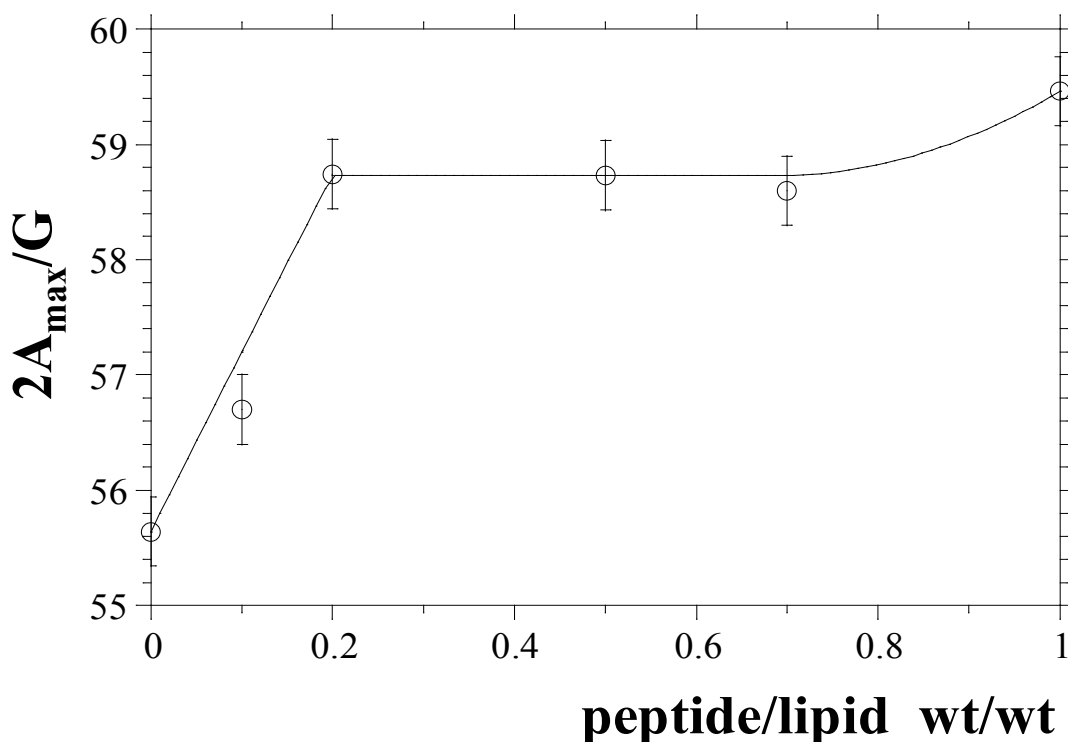


Figure 4.4.6 - Dependence on peptide/POPC:SM:CHOL ratio of the outer hyperfine splitting, $2A_{\max}$, of the 5-PCSL.

This evidence suggests a similarity between the peptide-lipid interaction modes in the two cases. The main difference is that the plateau for the pure POPC bilayer requires at high peptide concentration, while a less concentration is necessary in the case of POPC:SM:CHOL mixture. In this condition, one peptide molecule interacts with ~ 20 lipid molecules. This is probably due to the increasing bilayer rigidity which allows to smaller number of peptide molecules to insert in it.

As an integration of the microscopic investigation realized by ESR experiments, a study of the effect of the MPER domain on the lipids mesoscopic organization was performed by DLS measurements.

Figure 4.4.7 shows the hydrodynamic radius distribution functions obtained at 90° from inverse Laplace transform of the intensity correlation functions $g^{(2)}(t)-1$ for the two aqueous systems containing the pure POPC liposomes in the absence and in the presence of peptide.

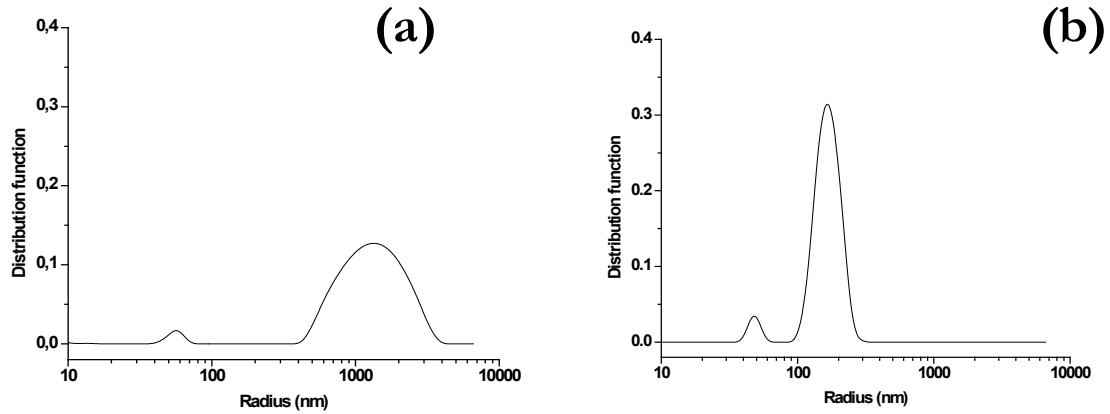


Figure 4.4.7 - Hydrodynamic radius distribution functions by means of DLS measurements for POPC vesicles in the absence **(a)** and in the presence **(b)** of the peptide.

Indeed, this procedure leads to the distribution of the particles' diffusion coefficients. However, provided that the solutions are quite dilute, the Stokes–Einstein equation, which rigorously holds at infinite dilution for spherical species diffusing in a continuum medium, may legitimately be used to evaluate the hydrodynamic radius R_H of the aggregates:

$$R_H = \frac{k_B T}{6\pi\eta D} \quad (5.4.1)$$

where k_B is the Boltzmann constant, T is the absolute temperature, and η is the medium viscosity. From Figure 4.4.7, it is possible to note that POPC forms aggregates with a broad distribution of hydrodynamic radius, centred on about 1000 nm, size compatible with the presence of multilamellar liposomes. Our results are in fairly good agreement with

those reported in the literature [16]. In the presence of the peptide, the distribution function assumes a bimodal pattern. Two population of aggregates with smaller hydrodynamic radii are obtained: a first peak is centred around 70 nm and the second is at 100 nm. A possible interpretation of this evidence is the coexistence of two populations formed by monolamellar vesicles and/or ellipsoidal micelles. This effect indicates that the destabilization of the microscopic phospholipid bilayer structure caused by the peptide also influences the mesoscopic organization. Therefore, the peptide has the ability to disrupt the phospholipids aggregates in line with its biological function within gp41. Figure 4.4.8 shows the hydrodynamic radius distribution functions obtained at 90° for the aqueous systems containing the POPC:SM:CHOL liposomes in the absence and in the presence of the peptide. The used solutions had a concentration of $5 \times 10^{-5} \text{M}$.

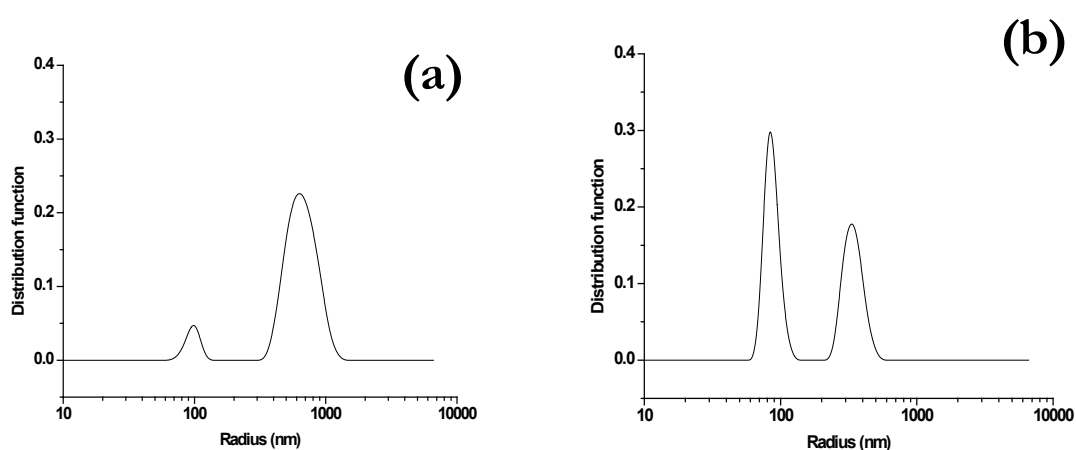


Figure 4.4.8 - Hydrodynamic radius distribution functions by means of DLS measurements for POPC:SM:CHOL vesicles in the absence (a) and in the presence (b) of the peptide.

In the absence of peptide, a bimodal distribution of aggregates with a broad peak centred at about 700 nm and a second one at about 100 nm is obtained. The first signal is in agreement with the presence of multi lamellar vesicles, while the second peak could be due to unilamellar vesicles or ellipsoid micellar aggregates. In the presence of the peptide, it is possible to note the presence of the same peaks observed in the absence of peptide, but with a clear variation of the relative population in which the smaller aggregates are more

abundant. The effect of the peptide is similar to the case previously studied. In fact, we find the same effect of reducing the size of the aggregates with respect to original liposomal system. The difference between the sizes of the aggregates can be noted also at the macroscopic level: the solution containing the peptide appears clear, differently from the solution containing only the lipid suspension.

These results indicate a strong destabilizing effect of the MPER domain on lipid systems: it causes a order loss in the lipid bilayers which also influences the mesoscopic organization.

4.5 Interaction of peptides deriving from different domains of HSV-1 gH and gB glycoproteins with lipid membranes

The attention was then focused on the behavior of different peptides corresponding to the known membrane interacting regions of HSV-1 fusion glycoproteins gH and gB, namely gH626-644, gH776-802, gB168-186 and gB632-650 [13]. The peptide sequences are indicated in Table 4.5.1. In particular, gH626-644 has been previously identified as the putative fusion peptide of gH [17], while gH776-802 corresponds to the pre-transmembrane domain of gH and has been shown to interact significantly with liposomes and thus to be involved in the fusion process [18]. gB168-186 of HSV gB has been identified by other methodologies as a fusion peptide [19], while gB632-650 has also been previously shown to interact with membranes and to have a significant inhibitory activity [20]. As control peptides we used the fusion peptide of HIV and melittin, a cationic antimicrobial peptide; the HIV fusion peptide was selected to determine the behaviour of a peptide able to stably interact with membranes at a certain depth, while melittin was selected as being responsible of the formation of pores through the bacterial membrane.

<i>Name</i>	<i>Sequence</i>
HSV peptides	
gH626-644	GLASTLTRWAHYNALIRAF
gH776-802	STALLFPNGTVIHLLAFDTQPVAIA
gB168-186	VTVSQVWFGHRYSQFMGIF
gB632-650	PCTVGHRRYFTFGGGYVYF
Control peptides	
gp41-FP	AVGIGALFLGFLGAAGSTMGARS
melittin	GIGAVLKVLTTGLPALISWIKRKRQQ

Table 4.5.1 - Peptide sequences

The ESR spectroscopy, by using phosphatidylcholine spin-labeled at different positions, n , in the sn -2 chain (n -PCSL, $n = 5, 7, 10, 14$) incorporated in PC/CHOL membranes (55/45 w/w), in the presence of the peptides. Preliminarily, the spectra in the absence of the peptides were also registered. Inspection of Figure 4.5.1 shows that all the spectra present a clearly defined axially anisotropic lineshape, an evidence that, due to the high cholesterol content, the PC/CHOL bilayer is in the liquid-ordered state.

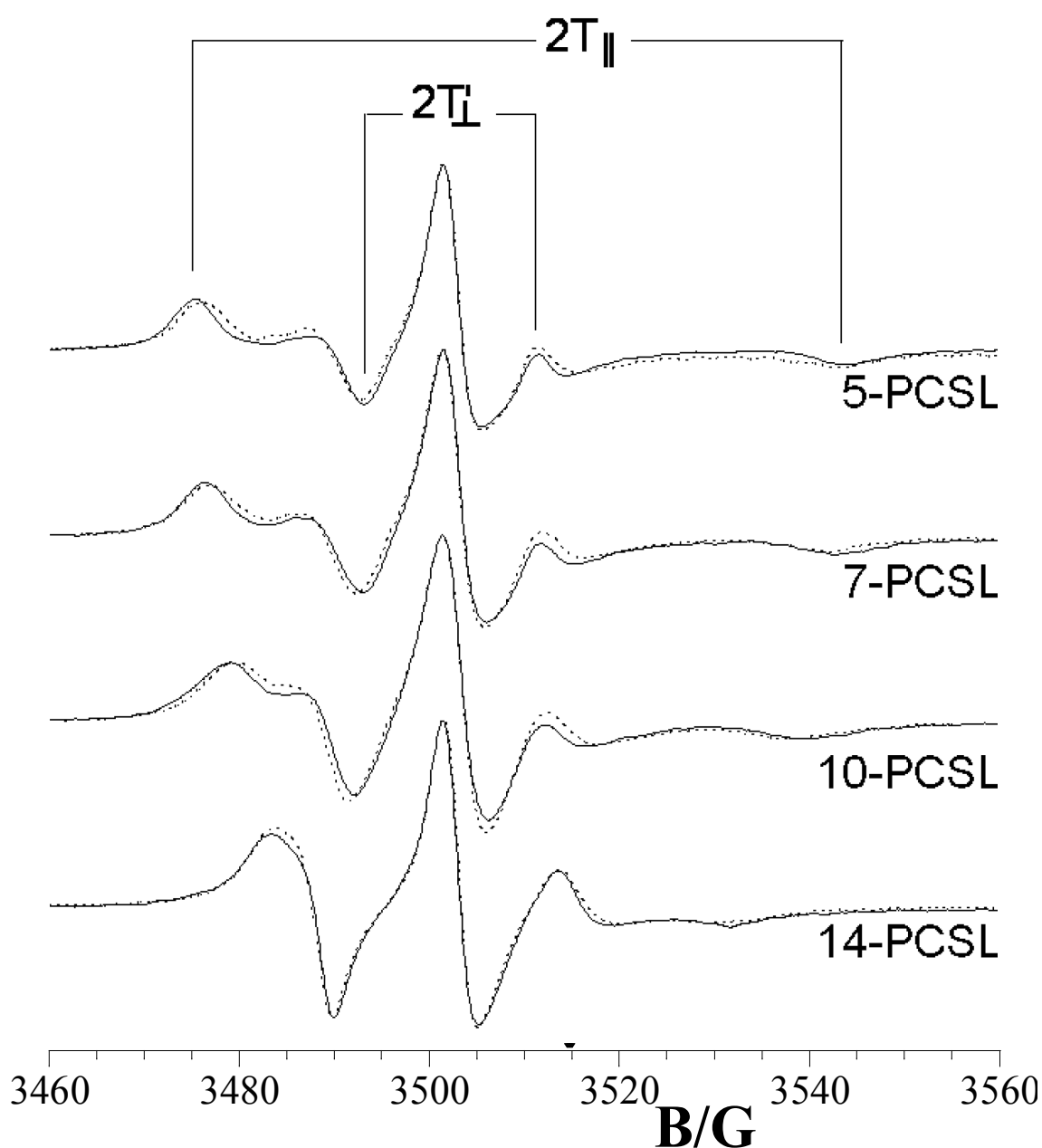


Figure 4.5.1 – ESR spectra of n -PCSL positional isomers in PC/CHOL membranes in presence (solid line) and absence (dashed line) of gH626-644.

In an attempt to quantitatively analyze the spectra, the order parameter, S , was calculated according to the relation:

$$S = \frac{(T_{\parallel} - T_{\perp}) a_{\text{N}}}{(T_{\text{zz}} - T_{\text{xx}}) a'_{\text{N}}} \quad [4.5.1]$$

where T_{\parallel} and T_{\perp} are two phenomenological hyperfine splitting parameters which can be determined experimentally for each spin-labeled phospholipid as shown in Figure 4.5.1 (note that $2T'_{\perp} = 2T_{\perp} - 1.6$). T_{xx} and T_{zz} are the principal elements of the real hyperfine splitting tensor in the spin Hamiltonian of the spin-label, which can be measured from the corresponding single-crystal ESR spectrum and are reported in the literature ($T_{\text{xx}} = 6.1$ G and $T_{\text{zz}} = 32.4$ G). a_{N} and a'_{N} are the isotropic hyperfine coupling constants for the spin-label in crystal state and in the membrane, respectively, given by:

$$a_{\text{N}} = \frac{1}{3}(T_{\text{zz}} + 2T_{\text{xx}})$$

$$a'_{\text{N}} = \frac{1}{3}(T_{\parallel} + 2T_{\perp})$$

The isotropic hyperfine coupling constant is an index of the micropolarity experienced by the nitroxide, and the $a_{\text{N}}/a'_{\text{N}}$ ratio in eq. 4.5.1 corrects the order parameter for polarity differences between the crystal state and the membrane. Both S and a'_{N} decrease progressively with increasing n , as the spin-label position is stepped down the chain toward the center of the membrane, see Figure 4.5.1. The S variation is an evidence of the flexibility gradient in segmental chain mobility, indicating that the lipid bilayer presents a relatively rigid surface and rigid interior. The a'_{N} decrease is related to the polarity gradient, indicating that the hydrophobicity increases as the nitroxide group moves to the center of the bilayer. Association of peptides to the lipid bilayer causes significant variation in the ESR spectra of spin-labeled phospholipids. As an example, Figure 4.5.2 gives the ESR spectra of n -PCSL in PC/Chol bilayer membranes, in the presence and

absence of gH626-644 at a lipid:peptide molar ratio of 10/1. The presence of the gH626-644 induces slight but significant changes in the spin-labels ESR spectra, which are mainly detectable from the low- and high-field components position and lineshape. In an attempt to quantify these evidences, the S and a'_N values were determined. Figure 4.5.2 shows the dependence of these parameters on chain position, n , for the n -PCSL spin labels in PC/Chol membranes, in the absence and in the presence of the peptides. In all cases, the flexibility and polarity gradients with chain position of the lipid bilayer membranes are preserved.

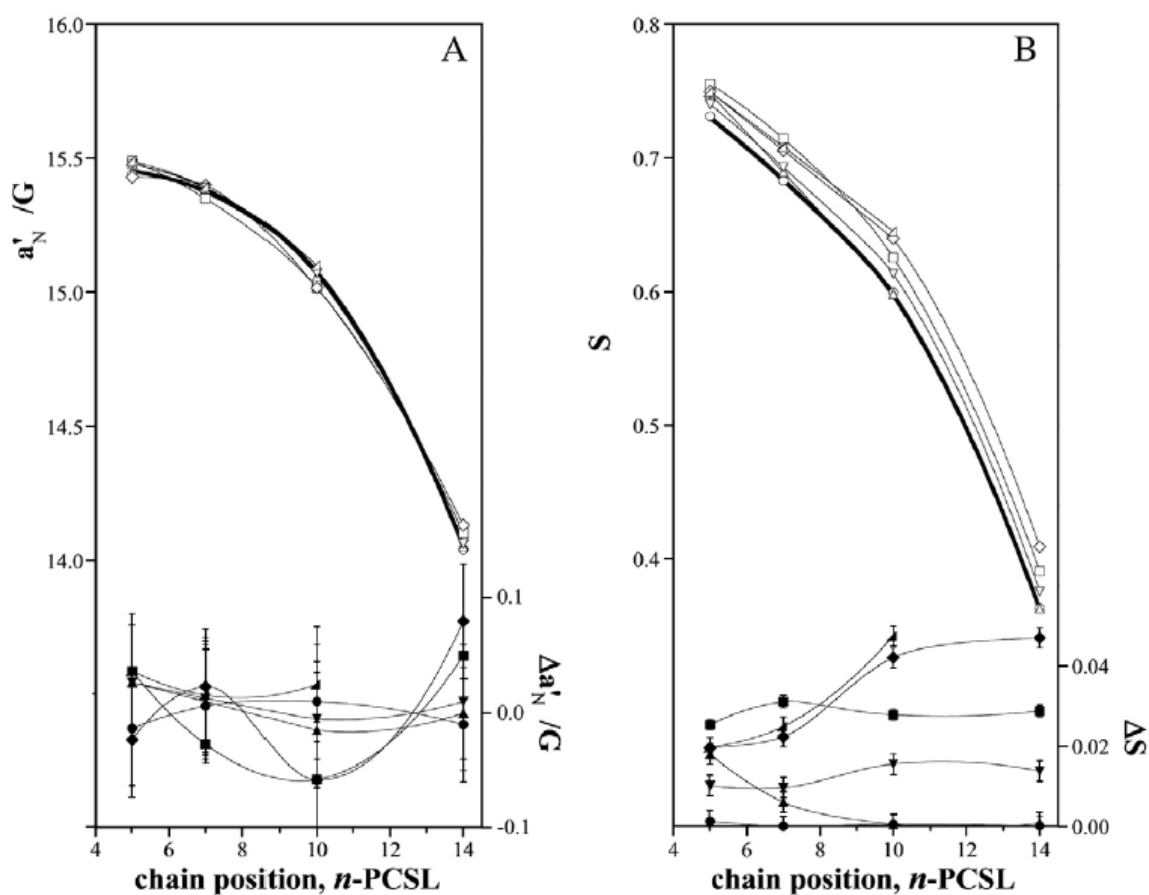


Figure 4.5.2 – Dependence on spin-label position, n , of the isotropic hyperfine coupling constant, a'_N (panel A, left-hand ordinate), and of the order parameter, S (panel B, left-hand ordinate), of the n -PCSL in PC/CHOL in the absence (bold line) and in the presence of gH626-644 (\square), gH776-802 (\circ), gB168-186 (Δ), gB632-650 (\diamond), melittin (∇), or gp41-FP (\triangleleft), $T=25$ °C. Variation of a'_N (panel A, right-hand ordinate), and S (panel B, right-hand ordinate) with respect to the unperturbed bilayer, on adding gH626-644 (\blacksquare), gH776-802 (\bullet), gB168-186 (\blacktriangle), gB632-650 (\blacklozenge), melittin (\blacktriangledown) or gp41-FP (\blacktriangleleft) to the membrane.

Concerning a'_N , it appears that its value is only marginally affected by the peptides, i.e., no evident variation in the local polarity is detectable. In contrast, inspection of the panel A of the figure reveals significantly different behaviour of the lipid chain mobility in the presence of the various peptides. In the same figure the S variation with respect to the value determined in the absence of any peptide, ΔS , is also reported. In the case of gH776-802, addition of peptide does not significantly affect the S value at any chain position. In the case of gB168-186, ΔS decreases - almost tending to zero - with increasing n . gH626-644 causes an increase in S to a comparable extent at all chain positions. The perturbations due to gB632-650 increase with n . This indicates that the increase in lipid packing density, which is induced by insertion of gH626-644, and even more by that of gB632-650, propagates down the chain more effectively than for the other peptides.

It is interesting to compare these results with those obtained for the two reference peptides, namely gp41-FP and melittin. In the case of gp41-FP, the spin-labels presenting the nitroxide group in position $n=5,7,10$ present a clearly detectable S increase, as shown in Fig. 4.5.2. Strikingly, for what concerns the spin-label presenting the nitroxide in a deeper position, 14-PCSL, the presence of gp41-FP causes the appearance of a second component in the ESR spectrum, see Figure 4.5.3. The second component is resolved in the outer wings of the spectrum and corresponds to spin-labelled lipid chains whose motion is restricted. This is a feature already encountered for all the peptides and proteins which stably inserts in the lipid bilayer, such as integral membrane proteins. The slow motional component is due to spin-labelled lipids participating to the “annular” structure surrounding the guest molecule, while the fluid component is due to relatively unperturbed spin-labels in bulk lipid. Thus, we can conclude that gp41-FP deeply inserts into the lipid bilayer. A similar experimental evidence has been found by Curtain et al. for the same peptide in egg yolk phosphatidylcholine [21]. In this context, it is relevant to note that the

same authors, by analysing ESR spectra of spin-labelled gp41-FP in lipid bilayers, concluded that the membrane-bound peptide could self-aggregate [22].

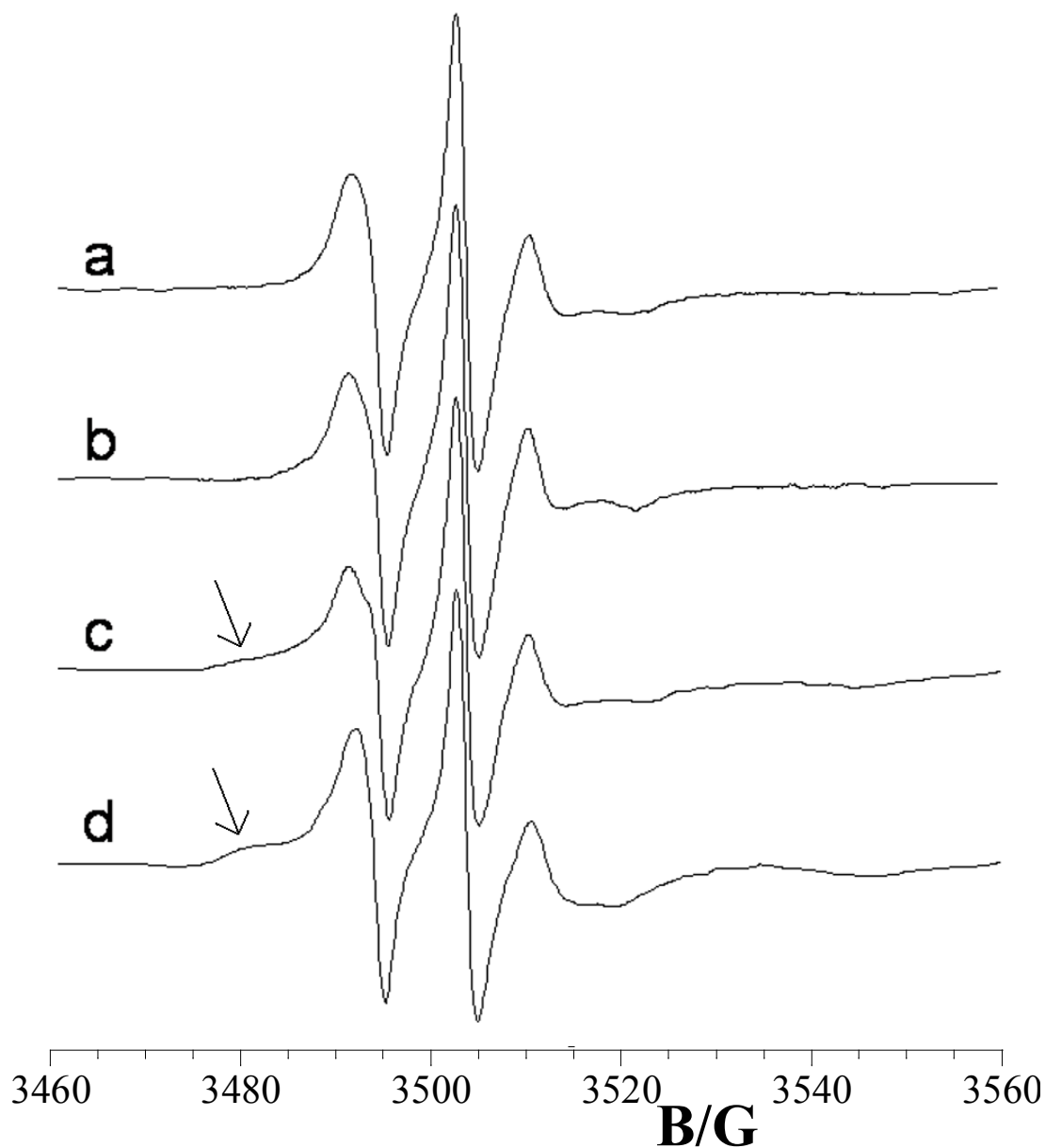


Figure 4.5.3 – ESR spectra of 14-PCSL positional isomers in PC/CHOL membranes in the absence (A) and presence of gH626-644 (B), gB632-650 (C) and gp41-FP (D). Arrows indicate the position of the second, more immobilised, spectral component.

In presence of melittin, the S increases to a comparable extent at all chain positions, similarly to that already reported in the literature by using different lipid bilayers [23]. However, no second component in the ESR spectra can be observed, at any n position of the spin label acyl chain. This evidence has been found in all cases where peptides or

proteins interact with the more external part of the bilayer, inducing a lipid chain perturbation that propagates to the inner part of the membrane [24]. Interestingly, these results are similar to those obtained for the C8 peptide derived from MPER region of the FIV gp36, which induces a destabilization of lipid bilayers [1,4], thus supporting the view that ESR alone is unable to discriminate between lytic and membranotropic domains.

Analysis of Figure 4.5.3 shows that, while gH626-644 only causes an enlargement of the spacing between the two more external signals, i.e. a *S* increase, in the case of gB632-650 the appearance of a shoulder at low field and of a broad minimum at high field suggest a behaviour more similar to that of gp41-FP. Thus, these experimental evidences indicate that gH626-644 interacts with the lipid bilayer being located in the more external part of it. In contrast, gB632-650 deeply penetrates in the bilayer, stably inserting into its inner region.

A tryptophan residue naturally present in the sequence of a protein or a peptide can serve as an intrinsic probe for the localization of the peptide within a membrane. Peptides gH626-644 and gB168-186 contain a tryptophan residue in the middle of the sequence; in particular it is the 9th residue in gH626-644 and the 7th residue in gB168-186. The fluorescence emission of a tryptophan residue increases when the amino acid enters a more hydrophobic environment, and together with an increase in quantum yield, the maximal spectral position is expected to be shifted toward shorter wavelengths (blue shift). Figure 4.5.4 shows the fluorescence emission spectra of the peptides gH626-644 and gB168-186 upon interaction with PC/Chol vesicles. In both cases changes in the spectral properties of the peptides were observed, suggesting that the tryptophan residue of the two peptides are located in a less polar environment upon interaction with lipids.

Furthermore, the position of the peptides inside the bilayer can be investigated by measuring the relative quenching of the fluorescence of the trp residue by the probes 11,12-Br-PC, 9,10-Br-PC and 6,7-Br-PC, which differ in the position of the quencher

moiety along the hydrocarbon chain and permit to establish the depth of the peptide in the membrane by comparing the quenching results obtained with each of them. 6,7-Br-PC is a better quencher for molecules near or at the interface, while the other two are better probes for molecules buried deeply in the membrane. With both peptides the largest quenching of tryptophan fluorescence was observed with 11,12- Br-PC vesicles (Table 4.5.1). Slightly less quenching was observed with 9,10-Br-PC, and 6,7-Br-PC. These results indicate that, upon binding to vesicles, the peptides were inserted into the membrane bilayer.

Lipid	Peptides	
	gH626-644	gB168-186
PC/Chol	100	100
6,7-BrPC/Chol	84±5	66±7
9,10-BrPC/Chol	68±3	76±8
11,12-BrPC/Chol	64±4	51±6

The fluorescence is reported as a percentage of the fluorescence in PC/Chol, standard deviations are calculated on three independent measurements

Table 4.5.1 - Fluorescence intensity of peptides in bromolipid vesicles

Since the structural conformation of peptides has been shown in many cases to correlate with fusogenic activity, and to understand whether secondary structure induction contributes to the initial stages of peptide binding, the secondary structure of the four HSV peptides and of the two control peptides in buffer and in PC/Chol 55/45 SUVs was determined by CD spectroscopy. As reported in literature [25], fusion peptides may change their secondary structure at different peptide/lipid ratios, in particular, they may show a beta and/or oligomeric structure at high peptide/lipid ratios, while they may assume an α -helical structure at low peptide/lipid ratios.

The secondary structure measurements for each peptide were thus performed at two different peptide/lipid ratios; in particular, we used a molar ratio of 0.1 (low peptide/lipid ratio) and a ratio of 0.5 (high peptide/lipid ratio). The ratio of 0.5 was tested because in this

condition we could clearly evidence a high fusion activity for all the peptides. All the spectra shown in Figure 4.5.5 for the 6 peptides are indicative of the formation of substantial secondary structure in PC/Chol. The melittin shows an helical spectrum in buffer and at both ratios with minima at 222 nm and 208 nm.

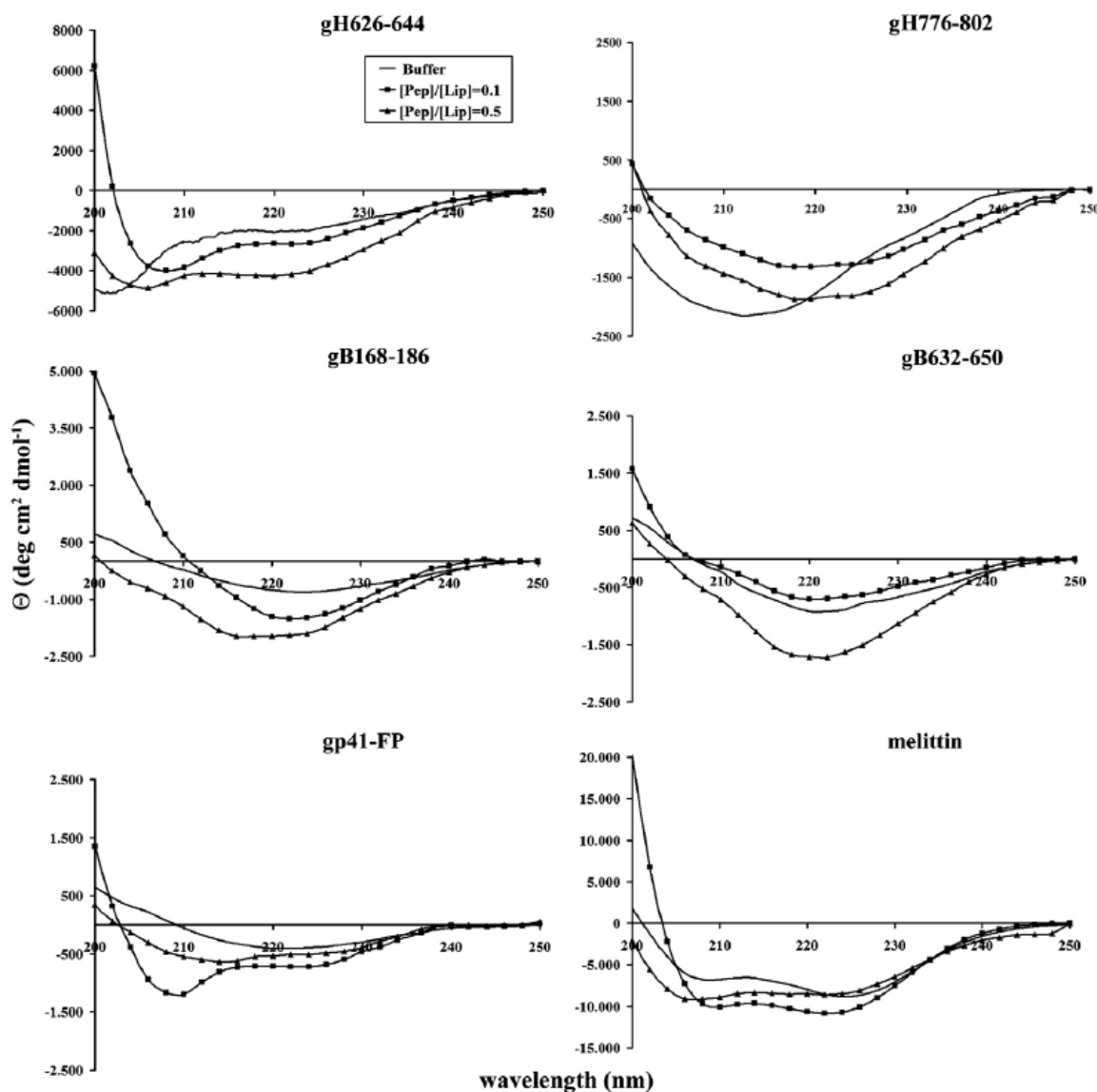


Fig. 8. Circular dichroism spectra of peptides in buffer and in PC/Chol at different peptide/lipid (mole/mole) ratios.

Figure 4.5.5 – Circular dichroism spectra of peptides in buffer and in PC/CHOL at different peptide/lipid (mol/mol) ratios.

The spectra for the peptide gp41-FP is consistent with the formation of a predominantly β -sheet conformation at high peptide/lipid ratios and an helical structure at low peptide/lipid ratios, as already reported for this peptide at the same ratios [25]. The

spectra for the peptide gH626-644 is consistent with a predominantly α -helical conformation. All the other peptides show spectra consistent with a predominantly β -sheet conformation in the condition tested.

The ratio of the ellipticities at 222 nm and 208 nm can be utilised to distinguish between monomeric and oligomeric states of helices [26]; when the ratio $\theta_{222}/\theta_{208}$ equals about 0.8, the peptide is in its monomeric state, and when the ratio exceeds the value of 1.0 is in its oligomeric state. The data reveal that the ratio $\theta_{222}/\theta_{208}$ for melittin is 1.3 in buffer, is 1.1 at a peptide/lipid ratio of 0.1 and is 0.96 at 0.5, clearly indicating that the monomer/oligomer equilibrium is shifted toward the oligomeric state. The ratio $\theta_{222}/\theta_{208}$ for gH626-644 is 0.67 at a peptide/lipid ratio of 0.1 and is 0.85 at 0.5, clearly indicating that the monomer/oligomer equilibrium is shifted toward the monomeric state.

4.6 Interaction of gH626-644 and gB632-650 peptides deriving from gH and gB glycoproteins with biomembranes

As demonstrated by the previous experiments, the peptides gH626-644 and gB632-650, deriving from HSV-1gH and gB glycoproteins, interact strongly with lipid bilayers and are the most fusogenic fragments of the native proteins. For this reason, our interest has focused on the mechanism of action of these two peptides in the presence of membranes with different lipid composition [27].

Because the peptide-lipid interaction can depend upon the state (gel or fluid phase) of the lipid bilayer, we performed a systematic temperature dependence. The samples investigated were phosphatidylcholine spin-labeled on the 5-C atom of the *sn*-2 chain (5-PCSL) incorporated in DMPC membranes, and correspondingly spin-labeled phosphatidylglycerol (5-PGSL) in DMPG membranes, in the presence and absence of the peptides gH626-644 or gB632-650. Selected ESR spectra from the zwitterionic lipid samples are shown in Figure 4.6.1; significant perturbations by the peptides are detected (compare solid and dashed lines). Figure 4.6.2 shows the temperature dependence of the outer hyperfine splitting, $2A_{\max}$, of 5-PCSL in DMPC membranes and of 5-PGSL in DMPG membranes. For DMPC alone (Figure 4.6.2A, solid line), a sharp decrease in $2A_{\max}$ is evident at ca. 25 °C, corresponding to the increase in lipid chain mobility on transition from the gel to the fluid phase of the DMPC bilayer. Addition of 1:1 wt/wt peptide (gH626-644 or gB632-650) with respect to lipid significantly affects the trend in $2A_{\max}$ with temperature. Particularly in the fluid membrane phase, $2A_{\max}$ is larger in the presence of peptide than in its absence, i.e., the mobility of the spin-labeled chains is decreased by interaction of the peptide with the membrane. The effect is stronger for the gB632-650 peptide (dotted line) than for the gH626-644 peptide (dashed line). Furthermore, the cooperativity of the DMPC chain-melting transition is reduced, while its position remains

approximately the same. Also in this respect, the effect of gB632–650 is stronger than that of gH626–644.

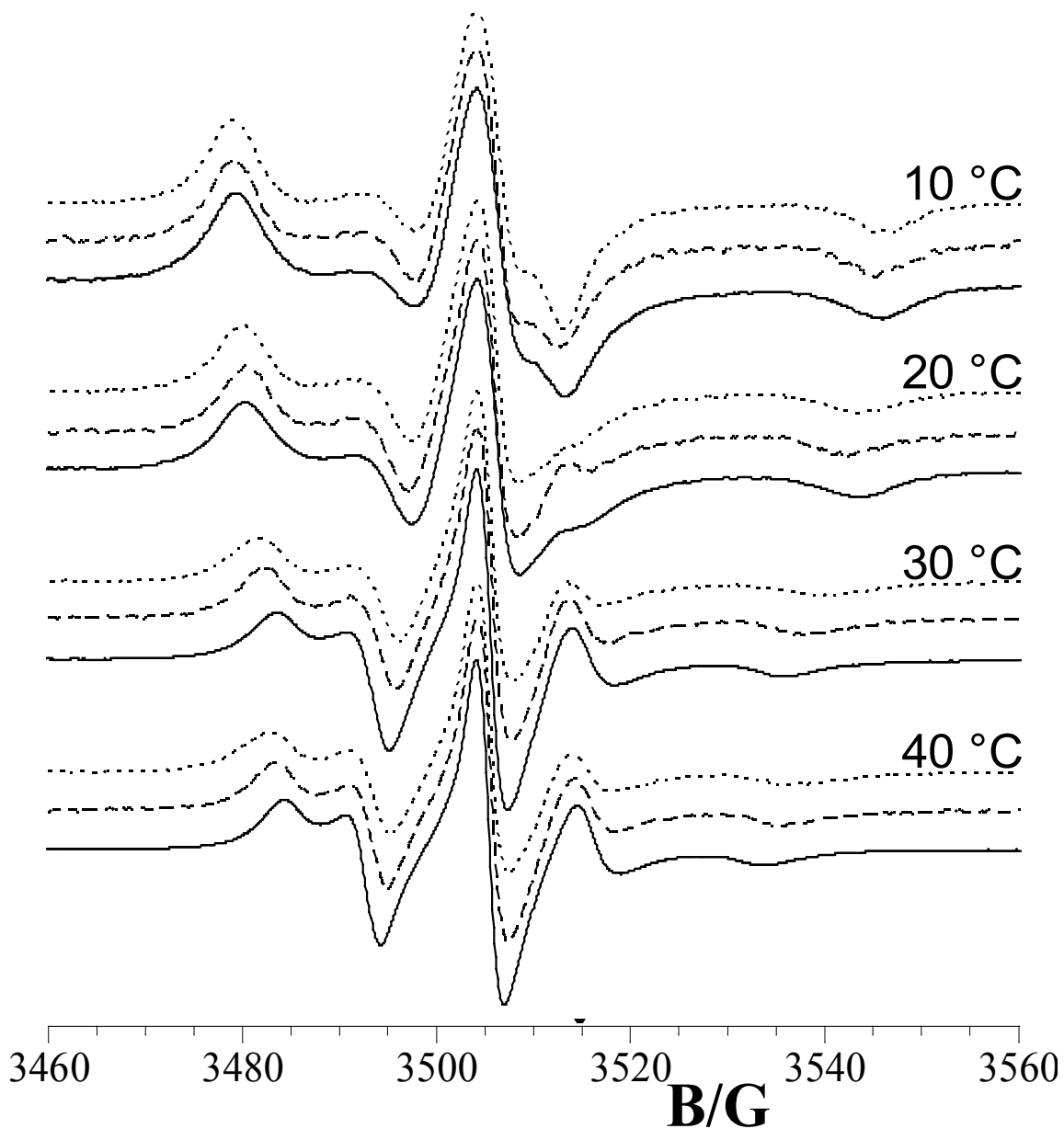


Figure 4.6.1 - ESR spectra of 5-PCSL in dimyristoyl phosphatidylcholine bilayer membranes, in the absence (continuous line) and presence of 1:1 wt/wt gH626–644 (dashed line) or gB632–650 (dotted line) peptide, at the temperatures indicated.

Figure 4.6.2B shows the behavior of DMPG membranes in the presence and absence of the gH626–644 and gB632–650 peptides. The chain-melting transition of the charged lipid (at 22–24 °C) is less sharp than that of zwitterionic DMPC and becomes almost undetectable in the presence of the peptides. In the gel phase, the outer hyperfine

splittings are less affected by the peptides, whereas in the fluid phase, a reduction of the spin-label mobility is very evident, particularly in the case of interaction with the gB632–650 peptide (dotted line). Comparison of Figure 4.6.2A and 4.6.2B indicates that the lipid chain perturbation by interaction with the peptides is stronger for the anionic lipid than for the zwitterionic lipid.

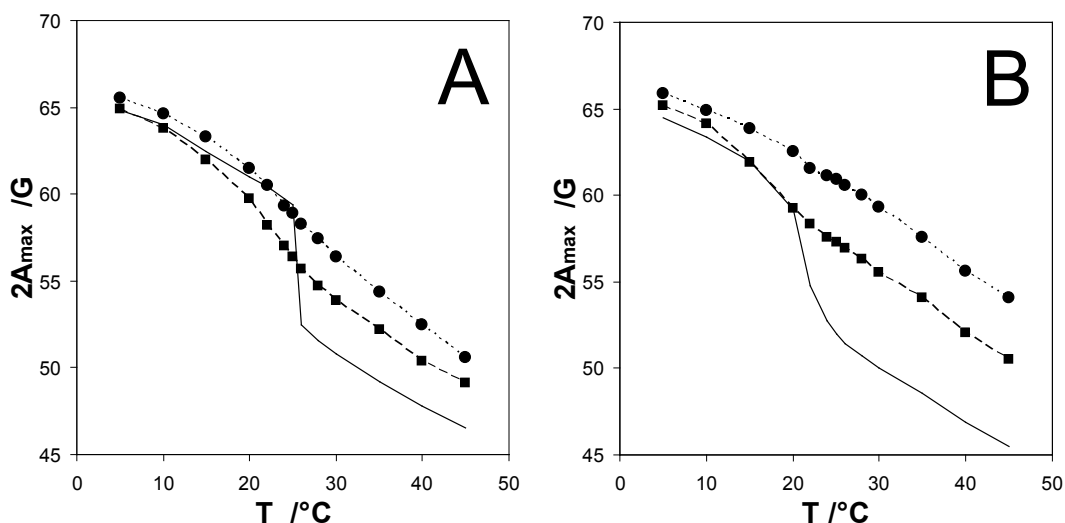


Figure 4.6.2 - Temperature dependence of the outer hyperfine splitting, $2A_{\max}$, of 5-position phospholipid spin labels in phospholipid membranes in the absence (continuous line) and presence of 1:1 wt/wt gH626–644 (■, dashed line) or gB632–650 (●, dotted line) peptide. (A) 5-PCSL in dimyristoyl phosphatidylcholine bilayer membranes and (B) 5-PGSL in dimyristoyl phosphatidylglycerol bilayer membranes.

Figure 4.6.3 shows the increase in outer hyperfine splitting, $2\Delta A_{\max}$, of the 5-position spin-labeled lipids in DMPC and DMPG membranes with increasing peptide (gH626–644 or gB632–650) concentration. In all cases, a typical saturation binding is registered. The extent of change in $2A_{\max}$ depends on the lipid, and for both peptides is higher in DMPG than in DMPC. On the other hand, the peptide/lipid weight ratio at which a constant value of $2A_{\max}$ is reached is not dependent on the particular lipid.

The peptide/lipid ratios at which binding saturates are ~ 0.5 and ~ 0.8 wt/wt for gH626–644 and gB632–650, respectively. These values correspond to ca. 2 and 1 wt/wt lipid/peptide ratios. The stoichiometry of the interaction can be estimated by extrapolation

of the increase in $2\Delta A_{\max}$, on initial tight binding, to the saturation value of $2\Delta A_{\max}$, as is shown in the figure. This gives a value of ~ 15 lipids per bound gH626–644 molecule, and ~ 5 lipids perbound gB632–650 molecule. These values are likely to be upper estimates because of a possible nonlinear dependence of $2\Delta A_{\max}$ on peptide binding.

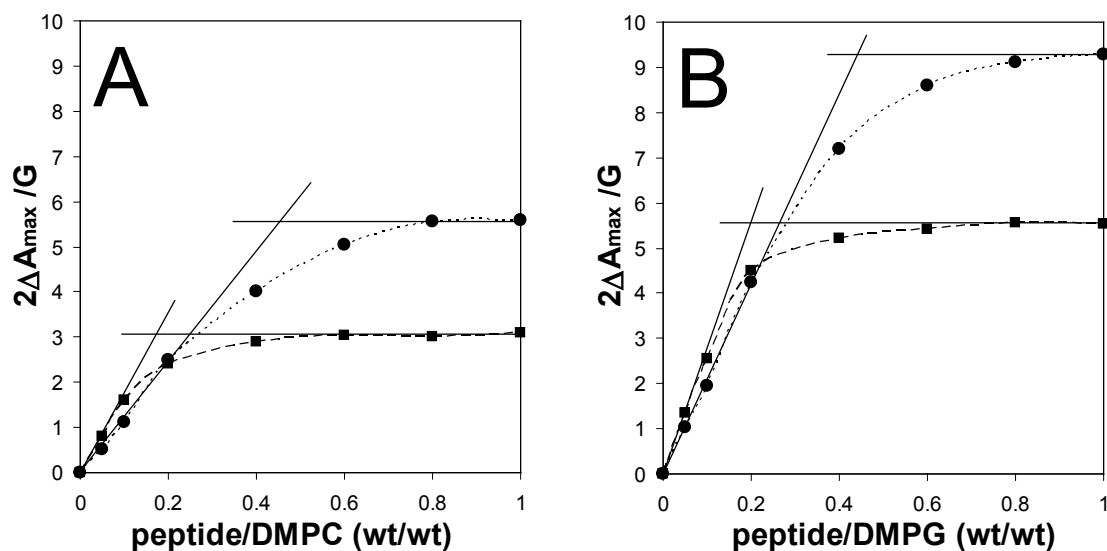


Figure 4.6.3 - Dependence of the increase, $2\Delta A_{\max}$, in outer hyperfine splitting of 5-position phospholipid spin labels at 30 °C on the peptide/lipid ratio for gH626–644 (■, dashed line) or gB632–650 (●, dotted line) peptides. (A) 5-PCSL in dimyristoyl phosphatidylcholine bilayer membranes, and (B) 5-PGSL in dimyristoyl phosphatidylglycerol bilayer membranes.

Perturbation of the ESR spectra from spin-labels at different positions, n , in the $sn-2$ chain of the lipid by binding the gH626–644 or gB632–650 peptide was also investigated. Figure 4.6.4 gives the ESR spectra of the n -PCSL phosphatidylcholine spin-label positional isomers in fluid DMPC bilayer membranes ($T = 30$ °C), in the presence and absence of the peptide at a peptide/lipid ratio of ~ 1 wt/wt. In the absence of peptide, the outer hyperfine splitting decreases progressively with increasing n , as the spin-label position is stepped down the chain towards the center of the membrane. As opposed to the clearly defined axially anisotropic spectra that are obtained for 5-PCSL towards the polar headgroup end of the chain, a narrow, three-line, quasi-isotropic spectrum is obtained for

14-PCSL that is positioned close to the terminal methyl region of the chain. This flexibility gradient in segmental chain mobility is a characteristic hallmark of the liquid-crystalline state of fluid phospholipid bilayers.

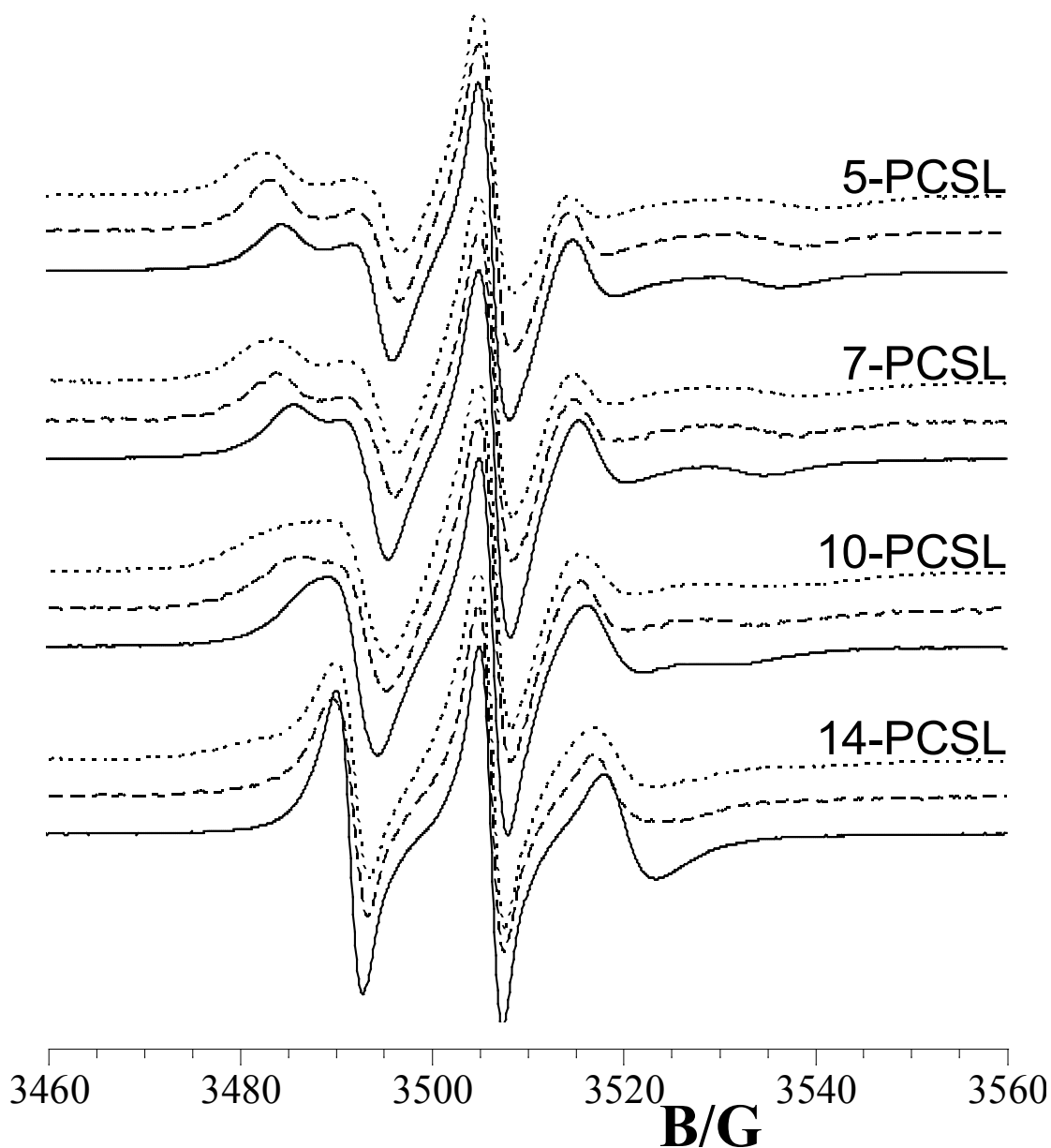


Figure 4.6.4 - ESR spectra of *n*-PCSL positional isomers of spin-labeled phosphatidylcholine in fluid-phase dimyristoyl phosphatidylcholine bilayer membranes, in the absence (continuous line) and presence of 1:1 wt/wt gH626-644 (dashed line) or gB632-650 (dotted line) peptide, at 30 °C.

Binding of the gH626-644 or gB632-650 peptide significantly affects the spectra of all spin-label positional isomers. In the presence of gH626-644, the outer hyperfine splitting is increased at all spin-label chain positions, although the line-shape remains

qualitatively similar. Figure 4.6.5 shows the dependence of the outer hyperfine splitting, $2A_{\max}$, on chain position, n , for the n -PCSL spin-labels in fluid DMPC membranes, with and without a saturating amount of bound peptide. The gH626–644 and gB632–650 peptides increase $2A_{\max}$ to roughly the same extent for the $n = 5, 7$ and 10 positions, whereas the increase in $2A_{\max}$ of 14-PCSL is smaller for the gH626–644 peptide and greater for the gB632–650 peptide. This profile of perturbations in $2A_{\max}$ indicates that the increase in lipid packing density, which is induced by surface association of the peptide, propagates down the acyl chains.

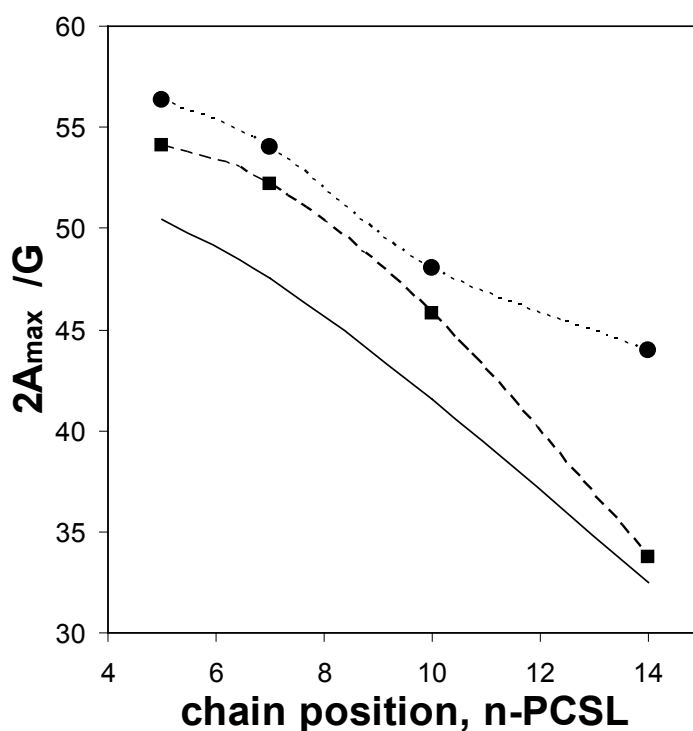


Figure 4.6.5 - Dependence on spin-label position, n , of the outer hyperfine splitting, $2A_{\max}$, of the n -PCSL phosphatidylcholine spin labels in fluid-phase membranes of DMPC, in the absence (continuous line) and presence of 1:1 wt/wt gH626–644 (■, dashed line) or gB632–650 (●, dotted line) peptide. $T = 30\text{ }^{\circ}\text{C}$.

In the case of the gB632–650 peptide, a second, more motionally restricted component appears in the spectra of spin labels positioned toward the terminal methyl end of the chain (10-PCSL and even more clearly for 14-PCSL). This is evidence that the peptide penetrates appreciably into the membrane interior [28].

We also investigated DMPC membranes containing cholesterol (CHOL) at 20% wt/wt. ESR spectra of *n*-PCSL in DMPC/CHOL lipid samples without peptide at 30 °C are shown by the solid lines in Figure 4.6.6. Inspection of this figure shows large changes with respect to the spectra for DMPC membranes without cholesterol that are shown by the solid lines in Figure 4.6.4.

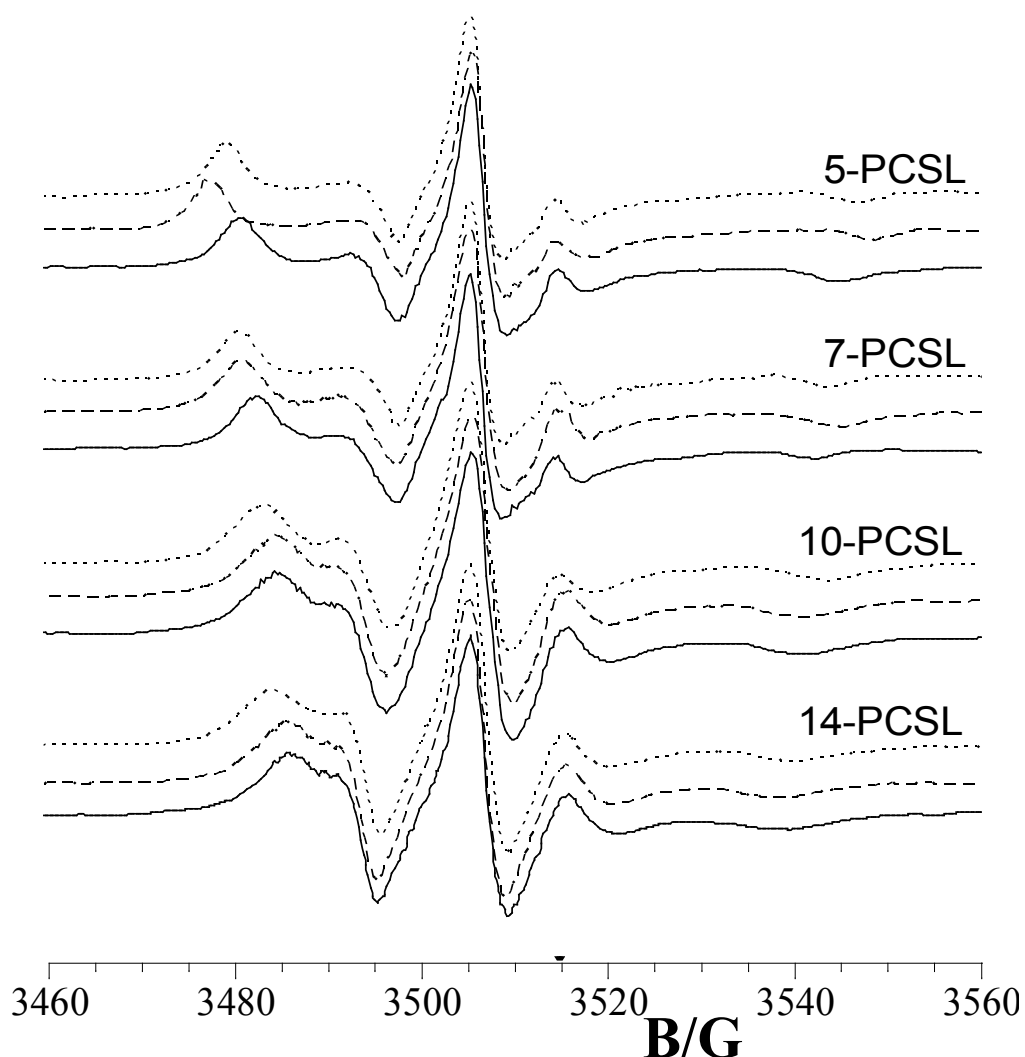


Figure 4.6.6 - ESR spectra of *n*-PCSL positional isomers of spin-labeled phosphatidylcholine in dimyristoyl phosphatidylcholine bilayer membranes containing 20 wt% cholesterol, in the absence (continuous line) and presence of 1:1 wt/wt gH626–644 (dashed line) or gB632–650 (dotted line) peptide, at 30 °C.

CHOL increases the spectral anisotropy, also for spin labels that are located deep in the bilayer inner core. This can be ascribed to the CHOL-induced transition of the bilayer from the liquid-disordered to the liquid-ordered state. Addition of 1:1 wt/wt gH626–644 or

gB632–650 peptide with respect to total lipid clearly perturbs the spectra of 5-PCSL in DMPC/CHOL membranes, gH626–644 (Figure 4.6.6, dashed line) being more effective than gB632–650 (Figure 4.6.6, dotted line). Interestingly, a different behavior is observed for the spectra of spin-labels further down the chain. Whereas gH626–644 perturbs the spectra of 5-PCSL and 7-PCSL in DMPC/CHOL membranes (Figure 4.6.6), the spectra of 10-PCSL and 14-PCSL appear to be almost unperturbed. In contrast, perturbations by gB632–650 at 1:1 wt/wt with respect to lipid are evident for all label positions throughout the chain. These observations reflect the quantitative trends in the outer hyperfine splitting, $2A_{max}$, which are shown in Figure 4.6.7, and indicate that the gB632–650 peptide (dotted line) penetrates appreciably into the DMPC/CHOL membrane interior, while the gH626–644 peptide (dashed line) adsorbs at the surface.

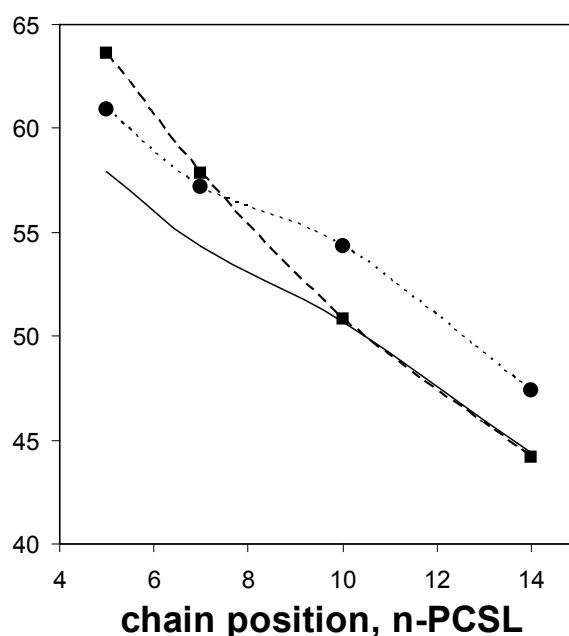


Figure 4.6.7 - Dependence on spin-label position, n , of the outer hyperfine splitting, $2A_{max}$, of the n -PCSL phosphatidylcholine spin labels in membranes of DMPC containing 20 wt% cholesterol, in the absence (continuous line) and presence of 1:1 wt/wt gH626–644 (■, dashed line) or gB632–650 (●, dotted line) peptide. $T = 30\text{ }^{\circ}\text{C}$.

The selectivity of interaction of different lipids with the gH626–644 or gB632–650 peptide bound to DMPC membranes was determined by using probe amounts of lipids spin

labeled at the 5-C atom of the *sn*-2 chain [45,46]. Table 4.6.1 gives the values of the outer hyperfine splitting, $2A_{max}$, for the spin labels at 30 °C, in the presence and absence of 1:1 wt/wt peptide. For all spin-labeled lipids tested, $2A_{max}$ is greater for peptide-bound membranes than for membranes of the lipid alone. The increase in $2A_{max}$ differs, however, for the two peptides and for the different spin-labeled lipids. This reflects a selectivity of interaction of both gH626–644 and gB632–650 with the different lipid polar head groups. Table 1 gives the increase, $2\Delta A_{max}$, in outer hyperfine splitting for the peptide-bound membranes, relative to that for peptide-free membranes. For both peptides, the increase in $2A_{max}$ is larger for spin-labeled lipids with anionic head groups (5-PGSL, 5-PASL, 5-PSSL) than for those bearing a zwitterionic head group (5-PESL and 5-PCSL). Furthermore, it is interesting to observe that, for each spin label, $2\Delta A_{max}$ is greater with the gB632–650 peptide than with the gH626–644 peptide.

spin label	$2A_{max}$ (G)			$2\Delta A_{max}$ (G) ^a	
	DMPC	DMPC+	DMPC+	DMPC+	DMPC+
		gH626-64	gB632-650	gH626-64	gB632-650
5-PCSL	50.8	54.1	56.4	3.3	5.6
5-PGSL	52.1	55.8	58.3	3.7	6.2
5-PASL	52.3	56.1	58.4	3.8	6.1
5-PESL	52.4	55.8	58.2	3.4	5.8
5-PSSL	53.0	56.7	59.7	3.7	6.7

^a ΔA_{max} is the difference in A_{max} with and without peptide.

Table 4.6.1 - Outer hyperfine splittings ($2A_{max}$) of phospholipid probes, spin labeled at the fifth position of the *sn*-2 chain, incorporated in DMPC bilayers with and without the gH626-64 or gB632-650 peptides at 30 °C.

Using the Wimley-White octanol scale [37], transfer of the gH626-644 and gB632-650 peptides from water to the hydrocarbon core of the membrane is predicted to be strongly disfavored energetically. In contrast, transfer of both peptides from water to the

polar-apolar interface of the membrane is predicted to be energetically favorable. On the Wimley-White interfacial hydrophathy scale, the free energy of transfer from water is $\Delta G_{\text{transf}} = -8.7 \text{ kJ mol}^{-1}$ for gH626-644 and $\Delta G_{\text{transf}} = -13.5 \text{ kJ mol}^{-1}$ for gB632-650, if the N and C termini are charged and the peptides are in a random conformation. These values are augmented by an additional $-14.1 \text{ kJ mol}^{-1}$, if the N and C termini are electroneutral. A further -1.7 kJ mol^{-1} per residue should be added when helix formation on surface association of the peptides is taken into account [30]. As found below from CD data, this additional contribution is needed only in the case of gH626-644 interacting with DMPG bilayers, or with DMPC bilayers at high peptide/lipid ratio. In an α -helical conformation, gH626-644 is predicted to have a hydrophobic moment of $\mu_{\text{H}} = 20.52 \text{ kJ mol}^{-1}$ on the interfacial scale, with the moment directed toward the tyrosine, Y637, of the peptide sequence. Summarizing, the free energy of transfer of gH626-644 from water to the membrane interface is predicted to lie within the range: $\Delta G_{\text{transf}} = -8.7$ to $-54.5 \text{ kJ mol}^{-1}$, while the corresponding value for gB632-650 lies within -13.5 and $-27.5 \text{ kJ mol}^{-1}$.

The secondary structure of the gH626–644 (Figure 4.6.8) and gB632–650 peptides in buffer and bound to sonicated liposomes was determined by CD spectroscopy. As reported in the literature [25], fusion peptides can change their secondary structure at different peptide/lipid ratios. In particular, they may show a beta and/or oligomeric structure at high peptide/lipid ratios, whilst assuming an α -helical structure at low peptide/lipid ratios. The secondary structure measurements were therefore performed at two different peptide/lipid ratios; specifically, we used molar ratios of 0.1 (low peptide/lipid ratio) and of 0.5 (high peptide/lipid ratio). The 0.5 mol/mol peptide/lipid ratio was used because we observed high fusion activity for both peptides at this molar ratio. All the CD spectra shown for gH626-644 indicate formation of substantial helical structure with DMPG, at low peptide/lipid ratios, whereas the spectra of this peptide with DMPC and DMPC/CHOL indicate a random conformation. At high peptide/lipid ratio, a gH626-

644 tendency to assume a helical conformation is evident also with DMPC, while inclusion of cholesterol in the bilayer formulation keeps the peptide in a random conformation.

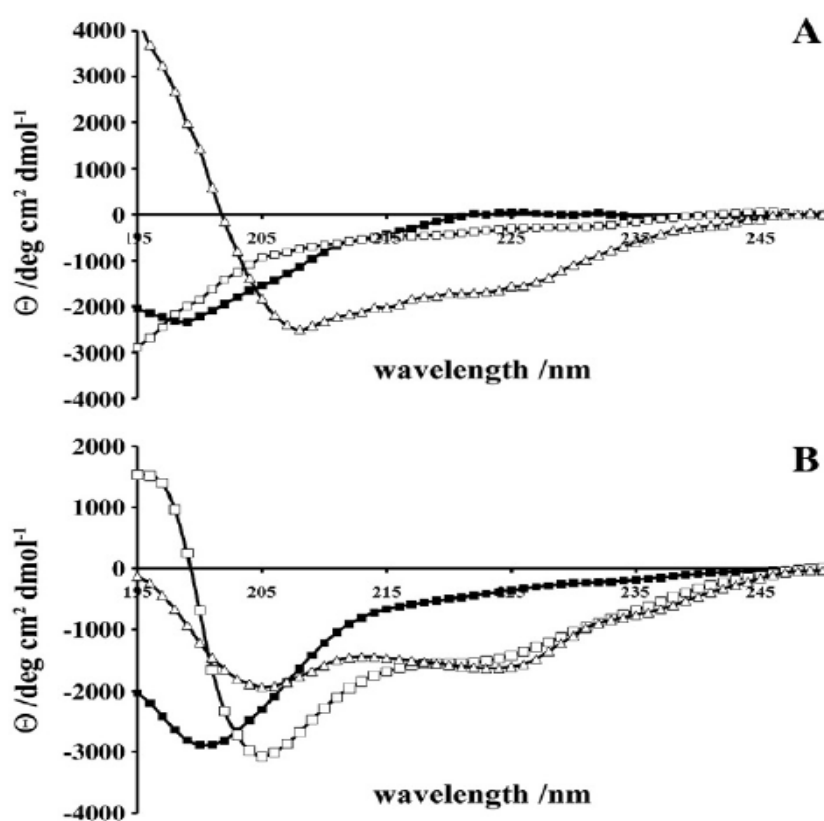


Figure 4.6.8 – CD spectra of gH626-644 10 μM (A) and 50 μM (B) in LUVs of DMPC (\square), DMPG (Δ) and DMPC containing 20wt.% cholesterol (\blacksquare), $T=30^\circ\text{C}$.

The ratio of ellipticities at 222 nm and 208 nm can be used to distinguish between monomeric and oligomeric states of helices. When the ratio $\theta_{222}/\theta_{208}$ equals about 0.8, the peptide is monomeric, and when the ratio exceeds 1.0 it is oligomeric. The $\theta_{222}/\theta_{208}$ ratio for gH626-644 in DMPG is ~ 0.7 at low peptide/lipid ratio and ~ 0.9 at high ratio indicating that, with increasing peptide concentration, the monomer/oligomer equilibrium shifts from the monomeric to the aggregated state for this peptide associated with DMPG. In contrast, in DMPC liposome the peptide does not show a self-aggregative tendency.

The CD spectra of gB632-650 are not shown because we observed a strong tendency of the peptide to aggregate under all conditions tested here, and consequently we were unable to obtain a reproducible CD spectrum.

In conclusion, this study has indicated that both gH626-644 and gB632-650 peptides interact with lipid bilayers, perturbing the local lipid packing. The mechanism of interaction depends on the specific peptide: gH626-644 tends to localise close to the bilayer hydrophilic surface, indirectly perturbing the acyl chain packing and dynamics, while gB632-650 penetrates deeply into the bilayer. The different behaviour is also confirmed by the peptide-lipid titration. Each molecule of gH626-644 interacts with a maximum of 15 lipids. On a per-residue basis, this value corresponds to ~ 0.8 lipids per amino acid, a stoichiometry typical of a peptide-surface adsorption. In the case of gB632-650, a single peptide molecule interacts with a smaller number of lipids (~ 5), as is expected in the case of peptide penetration in a transverse membrane orientation. Such a low value suggests possible association between gB632-650 molecules interacting with the bilayers, thus explaining the problems encountered in registering CD spectra in liposomes. Both peptides induce a stronger perturbation in packing and dynamics of negatively charged bilayers, relative to those of zwitterionic lipids. In particular, ESR results indicate a significant selectivity of different lipids for interaction with the peptides. The lipid selectivity pattern for interaction with the gH626-644 peptide in DMPC is in the order: $PA \approx PG \approx PS > PE \approx PC$, and that for the gB632-650 peptide is $PS > PG \approx PA > PE \approx PC$. Thus, both peptides interact preferentially with anionic lipids. Moreover, the gB632-650 peptide shows a significant selectivity for the phosphatidylserine headgroup. Also inclusion of cholesterol in the bilayer membrane affects the lipid chain ordering. These changes do not appear to change the ability of the gB632-650 peptide to penetrate deeply into the bilayer. In contrast, in the presence of cholesterol, the membrane perturbation by the gH626-644 peptide is limited to the more external layer.

Within this scheme, the experimental results obtained with the two most fusogenic fragments of gH and gB suggest that the mechanism of action of these two glycoproteins is modulated by the phospholipid bilayer properties and composition.

4.7 Characterization of the membrane interaction of the two fusion loops of glycoprotein B from HSV-type I

The association of the two peptides, gB168-186 and gB254-270, with lipid bilayers was investigated by analysing changes in ESR spectra of spin-labeled phospholipids. The samples investigated were phosphatidylcholine spin-labeled at different positions, n , in the *sn*-2 chain (n -PCSL, $n = 5, 7, 10, 14$) incorporated in DOPC/CHOL membranes (60:40 mol/mol), in the presence of the peptides. Preliminarily, the spectra in the absence of the peptides were registered. Inspection of Figure 4.7.1 (solid lines) shows that all the spectra present a clearly defined axially anisotropic lineshape, an evidence that, due to the high cholesterol content, the DOPC/CHOL bilayer is in the liquid-ordered state. In an attempt to quantitatively analyse the spectra, the outer hyperfine splitting, $2A_{\max}$, was calculated. The $2A_{\max}$ variation, shown in Figure 4.7.2, is an evidence of the flexibility gradient in segmental acyl chain mobility, indicating that the lipid bilayer presents a rigid surface and relatively fluid interior.

Association of peptides to the lipid bilayer causes a significant variation in the ESR spectra of spin-labeled phospholipids. In Figure 4.7.1, ESR spectra of 5-PCSL and 14-PCSL in DOPC/Chol bilayers, in the presence of gB168-186, gB254-270 and gB168-186:gB254-270 mixture at a lipid:peptide weight ratio of 1:1 are also reported. The presence of two peptide induces significant changes in the spin-label ESR spectra, which are mainly detectable from the low- and high-field component position and lineshape. In an attempt to quantify this evidence, the $2A_{\max}$ values were determined. Figure 4.7.2 shows the dependence of these parameters on chain position, n , for the n -PCSL spin-labels in DOPC/Chol membranes, in the absence and in the presence of the peptides. In all cases, the flexibility gradient with the chain position of the lipid bilayer membranes is preserved. However, inspection of the figure reveals a significantly different behaviour of the lipid chain mobility in the co-presence of the two peptides.

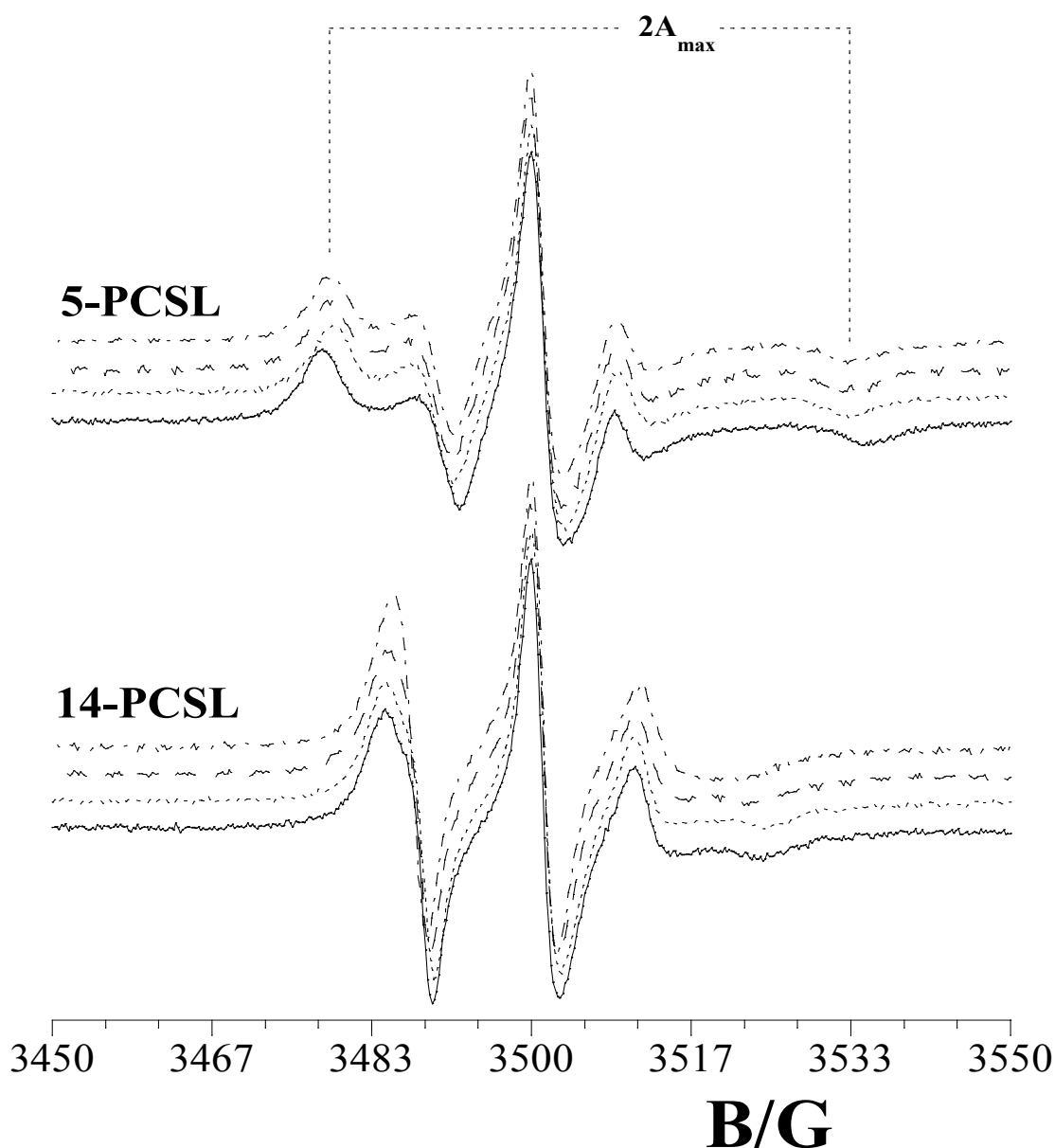


Figure 4.7.1 - ESR spectra of 5-PCSL and 14-PCSL spin-labels in DOPC/Chol membranes in the absence of peptides (solid line) and in the presence of gB168-186 (dotted line), gB254-270 (dashed line) and gB168-186 -gB254-270 mixture (dashed-dotted line).

In fact, addition of gB168-186 or gB254-270 significantly reduces the $2A_{\max}$ value of 5-PCSL. In both cases, no changes in the spectra of the spin-labels bearing the nitroxide group in the more interior positions were observed. Strikingly, addition of the gB168-186:gB254-270 mixture results in a strongly $2A_{\max}$ decrease for all the considered spin-labels. These results show a synergistic effect of the peptides in perturbing the bilayer

microstructure in that only in the presence of both of them the increase of segmental mobility propagates along the whole acyl chains. Thus, the contemporary interaction of both peptides with the lipid membrane surface effectively perturbs the local order and dynamics of the lipid leaflet they come in contact with.

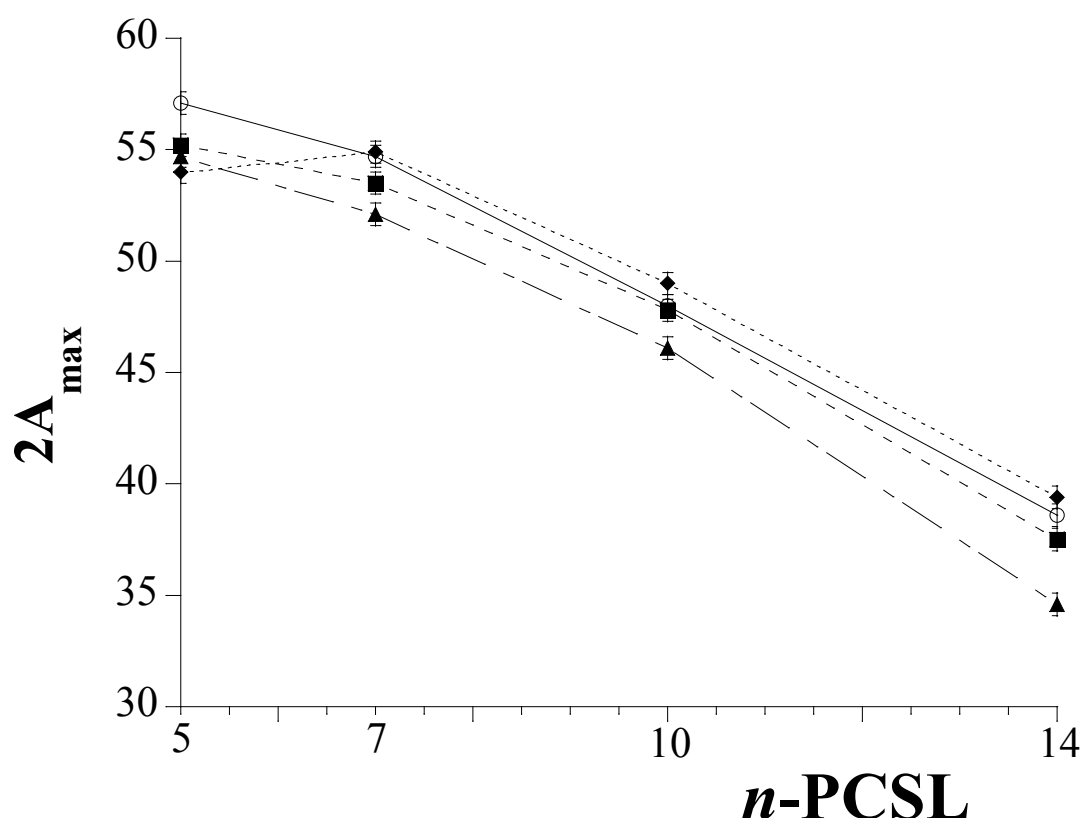


Figure 4.7.2 - Dependence on spin-label position, n , of the outer hyperfine splittings, $2A_{\max}$, of the n -PCSL in DOPC/Chol bilayers in the absence (○) and in the presence of gB168-186 (■), gB254-270 (●) or gB168-186: gB254-270 (▲) at $T=25$ °C.

In this study, the role played by the two fusion loops of HSV-1 gB in the mechanism of membrane fusion has been investigated [31]. In particular, their ability to interact with the membrane bilayer, alone or used in equimolar concentrations, were investigated by ESR spectroscopy. These two fusion loops constitute a structural subdomain wherein key hydrophobic amino acids form a ridge that is supported on both sides by charged residues. The two charged residues located on both sides of the ridge

represent a novel feature of viral fusion peptides and probably enhance the ability of the hydrophobic residues to interact with target membranes and to function in fusion.

The two peptides separately do not appear to be able to insert deeply into target membranes, while our liposome studies show that the peptides, when used together, have the ability to significantly destabilize the bilayer; thus being surely involved in the insertion of gB into cholesterol enriched membranes. The peptides associate with cholesterol containing liposomes, suggesting that the cholesterol dependence of the fusion process is not necessarily because of the protein receptor in rafts, but because cholesterol itself enhances insertion of the fusion loops. The presence of cholesterol in the membrane bilayer is likely to facilitate peptide/peptide interactions inside the membrane.

4.8 Interaction of gH625 peptide from HSV-1 with lipid membranes

The nineteen residues peptide gH625 was identified as a membrane-perturbing domain in the gH protein of Herpes simplex virus type I, which interacts with biological membranes, contributing to the merging of the viral envelope and the cellular membrane [13,32]. An experimental investigation on the action mechanism of this peptide in the presence of biomembranes was realized performing NR and ESR measurements. Lipid bilayers of POPC and POPC:SM:CHOL 1:1:1 wt/wt/wt were considered in order to discriminate a role of different lipid composition in modulating the peptide-membrane interaction.

First, lipid bilayers in the absence of peptide were characterized by NR using D₂O, SMW and H₂O as isotopic contrast solvents. The experimental curves are shown in Figure 4.8.1A-B and the parameters used to fit the curves simultaneously from all the contrasts are given in Table 4.8.1.

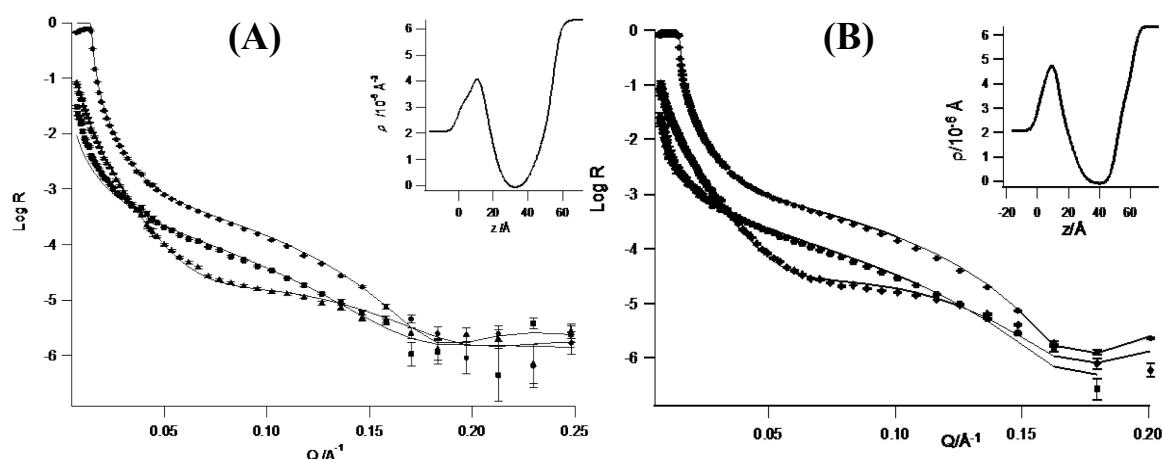


Figure 4.8.1 – Neutron Reflectivity profiles (points) and best fits (continuous lines) corresponding to bilayers of (A) POPC and (B) POPC:SM:CHOL 1:1:1 wt/wt/wt bilayers in (●) D₂O, (■) SMW and (◆) H₂O solvents. The insets show the ρ profiles for the lipid bilayers in D₂O.

For both systems, a five box model was found to best fit the data. The first two correspond to the silicon block and to the thin solvent layer interposed between the silicon surface and the adsorbed bilayer. The three other boxes describe the lipid bilayer, which is

subdivided in the inner headgroups, the hydrophobic chains, and the outer headgroups layers. The theoretical scattering length density, ρ , was calculated through $\rho(z) = \sum_j n_j(z) b_j$, where $n_j(z)$ is the number of nuclei per unit volume and b_j is the scattering length of nucleus j .

In this case of POPC, ρ of the lipid headgroups is equal to $1.86 \times 10^{-6} \text{ \AA}^{-2}$, while the ρ of acyl chains is equal to $-0.29 \times 10^{-6} \text{ \AA}^{-2}$ [11]. These values were kept constant during the data analysis, since their optimization was found to give no fitting improvement. Thus the parameters obtained from the best fit procedure are the thickness and the roughness of each box plus the solvent content expressed as volume percent. Inspection of Table 4.8.1 indicates that the overall thickness of the bilayer is $43 \pm 1 \text{ \AA}$ and the solvent content is $35\% \pm 10$ for both headgroups layers.

POPC	interfacial layer	thickness (Å)	% solvent	roughness (Å)
	water	3±1	100	3±1
	inner headgroups	7±1	35±10	5±1
	chains region	29±1	-	6±1
	outer headgroup	7±1	35±10	7±1
+ gH625	water	3±1	100	3±1
	inner headgroups	5±1	14±10	5±1
	chains region	28±1	-	3±1
	outer headgroup	4±1	35±10	4±1
	interacting peptide	6±1	84±10	3±1
POPC:SM:CHOL	water	5±1	100	4±1
	inner headgroups	7±1	23±10	4±1
	chains region	34±1	-	5±1
	outer headgroup	7±1	22±10	7±1
+ gH625	water	5±1	100	4±1
	inner headgroups	5±1	32±10	4±1
	chains region	37±1	-	9±1
	outer headgroup	9±1	40±10	8±1

Table 4.8.1 - Parameters derived from model fitting the reflectivity profiles for pure lipid bilayers and after the addition of gH625 peptide.

In the case of the lipid bilayer also containing SM and cholesterol, a total thickness of $48 \pm 1 \text{ \AA}$ and a solvent content in the headgroups region of $\sim 22\% \pm 10$ for the inner and outer polar layers were obtained. ρ is equal to $-0.11 \times 10^{-6} \text{ \AA}^{-2}$ for the acyl chains region, confirming the presence of cholesterol in this domain, while the ρ value for the headgroup region was equal to $1.7 \times 10^{-6} \text{ \AA}^{-2}$. For both considered bilayers, a model without the water layer between the substrate and the bilayer gave a worse fit to the data. These NR results are in agreement with those previously presented (paragraphs 4.3 and 4.4) about the membrane-C8 peptide interaction [8].

The effect of gH625 peptide in the bilayers was studied by measuring the neutron reflectivity curves of the fully hydrogenated pure POPC and POPC:SM:CHOL mixture to which the peptide was added. Four contrasts, D₂O, 4MW, SMW and H₂O, were used and NR curves are shown in Figure 4.8.2.

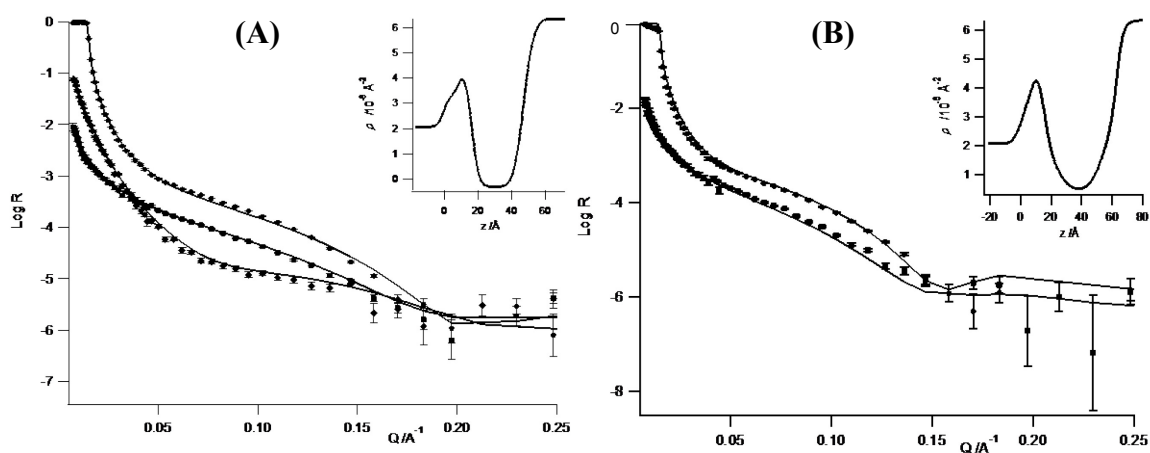


Figure 4.8.2 – Neutron Reflectivity profiles (points) and best fits (continuous lines) corresponding to bilayers of (A) POPC and (B) POPC:SM:CHOL 1:1:1 wt/wt/wt bilayers in the presence of gH625 peptide in (●) D₂O, (■) SMW and (◆) H₂O solvents. The inset shows the ρ profile for the lipid bilayers in D₂O.

Data from peptide-interacting POPC bilayer were fitted by an additional layer with respect to the case of pure lipid model. This layer prominently consists of the peptide interacting with the outer bilayer surface; the peptide ρ was calculated as previously

indicated and is equal to $1.9 \times 10^{-6} \text{ \AA}^{-2}$. Interestingly, in order to obtain a good curves fitting, the ρ values of all membrane layers are not changed while the other parameters of the various boxes are different with respect to the POPC bilayer. In particular, the thickness and roughness of the outer hydrophilic layer decrease of $\sim 3 \text{ \AA}$, indicating that gH625 peptide interacts with the membrane surface, perturbing only the external region. The values of all parameters optimized in curves fitting are reported in Table 4.8.1.

Then, NR profiles corresponding to the POPC:SM:CHOL bilayer in the presence of gH625 was analyzed. Different changes were caused by the peptide addition. In this case, a good curves fitting was obtained without the additional layer, but varying all parameters related to the hydrophobic and hydrophilic layers. In particular, ρ changes were observed for the hydrophobic region and the outer headgroups region. In the first case, ρ increases to value $\sim 0.36 \times 10^{-6} \text{ \AA}^{-2}$, while for the hydrophilic layer it becomes equal to $\sim 1.9 \times 10^{-6} \text{ \AA}^{-2}$. No changes in ρ values were observed for the inner hydrophilic region. These evidences indicate that the peptide strongly interacts with the lipid membranes, partially penetrating in the hydrophobic core. In addition, for both hydrophobic and outer hydrophilic regions the thickness of increases of $\sim 4 \text{ \AA}$, confirming the peptide insertion, while roughness values undergo only a slight variation. The gH625 addition also causes an increase of the solvent content in the external headgroup layer, while no changes in the solvent content for the acyl chains region was observed. Finally, for the inner hydrophilic layer a small decrease of the thickness and a slight increase of the roughness was detected, indicating that the it was slightly perturbed although the gH625 peptide does not interact with it. All this changes are well shown in Table 4.8.1.

The membrane-peptide interaction was also investigated by ESR measurements, incorporating phosphatidylcholine spin-labeled on the different positions of the *sn*-2 chain (*n*-PCSL, with $n = 5, 7, 10, 14$) in the lipid bilayers. *n*-PCSL spectra of POPC and POPC:SM:CHOL membranes in the absence and presence of peptide are shown in Figures

4.8.3 and 4.8.4, respectively. Considering the lipid bilayers without the peptide, it is possible to observe that 5-PCSL spectra show a clearly defined axially anisotropic lineshape (Figures 4.8.3 and 4.8.4, continuous lines). Spectra of 7-PCSL and 10-PCSL spin-labels also have an anisotropic lineshape, but this character is less evident as the nitroxide group is located close to the terminal methyl region of the chain. In fact, in this case of 14-PCSL a three-line, quasi-isotropic spectrum is obtained.

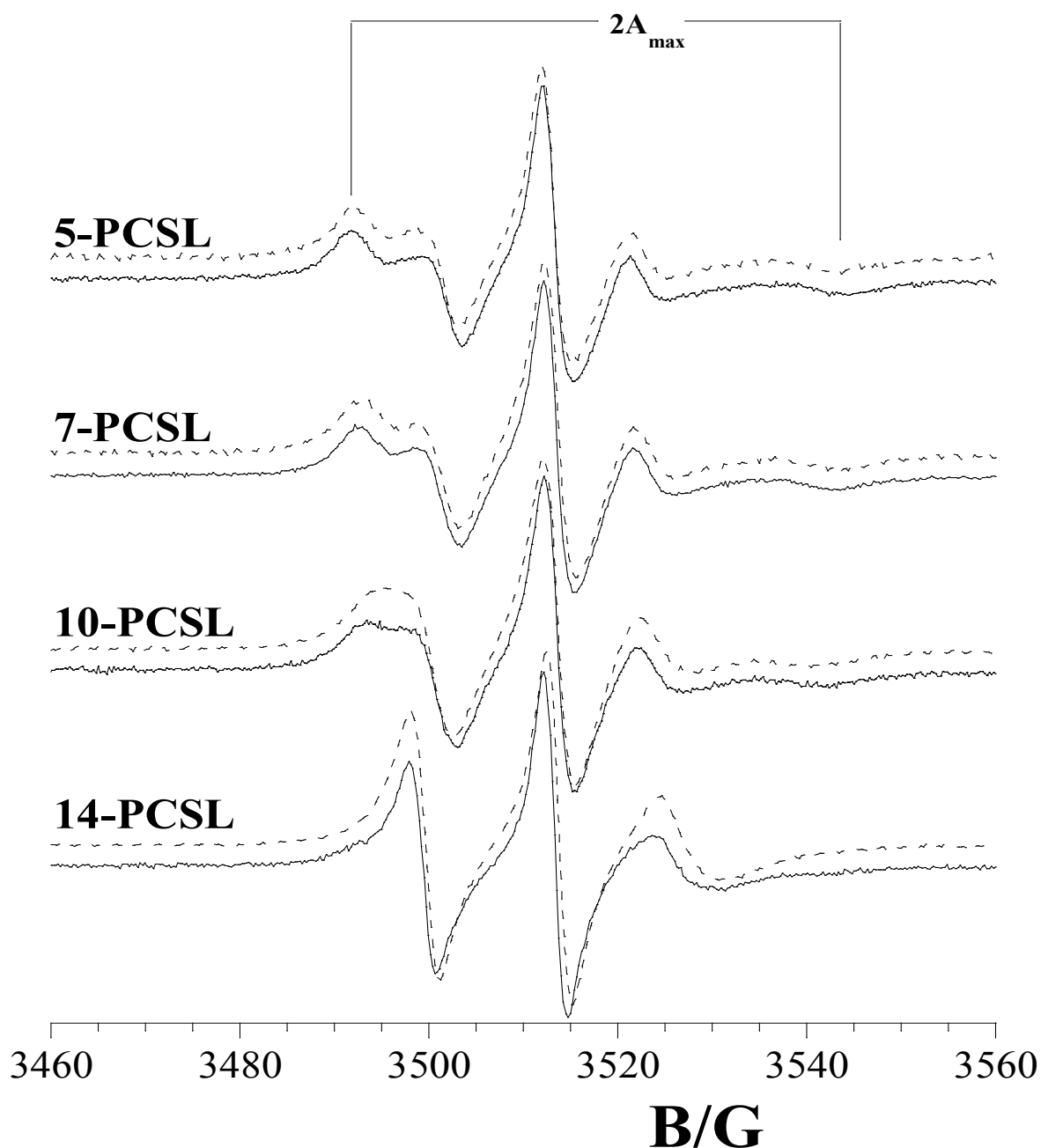


Figure 4.8.3 – ESR spectra of *n*-PCSL in POPC bilayers in the absence (solid line) of peptide and in the presence (dotted line) of gH625 peptide.

The higher isotropy of the 14-PCSL spectrum with respect to that obtained for 5-PCSL indicates a flexibility increase in segmental chain mobility in going from the polar headgroups to the inner hydrophobic core, which is a characteristic hallmark of the liquid-crystalline state of fluid phospholipids bilayers. In both cases, the addition of gH625 peptide causes significant variations in the *n*-PCSL's spectra although in different ways, see Figures 4.8.3 and 4.8.4 (dotted lines).

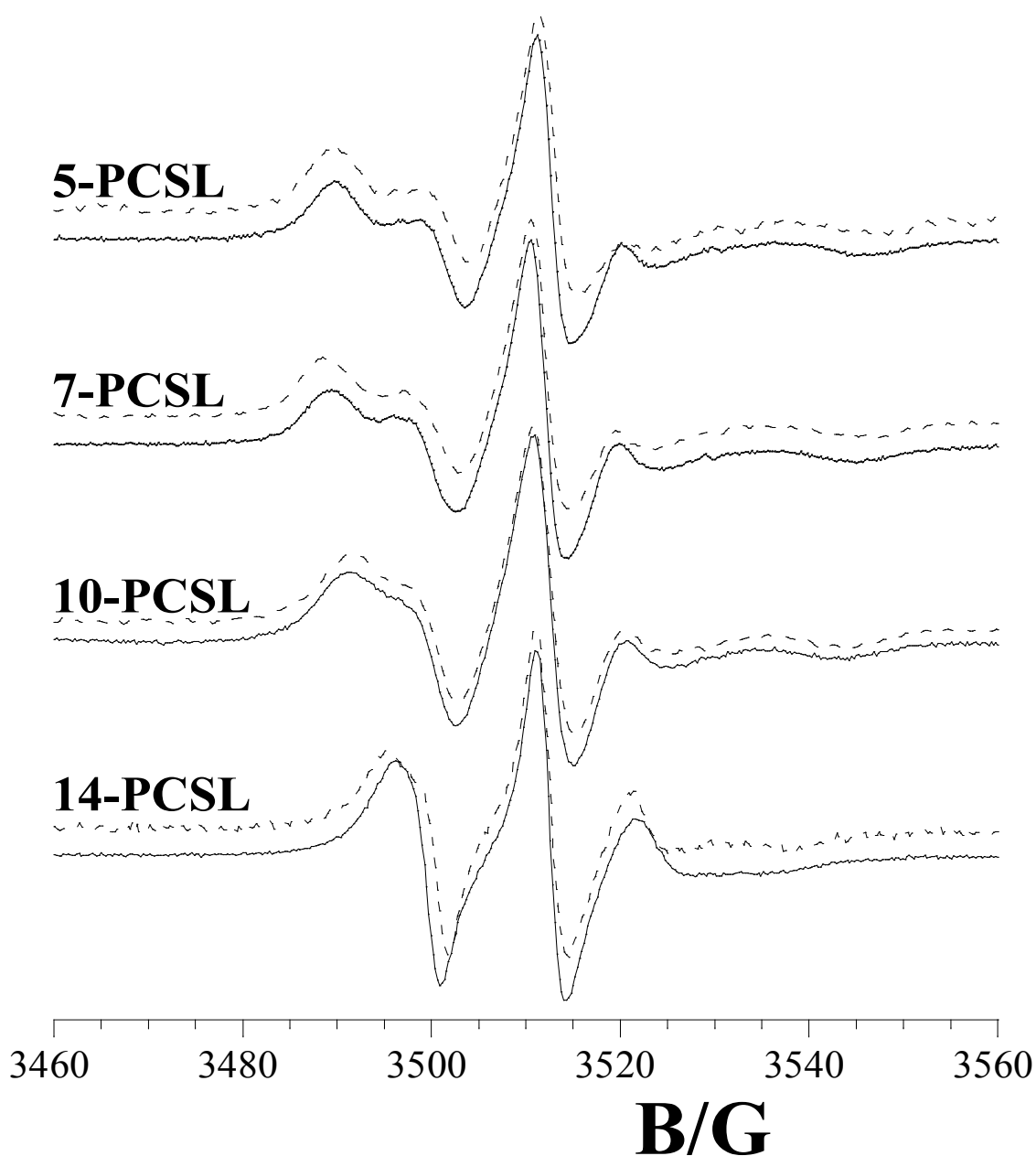


Figure 4.8.4 – ESR spectra of *n*-PCSL in POPC:SM:CHOL bilayers in the absence (solid line) of peptide and in the presence (dotted line) of gH625 peptide.

Analysis of n -PCSL' spectra was realized determining the outer hyperfine splitting ($2A_{\max}$). Figures 4.8.4 and 4.8.5 show the dependence of the $2A_{\max}$ on chain position, n , for the n -PCSL spin-labels in lipid membranes, with and without gH625 peptide.

In the case of POPC membranes, the addition of peptide causes a $2A_{\max}$ decrease for 5, 7 and 10-PCSL, as shown in Figure 4.8.5, which is of the same extent (~ 1.5 G). For the 14-PCSL spectrum, that is the spin-label presenting the nitroxide in a deeper position, no changes in the ESR spectrum were caused by the gH625 addition (Figure 4.8.4, dotted line). This is evidence that the peptide binds solely at the membrane surface and does not penetrate appreciably into the membrane interior, causing a major fluidity of the lipid bilayers.

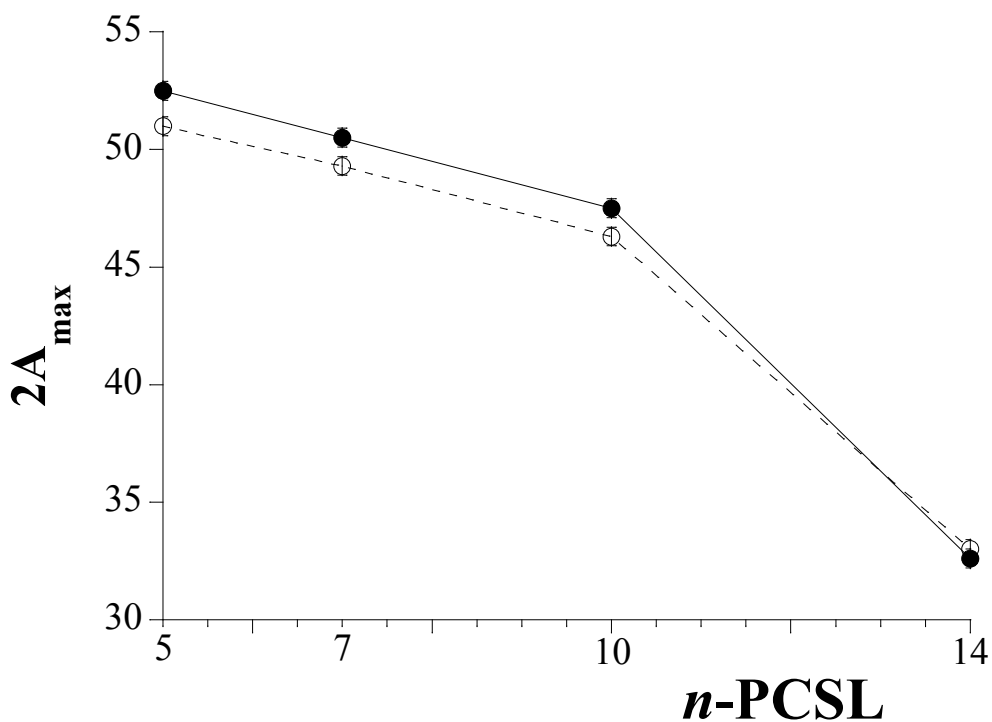


Figure 4.8.5 - Dependence on spin-label position, n , of the outer hyperfine splitting, $2A_{\max}$, of the n -PCSL phosphatidylcholine spin labels in membranes of POPC, in the absence (●, continuous line) and presence of 1:0.5 wt/wt gB625 (○, dotted line) peptide.

In contrast, the addition of gH625 peptide to the POPC:SM:CHOL membranes causes an increase of $2A_{\max}$ values for all spin-labels (see Figure 4.8.6). In particular, it is

increased at 5, 7 and 10 chain positions by the same extent (~1.2 G). For the 14-PCSL, a more significant change was observed in the ESR spectrum which present an evident anisotropic lineshape and a $2A_{\max}$ increase equal to 4.3 G. This is evidence that the peptide interacts strongly with the membrane, partially penetrating into the bilayer interior.

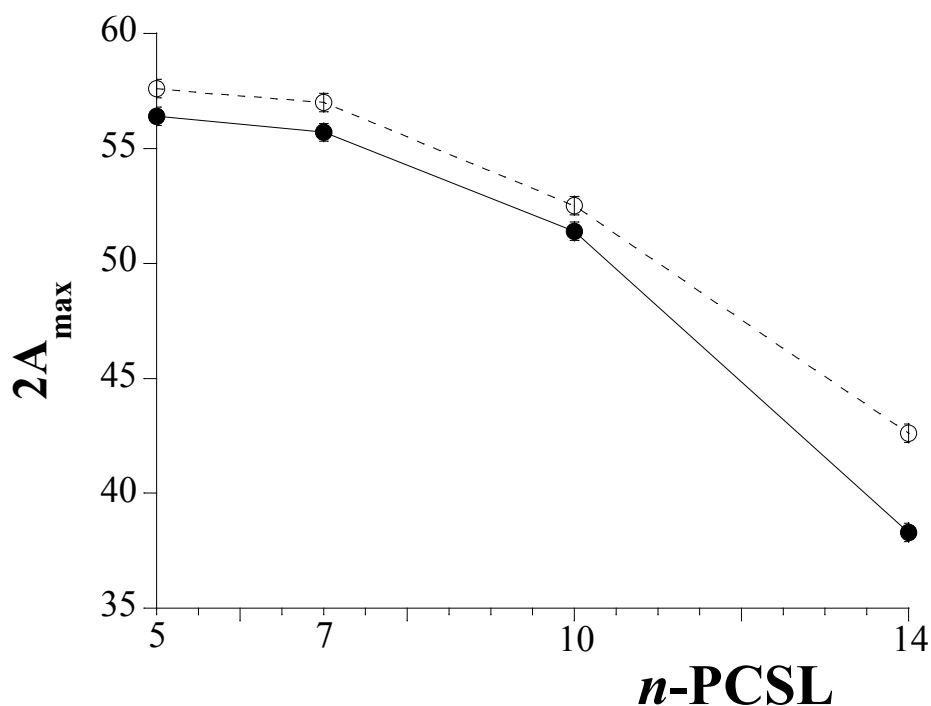


Figure 4.8.6 - Dependence on spin-label position, n , of the outer hyperfine splitting, $2A_{\max}$, of the n -PCSL phosphatidylcholine spin labels in membranes of POPC:SM:CHOL, in the absence (●, continuous line) and presence of 1:0.5 wt/wt gB625 (○, dotted line) peptide.

In conclusion, this study has permitted to discriminate the mechanism of action of the gH625 peptide in the presence of lipid membranes. In particular, experimental results have demonstrated that the lipid composition is fundamental to drive the membrane-peptide interaction, and particularly that the presence of lipid rafts favours the peptide insertion.

4.9 Clickable functionalization of liposomes with the gH625 peptide from HSV-1 for intracellular delivery

Recently, great attention has been devoted to the study of hydrophobic peptides that efficiently traverse biological membranes, promoting lipid-membrane reorganizing processes, such as fusion or pore formation and thus, involving temporary membrane destabilization and subsequent reorganization. The previously studied gH625 peptide was considered as a potential transporter of liposomes loaded with anticancer drugs, such as doxorubicin. It was used to decorate liposomes, loading doxorubicin, by using a post-aggregation strategy based on click-chemistry [33]. This procedure consists in the preparation of liposomes containing accessible azido functions on their external surface and subsequently in the coupling of the azido functions with alkyne moieties present in the peptide derivative, accordingly to click chemistry procedures.

The positioning of the coupled peptide relative to the liposome surface was investigated by ESR, using peptides modified according to a site-directed spin-labeling approach [33]. To this aim gH625-Pra analogues, labeled with the TOAC radical group through a site-directed spin-labeling approach, were used. ESR spectra of the free labeled peptides dissolved in HEPES buffer consist of three narrow lines (see Figure 4.9.1), typical of an unstructured peptide with few constraints on the motion of the reporter group. Subsequently, the labeled peptides were chemically linked to the DOPG/(C18)₂L-N₃ liposomes by following the same procedure used for the parent unlabeled peptide, obtaining four suspensions of functionalized liposomes. The analysis of their ESR spectra, reported in Figure 4.9.1, gives information on the positioning of the gH625 relative to the surface of the liposome to which it is linked. In all cases a clearly defined axially anisotropic line shape is observed, indicating that the reporter group, wherever positioned along the peptide sequence, assumes a well defined orientation relative to the bilayer. This behavior indicates that the peptide does not protrude in the aqueous medium surrounding

the liposome, in which the label would have assumed a much higher mobility freedom, but rather interacts with the surface of the lipid bilayer.

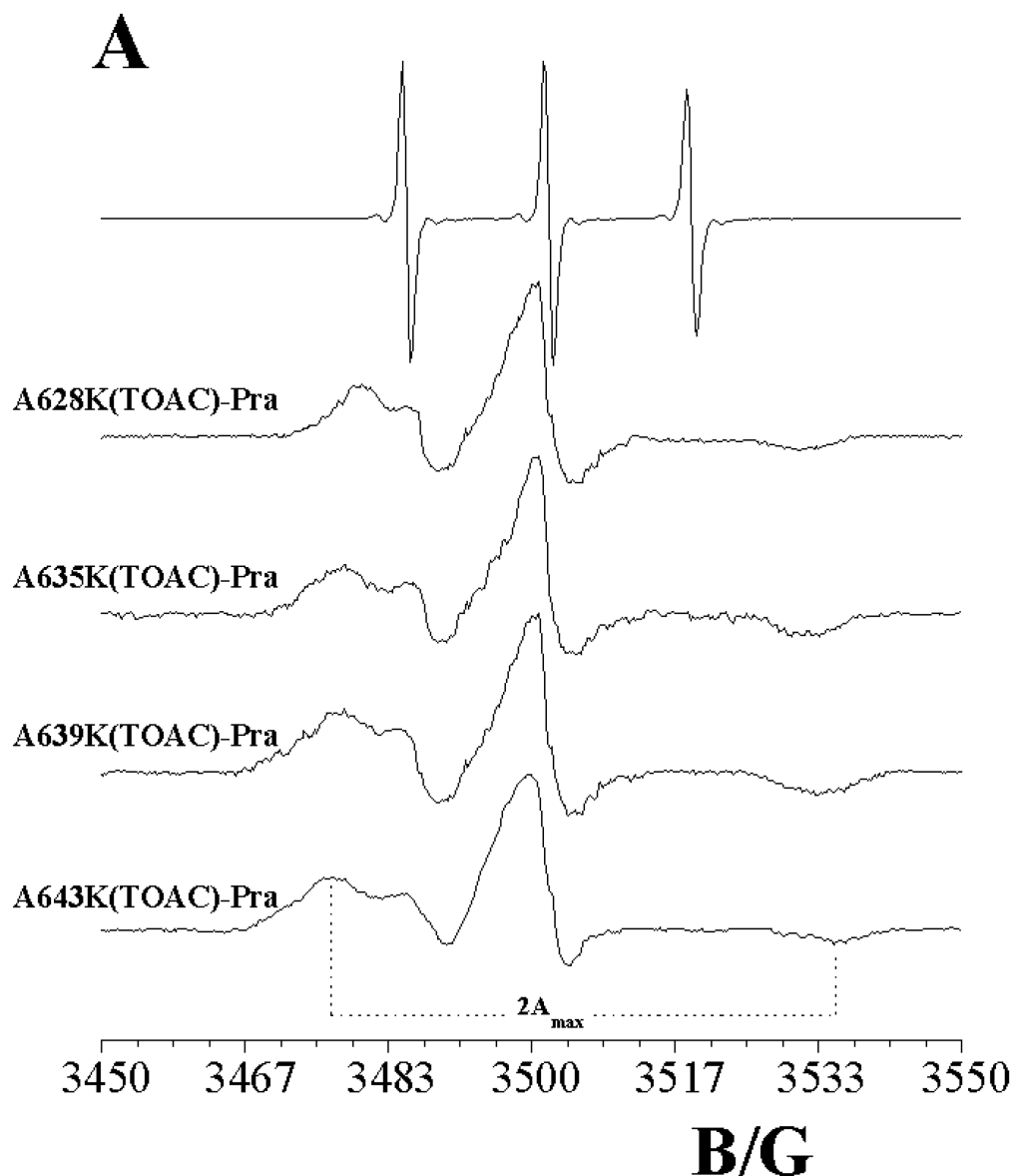


Figure 4.9.1 - ESR spectra of TOAC peptides linked to DOPG/(C18)₂L-N₃ liposomes. An EPR spectrum of the free peptide A639K(TOAC)-gH625-Pra in aqueous buffer is also shown.

Analysis of the figure shows that the spectrum anisotropy decreases in going from A643K(TOAC)-gH625 to A628K(TOAC)-gH625, indicating that the peptide segments closer to the C-terminus, which is chemically linked to the lipid, are more strictly oriented relative to the bilayer. This evidence can be easily quantified by measuring the outer

hyperfine splitting, $2A_{\max}$, which is a reliable and easy-to-perform estimate of the segmental chain mobility. $2A_{\max}$ is defined as separation, expressed in Gauss, between the low-field maximum and the high-field-minimum of the spectrum, and tends to increase with increasing the restriction in the label mobility. Figure 4.9.2 shows that, as the label position is moved from position 628 to 643, $2A_{\max}$ increases. This evidence suggest that the peptide does not insert in the bilayer hydrophobic core, but rather remain adsorbed on its surface remaining exposed to aqueous environment.

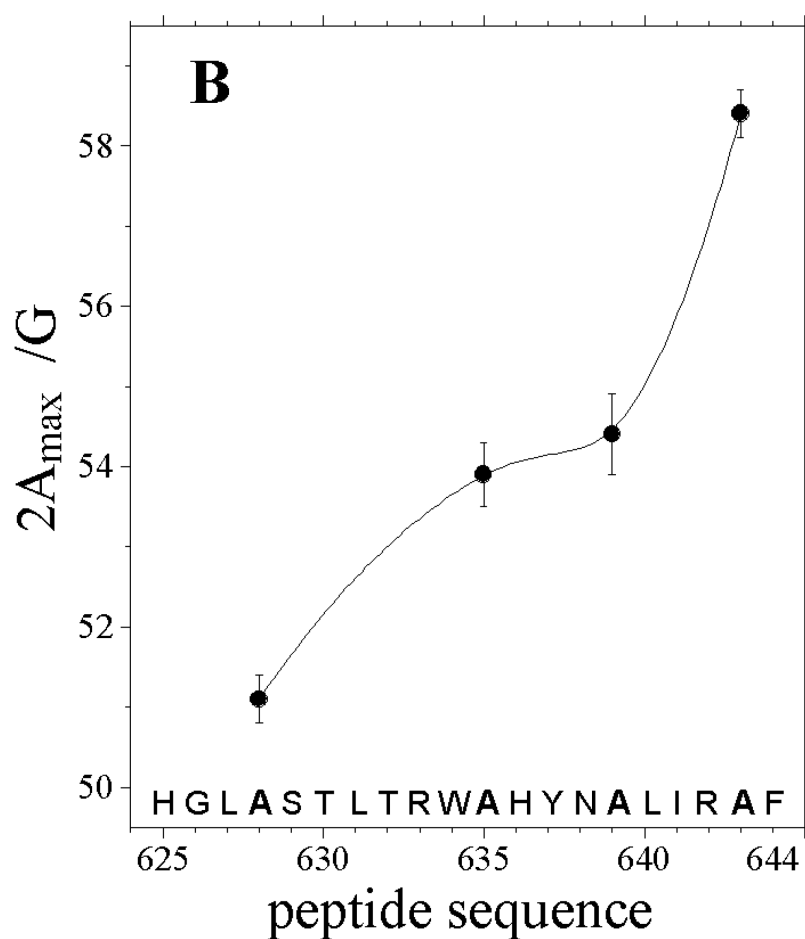


Figure 4.9.2 - Dependence on spin-label position along the peptide sequence of the outer hyperfine splitting, $2A_{\max}$, of TOAC peptides linked to DOPG/(C18)₂L-N₃liposomes.

4.10 Membrane charge dependent states of the β -amyloid fragment A β (16-35) with differently charged micelle aggregates

A β (16-35) peptide represents the hydrophobic central part of β -amyloid peptide, which is implicated in aggregation/disaggregation processes. In fibril structural models, it represents the repetitive unit of β -amyloid peptide aggregates and was found to be specifically linked to antibodies. A great deal of evidence implicates the plasma membrane in processes leading to the misfolding and aggregation of β -amyloid peptides. Accordingly, A β peptides have been extensively analyzed in membrane-mimicking systems that are characterized by different complexities and compositions. Although all evidence shows that membrane charge is a critical factor in modulating the conformational behavior of amyloid peptides, the exact definition for the role of charge in affecting conformations of amyloid peptide is controversial. Some data suggest that net negative charge is essential in favoring the presence of peptide monomers. Some others indicate that negatively charged membranes could catalyze the transition of A β -peptide to β -conformation and aggregation.

In this contest, a study on the behavior of A β (16-35) in pure SDS micelles and in mixed DPC/SDS 90/10 w:w micelles, in response to their negative charge modifications, was realized by an ESR investigation [34]. Two complementary series of experiments by randomly including spin-labeled peptides and spin-labeled lipids in micelle aggregates. For the formed experiment, spin labeled peptides, including A β (16-35)-MTSL^{C-term}, A β (16-35)G25C-MTSL, or A β (16-35)-MTSL^{N-term} (**II**, **III**, and **IV**, respectively, in Figure 4.10.1), were dissolved in the appropriate amount of aqueous buffer or micellar solution to obtain a 0.2 mM peptide concentration. The peptide/surfactant molar ratio was set to 1:100. Thus, in these experiments, the effect of micelles on the ESR spectrum of labeled peptides was observed. In the latter series of measurements, the spin probes 5-doxylstearic acid and 16-

doxylstearic acid (5-DSA and 16-DSA, respectively) were inserted into micellar aggregates at a 1:100 probe/surfactant mole ratio (surfactant concentration 20 mM). The effect of unlabeled peptides A β (16-35), at a 1:10 peptide/surfactant mole ratio, on their ESR spectrum was monitored. In both series of experiments, the samples were deoxygenated and successively sealed in 1.00 mm i.d. quartz capillaries in a nitrogen atmosphere.

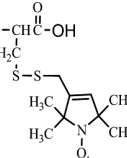
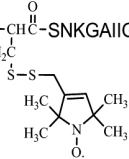
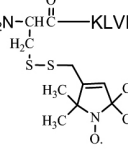
A β (16-35) Amyloid Peptide and the MTLs labeled derivatives	Name
KLVFFAEDVGSNKGAIIGLM	A β (16-35) (I)
$\text{KLVFFAEDVGSNKGAIIGLM}-\overset{\text{H}}{\underset{\text{H}_2\text{C}}{\text{N}}}-\overset{\text{O}}{\parallel}{\text{C}}-\text{OH}$ 	A β (16-35)-MTSLCterm (II)
$\text{KLVFFAEDV}-\overset{\text{H}}{\underset{\text{H}_2\text{C}}{\text{N}}}-\overset{\text{O}}{\parallel}{\text{C}}-\text{SNKGAIIGLM}$ 	A β (16-35) G25C-MTSL (III)
$\text{H}_2\text{N}-\overset{\text{O}}{\parallel}{\text{C}}-\text{KLVFFAEDVGSNKGAIIGLM}$ 	A β (16-35)-MTSLNterm (IV)

Figure 4.10.1 - Aminoacid sequence of A β (16-35) (I), A β (16-35) bearing MTSL spin label at the C- terminus (II), in the middle of the sequence (III) and at the N-terminus (IV).

In both cases, cyclic nitroxides were used as spin-labels due to their remarkable stability and to the localization of the spin density on the NO moiety, which allows to extract a great deal of information on the label solubilization site from the ESR spectrum. Indeed, because of the coupling between the electron spin and the nuclear spin of the nitrogen atom, the ESR spectrum of a cyclic nitroxide presents three lines (see Figure 4.10.2). The spacing between them corresponds to the nitrogen isotropic hyperfine coupling constant, A_N , which increases with the polarity of the medium in which the

nitroxide is embedded. Furthermore, a detailed analysis of the lines' amplitudes allows to obtain the nitroxide correlation time, τ_c , which depends on the label rotational mobility, as determined by the microenvironment viscosity and/or by specific interactions. From a qualitative viewpoint, narrow lines (low τ_c) indicate that the label is quite free to rotate, while broad lines (high τ_c) indicate that the motional freedom is reduced. Broadening is usually much more evident for the line at high field [35].

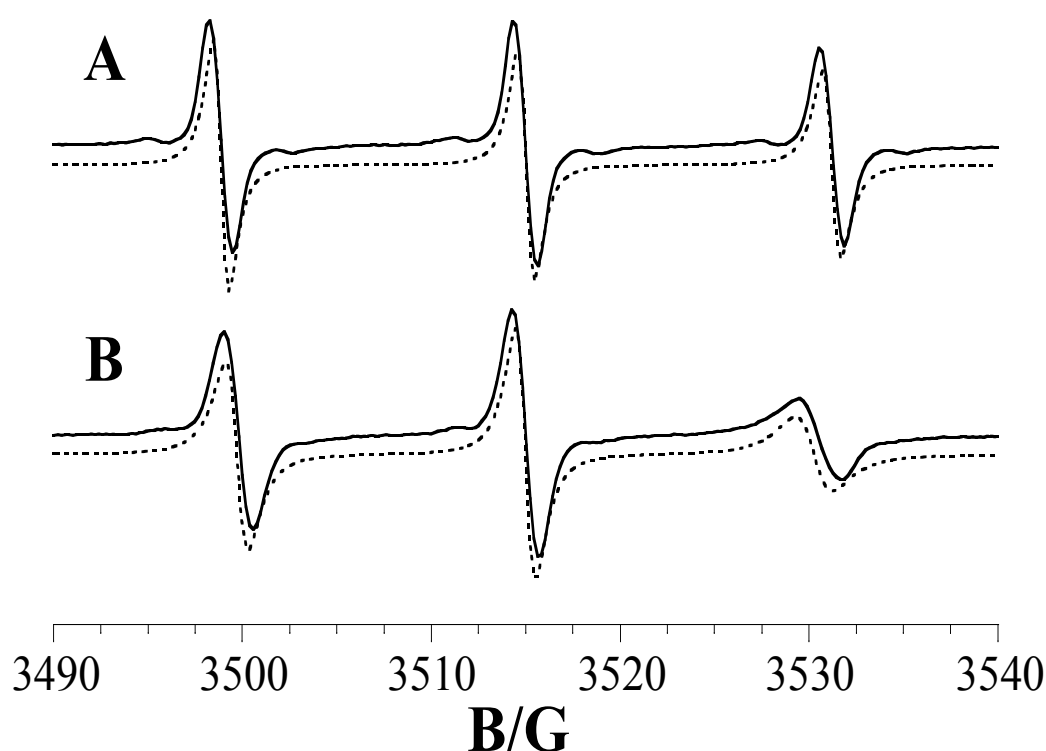


Figure 4.10.2 - Experimental (continuous line) and simulated (dotted line) EPR spectra of A β (16-35), labeled at the C terminus, in phosphate buffer (A) and in SDS solution (B).

ESR spectra of all spin-labeled peptides were acquired in phosphate buffer, SDS, and DPC/SDS (90:10) micellar solutions. In all cases, the expected three hyperfine lines were observed. This is evidence that no peptide self-aggregation took place. If this were the case, then spin-spin interactions would have provoked the collapse of the three lines, i.e., the appearance of a single very broad line [36].

Furthermore, in all the systems considered here, ESR spectra showed narrow lines indicative of an isotropic fast motion. This is despite the fact that a slight, but significant broadening, due to the interaction between spin-labeled peptides and micelles, was evident (see spectrum B in Figure 4.10.2 with respect to spectrum A).

	A_N /G	$\tau_C \times 10^{10}$ /s
Aβ(16-35)^{C-term}		
phosphate buffer	16.19 \pm 0.02	1.8 \pm 0.2
SDS	15.32 \pm 0.02	3.3 \pm 0.3
DPC/SDS 90:10	16.10 \pm 0.02	3.2 \pm 0.3
Aβ(16-35)^{N-term}		
phosphate buffer	16.20 \pm 0.02	1.7 \pm 0.2
SDS	15.81 \pm 0.02	2.8 \pm 0.3
DPC/SDS 90:10	15.68 \pm 0.02	3.1 \pm 0.3
Aβ (16-35)G25C-MTSL		
phosphate buffer	16.21 \pm 0.02	1.7 \pm 0.2
SDS	15.26 \pm 0.02	3.7 \pm 0.3
DPC/SDS 90:10	15.92 \pm 0.02	4.2 \pm 0.3
5-DSA		
SDS	15.07 \pm 0.04	17 \pm 2
SDS-A β (16-35)	14.96 \pm 0.04	28 \pm 3
DPC/SDS 90:10	14.48 \pm 0.04	27 \pm 3
DPC/SDS- A β (16-35)	14.39 \pm 0.04	30 \pm 3
16-DSA		
SDS	15.15 \pm 0.04	6.7 \pm 0.6
SDS-A β (16-35)	15.09 \pm 0.04	12.8 \pm 1.3
DPC/SDS 90:10	14.68 \pm 0.04	10.5 \pm 1.0
DPC/SDS- A β (16-35)	14.74 \pm 0.04	10.7 \pm 1.1

Table 4.10.1 - Nitrogen coupling constant, A_N , and spin label correlation time, τ_C , measured by ESR experiments on either spin-labeled A β (16-35) in phosphate buffer, SDS and DPC/SDS micelles or doxyl stearic acids in SDS and DPC/SDS micelles, in the absence and in the presence of A β (16-35).

Consequently, spectral analysis was carried out according to the classical theory of motional narrowing for ESR lines [37]. A_N and τ_C values for A β (16-35)-MTSL^{C-term} (II), A β (16-35)G25C-MTSL (III) and A β (16-35)-MTSL^{N-term} (IV) in the various systems analyzed in the present work are shown in Table 4.10.1.

In phosphate buffer, no difference was found between values for the three spin-labeled peptides. Thus, the environment in which the nitroxide label is embedded did not depend on its positioning along the peptide chain, indicating that the whole molecule was fully exposed to the aqueous medium. Overall, significant changes in the ESR parameters, owing to the presence of SDS or DPC/SDS micelles, were evident. Particularly, the τ_C value increased, a consequence of a decrease in the label mobility. This evidence indicates peptide interactions with the micellar aggregates to occur. The whole peptide was involved in the interaction, as the three spin-labeled peptides showed comparable τ_C changes, even though a slightly higher τ_C increase was found for A β (16-35)G25C-MTSL. At the same time, the decrease in A_N indicates that spin-labels were embedded in a less polar microenvironment with respect to the aqueous medium. Specifically, as far as DPC/SDS micelles are considered, the extent of the A_N reduction is quite low (from 0.1 to 0.5 G) for all the three spin-labeled peptides. Consequently, these evidences suggest a shallow insertion of the whole peptide in the mixed micellar aggregates (see Figure 4.10.3). In contrast, A β (16-35)-MTSL^{C-term}(II) and A β (16-35)G25C-MTSL (III) presented a more pronounced A_N decrease in SDS micelles (~1 G). This suggests a deep penetration of the second half of the A β (16-35) sequence in the SDS micellar apolar core, with the N-terminus being more exposed to the external medium (see Figure 4.10.3).

To see whether the interaction with A β (16-35) influenced the microstructure of SDS and DPC/SDS (90:10) micelles, ESR measurements on micellar solutions in the presence and absence of the peptide were performed. Spin labels used for this experiment were 5-doxylstearic acid (5-DSA) and 16-doxylstearic acid (16-DSA). The former provided information on the micellar layer just below the external surface, while the latter gave information on the interior of the micellar hydrophobic core.

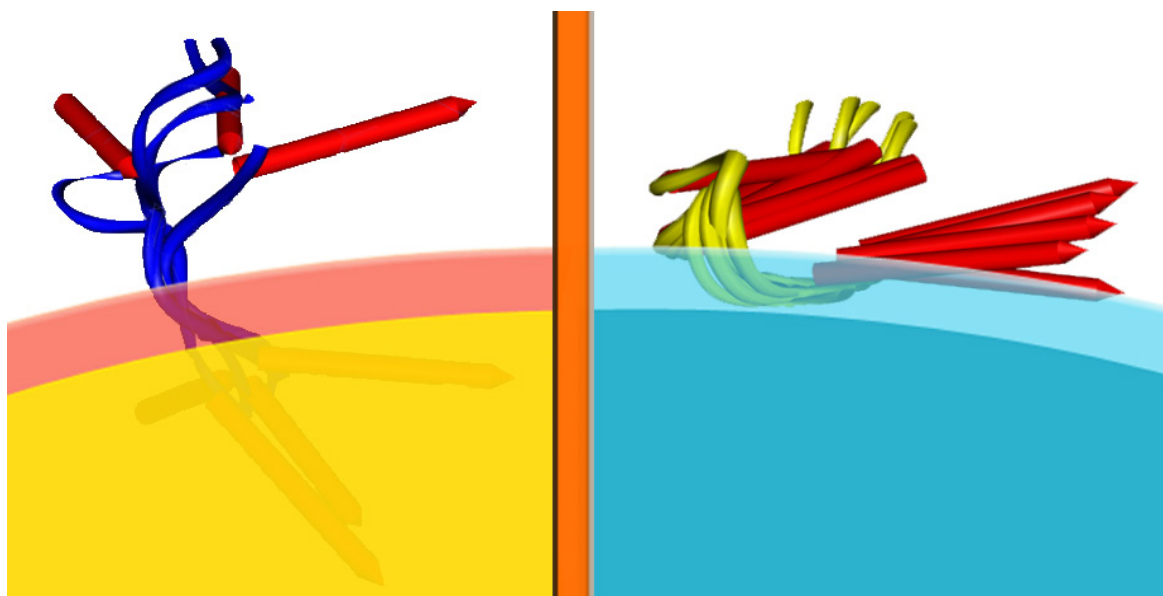


Figure 4.10.3 - Schematic representation of A β (16-35) orientation on SDS (left) and DPC/SDS (right) micelles. The portion of A β (16-35) spanning from the middle to the C-terminus is partially embedded in SDS micelles (left). Embedding of A β (16-35) is reduced in DPC/SDS, (right).

Spectroscopic parameters obtained from these spectra are shown in Table 4.10.1. In both micellar systems, the τ_C value was higher for 5-DSA than for 16-DSA. In other words, the motion of 5-DSA was slower than for 16-DSA. This indicates a flexibility increase in segmental chain mobility when going from surfactant polar headgroups to the inner hydrophobic core of micelles. The presence of A β (16-35) caused significant effects on SDS micelles. In fact, for both spin-labeled surfactants, τ_C significantly increased. The reduction of the label mobility is a clear evidence of the insertion of the peptide, or of a segment of it, into the micellar core, since the local structuring of the alkyl chain tends to be more ordered in proximity of a guest molecule [1,4]. In contrast, the spectra of both spin labels in DPC/SDS mixed micelles were almost unaffected by the presence of A β (16-35), indicating no significant insertion of the peptide into the micelle interior. Thus, evidences obtained using spin-labeled lipids are in perfect agreement with those obtained with spin-labeled peptides, and support the peptide-micelle relative positioning proposed in Figure 4.10.3.

4.11 Role of β -sheet breaker peptides in preventing A β self-aggregation

An attractive therapeutic strategy for Alzheimer's disease is the inhibition of the soluble β -amyloid aggregation using synthetic β -sheet breaker peptides capable of binding A β but unable to become part of a β -sheet structure. One of these is a 5-residue synthetic β -sheet breaker peptide, iA β 5p, which was found to be able to inhibit and disassemble amyloid fibrils *in vitro* [38]. Since the early stages of the A β aggregation process are supposed to occur close to the neuronal membrane, it is strategic to define the iA β 5p positioning with respect to lipid bilayers and to clarify the interplay between iA β 5p and A β . These studies were realized by ESR spectroscopy [39,40].

4.12 Interaction of a β -sheet breaker peptide with lipid membranes

First, the iA β 5p positioning in biomembranes was investigated by ESR experiments [39]. Two sets of experiments were performed. In the first one, spin-labeled β -sheet breaker peptides iA β 5p-SL^{Nterm} or iA β 5p-SL^{Cterm} were dissolved in the appropriate amount of aqueous buffer or liposome solution. Thus, in these experiments the effect of the liposomes on the ESR spectrum of the spin-labeled peptide was observed. In the second set of measurements spin-labeled phosphocholines, 5-PCSL and 14-PCSL, were inserted in the liposome aggregates at a 1:100 spin label/phospholipid mole ratio and the effect of unlabelled iA β 5p peptide on their ESR spectrum was monitored.

The ESR spectra of the two spin-labeled peptides were acquired in phosphate buffer at pH=7.4, DOPC and DOPC/CHOL (80:20 wt/wt) bilayers. In phosphate buffer, both ESR spectra show the typical lineshape of isotropic fast motion, indicating that the whole molecule is fully exposed to the aqueous medium (see Figure 4.12.1A for iA β 5p-SL^{Nterm}). According to the classical theory of motional narrowing of ESR lines, the nuclear spin

state dependence of the width of the nitroxide hyperfine line, ΔB , is described by the formula:

$$\Delta B = A + B m_I + C m_I^2 \quad (4.12.1)$$

where m_I is the nitrogen nuclear spin quantum number. As reported in literature [35], the values of A , B , and C can be determined by means of a least-squares fitting routine of experimental spectra using Eqn (4.12.1). In turn, their values allow calculation of the isotropic nitrogen hyperfine coupling constant, A_N , and the tumbling correlation time of the spin-probe, τ_C .

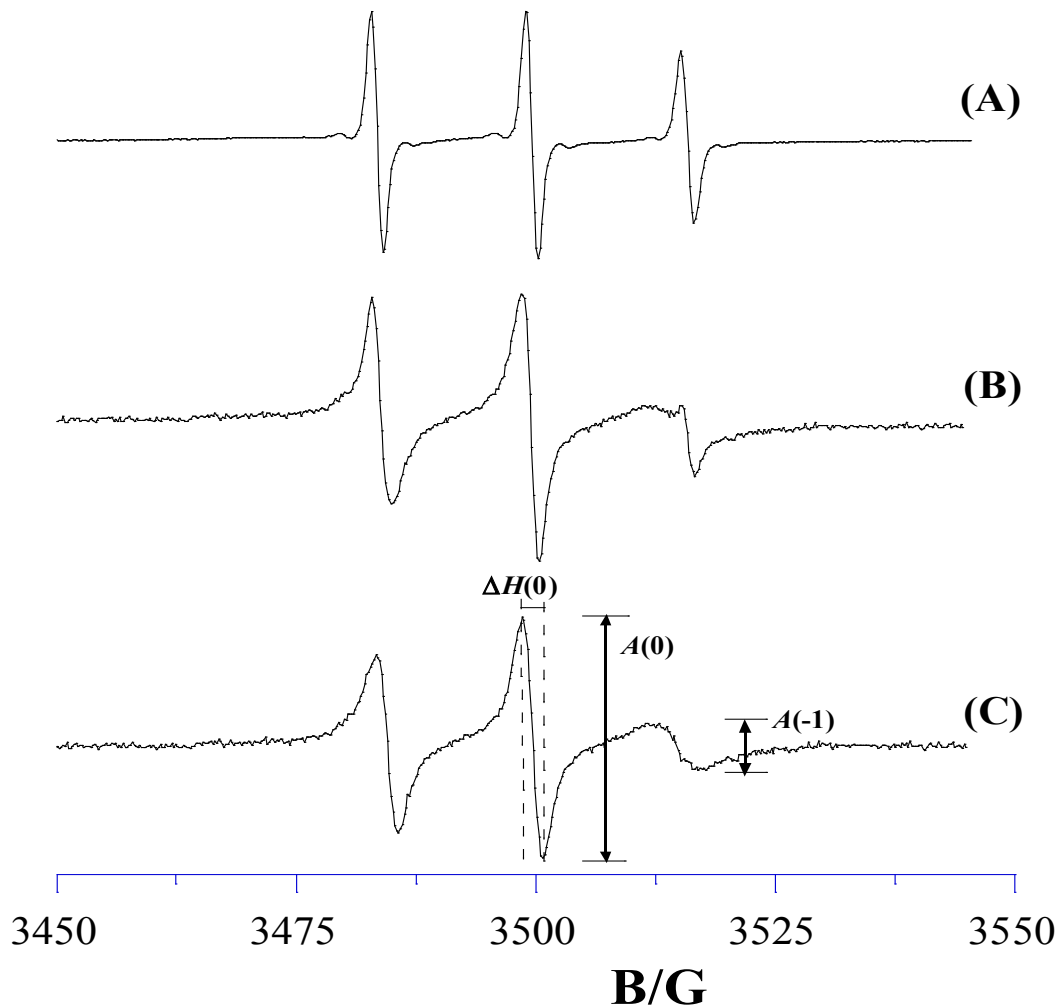


Figure 4.12.2 - ESR spectra of $iA\beta 5p-SL^{Nterm}$: (A) in phosphate buffer, (B) in DOPC membranes (peptide to lipid ratio 1.3:100 mol/mol) and (C) slow motion signal, obtained by subtracting spectrum A, multiplied by the weighting factor 0.3, from spectrum B.

These parameters furnish information about the local physicochemical properties of the label. Particularly, A_N depends on the polarity of the medium in which the nitroxide is embedded, whereas τ_C variations clearly show changes in the probe rotational mobility, as determined by the microenvironment viscosity and/or by specific interactions.

For iA β 5p-SL^{Nterm} in phosphate buffer we found $A_N=16.13\pm0.02$ G and $\tau_C=(5.6\pm0.2)\times10^{-9}$ s. These values are remarkably close to those found for iA β 5p-SL^{Cterm} ($A_N=16.12\pm0.02$ G and $\tau_C=(5.7\pm0.3)\times10^{-9}$ s).

The presence of DOPC liposomes strongly affects the ESR spectra of both spin-labeled peptides. In this case a complex lineshape characterized by the superposition of two signals is observed (see Figure 4.12.2B for iA β 5p-SL^{Nterm}): a fast motion spectrum, similar to that obtained for the peptide in buffer, and a slow motion spectrum. This evidence indicates that the spin-labeled peptide is distributed in two populations of which the first one is composed by unperturbed molecules dissolved in the aqueous medium, and the second one directly interacts with the phospholipid bilayer. By subtracting the peptide spectrum in buffer from that in DOPC bilayers, we obtained the isotropic slow motion spectrum shown in Figure 4.12.2C.

In the case of slow motion spectra, the theory on which Eqn (4.12.1) is based does not hold anymore, so that we analyzed this spectrum by graphically estimating A_N and τ_C . Particularly, the apparent correlation time τ_C was determined according to [41]:

$$\tau_C = (0.65 \times 10^{-9}) \Delta H_0 [(A_0/A_{-1})^{1/2} - 1] \quad (4.12.2)$$

where ΔH_0 is the peak-to-peak width of the center line in Gauss, A_0 is the amplitude of the center line, and A_{-1} is the amplitude of the high-field line.

For the spectrum reported in Figure 4.12.2C, we obtained $A_N=14.58\pm0.02$ G and $\tau_C=(1.9\pm0.2)\times10^{-8}$ s. The decrease of A_N , when compared to that obtained from the

spectrum registered in buffer, indicates that the label is embedded in a less polar microenvironment. At the same time, the increase of τ_C indicates that the label motion is hampered. Practically identical results were obtained for $iA\beta 5p-SL^{Cterm}$ (spectra not shown).

In the presence of DOPC/CHOL bilayers, the ESR spectra of the two spin-labeled peptides show an even more complex lineshape (see Figure 4.12.3B for $iA\beta 5p-SL^{Nterm}$) given by the overlap of a fast motion spectrum of unperturbed molecules with an anisotropic slow motion spectrum.

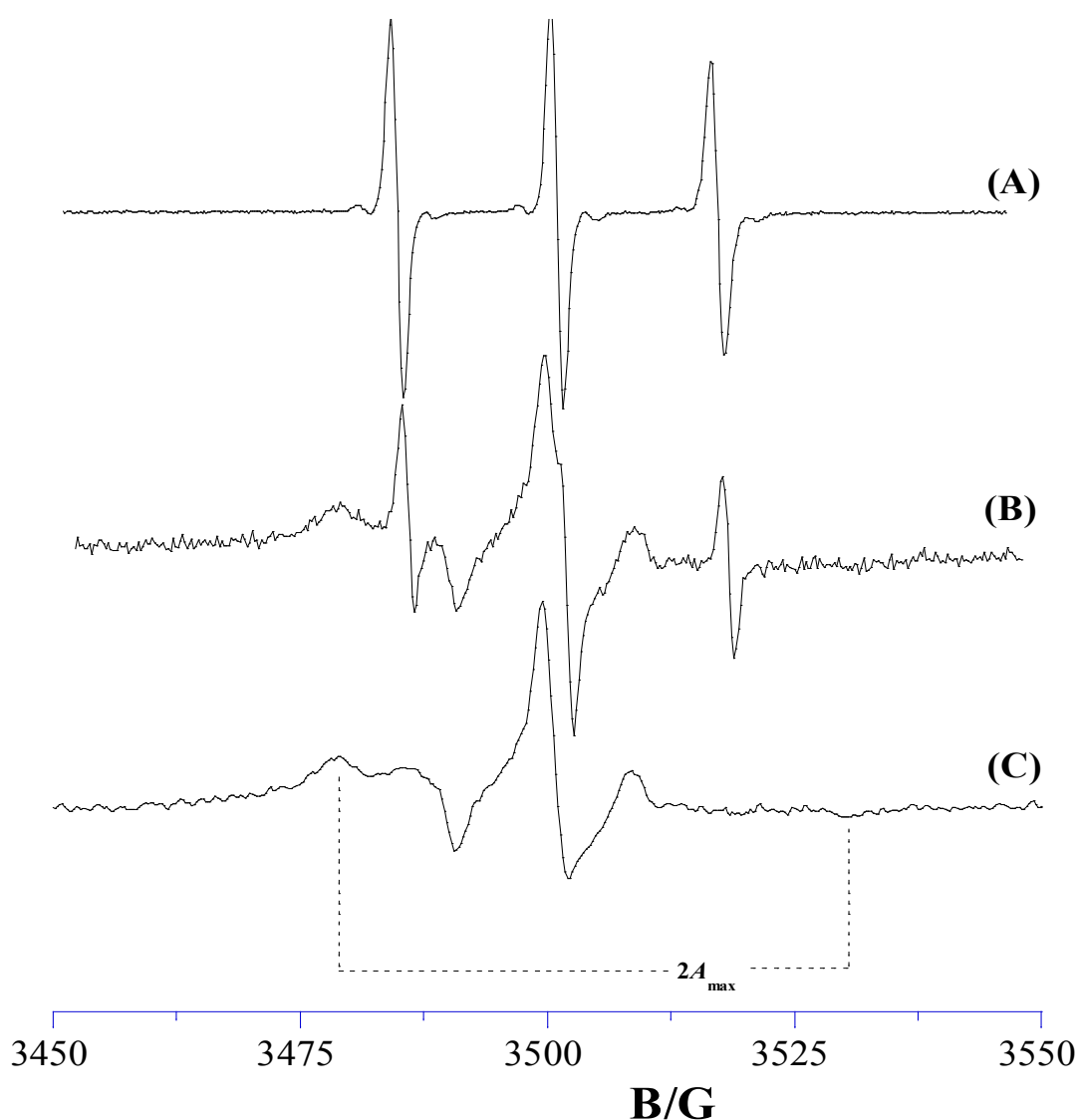


Figure 4.12.3 - ESR spectra of $iA\beta 5p-SL^{Nterm}$: (A) in phosphate buffer, (B) in DOPC/CHOL membranes (peptide to lipid ratio 1.3:100 mol/mol) and (C) slow motion signal, obtained by subtracting spectrum A, multiplied by the weighting factor 0.6, from spectrum B.

Subtraction of the spectrum in buffer from the experimental one results in the anisotropic spectrum shown in Figure 4.12.3C. For anisotropic spectra, evaluation of magnetic and diffusive parameters, analogue to A_N and τ_C , is an extremely difficult task. For this reason, analysis of this spectrum was realized determining the outer hyperfine splitting ($2A_{\max}$) value. This parameter, obtained by measuring the difference between the low-field maximum and the high-field minimum, through a home-made, MATLAB-based software routine, is dependent on both the amplitude (i.e., order) and rate of chain rotational motion, and is therefore a useful parameter for characterizing dynamics of molecules deeply inserted in phospholipid membranes. By analyzing Figure 4.12.3C, we found $2A_{\max}=51.7\pm 0.2$ G. Also in this case, very similar results were obtained for $iA\beta 5p$ -SL^{Cterm} (spectra not shown).

ESR spectroscopy allows to quantitatively estimate the partition coefficient of the labeled peptides between the lipid bilayer and the aqueous medium. The binding process can be described by the equilibrium [42]



where P and L stand for peptide and lipid, respectively. Consequently, it is possible to define the apparent partition coefficient:

$$K_{\text{app}} = \frac{[PL]}{[P][L]} \quad (4.12.4)$$

Eqn (4.12.4) can be easily rearranged as:

$$X_b = K_{\text{app}} C_f \quad (4.12.5)$$

where X_b is the molar fraction of bound peptide per lipid and C_f is the free peptide concentration. Thus, K_{app} can be determined as slope of the linear trend obtained by plotting X_b vs. C_f . Deviations from linearity of this graph indicate a cooperative peptide binding, i.e., strong interactions among the bound peptides. Methodology for obtaining K_{app} from ESR measurements is well established [43]. The fraction of bound peptide, f_b , is calculated according to the relation:

$$f_b = \frac{A(-1)_f - A(-1)_x}{A(-1)_f - A(-1)_b} \quad (4.12.6)$$

where $A(-1)_f$ and $A(-1)_x$ are the peak-peak amplitudes of the high-field ($M_I = -1$) line for the peptide free in solution and in the considered liposomal sample, respectively. $A(-1)_b$ is the amplitude of the high-field line for a fully bound peptide. C_f and C_b , the concentration of membrane-bound peptide, can be calculated from f_b and the known $[P]$. Finally, X_b , can be calculated as the ratio of C_b and $[L]$. Application of the method requires various measurements to be conducted at different peptide to lipid ratio.

In Figure 4.12.4 the trends of X_b vs. C_f for $iA\beta 5p-SL^{Nterm}$ in DOPC and DOPC/CHOL liposomal samples are reported. In both cases a linear trend is obtained, i.e., no cooperativity in peptide binding is evident. The K_{app} values are $62 \pm 2 \text{ M}^{-1}$ and $32 \pm 1 \text{ M}^{-1}$ for $iA\beta 5p-SL^{Nterm}$ in DOPC and DOPC/CHOL bilayers, respectively.

As a complementary part of this research, we investigated the interaction between the unlabeled peptide $iA\beta 5p$ and DOPC or DOPC/CHOL bilayers incorporating spin-labeled phosphatidylcholines. Analysis of spin-labeled phosphatidylcholines' spectra was also realized determining the outer hyperfine splitting ($2A_{max}$) values, which are reported in Table 4.12.1.

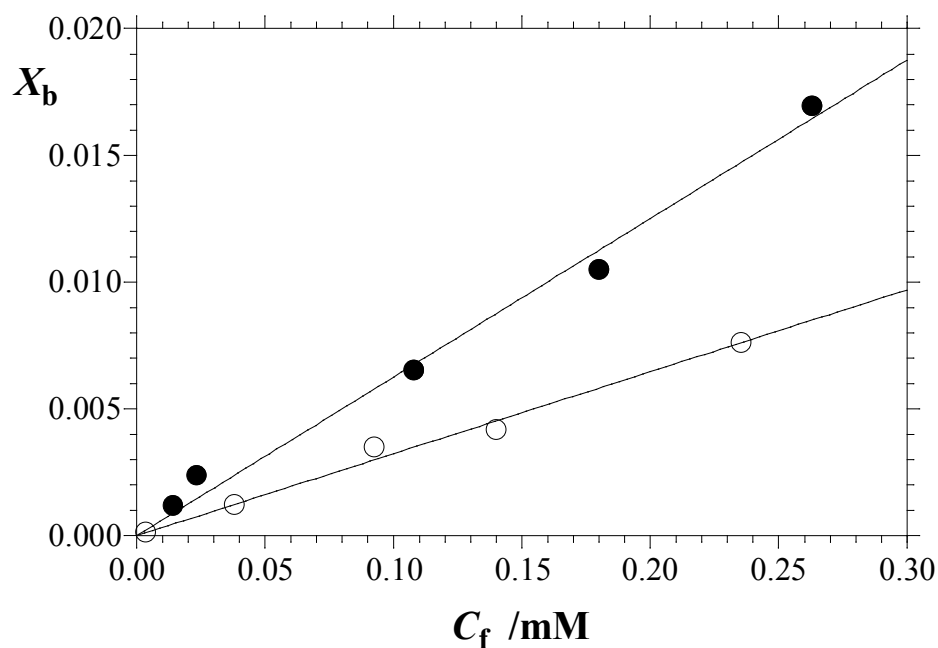


Figure 4.12.4 - Binding isotherms obtained for $iA\beta 5p-SL^{Nterm}$ in: DOPC (*full circles*) and DOPC/CHOL bilayers (*open circles*).

	$2A_{max} / G$
5-PCSL	
DOPC	51.9 ± 0.1
DOPC/ $iA\beta 5p$	53.3 ± 0.2
DOPC/CHOL	53.5 ± 0.1
DOPC/CHOL/ $iA\beta 5p$	56.0 ± 0.2
14-PCSL	
DOPC	32.9 ± 0.1
DOPC/ $iA\beta 5p$	32.7 ± 0.1
DOPC/CHOL	33.7 ± 0.2
DOPC/CHOL/ $iA\beta 5p$	37.4 ± 0.2

Table 4.12.1 - Outer hyperfine splitting, $2A_{max}$, values of 5-PCSL and 14-PCSL in DOPC and DOPC/CHOL bilayers in the absence and in the presence of $iA\beta 5p$.

The ESR spectrum of 5-PCSL in DOPC bilayers, shown in Figure 4.12.5 (lower spectrum, solid line), presents a clearly defined axially anisotropic lineshape, with a value of the outer hyperfine splitting, $2A_{max}$, equal to 51.9 ± 0.1 G. We also investigated DOPC bilayers including phosphatidylcholine spin labeled on the 14 C-atom of the sn-2 chain (14-PCSL), in which the nitroxide group is positioned close to the terminal methyl region

of the chain. In this case a narrow three-line, quasi-isotropic spectrum is obtained, see Figure 5 (upper spectrum, solid line). The higher isotropy of the 14-PCSL spectrum with respect to that obtained for 5-PCSL indicates a flexibility increase in segmental chain mobility in going from the polar headgroups to the inner hydrophobic core, which is a characteristic hallmark of the liquid-crystalline state of fluid phospholipid bilayers.

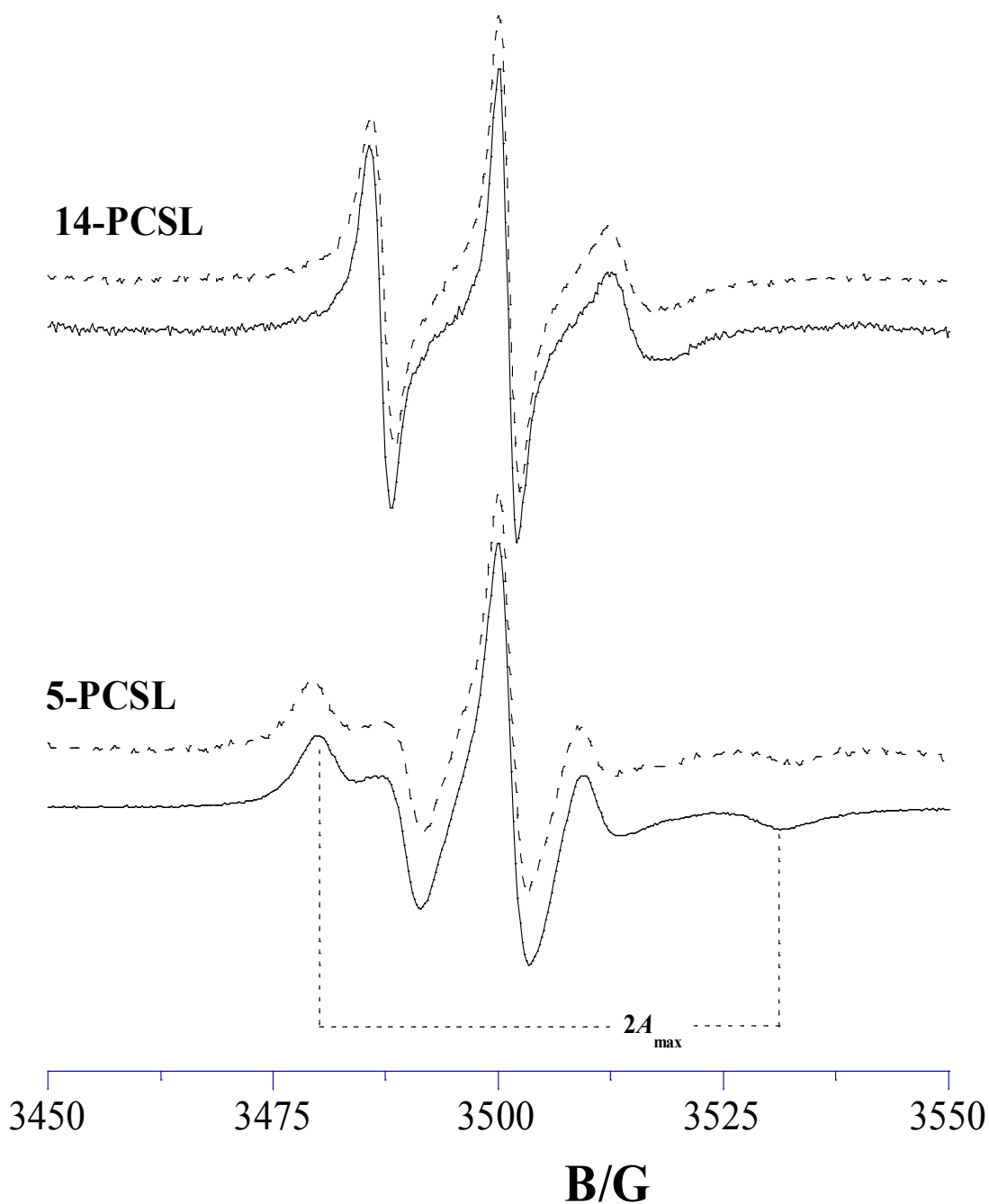


Figure 4.12.5 - ESR spectra of 5-PCSL and 14-PCSL positional isomers of spin-labeled phosphatidylcholine in DOPC bilayers in the absence (*solid line*) and in the presence (*dashed line*) of 1:1 wt/wt iA β 5p peptide.

The association of β -sheet breaker peptide with lipid membranes can be detected by the perturbation of the chain mobility of spin-labeled lipids, by using ESR spectroscopy as found for classical water-soluble peripheral membrane proteins and derived peptides [51,52]. Addition of iA β 5p peptide to pure DOPC bilayers, at a 8:100 mol/mol ratio, significantly affects the 5-PCSL spectrum, see Figure 4.12.5, dashed line. In fact, the peptide causes a slight but significant $2A_{\max}$ increase (from 51.9 ± 0.1 G to 53.3 ± 0.2 G), i.e., the mobility of the spin-labeled chains decreases by interaction of the peptide with the membrane. In contrast, the addition of iA β 5p to pure DOPC bilayers does not cause any change in the 14-PCSL spectrum, as shown in Figure 4.12.5.

We also investigated DOPC bilayers at 20% wt/wt concentration of CHOL, in absence and in the presence of the peptide. The 5-PCSL and 14-PCSL ESR spectra in DOPC/CHOL bilayers are shown in Figure 4.12.6 and the corresponding $2A_{\max}$ values are reported in Table 4.12.1. Cholesterol induces a $2A_{\max}$ increase for both spin-labels. It is interesting to observe that the 14-PCSL spectrum keeps a quasi-isotropic lineshape, an evidence that, despite a certain stiffening, at the considered cholesterol content, the DOPC/CHOL bilayer is still in the liquid disordered state.

Addition of peptide at a 8:100 mol/mol ratio significantly affects the 5-PCSL spectrum. Indeed, the peptide causes a slight $2A_{\max}$ increase (from 53.5 ± 0.1 G to 56.0 ± 0.2 G), i.e., the mobility of the spin-labeled chains decreases by interaction of the peptide with the bilayer. The effect of the addition of peptide on the 14-PCSL spectra in DOPC/CHOL bilayers is shown in Figure 4.12.6. In this case a clearly anisotropic spectrum is obtained, as opposed to the quasi-isotropic spectrum obtained in peptide absence. This is particularly revealed by the appearance of a second high-field minimum. The $2A_{\max}$ trend confirms what is inferred from the spectra. Indeed, the presence of the peptide causes a significant $2A_{\max}$ increase with respect to that registered in its absence (from 33.7 ± 0.2 G to 37.4 ± 0.2 G), indicating that the peptide is deeply inserted into the lipid bilayer.

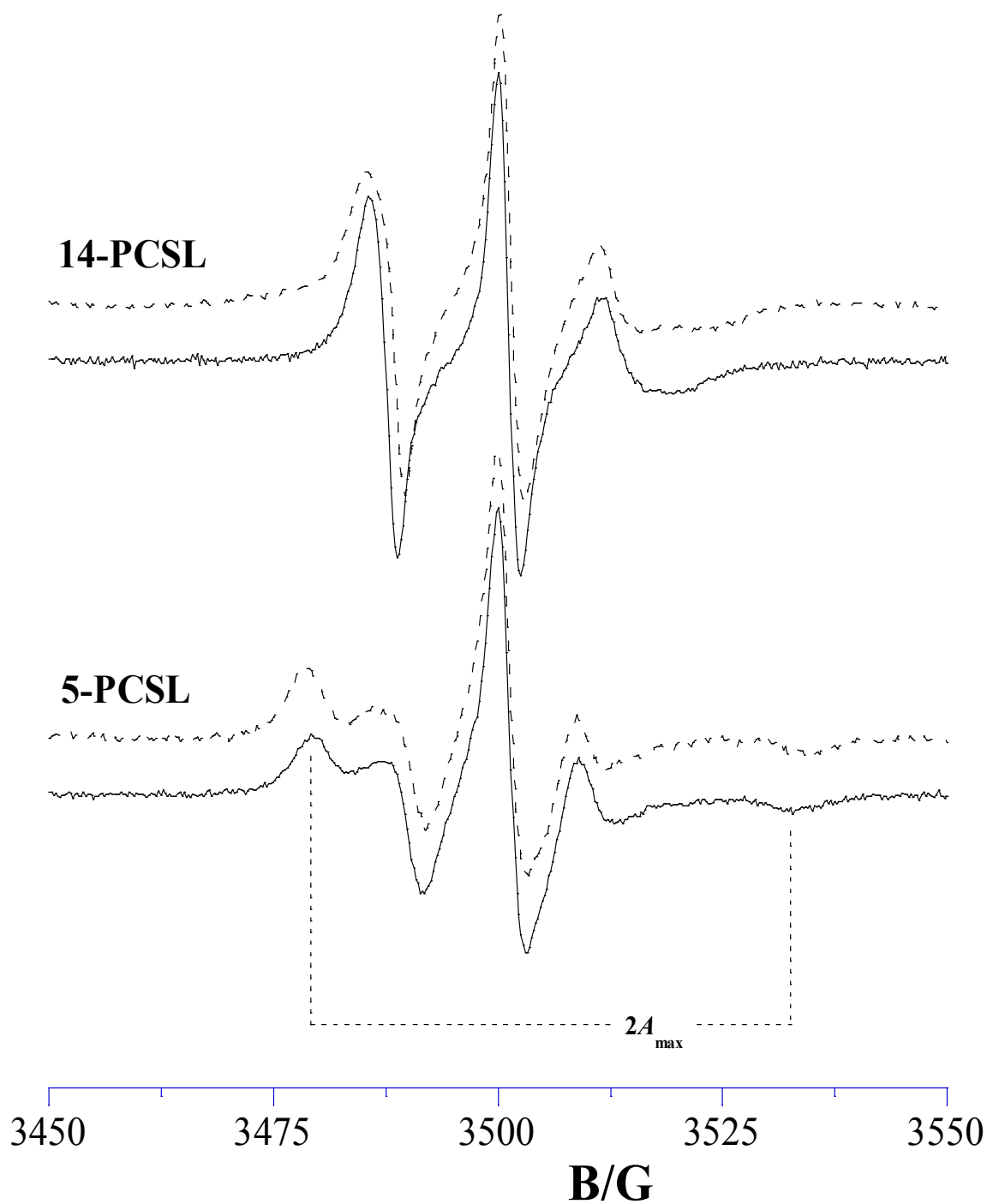


Figure 4.12.6 - ESR spectra of 5-PCSL and 14-PCSL positional isomers of spin-labeled phosphatidylcholine in DOPC/CHOL bilayers in the absence (*solid line*) and in the presence (*dashed line*) of 1:1 wt/wt iAβ5p peptide.

These experimental results indicate that the presence of CHOL has a significant influence on the iAβ5p/bilayers interaction. When iAβ5p is inserted into the DOPC/CHOL membrane environment, two differently abundant populations result evident. Peculiarly,

the fraction of molecules interacting with lipid bilayer is characterized by an anisotropic slow motion spectrum, opposed to the quasi-isotropic spectrum obtained in the absence of CHOL. Furthermore, the presence of CHOL enhances the changes in the 5-PCSL spectrum due to the presence of the peptide. This evidence indicates that the peptide is still able to penetrate the bilayer and that CHOL and peptide exert a synergistic rigidifying action on the bilayer structure. At the same time, in the co-presence of CHOL and peptide the 14-PCSL spectrum shows that the iA β 5p peptide is inserted deeply into the lipid bilayer.

In conclusion, the experiments show that the β -sheet breaker peptide iA β 5p is partially localized in phospholipid bilayers. In the framework of the model according to which early stages of A β peptides self-aggregation occur close to the membrane surface, this β -sheet breaker localization could be strategic for its anti-aggregative activity. The membrane fluidity, modulated by the CHOL amount, is critical to drive the positioning of iA β 5p peptide at the membrane interface.

4.13 The iA β 5p β -breaker peptide regulates the interaction of the A β (25–35) fragment with lipid bilayers through a cholesterol-mediated mechanism.

Association of the iA β 5p and A β (25-35) peptides with lipid bilayers was investigated by analysing changes in ESR spectra of spin-labeled lipids [40]. Two sets of ESR experiments were performed. In the first one, the samples investigated were phosphatidylcholine spin-labeled at different positions, n , in the sn -2 chain (n -PCSL, $n=5,12$) incorporated in membranes of DLPC:CHOL 80:20 wt/wt, in the absence and in the presence of A β (25-35), iA β 5p, or both. In the second set of measurements, a radical analogue of CHOL, 3 β -doxil-5 α -cholestane, was used in order to directly investigate the cholesterol behavior in the systems.

The 5-PCSL and 12-PCSL spectra in the investigated lipid/peptide(s) mixtures are shown in Figure 4.13.1 and Figure 4.13.2, respectively. The former spin-label presents the nitroxide reporter group close to the hydrophilic lipid headgroup, while in the latter one the nitroxide group is positioned close to the terminal methyl group. In DLPC:CHOL bilayers, the spectra of both spin-labels present a clearly defined axially anisotropic lineshape, see Figure 4.13.1A and Figure 4.13.2A, an evidence that, due to the high cholesterol content, the membrane is in the liquid-ordered state. These ESR spectra were quantitatively analyzed by the determination of the acyl chain order parameter, S , and the isotropic hyperfine coupling constant, a'_N , which is an index of the micropolarity experienced by the nitroxide. The S and a'_N values reported in Table 4.13.1 show that, in the absence of any added peptide, the DLPC:CHOL bilayers are characterized by a decrease of both the micropolarity and the local acyl chain ordering in going from the polar headgroups to the inner hydrophobic core of the bilayer. Particularly, the S reduction indicates that, even in the presence of CHOL, the gradient of segmental chain mobility in DLPC bilayers is

preserved. The a'_N decrease is related to the polarity gradient, indicating that the hydrophobicity increases as the nitroxide group moves to the center of the bilayer.

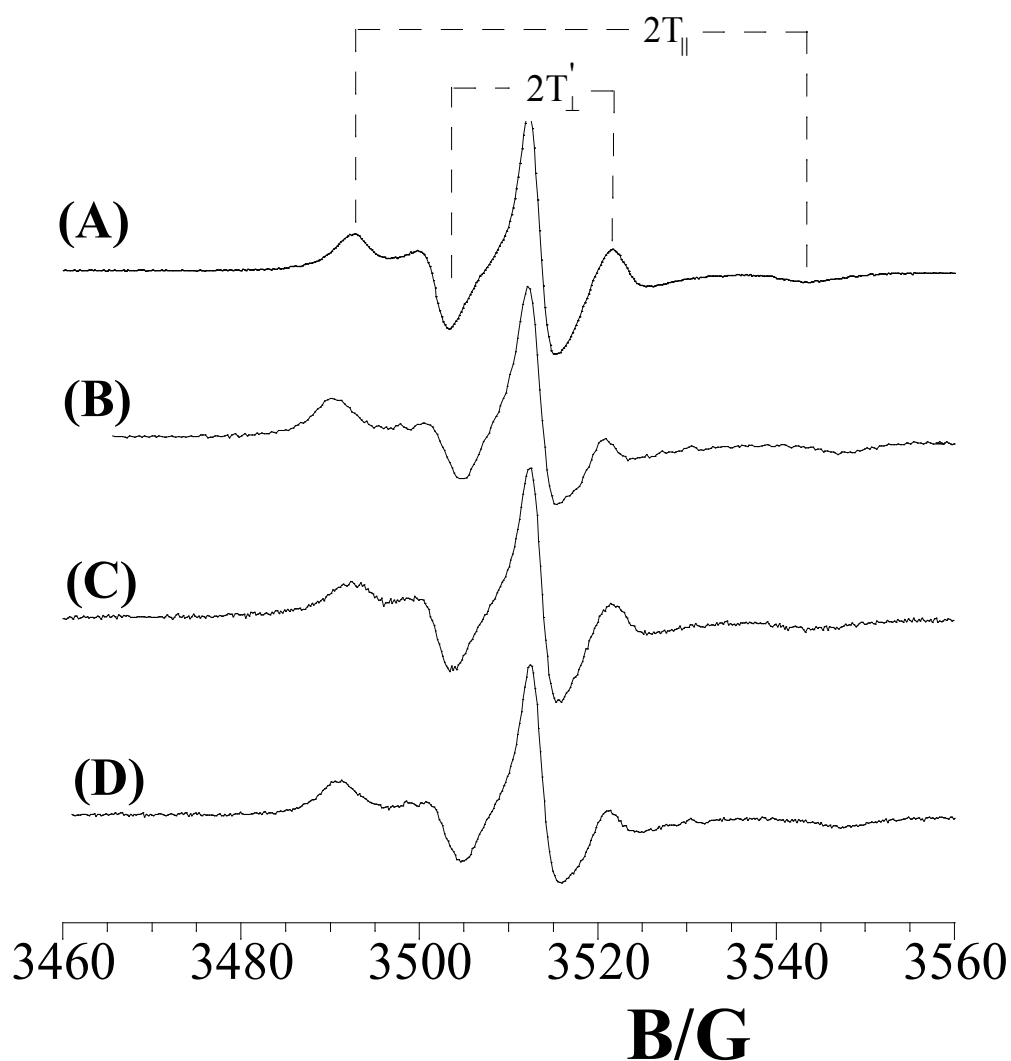


Figure 4.13.1 - ESR spectra of 5-PCSL in bilayers of DLPC:CHOL at 80:20 weight ratio: **(A)** in the absence of peptides; **(B)** in the presence of $A\beta(25-35)$; **(C)** in the presence of $iA\beta 5p$ and **(D)** in the presence of $A\beta(25-35)$ and $iA\beta 5p$ at equimolar ratio.

Association of peptides to the lipid bilayer causes significant variations in the ESR spectra of spin-labeled phospholipids. Particularly, the anisotropy of the 5-PCSL spectrum clearly increases in samples containing $A\beta(25-35)$, see Figure 4.13.1B and Figure 4.13.1D, while the effect of $iA\beta 5p$ alone is much lower. In contrast, the 12-PCSL spectrum is much

more affected by iA β 5p, alone or in combination, than by A β (25-35), see Figure 4.13.2C and Figure 4.13.2D. The S and a'_N values are collected in Table 4.13.1. Below, they are commented separately for each peptide or peptides combination.

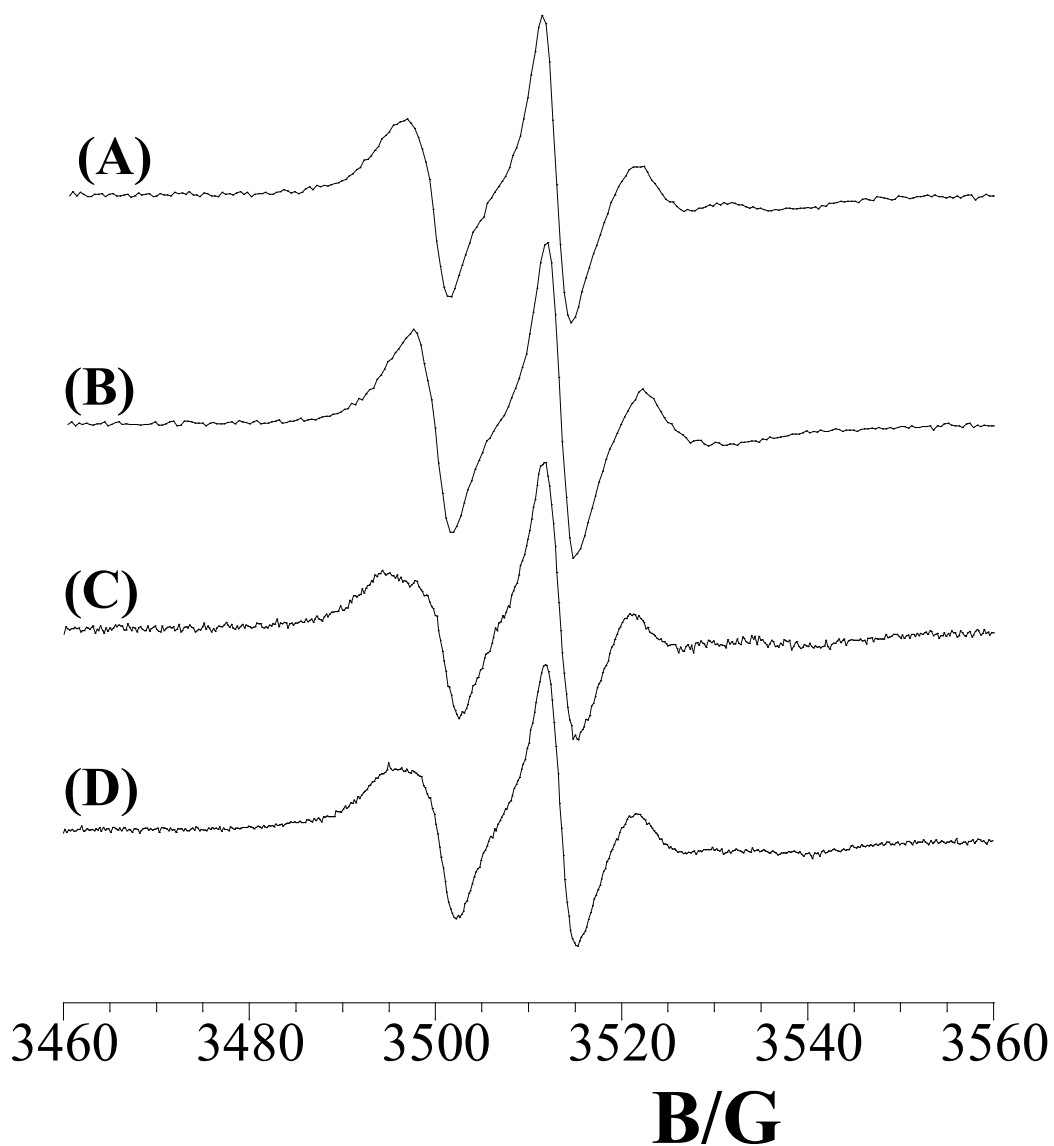


Figure 4.13.2 - ESR spectra of 12-PCSL in bilayers of DLPC:CHOL at 80:20 weight ratio: **(A)** in the absence of peptides; **(B)** in the presence of A β (25-35); **(C)** in the presence of iA β 5p and **(D)** in the presence of A β (25-35) and iA β 5p at equimolar ratio.

First, addition of A β (25-35) causes a clear S increase of 5-PCSL spectrum, with respect to that registered in the peptide absence, while the S value of 12-PCSL decreases. Moreover, a'_N of 12-PCSL spectrum also decreases indicating a reduction of the local

polarity. These evidences indicate that A β (25-35) interacts with the external region of DLPC:CHOL bilayers, only partially penetrating in hydrophobic inner core. At the same time, this peptide causes a re-positioning of cholesterol closer to the hydrophilic external layer, making the inner part of the lipid acyl tail more flexible than in the presence of cholesterol alone [44].

Addition of iA β 5p causes a slight S increase for 5-PCSL, while a much stronger effect is observed for 12-PCSL. The a'_N is marginally affected by this peptide, i.e., no evident variation in the local polarity is detectable. The acyl chains tend to assume a more ordered local structure in the vicinity of guest molecules: consequently, these evidences suggest a deeper penetration of iA β 5p in the bilayer with respect to A β (25-35).

	S	a'_N / G
5-PCSL		
DLPC:CHOL	0.58 ± 0.01	15.2 ± 0.1
DLPC:CHOL+A β (25-35)	0.73 ± 0.01	15.4 ± 0.2
DLPC:CHOL+iA β 5p	0.62 ± 0.02	15.4 ± 0.1
DLPC:CHOL+A β (25-35)+iA β 5p	0.72 ± 0.02	15.4 ± 0.2
12-PCSL		
DLPC:CHOL	0.38 ± 0.02	14.2 ± 0.1
DLPC:CHOL+A β (25-35)	0.24 ± 0.01	12.8 ± 0.1
DLPC:CHOL+iA β 5p	0.45 ± 0.02	14.3 ± 0.1
DLPC:CHOL+A β (25-35)+iA β 5p	0.52 ± 0.01	14.3 ± 0.1

Table 4.13.1 - The order parameter, S , and the isotropic hyperfine coupling constant, a'_N of 5-PCSL and 12-PCSL in lipid bilayers of DLPC:CHOL at 80:20 weight ratio, with and without A β (25-35) peptide, in the absence and in the presence of the β -sheet breaker iA β 5p.

Finally, in the presence of both A β (25–35) and iA β 5p peptides, the S value for 5-PCSL is nearly equal to that obtained in the case of DLPC:CHOL bilayers containing A β (25-35) peptide alone. This evidence suggests that A β (25-35) location relative to the bilayer is not affected by iA β 5p. Interestingly, for 12-PCSL an S value significantly higher than that registered in the presence of A β (25-35) or iA β 5p alone is found. The increase

in the order parameter indicates that not only iA β 5p remains deeply inserted in the bilayer, but also that this peptide inhibits the cholesterol re-positioning observed in samples containing A β (25-35) alone.

Complementary information on the effect of the peptides on the CHOL positioning in the bilayer has been obtained by using 3 β -doxil-5 α -cholestane as spin-probe. Figure 4.13.3 shows ESR spectra of the 3 β -doxil-5 α -cholestane in DLPC:CHOL bilayers, in absence and presence of A β (25-35), iA β 5p, or their equimolar mixture. All the spectra present an almost isotropic slow-motion lineshape. A quantitative analysis of these spectra was realized by determining the isotropic nitrogen hyperfine coupling constant, a'_N , and the tumbling correlation time of the spin-probe, τ_c . These parameters furnish information about the local physicochemical properties of the label. In particular, τ_c variations clearly show changes in the probe rotational mobility, as determined by the microenvironment viscosity and/or by specific interactions. τ_c values were determined according to [41]:

$$\tau_c = (0.65 \times 10^{-9}) \Delta H_0 [(A_0/A_{-1})^{1/2} - 1] \quad (2)$$

where ΔH_0 is the peak-to-peak width of the center line in Gauss, A_0 is the amplitude of the center line, and A_{-1} is the amplitude of the high-field line. All the a'_N and τ_c values are reported Table 4.13.2.

	a'_N / G	$\tau_c \times 10^{-9} / s$
DLPC:CHOL	21.01 \pm 0.01	2.7 \pm 0.1
DLPC:CHOL+A β (25-35)	23.35 \pm 0.02	7.8 \pm 0.2
DLPC:CHOL+iA β 5p	20.61 \pm 0.01	5.2 \pm 0.1
DLPC:CHOL+A β (25-35):iA β 5p	20.49 \pm 0.01	5.0 \pm 0.1

Table 4.13.2 - The isotropic hyperfine coupling constant, a'_N , and the correlation time, τ_c , of the 3 β -doxil-5 α -cholestane in lipid bilayers of DLPC:CHOL at 80:20 weight ratio, with and without A β (25-35) peptide, in the absence and in the presence of the β -sheet breaker iA β 5p.

In the presence of A β (25-35), a'_N increases indicating that the nitroxide reporter group experiences a more polar environment with respect to that found in the absence of peptide. At the same time τ_c increases, indicating that the motion of the spin probe molecules is hampered by a more viscous and structurally ordered microenvironment. Both evidences agree in suggesting that, in the presence of A β (25-35), CHOL molecules move towards the more external region of the bilayer. This part of the bilayer is more hydrated [36] and stiffer with respect of the inner core, as discussed above.

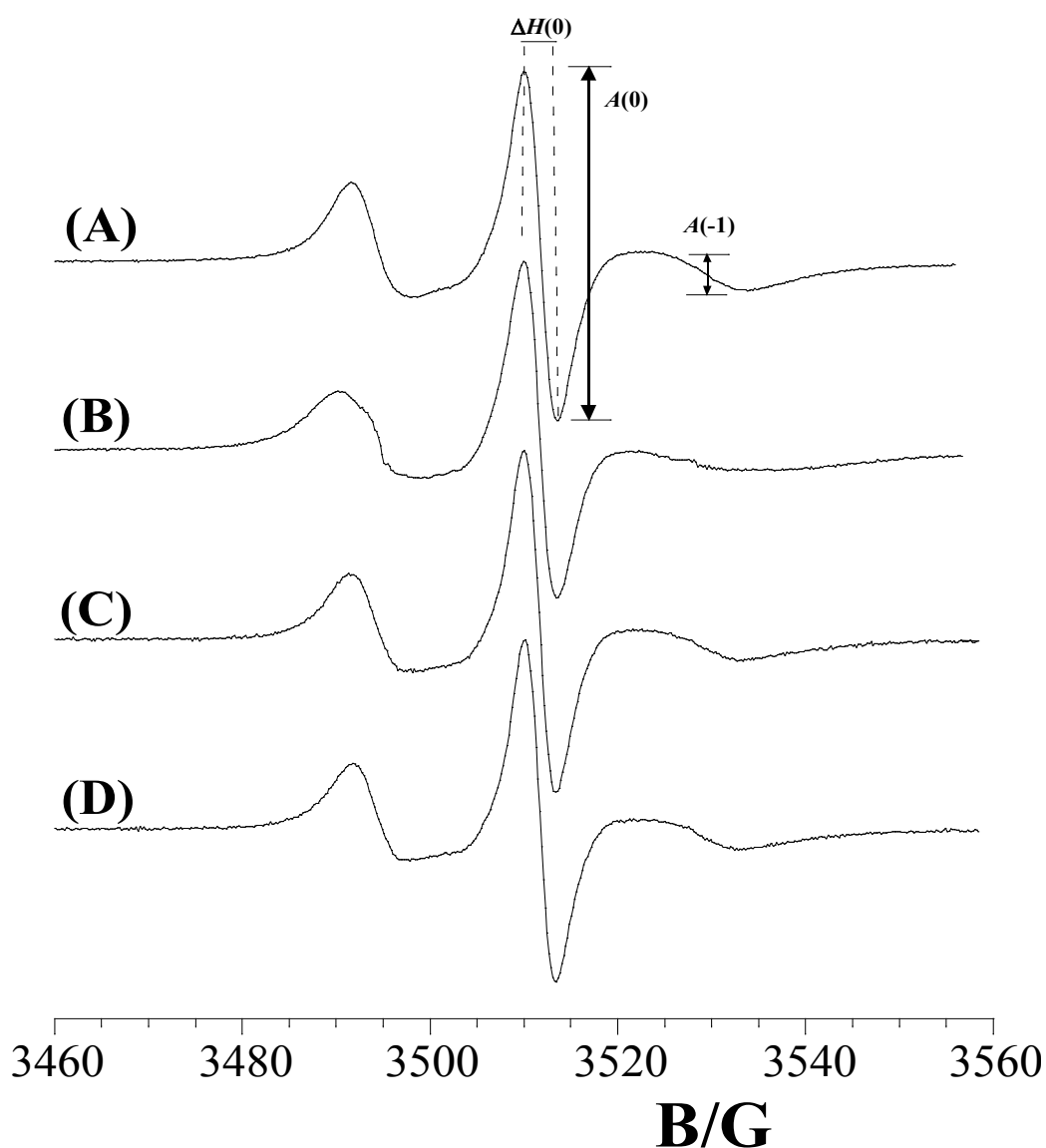


Figure 4.13.3 - ESR spectra 3 β -doxil-5 α -cholestane spin-label in bilayers of DLPC:CHOL at 80:20 weight ratio: (A) in the absence of peptides; (B) in the presence of A β (25-35); (C) in the presence of iA β 5p and (D) in the presence of A β (25-35) and iA β 5p at equimolar ratio.

In the presence of iA β 5p, a'_N slightly decreases indicating a deep insertion of CHOL in the bilayer. This evidence indicates that CHOL tends to position close to iA β 5p peptide, which solubilizes in the inner core of DLPC:CHOL bilayers. The presence of the peptide has a rigidifying effect on the bilayer, which causes the concomitant τ_c increase, which however is much lower than that observed for A β (25-35). Finally, a behavior similar is observed in the co-presence of A β (25-35) and iA β 5p, indicating that the β -breaker peptide plays a major role in determining the CHOL positioning.

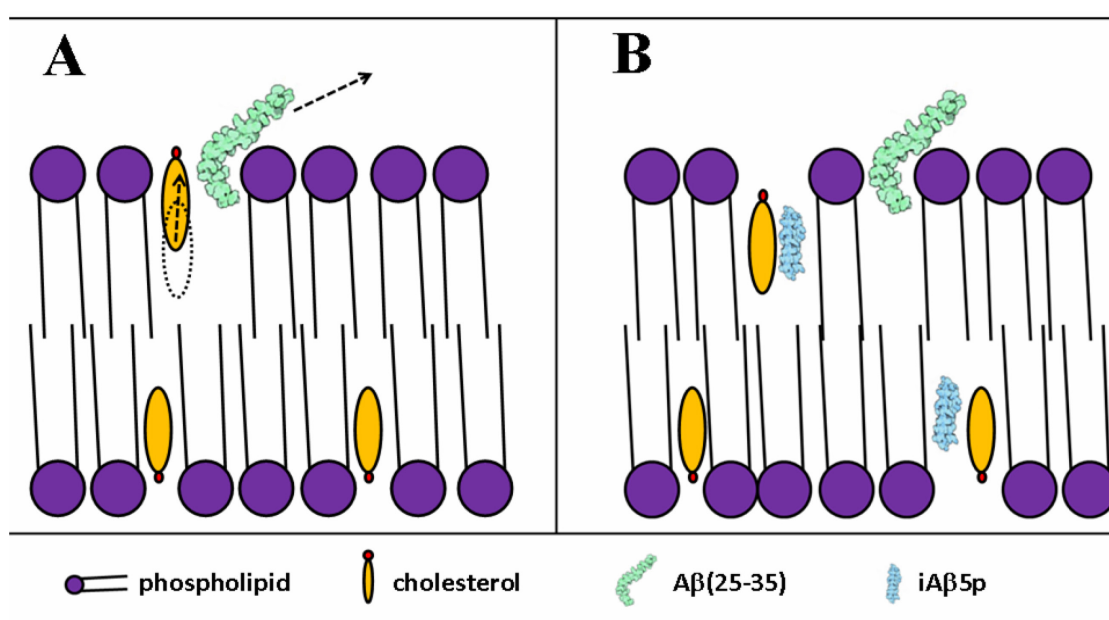


Figure 4.13.4 - Schematic representation of DLPC:CHOL bilayers containing the A β (25-35) peptide in the absence (A) and in the presence of iA β 5p peptide (B).

In conclusion, ESR results presented above show that iA β 5p influences the A β (25-35) interaction with the bilayer through a cholesterol-mediated mechanism, although the two peptides do not directly interact in the membrane environment. Indeed, A β (25-35) causes a crowding of CHOL in the more external region of the bilayer (Figure 4.13.4A). As a consequence, this region becomes stiffer, causing the amyloid fragment expulsion to the external medium and favouring the subsequent fibrillation process. The addition of the

iA β 5p withholds cholesterol, which tends to place close it, in the inner hydrophobic core of the bilayer. This results in a more fluid bilayer external region, thus disfavoring A β (25-35) release (Figure 4.13.4B). In this context we would like to emphasize the CHOL involvement, at molecular level, in finely-tuned membrane processes. Finally, these results indicate that iA β 5p peptide prevents the A β (25-35) exit from the lipid membrane, that is the first step of the A β aggregation process, suggesting a possible mechanism through which membrane-buried β -breaker could help in hampering the β -amyloid self-aggregation.

References

- [1] D'Errico G., Vitiello G., D'Ursi A.M., Marsh D. Interaction of short modified peptides deriving from glycoprotein gp36 of feline immunodeficiency virus with phospholipids membranes, *Eur. Biophys. J.* 38 (2009) 873–882.
- [2] D'Ursi A.M., Giannecchini S., Esposito C., Alcaro M.C., Sichi O., Armenante M.R., Carotenuto A., Papini A.M., Bendinelli M., Rovero P. Development of antiviral fusion inhibitors: short modified peptides derived from the transmembrane glycoprotein of feline immunodeficiency virus. *ChemBioChem* 7 (2006) 774–779.
- [3] Ramakrishnan M., Jensen P.H., Marsh D. a-Synuclein association with phosphatidylglycerol probed by lipid spin labels. *Biochemistry* 42 (2003) 12919–12926.
- [4] D'Errico G., D'Ursi A.M., Marsh D. Interaction of a peptide derived from glycoprotein gp36 of feline immunodeficiency virus and its lipoylated analogue with phospholipid membranes. *Biochemistry* 47 (2008) 5317–5327.
- [5] Sankaram M.B., Marsh D. Protein–lipid interactions with peripheral membrane proteins. In: Watts A (ed) *New comprehensive biochemistry: protein–lipid interactions*, Elsevier, 25 (1993) 127–162.
- [6] Ambrosone L., D'Errico G., Ragone R. Interaction of tryptophan and N-acetyltryptophanamide with dodecylpentaoxyethyleneglycol ether micelles. *Spectrochim. Acta* 53 (1997) 1615–1620.
- [7] Callis P.R., Liu T. Quantitative prediction of Xuroescence quantum yields for tryptophan in proteins, *J. Phys. Chem. B* 108 (2004) 4248–4259
- [8] Merlino A., Vitiello G., Grimaldi M., Sica F., Busi E., Basosi R., D'Ursi A.M., Fragneto G., Paduano L., D'Errico G. On the destabilization of lipid membranes by a peptide derived from glycoprotein gp36 of feline immunodeficiency virus: a combined molecular dynamics/experimental study, *J. Phys. Chem. B* accepted.
- [9] Mitchell T.W., Ekroos K., Blanksby S.J., Hulbert A.J., Else P.L., Differences in membrane acyl phospholipid composition between an endothermic mammal and an ectothermic reptile are not limited to any phospholipid class, *J. Exp. Biol.* 210 (2007) 3440-3450.
- [10] Higgins J.S., Benoitt H.C. *Polymers and Neutron scattering*, Clarendon Press, Oxford, 1994.
- [11] Vacklin H.P., Tiberg F., Fragneto G., Thomas R.K. Composition of supported model membranes determined by Neutron Reflection, *Biochemistry* 44 (2005) 2811-2821.
- [12] Zamyatin A. A. Protein volume in solution, *Prog. Biophys. Mol. Biol.* 24 (1972) 107-123.

- [13] Galdiero S., Falanga A., Vitiello G., Vitiello M., Pedone C., D'Errico G., Galdiero M. Role of membranotropic sequences from herpes simplex virus type I glycoproteins B and H in the fusion process, *Biochim. Biophys. Acta* 1798 (2010) 579–591.
- [14] Vaccaro L., Cross K.J., Kleinjung J., Strauss S.K., Thomas D.J., Wharton A.S., Skehel J.J., Fraternali F. Plasticity of influenza haemagglutinin fusion peptides and their interaction with lipid bilayers, *Biophys. J.* 88 (2005) 25-36.
- [15] Kinoshita K., Furuike S., Yamazaki M. Intermembrane distance in multilamellar vesicles of phosphatidylcholine depends on the interaction free energy between solvents and the hydrophilic segments of the membrane surface, *Biophys. Chem.* 74 (1998) 237-249.
- [16] Stano P., Bufali S., Domazou A., Luisi P.L. Effect of tryptophan oligopeptides on the size distribution of POPC liposomes: a dynamic light scattering and turbometric study, *J. Lipos. Res.* 15 (2005) 29-47.
- [17] Galdiero S., Falanga A., Vitiello M., Browne H., Pedone C., Galdiero M. Fusogenic domains in herpes simplex virus type 1 glycoprotein H, *J. Biol. Chem.* 280 (2005) 28632–28643.
- [18] Galdiero S., Falanga A., Vitiello M., D'Isanto M., Collins C., Orrei V., Browne H., Pedone C., Galdiero M. Evidence for a role of the membrane-proximal region of Herpes Simplex Virus Type 1 glycoprotein H in membrane fusion and virus inhibition, *ChemBiochem* 8 (2007) 885–895.
- [19] Heldwein E.E., Lou H., Bender F.C., Cohen G.H., Eisenberg R.J., Harrison S.C., Crystal structure of glycoprotein B from herpes simplex virus 1, *Science* 313 (2006) 217–220.
- [20] Galdiero S., Vitiello M., D'Isanto M., Falanga A., Cantisani M., Browne H., Pedone C., Galdiero M. The identification and characterisation of fusogenic domains in herpesvirus glycoprotein B molecules, *ChemBioChem* 9 (2008) 758–767.
- [21] Curtain C.C., Separovic F., Nielsen K., Craik D., Zhong Y., Kirkpatrick A. The interactions of the N-terminal fusogenic peptide of HIV-1 gp41 with neutral phospholipids, *Eur. Biophys. J.* 28 (1999) 427–436.
- [22] Gordon L.M., Curtain C.C., Zhong Y.C., Kirkpatrick A., Mobley P.W., Waring A.J. The amino-terminal peptide of HIV-1 glycoprotein 41 interacts with human erythrocyte membranes: peptide conformation, orientation and aggregation, *Biochim. Biophys. Acta* 1139 (1992) 257–274.

- [23] Kleinschmidt J.H., Mahaney J.E., Thomas D.D., Marsh D. Interaction of bee venom melittin with zwitterionic and negatively charged phospholipid bilayers: a spinlabel electron spin resonance study, *Biophys. J.* 72 (1997) 767–778.
- [24] Ramakrishnan M., Jensen P.H., Marsh D. α -synuclein association with phosphatidylglycerol probed by lipid spin labels, *Biochemistry* 42 (2003) 12919–12926.
- [25] Rafalski M., Lear J., DeGrado W. Phospholipid interactions of synthetic peptides representing the N-terminus of HIV gp41, *Biochemistry* 29 (1990) 7917–7922.
- [26] Gianni T., Martelli P.L., Casadio R., Campadelli-Fiume G. The ectodomain of herpes simplex virus glycoprotein H contains a membrane α -helix with attributes of an internal fusion peptide, positionally conserved in the Herpesviridae family, *J. Virol.* 79 (2005) 2931–2940.
- [27] Vitiello G., Falanga A., Galdiero M., Marsh D., Galdiero S., D'Errico G. Lipid composition modulates the interaction of peptides deriving from herpes simplex virus type I glycoproteins B and H with biomembranes, *Biochim. Biophys. Acta* 1808 (2011) 2517–2526.
- [28] Sankaram M.B., Brophy P.J., Marsh D. Interaction of two complementary fragments of the bovine spinal cord myelin basic protein with phospholipids bilayers. An ESR spin label study, *Biochemistry* 28 (1989) 9692–9698.
- [29] White S.H., Wimley W.C. Hydrophobic interactions of peptides with membrane interfaces, *Biochim. Biophys. Acta* 1376 (1998) 339–352.
- [30] Ladokhin A.S., White S.H. Folding of amphipathic α -helices on membranes: Energetics of helix formation by melittin, *J. Mol. Biol.* 285 (1999) 1363–1369.
- [31] Falanga A., Tarallo R., Vitiello G., Vitiello M., Perillo E., Cantisani M., D'Errico G., Galdiero M., Galdiero S. Biophysical characterization and membrane interaction of the two fusion loops of glycoprotein B from herpes simplex type I virus, *submitted*.
- [32] Falanga A., Vitiello M., Cantisani M., Tarallo R., Guarnieri D., Mignogna E., Netti P., Pedone C., Galdiero M., Galdiero S. A peptide derived from herpes simplex virus type 1 glycoprotein H: membrane translocation and applications to the delivery of quantum dots, *Nanomedicine* 2011, DOI: 10.1016/j.nano.2011.04.009.
- [33] Tarallo R., Accardo A., Falanga A., Guarnieri D., Vitiello G., Netti P., D'Errico G., Morelli G., Galdiero S. Clickable functionalization of liposomes with gH625 peptide from Herpes simplex virus type I for intracellular delivery, *Chem. Eur. J.* 17 (2011) 12659 – 12668.

- [34] Grimaldi M., Scrima M., Esposito C., Vitiello G., Ramunno A., Limongelli V., D'Errico G., Novellino E., D'Ursi A.M. Membrane charge dependent states of the β -amyloid fragment A β (16-35) with differently charged micelle aggregates, *Biochim. Biophys. Acta* 1798 (2010) 660-67.
- [35] Tedeschi A., Franco L., Ruzzi M., Paduano L., Corvaja C., D'Errico G. Micellar aggregation of alkyltrimethylammonium bromide surfactants studied by electron paramagnetic resonance of an anionic nitroxide, *Phys. Chem. Chem. Phys.* 5 (2003) 4204-4209.
- [36] Esposito C., Tedeschi A., Scrima M., D'Errico G., Ottaviani M.F., Rovero P., D'Ursi A.M. Exploring interaction of beta-amyloid segment (25-35) with membrane models through paramagnetic probes, *J. Pept. Sci.* 12 (2006) 766-774.
- [37] Kivelson D. Theory of ESR linewidths of free radicals, *J. Chem. Phys.* 33 (1960) 1094.
- [38] Soto C., Sigurdsson E.M., Morelli L., Kumar R.A., Castano E.M., Frangione B. β -sheet breaker peptides inhibit fibrillogenesis in a rat brain model of amyloidosis: implications for Alzheimer's therapy., *Nat. Med.* 4 (1998) 822-826.
- [39] Vitiello G., Grimaldi M., Ramunno A., Ortona O., De Martino G., D'Ursi A.M., D'Errico G. Interaction of a β -sheet breaker peptide with lipid membranes, *J. Pept. Sci.* 16 (2010) 115-122.
- [40] Vitiello G., Grimaldi M., D'Ursi A.M., D'Errico G. The iA β 5p β -breaker peptide regulates the A β (25-35) interaction with lipid bilayers through a cholesterol-mediated mechanism, *Biochem. Biophys. Res. Comm.*, accepted.
- [41] Bates I.R., Boggs J.M., Feix J.B., Harauz G. Membrane-anchoring and charge effects in the interaction of myelin basic protein with lipid bilayers studied by site-directed spin labelling, *J. Biol. Chem.* 278 (2003) 29041-29047.
- [42] Seelig J. Thermodynamics of lipid-peptide interactions, *Biochim. Biophys. Acta* 1666 (2004) 40-50.
- [43] Bhargava K., Feix J.B. Membrane binding, structure, and localization of cecropin-mellitin hybrid peptides: a site-directed spin-labeling study, *Biophys. J.* 86 (2004) 329-336.
- [44] D'Errico G., Vitiello G., Ortona O., Tedeschi A., Ramunno A., D'Ursi A.M., Interaction between Alzheimer's A β (25-35) peptide and phospholipid bilayers: The role of cholesterol, *Biochim. Biophys. Acta* 1778 (2008) 2710-2716.

CONCLUSIONS

In this work, a physico-chemical characterization of lipid membranes and a study of their interaction with peptides involved in important biological processes have been performed by an experimental approach combining different experimental techniques, mainly ESR spectroscopy and Neutron Reflectivity.

The attention has been focused on the biomembranes microstructural properties, as determined by the molecular geometry and charge distribution of the various lipid components. In details, the lipid systems investigated in this work were: i. lysophosphatidylcholine micellar aggregates; ii. POPC and DOPC phospholipid membranes in the presence of cholesterol; iii. POPC membranes containing polyunsaturated phospholipids and iv. liposomes formed by lipopolysaccharides. Although the considered systems presented many differences in terms of components and composition, the driving forces ruling the aggregation process and the properties of the resulting aggregates had a common origin: hydrophobic attraction among the apolar moieties, and electrostatic repulsion among the charged moieties. Steric constraints also play a fundamental role. As a result of the comparative study, the relationship between the aggregates microstructure and their mesoscopic arrangement has been highlighted.

Subsequently, the interaction of peptides with lipid membranes has been investigated. Peptides deriving from the membrane-proximal external region (MPER) of the gp36 and gp41 glycoproteins of Feline and Human Immunodeficiency Viruses, respectively, have been studied in the presence of biomembranes with different lipid composition. Furthermore, peptides deriving from different membranotropic domains of gH and gB glycoproteins of the Herpes simplex virus – type 1, which are considered decisive in favoring the fusion process, have been studied. Finally, two β -amyloid

fragments and one peptide inhibitor of the amyloid self-aggregation have been analyzed in the presence of biomimicking systems.

In all these cases, the main interest has been addressed to the comprehension of the specific mechanism of lipid-peptide interactions and, at the same time, to the role played by the lipid composition in influencing directly or indirectly these interactions. Using different physico-chemical techniques it was possible to realize a broad investigation of the all systems described above, obtaining complementary informations. ESR and NR experiments have furnished many details about the biomembranes microstructure and on its variations induced by the presence of different lipids and of peptides. DLS and SANS measurements have permitted to investigated the mesoscopic structure of the lipid aggregates and, finally, CD and spectrofluorimetric investigations have been allowed the direct monitoring of the peptide behavior and conformational changes in the presence of lipid systems.

The combination of these techniques allowed to highlight, in all the considered systems, the fine interplay between protein/peptides and lipids. Indeed, lipids affect peptides conformation and at the same time, peptides perturb lipid packing and dynamics.

Finally, the presented results shed light on the specificity of the lipid components in determining the bilayer biophysical properties and in modulating their interactions with proteins and peptides, supporting the lipid relevance in all the membrane-related biological processes.

APPENDIX

A1 Electron Spin Resonance spectroscopy

A1.1 Introduction

Electron Spin Resonance (ESR) spectroscopy, or Electron Paramagnetic Resonance (EPR), is a powerful technique for the investigation of paramagnetic species, including organic radicals, inorganic radicals, and triplet states. The basic principles behind ESR are very similar to the more ubiquitous NMR spectroscopy, except that ESR focuses on the interaction of an external magnetic field with the unpaired electron(s) in a molecule, rather than the nuclei of individual atoms [1]. ESR has been used to investigate kinetics, mechanisms, and structures of paramagnetic species and along with general chemistry and physics, has applications in biochemistry, polymer science, and geosciences.

A1.2 Basic theoretical principles

As known, a molecule or atom has discrete (or separate) states, each with a corresponding energy. Spectroscopy is the measurement and interpretation of the energy differences between the atomic or molecular states. With knowledge of these energy differences, the identity, structure, and dynamics of the sample under study can be investigated. It is possible to measure these energy differences, ΔE , because of an important relationship between ΔE and the absorption of electromagnetic radiation. According to Planck's law, electromagnetic radiation will be absorbed if:

$$\Delta E = h\nu \quad (\text{A1.2.1})$$

where h is Planck's constant and ν is the frequency of the radiation. The absorption of energy causes a transition from the lower energy state to the higher energy state.

The energy differences studied in ESR spectroscopy are predominately due to the interaction of unpaired electrons in the sample with a magnetic field produced by a magnet [1]. This effect is called the Zeeman effect. Because the electron has a magnetic moment, it acts like a compass or a bar magnet when you place it in a magnetic field, B_0 . It will have a state of lowest energy when the moment of the electron, μ , is aligned with the magnetic field and a state of highest energy when μ is aligned against the magnetic field. The two states are labeled by the projection of the electron spin, M_s , on the direction of the magnetic field. Because the electron is a spin $\frac{1}{2}$ particle, the parallel state is designated as $M_s = -\frac{1}{2}$ and the antiparallel state is $M_s = +\frac{1}{2}$. From quantum mechanics, the most basic equations of ESR is obtained:

$$E = g\mu_B B_0 M_s = \pm \frac{1}{2} g\mu_B B_0 \quad (\text{A1.2.2})$$

and

$$\Delta E = h\nu = g\mu_B B_0 \quad (\text{A1.2.3})$$

g is the g -factor, which is a proportionality constant and equal to 2.0023 for most samples, but which varies depending on the electronic configuration of the radical or ion. μ_B is the Bohr magneton, which is the natural unit of electronic magnetic moment.

Eqs. A1.2.2 and A1.2.3 suggest that the two spin states have the same energy in the absence of a magnetic field and that the energies of the spin states diverge linearly as the magnetic field increases. In addition, without a magnetic field there is no energy difference to measure and the measured energy difference depends linearly on the magnetic field. Because the energy differences between the two spin states can be changed by varying the magnetic field strength, there are alternative means to obtain spectra. It is possible to apply a constant magnetic field and scan the frequency of the electromagnetic radiation as in conventional spectroscopy. Alternatively, it is possible to keep the electromagnetic radiation frequency constant and scan the magnetic field. A peak in the absorption will

occur when the magnetic field tunes the two spin states so that their energy difference matches the energy of the radiation. This field is called the field for resonance.

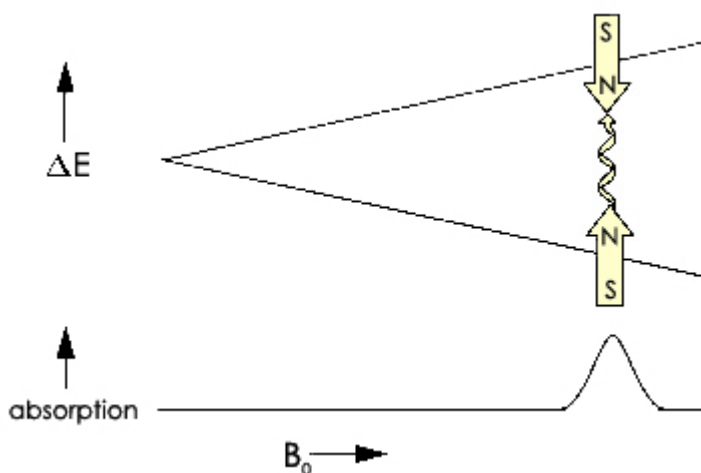


Figure A1.2.1 - Variation of the spin state energies as a function of the applied magnetic field [2].

The field for resonance is not a unique fingerprint for identification of a compound because spectra can be acquired at several different frequencies. Being independent of the microwave frequency, the g -factor $g = h\nu/(\mu_B B_0)$ is much better for that purpose. Notice that high values of g occur at low magnetic fields and vice versa.

Measurement of g -factors can give us some useful information; however, it does not tell us much about the molecular structure of our sample. Fortunately, the unpaired electron, which gives the ESR spectrum, is very sensitive to its local surroundings. The nuclei of the atoms in a molecule or complex often have a magnetic moment, which produces a local magnetic field at the electron. The interaction between the electron and the nuclei is called the hyperfine interaction. It gives us a wealth of information about our sample such as the identity and number of atoms which make up a molecule or complex as well as their distances from the unpaired electron.

Figure A1.2.2 depicts the origin of the hyperfine interaction. The magnetic moment of the nucleus acts like a bar magnet and produces a magnetic field at the electron, B_1 . This

magnetic field opposes or adds to the magnetic field from the laboratory magnet, depending on the alignment of the moment of the nucleus.

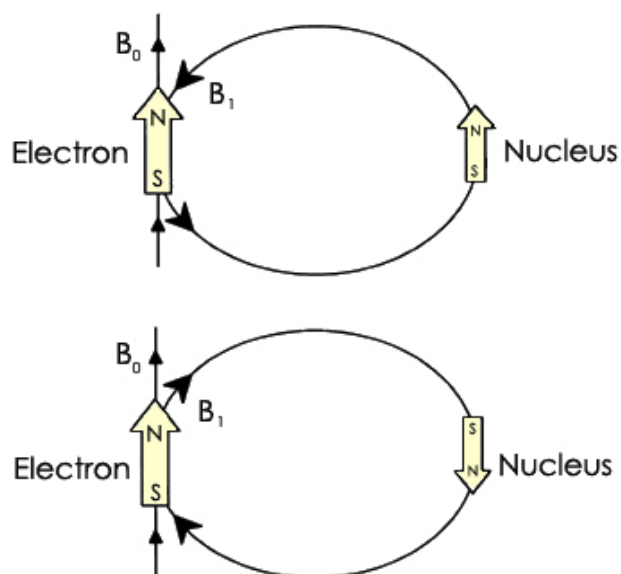


Figure A1.2.2 - Local magnetic field at the electron, B_1 , due to a nearby nucleus [2].

When B_1 adds to the magnetic field, we need less magnetic field from our laboratory magnet and therefore the field for resonance is lowered by B_1 . The opposite is true when B_1 opposes the laboratory field. For a spin $\frac{1}{2}$ nucleus such as a hydrogen nucleus, it is possible to observe that the single ESR absorption signal splits into two signals which are each B_1 away from the original signal, as shown in Figure A1.2.3.

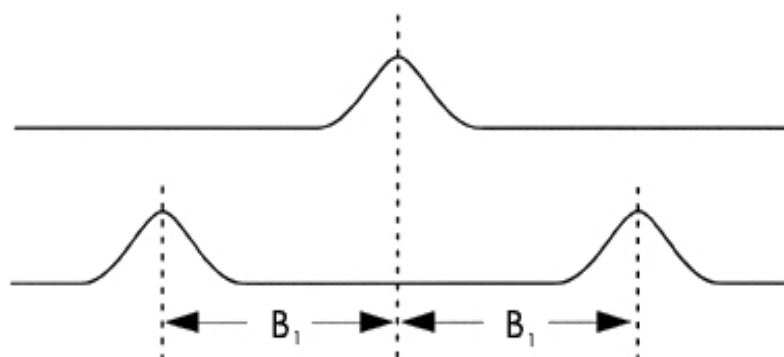


Figure A1.2.3 - Splitting in an ESR signal due to the local magnetic field of a nearby nucleus [2].

If there is a second nucleus, each of the signals is further split into a pair, resulting in four signals. For N spin $1/2$ nuclei, 2^N ESR signals will be generally observed. As the number of nuclei gets larger, the number of signals increases exponentially. Sometimes there are so many signals that they overlap and we only observe the one broad signal.

A1.3 ESR instrument

An ESR spectrometer is composed by four fundamental elements: i. a monochromatic microwave source; ii. a waveguide for guiding the microwave power to the sample; iii. a cavity designed to ensure a proper coupling between the sample and the incoming wave; iv. a detector for microwave power to detect the response of the sample to microwave irradiation. A schematic drawing of an ESR spectrometer is represented in Figure A1.3.1.

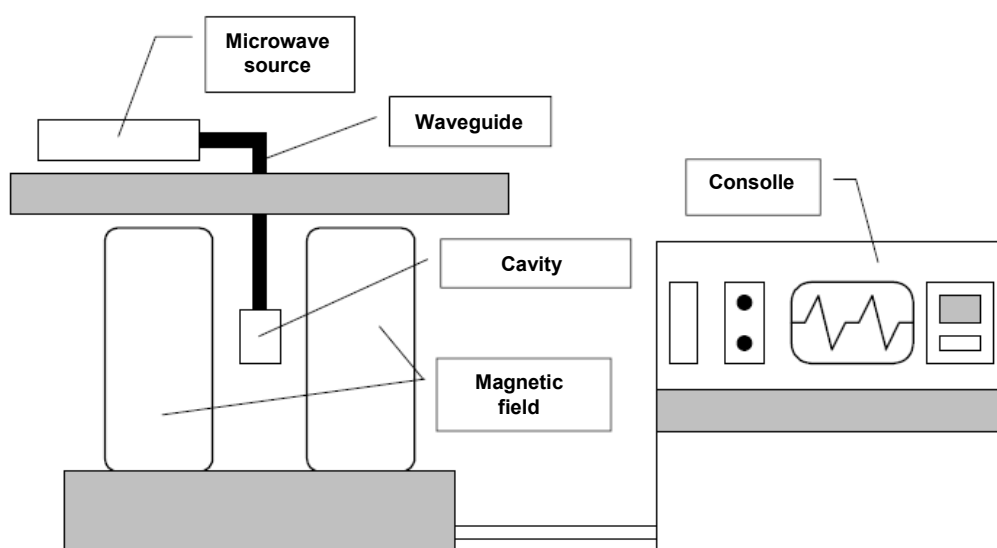


Figure A1.3.1 – Schematic representation of an ESR spectrometer.

The magnetic field is generated by an electromagnet, usually water-cooled, which is able to provide a stable and uniform field in the area where the sample is placed. The microwave source can be a gunn diode or a klystron; in both cases, a microwaves beam is

generated at a fixed frequency between 9 and 10 GHz (X-band). This generated microwave beam go to the sample is sent through the waveguide. The cavity, in which the sample is placed, is at the center of the two magnetic field poles and receives the microwaves through the waveguide. The cavity is designed in order to get inside a regular distribution of the magnetic field lines generated by the electromagnetic radiation coming from the source and perpendicular to the static magnetic field generated by a solenoid. Finally, the “consoles” is the interface between the spectrometer and the user from which it is possible to make all the settings and set the parameters for the spectra recording.

Samples for ESR can be gases, single crystals, solutions, powders, and frozen solutions. For solutions, solvents with high dielectric constants are not advisable, as they will absorb microwaves. For frozen solutions, solvents that will form a glass when frozen are preferable. Good glasses are formed from solvents with low symmetry and solvents that do not hydrogen bond. A sample is usually placed in a quartz tube, which is the material devoid of paramagnetic impurities, of 3-5 mm in diameter that is inserted into the cavity and secured in place by the media. The side walls of the resonant cavity are coils that modulate the amplitude of the signal, usually at a frequency of 100 kHz, generating the first derivative of the absorption curve (Figure A1.3.2).

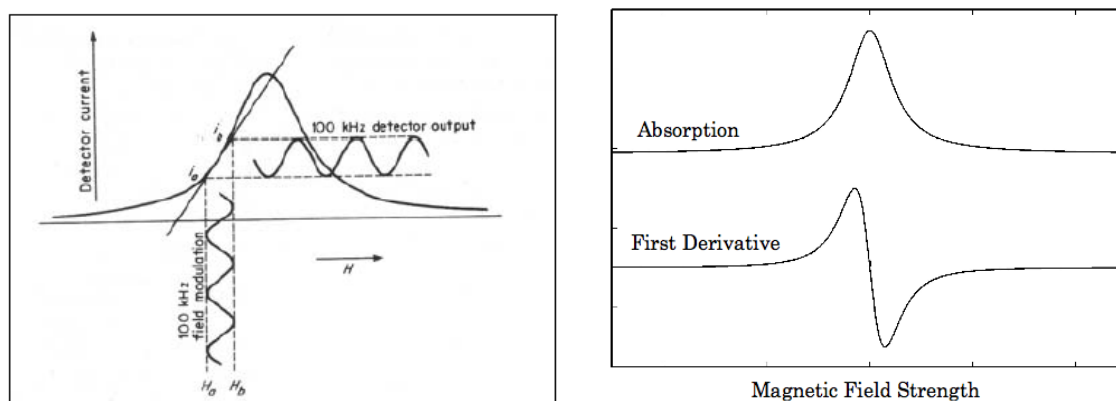


Figure A1.3.2 – The effect of the modulation in the ESR signal (*on the left*) and an example of first and second derivative ESR spectrum (*on the right*).

A1.4 Application of ESR spectroscopy in biophysics

ESR technique is very used in biophysical studies, although all biological systems possess no intrinsic paramagnetism and hence in the unlabeled state do not give rise to a spectrum. For this reason, the introduction of a stable free radical (“spin-label”) in the samples allows to use ESR spectroscopy to study specific environments, for example biological membranes [3]. The spin-label, which is invariably used, is the nitroxide radical, which has a three-line nitrogen hyperfine structure whose splitting varies with the orientation of the magnetic field relative to the nitroxide axes. The two classes of nitroxide spin-labels which are used in membrane studies are those derived from the oxazolidine and the piperidine or pyrrolidine rings. In both cases the nitroxide group is flanked by quaternary carbon atoms, protecting the radical from disproportionation reactions, which accounts for the high stability. Generally, these spin-labels are used to probe the biological molecules, allowing to also study the non-paramagnetic systems. Consequently, by using spin-labeled substances, ESR spectroscopy provides to be a fruitful experimental approach to the study of the interactions between peripheral as well as integral proteins and membranes. Both the proteins and the lipids can be labeled, so that the systems can be studied by different “points of view”.

A2 Neutron Reflectivity

A2.1 Introduction

Neutron Reflectivity (NR) is a powerful technique for the probing of surface structures and buried interfaces on the nanometer length scale [4]. This technique involves shining a highly collimated beam of neutrons onto a planar surface and measuring the intensity of reflected radiation as a function of angle or neutron wavelength. For biological systems it presents the advantage that light elements as H, C, O, and N are strong scatterers and different isotopes of the same element have different scattering lengths so that isotopic substitution may be used to highlight different parts of the interface. In addition, the possibility of measuring at different contrasts allows for the application of more suitable multilayer models to interpret the adsorption data with a good degree of confidence. Data from all profiles are fitted simultaneously, and this reduces the uncertainty in the structural parameters to the fraction of nanometer scale. It represents a powerful method to provide structural details in lipid bilayers and in their interaction with proteins or peptides [4]. For biophysics studies, a great advantage is represented by the possibility to use very small sample quantity ($<10^{-6}$ g) and it is suitable for work with expensive or rare macromolecules.

While specular reflection (angle of incoming beam equal to angle of reflected beam) gives information in the direction perpendicular to the interface, the lateral structure of the interface may be probed by the nonspecular scattering measured at reflection angles different from the specular one [5]. This technique is widely used with x-rays while there are far fewer data in the neutron case due to the smaller intensity of neutron beams. An example relevant in biophysics where the neutron technique has been applied is the off-specular scattering from highly oriented multilamellar phospholipid membranes [6]. For this reason, neutron reflection is much used for studies of surface chemistry, including lipids, proteins, surfactants, polymers and mixtures adsorbed at liquid/fluid and solid/fluid interfaces. It is also used to study the surface magnetism, for example ultrathin Fe films,

magnetic multilayers, superconductors and solid films, as Langmuir–Blodgett films, thin solid films, multilayers, polymer films [7].

Since many biological processes occur at interfaces, the possibility of using neutron reflection to study structural and kinetic aspects of model as well as real biological systems is of considerable interest. However, the number of such experiments so far performed is small. The reason for this is probably because it is well known that the most effective use of neutron reflection involves extensive deuterium substitution and this is not usually an available option in biological systems. This problem may be partially solved by deuterating other parts of the interface [8].

A2.2 Basic theoretical principles

In a neutron reflectivity experiment, the specular reflection at the silicon/water interface, R , is measured as a function of the wave vector transfer, q :

$$q = \frac{4\pi}{\lambda} \sin \theta \quad (1.2.1)$$

where λ is the wavelength and θ the angle of the incoming beam to the surface. $R(q)$ is related to the scattering length density across the interface, $\rho(z)$, by:

$$R(q) = \frac{16\pi^2}{q^2} |\hat{\rho}(q)|^2 \quad (1.2.2)$$

where $\hat{\rho}(q)$ is the one dimensional Fourier transform of $\rho(z)$:

$$\hat{\rho}(q) = \int_{-\infty}^{+\infty} \exp(-iqz) \rho(z) dz \quad (1.2.3)$$

$\rho(z)$ being a function of the distance perpendicular to the interface (Figure 2.2.1). ρ is related to the composition of the adsorbed species by:

$$\rho(z) = \sum_j n_j(z) b_j \quad (1.2.4)$$

where $n_j(z)$ is the number of nuclei per unit volume and b_j is the scattering length of nucleus j .

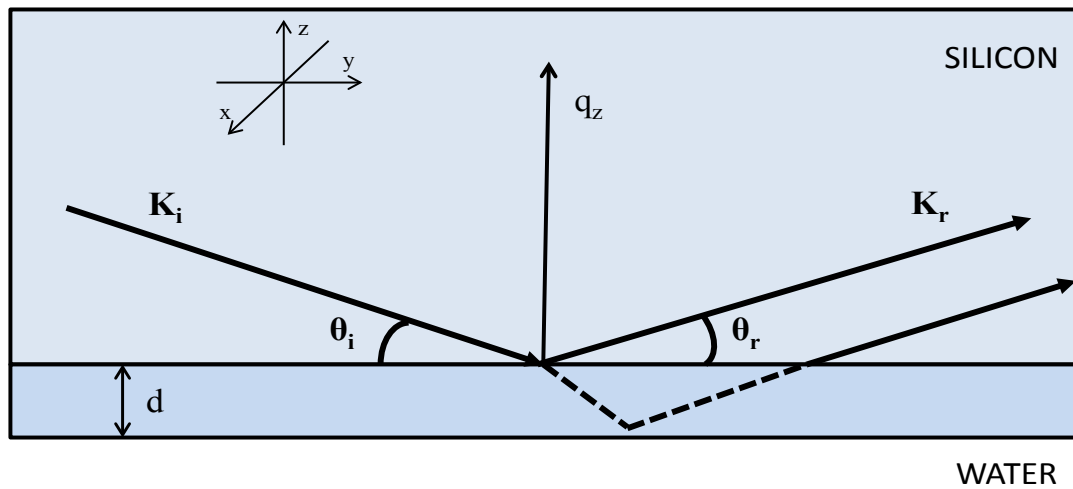


Figure 2.2.1 – Reflection of an incident beam from two flat interfaces; K_i and K_r are the incident and reflected wave vectors; q_z is the component of the momentum transfer perpendicular to the interface.

The scattering lengths of the constituent fragments of any species adsorbed at the surface are the fundamental quantities from which the interfacial properties and microstructural information on the lipid bilayer are derived. Measurement of a sample in different solvent contrasts greatly enhances the sensitivity of the technique [4].

A2.3 NR measurements

The basic features of a reflection experiment are: i. a radiation source; ii. a wavelength selector (or choppers); iii. a system of collimation; iv. the sample and v. a detection system. The production of neutrons requires either a nuclear reactor, where a continuous neutron beam is produced by nuclear fission, or a pulsed source, where a pulsed beam is obtained when a burst of high-energy protons or electrons from a particle accelerator hits a heavy nucleus. In both cases, neutron energies are too high for structural or dynamical studies and are reduced in a moderator tank where the neutrons are repeatedly scattered losing energy at each collision until thermal equilibrium is reached.

Thermal neutron energies are of the order of $k_B T$ where T is the temperature of the water moderator and k_B the Boltzmann constant. Neutrons can interact with nuclei via nuclear forces or with the magnetic moment of unpaired electrons.

A2.4 Neutron reflectometers

A specular NR experiment measures the reflectivity as a function of the wave vector perpendicular to the reflecting surface, q_z . The measurement can be made by varying either or both the glancing angle of incidence θ and the neutron wavelength λ . Generally, the different mode is related to the type of the neutron source. Indeed, in most nuclear reactors, measurements are usually made at a fixed value of λ using long wavelength neutrons and a θ (reflection angle)– 2θ (detector angle) scan. Wavelength selection may be achieved by Bragg scattering from a crystal monochromator or by velocity selection through a mechanical chopper. The resolution in such measurements is determined by both angular, $\Delta\theta$, and wavelength, $\Delta\lambda$, spread. In contrast, at spallation sources time-of-flight instruments (TOF) operate at fixed θ and the range of momentum transfer results from the different wavelengths that comprise a polychromatic neutron beam. The values of q are determined from the time of arrival of each neutron as a function of its wavelength, the shorter wavelengths neutrons arriving first, so that each pulse gives information over the whole q range. The relative resolution $\Delta q/q$ is dominated by the angular divergence $\Delta\theta$ of the beam and is therefore constant over the measurement of the reflectivity profile. However the actual resolution Δq varies widely over the whole range.

Two important examples of reflectometers are D17 and FIGARO instruments at the Institut Laue-Langevin (ILL) in Grenoble (France).

The reflectometer D17 has already proved to be an excellent tool for investigating surfaces and interfaces in the realms of physics, biology and chemistry. The instrument has two modes of operation, time-of-flight and monochromatic, the latter incorporating the

polarised-neutron option [9]. Both modes are flexible in the wave-vector-transfer (q) resolution. The loosest resolution required to resolve the sample structure can be chosen (and hence the highest flux), enabling the lowest reflectivities and hence the widest q -range to be measured. Figure A2.4.1 shows a simplified layout of the instrument.

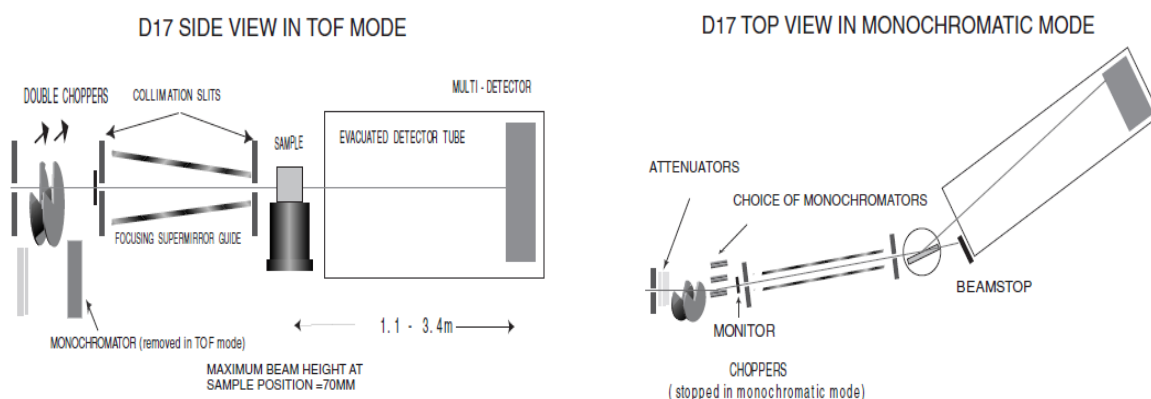


Figure A2.4.1 - Layout of D17 showing the two modes of operation [9].

Starting with a vertical guide implied that, with the aid of focusing, the instrument would only be optimised for a horizontal reflection plane (vertical samples). Due to the focusing the white beam flux at the sample position is 9.6×10^9 n/s/cm². The complication of having both monochromatic and TOF modes was justified by the specific advantages of each case and that neither option would adversely affect the other. TOF allows continuously variable resolution and as an entire order of magnitude in q can be measured simultaneously in less than a minute, kinetic studies are possible. On the other hand a monochromatic beam is far easier for magnetic experiments (no q -dependent polarisation efficiency) and is the most efficient in that the peak flux is used for each point in q .

Fluid Interfaces Grazing Angles Reflectometer (FIGARO) is a new world-class neutron reflectometer, designed to deliver a complementary range of features to the neighbouring reflectometer D17, which is optimised for vertical surfaces [9]. In Figure A2.4.2 a schematic representation of FIGARO and its principal components is shown [10].

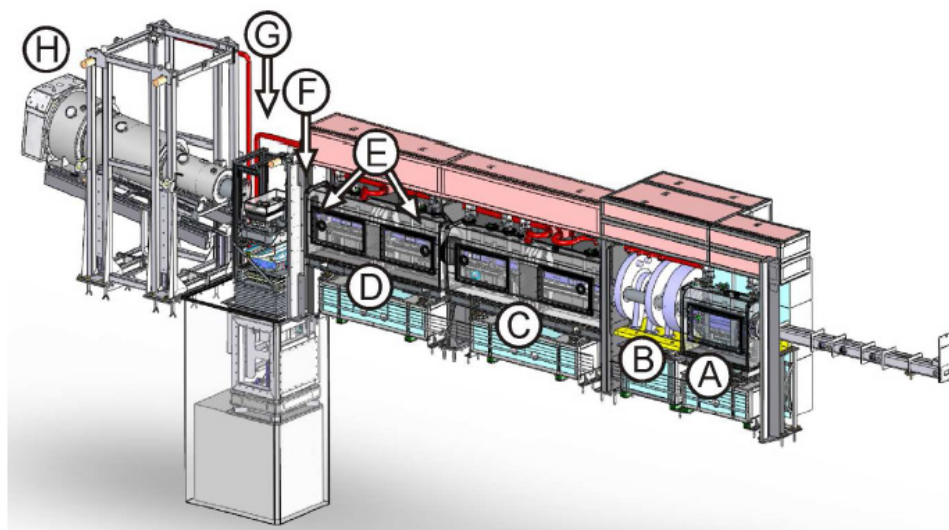


Figure A2.4.2 - Schematic of the instrument highlighting the following primary components: (A) frame overlap mirrors, (B) chopper assembly, (C) deflector mirrors, (D) collimation guide, (E) collimation slits, (F) beam attenuator, (G) sample position and (H) area detector [10].

Important strengths lie in its high flux, its versatility to tune flux, q range, resolution and instrument geometry for any given experiment, and its expanding range of sophisticated sample environments. The stable reactor source and very fast data acquisition at low q makes the instrument particularly suited to kinetic studies. For example, useful kinetic measurements as short as 1s have been successfully fitted in user experiments, and the product of scattering length density and thickness for compositional analysis of adsorption layers at the air/water interface can be determined to high precision in less than one minute. Data acquisition over the full q range can be done with just two incident angles in minutes and rarely requires more than one hour [10].

A2.5 Background subtraction

As q_z increases the noise level increases since not all the neutrons detected are from specular reflection. At high values of q_z the reflectivity is very small and most of the beam passes into the subphase (e.g. water) where it is scattered either incoherently or by multiple diffraction. A proportion of this scattering enters the detector with the specular reflection

and contributes a background, which has to be subtracted from the profile. There are other sources of background related to the environment of the sample and the components of the reflectometer, although the incoherent scattering from the sample itself is the major source.

The principle of background subtraction is the same in every reflectometer. On zero or one-dimensional detectors, the off specular scattering at each incident angle is measured and subtracted from the profile. This may be done by rotating the detector to higher and lower angles, averaging the two measurements and subtracting the resulting profile from the reflectivity. In the case of solid/liquid samples, the background is high because of the incoherent scattering of the liquid and the scattering from Teflon and aluminium which constitute the cell used for a NR experiments, and usually a maximum of six orders of magnitude in reflectivity are measured [4].

A2.6 Data analysis

As introduced in the Section 3.10, the method of analysis often used for specular reflection data involves the construction of a model of the interface that may be represented by a series of parallel layers of homogeneous material. Each layer is characterized by a scattering length density, ρ , a thickness, d , a solvent volume fraction, and an interfacial roughness, σ , which are used to calculate a model reflectivity profile. The calculated profile is compared to the measured profile and the quality of the fitting is assessed either visually or by using χ^2 in the least-squares method. There are different fitting programs, as AFIT or MOTOFIT programs [11,12]. They allow the simultaneous analysis of reflectivity profiles from the same sample in different water contrasts, characterizing each layer by varying the defined parameter until the optimum fit to the data is found. In particular, in a solid/liquid experiment the solid medium and the liquid solution are considered as having infinite thickness and have a fixed scattering length density. The adsorbate may form a single layer or a more complicated structure on the surface. By variation of ρ and for each layer, the

calculated profile may be compared with the measured profile until the optimum fit to the data is found. Although any one profile may not provide a unique solution, the use of different isotopic contrasts together with the physical and chemical constraints of the system can usually ensure that an unambiguous model of the interface is obtained.

Contrast variation relies on the fact that the different nuclei scatter neutrons with different amplitude, and sometimes, as in the case of protons and deuterons, with opposite phase. By using a combination of hydrogenated and deuteriated materials the reflectivity profile of a system can be substantially changed while keeping the same chemical structure at the interface. It is also possible, by adjustment of the H/D ratio, to prepare solvents which are contrast matched to the medium through which neutrons pass before reaching the interface, that is the bulk solid in a solid/fluid experiment or air in a liquid/air experiment [5]. The water contrasts more commonly used are: i. H₂O with $\rho = -0.56 \times 10^{-6} \text{ \AA}^{-2}$; ii. SMW (*silicon-matched water*), a mixture of H₂O and D₂O with the same refraction index for neutrons as bulk silicon, with $\rho = 2.07 \times 10^{-6} \text{ \AA}^{-2}$; iii. 4MW, a mixture of H₂O and D₂O with $\rho = 4 \times 10^{-6} \text{ \AA}^{-2}$ and iv. D₂O, with a $\rho = 6.35 \times 10^{-6} \text{ \AA}^{-2}$. The contrast between the solid (or air) and the solvent is then zero, giving a reflectivity profile arising only from the interfacial region. From the value of the scattering length density of the layer information about its composition is obtained.

References

- [1] Weil J.A., Bolton J.R., Wertz J.E. *Electron Paramagnetic Resonance, Elementary Theory and Practical Applications*, Wiley-Interscience, New York (1994).
- [2] <http://www.bruker-biospin.com/cw.html>
- [3] Marsh D. *Electron Spin Resonance: spin-labels in Membrane Spectroscopy*, E. Grell, Ed. Springer-Verlag, Berlin (1981) 51-142.
- [4] Fragneto-Cusani G. Neutron reflectivity at the solid/liquid interface: examples of applications in biophysics, *J. Phys. Condens. Matter* 13 (2001) 4973–4989.
- [5] Sinha S.K., Sirota E.B., Garoff S., Stanley H.B. X-ray and neutron scattering from rough surfaces, *Phys. Rev. B* 38 (1998) 2297-2311.
- [6] Münster C., Salditt T., Vogel M., Siebrecht R., Peisl J. Nonspecular neutron scattering from highly aligned phospholipid membranes, *Europhys. Lett.* 46 (1999) 486.
- [7] Penfold J. Neutron reflectivity and soft condensed matter, *Curr. Opin. Coll. Interf. Sci.* 7 (2002) 139-147.
- [8] Fragneto G., Su T.J., Lu J.R., Thomas R.K., Rennie A.R. *Phys. Chem. Chem. Phys.* 2 (2000) 5214-5221.
- [9] Cubitt R., Fragneto G. D17: The new reflectometer at the ILL, *Appl. Phys. A (Suppl.)* 74 (2004) S329-S331.
- [10] Campbell R.A., Wacklin H.P., Sutton I., Cubitt R., Fragneto G. FIGARO: The new horizontal neutron reflectometer at the ILL, *Eur. Phys. J. Plus* 126 (2011) 107-129.
- [11] Thirtle P.N. *Afit simulation program*, v. 3.1, Oxford University, 1997.
- [12] Nelson A.J. Co-refinement of multiple-contrast neutron/X-ray reflectivity data using MOTOFIT, *Appl. Crystallogr.* 39 (2006) 273-276.

PUBLICATIONS

- Vitiello G., Ciccarelli D., Ortona O., D'Errico G. **Microstructural characterization of lysophosphatidylcholine micellar aggregates: the structural basis for their use as biomembrane mimics**, *J. Coll. Int. Sci.* 336 (2009) 827–833.
- D'Errico G., Vitiello G., D'Ursi A.M., Marsh D. **Interaction of short modified peptides deriving from glycoprotein gp36 of feline immunodeficiency virus with phospholipid membranes**, *Eur. Biophys. J.* 38 (2009) 873-882.
- Vitiello G., Grimaldi M., Ramunno A., Ortona O., De Martino G., D'Ursi A.M., D'Errico G. **Interaction of a β -sheet breaker peptide with lipid membranes**, *J. Pept. Sci.* 16 (2010) 115-122.
- Galdiero S., Falanga A., Vitiello G., Vitiello M., Pedone C., D'Errico G., Galdiero M. **Role of membranotropic sequences from Herpes Simplex virus type I glycoproteins B and H in the fusion process**, *Biochim. Biophys. Acta Biomembranes* 1798 (2010) 579-591.
- Grimaldi M., Scrima M., Esposito C., Vitiello G., Ramunno A., Limongelli V., D'Errico G., Novellino E., D'Ursi A.M. **Membrane charge dependent states of the β -amyloid fragment A β (16-35) with differently charged micelle aggregates**, *Biochim. Biophys. Acta Biomembranes* 1798 (2010) 660-667.
- D'Errico G., Silipo A., Mangiapia G., Vitiello G., Molinaro A., Lanzetta R., Paduano L. **Mesoscopic and microstructural characterization of liposomes formed by the lipooligosaccharide from salmonella minnesota strain 595 (Re mutant)**, *Phys. Chem. Chem. Phys.* 12 (2010) 13574–13585.
- Mangiapia G., Coppola C., Vitiello G., D'Errico G., Radulescu A., De Napoli L., Montesarchio D., Paduano L. **Nanostructuring of CyPLOSes (Cyclic Phosphate-linked OligoSaccharides), novel saccharide-based synthetic ion transporters**, *J. Coll. Int. Sci.* 354 (2011) 718–724.
- Vitiello G., Falanga A., Galdiero M., Marsh D., Galdiero S., D'Errico G. **Lipid composition modulates the interaction of peptides deriving from Herpes Simplex Virus type I glycoproteins B and H with biomembranes**, *Biochim. Biophys. Acta Biomembranes* 1808 (2011) 2517-2526.
- Tarallo R., Accardo A., Falanga A., Guarnieri D., Vitiello G., Netti P., D'Errico G., Morelli G., Galdiero S. **Clickable functionalization of liposomes with gH625 peptide from *Herpes simplex virus* type I for intracellular delivery**, *Chemistry* 17 (2011) 12659-12668.
- Vitiello G., Grimaldi M., D'Ursi A.M., D'Errico G. **The iA β 5p β -breaker peptide regulates the A β (25–35) interaction with lipid bilayers through a cholesterol-mediated mechanism**, *Biochem. Biophys. Res. Comm.* accepted.
- Merlino A., Vitiello G., Grimaldi M., Sica F., Busi E., Basosi R., D'Ursi A.M., Fragneto G., Paduano L., D'Errico G. **Interaction between a peptide derived from glycoprotein gp36 of feline immunodeficiency virus and a phospholipid bilayer: a combined molecular dynamics/experimental study**, *J. Phys. Chem. B* accepted.